UNIVERSITAT
POLITÈCNICA
DE VALÈNCIA

Doctoral Thesis

Filter Optimization for Personal Sound Zones Systems

by

Vicent Molés-Cases

Supervisors:

Dr. Gema Piñero Sipán
Dr. Alberto González Salvador

Valencia, Spain
June, 2022

Abstract

Personal Sound Zones (PSZ) systems deliver different sounds to a number of listeners sharing an acoustic space through the use of loudspeakers together with signal processing techniques. These systems have attracted a lot of attention in recent years because of the wide range of applications that would benefit from the generation of individual listening zones, e.g., domestic or automotive audio applications. A key aspect of PSZ systems, at least for low and mid frequencies, is the optimization of the filters used to process the sound signals. Different algorithms have been proposed in the literature for computing those filters, each exhibiting some advantages and disadvantages. In this work, the state-of-the-art algorithms for PSZ systems are reviewed, and their performance in a reverberant environment is evaluated. Aspects such as the acoustic isolation between zones, the reproduction error, the energy of the filters, and the delay of the system are considered in the evaluations. Furthermore, computationally efficient strategies to obtain the filters are studied, and their computational complexity is compared too. The performance and computational evaluations reveal the main limitations of the state-of-the-art algorithms. In particular, the existing solutions can not offer low computational complexity and at the same time good performance for short system delays. Thus, a novel algorithm based on subband filtering that mitigates these limitations is proposed for PSZ systems. In addition, the proposed algorithm offers more versatility than the existing algorithms, since different system configurations, such as different filter lengths or sets of loudspeakers, can be used in each subband. The proposed algorithm is experimentally evaluated and tested in a reverberant environment, and its efficacy to mitigate the limitations of the existing solutions is demonstrated. Finally, the effect of the target responses in the optimization is discussed, and a novel approach that is based on windowing the target responses is proposed. The proposed approach is experimentally evaluated in two rooms with different reverberation levels. The evaluation results reveal that an appropriate windowing of the target responses can reduce the interference level between zones.

Keywords: personal sound zones, least squares, weighted pressure matching, subband filtering.

Resumen

Los sistemas de zonas de sonido personal (o sus siglas en inglés PSZ) utilizan altavoces y técnicas de procesado de señal para reproducir sonidos distintos en diferentes zonas de un mismo espacio compartido. Estos sistemas se han popularizado en los últimos años debido a la amplia gama de aplicaciones que podrían verse beneficiadas por la generación de zonas de escucha individuales. El diseño de los filtros utilizados para procesar las señales de sonido es uno de los aspectos más importantes de los sistemas PSZ, al menos para las frecuencias bajas y medias. En la literatura se han propuesto diversos algoritmos para calcular estos filtros, cada uno de ellos con sus ventajas e inconvenientes. En el presente trabajo se revisan los algoritmos para sistemas PSZ propuestos en la literatura y se evalúa experimentalmente su rendimiento en un entorno reverberante. Los distintos algoritmos se comparan teniendo en cuenta aspectos como el aislamiento acústico entre zonas, el error de reproducción, la energía de los filtros y el retardo del sistema. Además, se estudian estrategias computacionalmente eficientes para obtener los filtros y también se compara su complejidad computacional. Los resultados experimentales obtenidos revelan que las soluciones existentes no pueden ofrecer una complejidad computacional baja y al mismo tiempo un buen rendimiento con baja latencia. Por ello se propone un nuevo algoritmo basado en el filtrado subbanda, y se demuestra experimentalmente que este algoritmo mitiga las limitaciones de los algoritmos existentes. Asimismo, este algoritmo ofrece una mayor versatilidad que los algoritmos existentes, ya que se pueden utilizar configuraciones distintas en cada subbanda, como por ejemplo, diferentes longitudes de filtro o distintos conjuntos de altavoces. Por último, se estudia la influencia de las respuestas objetivo en la optimización de los filtros y se propone un nuevo método en el que se aplica una ventana temporal a estas respuestas. El método propuesto se evalúa experimentalmente en dos salas con diferentes tiempos de reverberación y los resultados obtenidos muestran que se puede reducir la energía de las interferencias entre zonas gracias al efecto de la ventana temporal.

Palabras clave: zonas de sonido personal, *weighted pressure matching*, mínimos cuadrados, filtrado subbanda.

Resum

Els sistemes de zones de so personal (o les seves sigles en anglés PSZ) fan servir altaveus i tècniques de processament de senyal per a reproduir sons distints en diferents zones d'un mateix espai compartit. Aquests sistemes s'han popularitzat en els últims anys a causa de l'àmplia gamma d'aplicacions que podrien veure's beneficiades per la generació de zones d'escolta individuals. El disseny dels filtres utilitzats per a processar els senyals de so és un dels aspectes més importants dels sistemes PSZ, particularment per a les freqüències baixes i mitjanes. En la literatura s'han proposat diversos algoritmes per a calcular aquests filtres, cadascun d'ells amb els seus avantatges i inconvenients. En aquest treball es revisen els algoritmes proposats en la literatura per a sistemes PSZ i s'avalua experimentalment el seu rendiment en un entorn reverberant. Els distints algoritmes es comparen tenint en compte aspectes com l'aïllament acústic entre zones, l'error de reproducció, l'energia dels filtres i el retard del sistema. A més, s'estudien estratègies de còmput eficient per obtindre els filtres i també es comparen les seves complexitats computacionals. Els resultats experimentals obtinguts revelen que les solucions existents no poder oferir al mateix temps una complexitat computacional baixa i un bon rendiment amb latència baixa. Per això es proposa un nou algoritme basat en el filtrat subbanda que mitiga aquestes limitacions. A més, l'algoritme proposat ofereix una major versatilitat que els algoritmes existents, ja que en cada subbanda el sistema pot utilitzar configuracions diferents, com per exemple, distintes longituds de filtre o distints conjunts d'altaveus. L'algoritme proposat s'avalua experimentalment en un entorn reverberant, i es mostra com pot mitigar satisfactòriament les limitacions dels algoritmes existents. Finalment, s'estudia la influència de les respostes objectiu en l'optimització dels filtres i es proposa un nou mètode en el que s'aplica una finestra temporal a les respostes objectiu. El mètode proposat s'avalua experimentalment en dues sales amb diferents temps de reverberació i els resultats obtinguts mostren que es pot reduir el nivell d'interferència entre zones gràcies a l'efecte de la finestra temporal.

Paraules clau: zones de so personal, *weighted pressure matching*, mètode dels mínims quadrats, filtrat subbanda.

Acknowledgements

First and foremost I would like to thank my supervisors, Dr. Gema Piñero and Dr. Alberto González, for all their help, advise, and support during the four years that I have been working on this thesis, and for giving me freedom to work in my own way.

I would also like to express my sincere gratitude to Dr. Stephen Elliott and Dr. Jordan Cheer from the University of Southampton, for their help and commitment with our research project on personal sound zones during the challenging times of the COVID-19 pandemic.

I am thankful to the reviewers and the members of the committee of this thesis: Dr. Mikael Sternad from Uppsala Universitet, Dr. Felipe Orduña from Universidad Nacional Autónoma de México, Dr. Luis Azpicueta from Universidad Carlos III de Madrid, Dr. Luis Vergara from Universitat Politècnica de València, and Dr. Pedro Vera from Universidad de Jaén.

I can not forget all my colleagues at the Audio and Communications Signal Processing Group with whom I shared my days in the last four years. Thank you for making my workplace a very pleasant and rewarding environment. Special thanks to Dr. Pablo Gutiérrez, Dr. Juan Estreder, Javier García, Dr. Laura Fuster, Dr. Christian Antoñanzas, Dr. Marian Simarro, Ariel Álvarez, Enrique Palazón, Eric Beaucamps, David Salvo, Fabián Aguirre, Emanuel Aguilera, and Dr. Jenely Villamediana, as well as to professors Dr. Miguel Ferrer, Dr. María de Diego, and Dr. Germán Ramos.

Finalment, en la meua llengua, vull donar-los les gràcies a tots aquells que m'han acompanyat aquests anys i que, sense estar directament implicats en la part tècnica, són els grans responsables de què haja pogut acabar amb èxit aquest treball. Al grup d'amics del CIPF, moltes gràcies per acollir-me com a un més en la vostra xicoteta família. A la família Arámbul-Anthony, moltes gràcies per fer-nos la vida més fàcil i donar-nos suport constantment. Als membres i amics de la Banda de Nules, tots els concerts, actes i festes amb vosaltres són enriquidors i meravellosos. Als meus amics de Nules, amb vosaltres he compartit viatges, festes i incomptables bons moments que no canviaria per res, moltes gràcies per ser els millors amics que mai haguera pogut imaginar. Per suposat, moltes

gràcies als meus pares, Maria Teresa i Vicente, per l'amor incondicional, per sempre ajudar-me en tot allò que està al vostre abast i més enllà, i per ensenyar-me que una bona educació és el millor regal que uns pares li poden fer al seu fill. A la meua germana, Teresa, per ser un exemple a seguir i per tots els consells acadèmics i lingüístics que m'has donat en tots aquests anys. A ma tia Marisol, per ser una inspiració i mostrar-me la bellesa de les matemàtiques. A ma *güela* Teresa, per estimar-nos incondicionalment i per ser un referent de bona persona. Per últim i en especial, a María José, perquè no puc imaginar-me una millor companya per a aquest viatge doctoral. Moltes gràcies per tot l'amor i la felicitat que has dut a la meua vida.

Contents

Acronyms

AC	Acoustic Contrast
ACC	Acoustic Contrast Control
AE	Array Effort
ASR	Alias-To-Signal Ratio
BACC	Broadband Acoustic Contrast Control
BACC-RD	BACC with Response Differential constraint
BACC-RTE	BACC with Response Trend Estimation
BACC-RV	BACC with Response Variation constraint
DFT	Discrete Fourier Transform
DS	Double-Sided
DTFT	Discrete Time Fourier Transform
EDM	Energy Difference Maximization
FAEST	Fast a Posteriori Error Sequencial Technique
FARLS	Fast Array Recursive Least Squares
FFT	Fast Fourier Transform
FIR	Finite Impulse Response
FR	Frequency Response
FT	Full Target
FT-FD	Full Target with Frequency-Dependent weighting
FTF	Fast Transversal Filters
GDFT	Generalized Discrete Fourier Transform
IDFT	Inverse Discrete Fourier Transform
IDI	Iterative DFT-Domain Inverse
IIR	Infinite Impulse Response
ILS	Iterative Least Squares
IR	Impulse Response
LS	Least Squares
LTI	Linear Time-Invariant
MSE	Mean Squared Error
NMSE	Normalized Mean Squared Error
NPR	Near Perfect-Reconstruction

PC	Planarity Control
PM	Pressure Matching
PR	Perfect-Reconstruction
PSZ	Personal Sound Zones
QMF	Quadrature Mirror Filters
RE	Reconstruction Error
RFR	Room Frequency Response
RIR	Room Impulse Response
RLS	Recursive Least Squares
SS	Single-Sided
VAST	Variable Span Trade-off
wPM	Weighted Pressure Matching
wPM-F	wPM with Frequency-Domain formulation
wPM-S	wPM with Subband-Domain formulation
wPM-T	wPM with Time-Domain formulation
WT	Windowed Target

Notation

Measurement units

dB	Decibel
m	Meter
s	Second
FLOPs	Floating Point Operations
Hz	Herz

Metrics

E_b	Mean energy in the bright zone
E_d	Mean energy in the dark zone
K_x	Kurtosis of a random variable x
ϵ	Mean Squared Error
ε	Normalized Mean Squared Error
ξ	Array Effort

Operators

$\arg\min$	Argument of the minimum
$\lvert\cdot\rvert$	Absolute value
$\lVert\cdot\rVert$	l_2-norm
$\lceil\cdot\rceil$	Ceiling function
$\lfloor\cdot\rfloor$	Floor function
$*$	Linear convolution
$\otimes$	Kronecker product
∇	Gradient operator
$(\cdot)^*$	Complex conjugate
$(\cdot)^T$	Transpose
$(\cdot)^H$	Hermitian transpose
$(\cdot)^{-1}$	Inverse
$(\cdot)^\dagger$	Pseudoinverse

$(\cdot)_{\downarrow R}$	Decimation by a factor R
$(\cdot)_{\uparrow R}$	Interpolation by a factor R
$[\cdot]_{(a:b)}$	Elements of the vector in positions a to b
$[\cdot]_{(a:b,c:d)}$	Elements of the matrix in rows a to b and columns c to d
$[\cdot]_{(a:b,:)}$	Elements of the matrix in rows a to b and all columns
$\mathbb{E}\{\cdot\}$	Expected value
$\mathcal{F}_N$	Discrete Fourier Transform of size N
$\log_2(\cdot)$	Logarithm to the base 2
$a \bmod b$	Modulo operator, i.e., remainder of the division of a by b
$O(\cdot)$	Big O notation
$\Re\{\cdot\}$	Real part of a complex number
$\Im\{\cdot\}$	Imaginary part of a complex number

Scalars

β	Regularization factor for wPM-T
$\dot{\beta}_k$	Regularization factor for wPM-S and subband k
$\bar{\beta}_f$	Regularization factor for wPM-F and frequency f
β_0	Relative regularization factor for wPM-T
$\bar{\beta}_{0,f}$	Relative regularization factor for wPM-F and frequency f
λ	Wavelength
μ	Weighting factor for wPM-T
$\dot{\mu}_k$	Weighting factor for wPM-S and subband k
$\bar{\mu}_f$	Weighting factor for wPM-F and frequency f
ρ_f	Filter bank scaling
τ	System delay
τ_d	Modelling delay
τ_f	Filter bank delay
ω	Angular frequency
c	Sound speed
e	Euler's number
f	Frequency
f_s	Sampling frequency

j	Imaginary unit $j = \sqrt{-1}$
l	Loudspeaker index
m	Control/Validation point index
n	Discrete time index
t	Continuous time index
z	z-transform variable
I_d	Length of the target response
$I_{\mathrm{d},k}$	Length of the target for subband k
I_g	Length of the filters
$I_{\mathrm{g},k}$	Length of the subband filters for subband k
I_h	Length of the RIR
$I_{\mathrm{h},k}$	Length of the RIR subband components for subband k
I_p	Length of the prototype filter
I_w	Length of the window
K	Number of subbands
L	Number of loudspeakers
M	Number of control/validation points
M_b	Number of control/validation points in the bright zone
M_d	Number of control/validation points in the dark zone
N	DFT size
P	Approximation order
R	Resampling factor
T_{60}	Reverberation time, i.e., 60 dB decay time

Sets

$\mathcal{B}$	Set of control/validation points in the bright zone
$\mathcal{D}$	Set of control/validation points in the dark zone
$\mathbb{C}$	Set of complex numbers
$\mathbb{N}$	Set of natural numbers
$\mathbb{R}$	Set of real numbers
$\mathbb{R}^+$	Set of positive real numbers (including 0)
$\mathbb{Z}$	Set of integer numbers

Impulse Responses (IR)

$\delta(n)$	Unit impulse
$d_m(n)$	Target IR for control point m
$d_{m,k}(n)$	Target IR for control point m and subband k
$g_l(n)$	Filter IR for loudspeaker l
$g_{l,k}(n)$	Subband filter IR for loudspeaker l and subband k
$h_{ml}(n)$	RIR from loudspeaker l to control point m
$h_{ml,k}(n)$	Subband component of h_{ml} for subband k
$h_{\mathrm{v},ml}(n)$	RIR from loudspeaker l to validation point m
$p(n)$	Prototype filter IR
$q_l(n)$	Filter IR before truncation for wPM-F and loudspeaker l
$s(n)$	Input signal
$u_k(n)$	Analysis filter for subband k
$v_k(n)$	Synthesis filter for subband k
$x_m(n)$	Cascade IR for control point m
$x_{m,k}(n)$	Cascade IR for control point m and subband k
$y_l(n)$	Signal fed to loudspeaker l

Frequency Responses (FR)

$D_m(f)$	Target FR for control point m
$G_l(f)$	Filter FR for loudspeaker l
$H_{ml}(f)$	RFR from loudspeaker l to control point m
$H_{\mathrm{v},ml}(f)$	RFR from loudspeaker l to validation point m
$Q_l(f)$	Filter FR before truncation for wPM-F and loudspeaker l
$X_m(f)$	Cascade FR for control point m

Vectors and matrices

$\mathbf{a}$	Vectors are represented by lower-case boldface letters
$\mathbf{A}$	Matrices are represented by upper-case boldface letters
$\mathbf{0}_{L\times M}$	Zero matrix of size $L\times M$
$\mathbf{I}_L$	Identity matrix of size $L\times L$

Related to wPM-T

$\mathbf{d}_n$	Vector of $d_m(n)$ for all control points
$\mathbf{d}$	Vector of $\mathbf{d}_n$ for all time instants
$\mathbf{g}_n$	Vector of $g_l(n)$ for all loudspeakers
$\mathbf{g}$	Vector of $\mathbf{g}_n$ for all time instants
$\mathbf{g}_{\text{opt}}$	Vector of the optimal filters
$\mathbf{x}_n$	Vector of $x_m(n)$ for all control points
$\mathbf{x}$	Vector of $\mathbf{x}_n$ for all time instants
$\mathbf{H}_n$	Matrix of h_{ml} for all loudspeakers and control points
$\mathbf{H}$	Matrix of $\mathbf{H}_n$ for all time instants
$\mathbf{W}$	Matrix of the weighting terms

Related to wPM-S

$\dot{\mathbf{d}}_{n,k}$	Vector of $d_{m,k}(n)$ for all control points
$\dot{\mathbf{d}}_k$	Vector of $\dot{\mathbf{d}}_k$ for all time instants
$\dot{\mathbf{g}}_{n,k}$	Vector of $g_{l,k}(n)$ for all loudspeakers
$\dot{\mathbf{g}}_k$	Vector of $\dot{\mathbf{g}}_{n,k}$ for all time instants
$\dot{\mathbf{g}}_{\text{opt},k}$	Vector of the optimal subband filters for subband k
$\dot{\mathbf{x}}_{n,k}$	Vector of $x_{m,k}(n)$ for all control points
$\dot{\mathbf{x}}_k$	Vector of $\dot{\mathbf{x}}_{n,k}$ for all time instants
$\dot{\mathbf{H}}_{n,k}$	Matrix of $h_{ml,k}$ for all loudspeakers and control points
$\dot{\mathbf{H}}_k$	Matrix of $\dot{\mathbf{H}}_{n,k}$ for all time instants
$\dot{\mathbf{W}}_k$	Matrix of the weighting terms for subband k

Related to wPM-F

$\bar{\mathbf{d}}_f$	Vector of $D_m(f)$ for all control points
$\bar{\mathbf{q}}_f$	Vector of $Q_l(f)$ for all loudspeakers
$\bar{\mathbf{q}}_{\text{opt},f}$	Vector of the optimal responses for frequency f
$\bar{\mathbf{x}}_f$	Vector of $X_m(f)$ for all control points
$\bar{\mathbf{H}}_f$	Matrix of $H_{ml}(f)$ for all loudspeakers and control points
$\bar{\mathbf{W}}_f$	Matrix of the weighting terms for frequency f

Related to the Cholesky solver

$\mathbf{c}$	Vector of the cross-correlation of the RIRs and the targets
$\mathbf{L}$	Cholesky factor of $\mathbf{R}$
$\mathbf{R}$	Matrix of the auto and cross-correlation of the RIRs

Related to the superfast solver

$\mathbf{g}_{\mathrm{ap},P}$	Vector of the P-th order approximation of $\mathbf{g}_{\mathrm{opt}}$
$\mathbf{g}_{\mathrm{fd}}$	Vector of the filters for the frequency-domain optimization
$\bar{\mathbf{q}}_{\mathrm{opt}}$	Vector of $\bar{\mathbf{q}}_{\mathrm{opt},f}$ for all control frequencies
$\bar{\mathbf{r}}_p$	Vector of the correction terms of order p
$\mathbf{F}_L$	DFT matrix with blocks of size L
$\mathbf{H}_{\mathrm{e}}$	Circular extension of matrix $\mathbf{H}$
$\bar{\mathbf{H}}$	Matrix of $\bar{\mathbf{H}}_f$ for all control frequencies
$\mathbf{T}$	Truncation matrix

Related to the subband decomposition

$\widetilde{\mathbf{\Delta}}_k$	Matrix of the decimated analysis filter for subband k
$\mathbf{E}_k$	Matrix of exponential terms for subband k
$\mathbf{F}_k$	Matrix of exponential terms for subband k
$\mathbf{P}$	Matrix of the decimated prototype filter

List of Figures

List of Tables

List of Algorithms

Chapter 1

Introduction

Personal Sound Zones (PSZ) systems, as proposed by Druyvesteyn and Garas [1], aim to deliver different sounds to a number of listeners sharing an acoustic space through the use of loudspeakers together with signal processing techniques. This thesis deals with the development and performance evaluation of PSZ systems based on arrays of loudspeakers in real acoustic environments. Next, we discuss the motivation, the main objectives, and the structure of this work.

1.1 Motivation

Nowadays, due to the fast-paced development of technology, audio-visual contents can be accessed in a growing number of devices, e.g., smartphones, tablets, laptops, televisions, sound systems, smart speakers, etc. Thus, it is likely that a number of users accessing different audio-visual contents coexist in a shared space. For example, a typical living room may comprise several users watching television while others access a different content via their laptops or smartphones. Similarly, a driver may be listening to the navigation information in a car cabin whereas the other passengers listen to music or talk with a hands-free system. Moreover, other shared spaces that typically include many users, as museums or exhibition centers, may benefit from delivering different sounds to different regions of space. In all these situations, the users want to listen to the specific audio content that they are interested in without interferences from the sounds delivered to the other users. Therefore, the generation of individual listening zones, in which personalized audio content is delivered to each user, is a timely and interesting topic with a wide range of applications.

An obvious solution to provide independent audio programs to different users in shared spaces is the use of headphones. However, this solution presents several disadvantages. The main drawback is that headphones isolate the listener from the surrounding environment to some extent. For example, in the transportation context, the use of headphones may impede the driver to react to events on the road [2], which could originate dangerous situations. Also, the use of headphones may prevent the users to interact with each other, which is an important limitation in a social context. Moreover, headphones listening tends to be more uncomfortable than loudspeaker listening, leading to a higher fatigue from prolonged listening times [3, 4]. Thus, reproduction systems making use of loudspeakers may be preferred to generate individual listening zones, since these systems do not produce as much fatigue as systems using headphones and do not isolate the listeners from the surrounding environment (if moderate reproduction levels are selected).

Druyvesteyn and Garas [1] first proposed using loudspeakers to generate individual listening zones in their pioneer work on Personal Sound Zones (PSZ) systems in 1997. In particular, they proposed using a set of loudspeakers together with a signal processing stage to create regions of high and low acoustic pressure inside a shared space. A key aspect of PSZ systems, at least for low and mid frequencies, is the design of the filters used in the signal processing stage. In recent years, PSZ systems have attracted a lot of attention due to the large number of applications that would benefit from the generation of individual listening zones, and consequently, many different optimization algorithms have been proposed for computing the filters of the system, each presenting some advantages and disadvantages. The most suitable algorithm for a PSZ system depends on its specific application, since each application presents different requirements. For example, for PSZ systems in which the users are moving, the filters should be frequently recalculated, thus, a suitable algorithm for these systems should require low computational effort. Likewise, PSZ systems in which the sounds delivered to the users must be synchronized with other multimedia content require low latency, consequently, a suitable algorithm should provide filters that introduce short delays. This thesis focuses on the optimization of the filters required by PSZ systems operating in realistic acoustic environments. In particular, we aim to study the main limitations of the state-of-the-art algorithms and to propose novel approaches that overcome these limitations.

1.2 Objectives

Taking into account the context introduced previously, the main objectives of this thesis are the following:

- To identify and evaluate the main limitations of the state-of-the-art optimization algorithms to compute the filters for PSZ systems in realistic acoustic environments. Aspects such as the level of acoustic isolation between zones, the reproduction error, the energy of the filters, the computational complexity, and the system delay will be taken into consideration.
- To analyse and evaluate efficient solvers to compute the filters for those algorithms that are more computationally challenging. In particular, the accuracy of the solvers and their computational complexity will be considered.
- To develop, propose, and test novel algorithms to compute the filters for PSZ systems in realistic acoustic environments that overcome the main limitations of the state-of-the-art algorithms.

1.3 Structure of the thesis

The rest of this work is structured as follows:

- **Chapter 2:** This chapter provides necessary background on PSZ systems. Special focus is given to the state-of-the-art optimization algorithms for computing the filters of the system and to the performance metrics used to evaluate those filters. Furthermore, novel experimental results in a reverberant environment are presented to compare the performance of the time and frequency domain formulations of the weighted Pressure Matching (wPM) algorithm. Aspects such as the filter length, the system delay, and the regularization level are taken into account in this comparison.
- **Chapter 3:** This chapter focuses on the Least Squares (LS) problem associated with the time-domain formulation of the wPM algorithm.

First, different solvers that can be used to compute the optimal solution for the LS problem are reviewed and discussed. Then, experimental results are presented to evaluate the accuracy of those solvers and to show how this accuracy influences the performance of a PSZ system. Finally, the computational complexity of the solvers is compared.

- **Chapter 4:** This chapter presents a novel formulation for PSZ systems based on subband filtering. The presented formulation makes use of the subband decomposition of the Room Impulse Responses (RIR) by means of a Generalized Discrete Fourier Transform (GDFT) filter bank. Also, the novel weighted Pressure Matching with Subband-Domain Formulation (wPM-S) algorithm is proposed to compute the subband filters for the system. The proposed algorithm is experimentally evaluated in a reverberant environment, and its performance and computational complexity are compared with those for the time and frequency formulations of wPM. Finally, the versatility of wPM-S to deal with different configurations in each subband is evaluated.

- **Chapter 5:** This chapter presents a novel approach for selecting the target responses for the wPM algorithm. The proposed approach is based on windowing the target impulse responses, such that certain reverberation components are suppressed. The efficacy of the proposed approach to improve the acoustic isolation between zones is experimentally evaluated in two rooms with different reverberation levels.

- **Chapter 6:** This chapter summarizes the main conclusions of this work and proposes further research questions arising from this thesis.

- **Appendix A:** This appendix presents an in-depth analysis of the computational complexity of the algorithms discussed throughout this work.

- **Appendix B:** This appendix presents a novel method to design the prototype filters for GDFT filter banks.

Chapter 2

Background

This chapter provides some background on Personal Sound Zones (PSZ) systems that is necessary for the understanding of this dissertation. First, PSZ systems are described, including their main goal, their requirements, and the different approaches that can be used for these kind of systems. Afterwards, PSZ systems using arrays of loudspeakers together with a filtering stage, i.e., loudspeaker array processing, are discussed. In particular, the model for a PSZ system using loudspeaker array processing is presented, followed by a description of the time and frequency domain formulations of this model. Also, a detailed review of the state-of-the-art algorithms used to compute the filters for PSZ systems and a description of the control metrics used to evaluate their performance are included. Later, experimental evaluation results in a reverberant environment are presented to compare the performance of the time and frequency domain formulations of the weighted Pressure Matching (wPM) algorithm. Aspects such as the filter length, the modelling delay, and the regularization level are taken into account in this comparison. Experimental results show that the filters obtained with the time-domain formulation outperform the filters obtained with the frequency-domain formulation when either short modelling delays or short filters are considered.

2.1 Personal Sound Zones (PSZ) systems

2.1.1 Description and problem definition

Personal Sound Zones (PSZ) systems, also known as Personal Audio systems, aim to render different sounds to a set of spatially confined regions, where the users of the system are located, making use of loudspeakers [1, 5]. Then, PSZ systems aim to create individual listening regions without requiring the use of headphones. In the last years, PSZ systems have drawn more attention due to the need of creating individual listening regions in shared spaces (such as cars, museums, or shared offices) [6]. Also, PSZ systems can be used to generate independent listening zones in the ears of a single user, which offer the possibility of delivering binaural sound signals without the use of headphones [7].

To exemplify the fundamental idea behind PSZ systems, let us consider two users, U_a and U_b, which are located in a shared space in zones Z_a and Z_b, respectively. In this scenario, user U_a wants to listen to sound S_a, and user U_b to sound S_b. To obtain a good listening experience, the interference produced by sound S_a in zone Z_b and by sound S_b in zone Z_a should be ideally 0 (or at least very low). Then, we aim to render sound S_a with

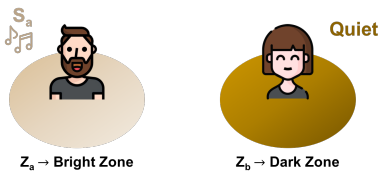

(a) Soundfield control problem for U_a

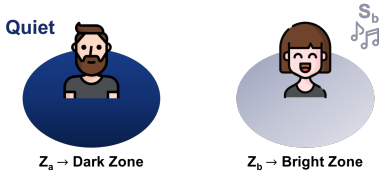

(b) Soundfield control problem for U_b

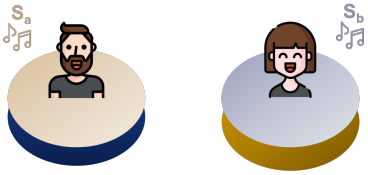

(c) Superposition

Figure 2.1: Schematic to illustrate the superposition of two soundfield control problems to create PSZ for two users U_a and U_b.

high level in zone Z_a and with low level in zone Z_b, and similarly, sound S_b with high level in zone Z_b and with low level in zone Z_a, as shown in Fig. 2.1. Consequently, PSZ systems can be seen as a superposition of several soundfield control problems, since for each user we want to synthesize a soundfield that exhibits high acoustic energy in the region where he/she is located, and low acoustic energy in the regions where the other users are located. The different soundfield control problems can be considered independent as long as the sound signals are independent [8], and then, the PSZ related works usually study a single soundfield control problem in which high acoustic energy is desired in one region, denoted as bright zone, and low acoustic energy in another region, denoted as dark zone [9].

2.1.2 Requirements

The requirements of a PSZ system, as the number of loudspeakers, the computational capabilities or the system delay, are specific for each application. For example, PSZ systems in which a high number of individual listening zones are desired, as in museums and shared offices, require the use of a high number of loudspeakers. Also, systems in which the sound rendered in the listening zones must be synchronized with other multimedia content, as video, can require very low latency. This aspect is studied in detail in [10], in which a PSZ system is used to enhance the audio signal rendered to the hearing impaired from a television. Similarly, systems used for two-way telecommunication applications, as individual hands-free systems, must also present very low delay [11]. Finally, low computational requirements are desired for domestic PSZ systems due to the limited computational capabilities of the processors that are usually employed in this kind of systems.

2.1.3 Approaches for creating PSZ

To create regions of high and low acoustic energy, PSZ systems must be able to focus sound in certain directions. The capacity of a loudspeaker to focus sound in certain directions is governed by its directivity [12]. Conventional piston-like loudspeakers present a frequency-dependent directivity that is determined by the size of its driver compared to the wavelength of the sound being produced. For frequencies in which the size of the driver is small compared to the wavelength, the driver operates approximately as a single point source of pressure, i.e., it radiates sound uniformly in all directions

[12]. On the contrary, for frequencies in which the size of the driver is bigger than the wavelength, the pressure distribution is not uniform over all the surface of the driver, and then, constructive and destructive interferences are created in the far-field, which leads to a narrow directivity towards the axis of the loudspeaker [13]. Thus, we can assume that a loudspeaker has high directivity, i.e., it only radiates sound in a specific direction, for frequencies in which the wavelength is small compared to the size of the driver. Consequently, the ability of a single loudspeaker to focus sound is restricted to high frequencies, as very big drivers are required for lower frequencies.

The directivity of a single loudspeaker can be improved at low frequencies by using parabolic reflectors [14]. In this case, the source is located close to the focal point of the parabolic reflector, as shown in Fig. 2.2. The effective aperture of the loudspeaker is increased by the parabolic reflector, and then, the directivity at lower frequencies is improved even if the driver is not very big. In this case, the lowest frequency at which a narrow beam can be generated depends on the aperture of the parabolic reflector [14]. A commercial example of parabolic loudspeaker is the *Meyer SB-1 Parabolic Sound Beam*, which uses a parabolic structure with aperture 1.37 m that can generate a beam of width 10 degrees in the frequency range 500 Hz to 15 kHz [15]. This frequency range is acceptable for reproduction of intelligible speech signals [16], so these kind of speakers have been used in museums and exhibitions to generate PSZ in which speech is rendered. However, this operation range is not suitable for other audiovisual applications where we want to play music and other sounds that have important energy components below 500 Hz.

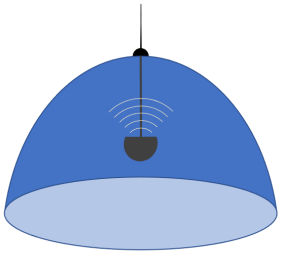

Figure 2.2: Diagram of a parabolic loudspeaker, in which the source is located in the focal point and radiating towards the vertex of the parabola.

As an alternative, directive patterns can be generated with parametric loudspeakers [17]. This kind of loudspeakers are based on using the non-linear interaction of waves to generate a secondary wave with a different frequency [18]. In particular, parametric loudspeakers use an array of ultrasound transducers to radiate primary waves in the ultrasound frequency spectrum, whose interaction generates a secondary wave in the audible spectrum (if the primary waves are properly designed) [17]. The radiated ultrasonic waves are highly directive, so the audible wave generated by the non-linear interaction is also highly directive. Originally, this kind of loudspeakers presented high levels of harmonic distortion in the audible spectrum, but the development of new signal processing techniques led to distortion levels similar to those for conventional loudspeakers [19]. However, high sound pressure levels can not be generated with parametric loudspeakers at low and mid frequencies. In particular, frequency response decays of 40 dB/decade for frequencies below 1 kHz where reported in [19, 20]. Then, similarly to the case of parabolic loudspeakers, parametric loudspeakers are not suitable for the reproduction of music and other sounds that have important low frequency components. The Focusonics Model A [21] and the Audio Spotlight 16iX [22] are examples of commercial parametric loudspeakers.

At low and mid frequencies, higher directivity and sound pressure levels can be obtained if an array of conventional loudspeakers is used. This is because the signals played by the loudspeakers of the array can be designed such that constructive and destructive interferences are created in some specific directions. The technique used to design the signals radiated by the elements of the array is commonly called loudspeaker array processing, which is based on using a set of filters to process the signals that are fed to the loudspeakers. The frequency range in which an array of loudspeakers can obtain high directivity depends on its dimensions. The first practical demonstration of PSZ system using arrays of loudspeakers was presented by Droppo et al. [23] at Microsoft Research TechFest 2007, in which a linear array of 16 loudspeakers was used to enhance sound in one area and cancelling sound in another area within the same physical space. Also, researchers from the University of Southampton and Audioscenic Ltd. demostrated at the Consumer Electronics Show (CES) 2019 the use of a linear array of 7 loudspeakers to generate individual listening zones in the ears of a user to deliver binaural sound signals [24].

One of the early works on PSZ systems was presented by Druyvesteyn and Garas [1]. In this work, the authors discussed the fundamental theory for PSZ reproduction. Due to the directivity properties of loudspeakers, Druyvesteyn and Garas determined that different approaches must be used in different frequency bands to achieve high isolation levels between zones. In particular, they showed that an array of loudspeakers must be used for low and mid frequencies, while individual directional loudspeakers for higher frequencies. The specific frequency limits in which each of these approaches must be used depend on the number of elements and the size of the array, and on the properties of the directional loudspeaker. Then, PSZ systems in which broadband signals (e.g., music) are rendered must combine different loudspeaker setups. In this work, we focus on the filter optimization required for PSZ systems using loudspeaker array processing, i.e., for low and mid frequencies. Next, we review the fundamental theoretical framework related to loudspeaker array processing.

2.2 Loudspeaker array processing

Loudspeaker array processing can be considered as a subset of the broader discipline of array signal processing, which is based on using multiple spatially distributed sensors/transmitters together with a signal processing stage to modify the properties of the received/transmitted signals [25]. Array signal processing has been extensively used in a wide range of applications, e.g., arrays of antennas are used to focus the radiation in certain directions in mobile communications systems [26], and arrays of microphones are used in voice recognition systems to increase the Signal-To-Noise ratio for certain directions of arrival [27]. The terms beamforming and spatial filtering are also used to refer to array signal processing techniques.

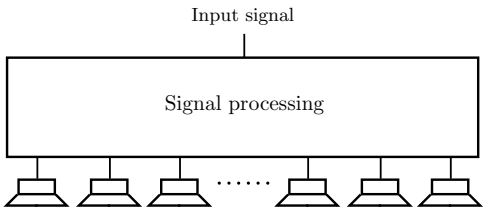

Figure 2.3: Model of a loudspeaker array processing system.

Following the principles of array signal processing, loudspeaker array processing is based on using an array of loudspeakers together with a set of filters to focus sound in certain directions and cancel sound in other directions. We show in Fig. 2.3 the basic model of a system using loudspeaker array processing. The fundamental idea behind these systems is that the signals radiated by the loudspeakers can be designed such that the superposition of the acoustic waves radiated by each element creates constructive and destructive interferences in certain positions. Wolff and Malter [28] first studied the radiation properties of arrays of loudspeakers, and showed that directional patterns can be obtained by combining multiple sources even if the individual sources are not directional. Thus, arrays of loudspeakers can obtain high directivity at low frequencies, even if the loudspeakers are not very big, but at the cost of increasing the number of loudspeakers of the system. It is important to mention that loudspeaker array processing can be used for other soundfield control applications such as, for example, wavefield synthesis [29] or room equalization [30].

Different geometries have been considered for the arrays of loudspeakers used in PSZ systems. A circular geometry has been considered in many works [31, 32, 33]. The motivation is that this geometry is convenient for certain formulations of the PSZ model that are based on harmonic decompositions. However, a circular array is not practical in many scenarios due to the limited space where the array of loudspeakers can be placed. Alternatively, linear arrays also offer good performance [34, 35, 36, 37], but they are much easier to integrate in a reproduction space. Other geometries have been considered in the literature. Choi and Kim [9] employed two linear arrays arranged on the same plane with a shape of X. Shin et al. [38] used a spherical array of loudspeakers. Simón Gálvez et al. [39] used a planar array of loudspeakers, which offers improved vertical directivity with respect to the linear array. House et al. [40] proposed a geometry in which the consecutive elements of a line array are vertically displaced from each other to obtain lower spacing between the drivers, and consequently, to extend the frequency range in which the array offers directional radiation. Olivieri et al. [41] used a cylindrical array of loudspeakers, which offers higher control of the soundfield. In general, the most suitable array geometry for a PSZ system depends on the available space for the installation of the array. In this work, we consider linear arrays of loudspeakers, which in general offer a good compromise between performance and compactness. However, the algorithms discussed next can be used with any arbitrary geometry.

2.2.1 Superposition of sources

Arrays of loudspeakers can focus sound towards an specific direction thanks to the superposition of the signals radiated by the elements of the array. In order to understand this phenomenon, let us consider a point source radiating in a scenario with free-field propagation. The pressure produced by the point source in a point $\mathbf{r} = [x, y]$ when radiating a signal of amplitude $A(f) \in \mathbb{C}$ at frequency f can be defined using Green's function [12] as

$$p_{\text{mo}}(t, f, \mathbf{r}) = A(f) \frac{e^{j2\pi f\left(t - \frac{1}{c}\|\mathbf{r} - \mathbf{r}_{\text{mo}}\|\right)}}{\|\mathbf{r} - \mathbf{r}_{\text{mo}}\|}, \tag{2.1}$$

where c is the sound speed and $\mathbf{r}_{\text{mo}} = [x_{\text{mo}}, y_{\text{mo}}]$ are the coordinates of the point source. We can see from (2.1) that the magnitude of the pressure produced by the point source in a certain position only depends on the distance between this position and the point source, which indicates that it radiates equal energy in all directions. Now, let us consider an array of L point sources. The pressure produced by the array in a point $\mathbf{r} = [x, y]$ when all the elements of the array are radiating a signal of constant amplitude $A(f) \in \mathbb{C}$ at frequency f is given by [42]

$$p_{\text{ar}}(t, f, \mathbf{r}) = A(f) \sum_{l=0}^{L-1} \frac{e^{j2\pi f\left(t - \frac{1}{c}\|\mathbf{r} - \mathbf{r}_l\|\right)}}{\|\mathbf{r} - \mathbf{r}_l\|}, \tag{2.2}$$

where $\mathbf{r}_l = [x_l, y_l]$ are the coordinates of the l-th element in the array. We can interpret (2.2) as the superposition of the individual contributions of all the elements of the array. In this case, we can see that constructive interferences appear for those points of the space in which the contributions arrive with the same phase (in the far-field). On the contrary, when the phase of the different contributions is different, destructive interferences can appear. Now, we show in Fig. 2.4a and 2.4b the magnitude of the pressure produced by a point source and by a linear array of $L = 8$ point sources at a frequency $f = 400$ Hz, respectively. We can see that the point source has an omnidirectional radiation, i.e., it radiates the same energy in all directions. However, the array radiates higher energy towards the perpendicular direction of the array, while low energy is radiated towards other directions. Then, these results exemplify how an array of non-directional loudspeakers can focus sound thanks to the superposition of the waves generated by each element of the array. From now on, we will refer to the direction that is perpendicular to the linear array as the on-axis direction.

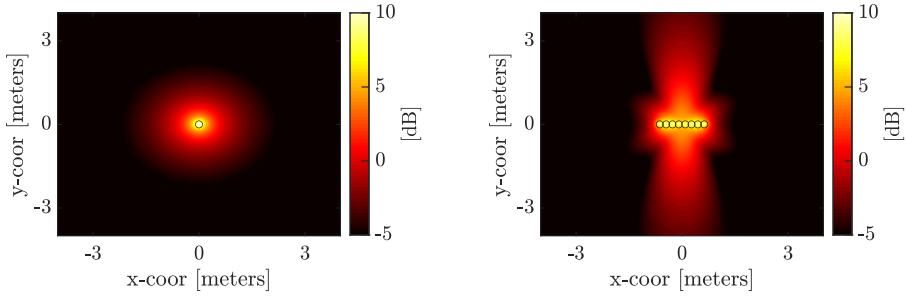

(a) Point source **(b)** Array of point sources

Figure 2.4: Magnitude of the pressure produced at a frequency $f = 400$ Hz by: a point source (a); a linear array of 8 point sources spaced by 18 cm radiating the same amplitude and phase (b). Free-field propagation is assumed with a sound speed of $c = 343$ m/s.

Array limitations

The frequency range for which an array of loudspeakers can focus sound is limited. The distance d between consecutive elements of the array and its total length $D = (L-1)d$, which are also known as inter-element distance and aperture, respectively, influence the frequency range for which the array offers high directivity. For frequencies in which the wavelength is smaller or similar than the inter-element distance, i.e., $\lambda \lesssim d$, high energy secondary lobes appear in the radiation pattern of the array. This is produced by the spatial aliasing, which appears when sound waves are emitted by equidistant sources [43]. For frequencies in which the wavelength is larger or similar than the aperture of the array, i.e., $\lambda \gtrsim D$, the array can not generate narrow beams [43]. To exemplify these phenomena, we show in Fig. 2.5 the magnitude of the pressure at 80 and 1750 Hz produced by a linear array of $L = 8$ point sources with inter-element distance $d = 0.18$ m and aperture $D = 1.26$ m. This array can not generate a narrow beam at 80 Hz, and secondary lobes appear in multiple directions at 1750 Hz due to spatial aliasing. Then, arrays of loudspeakers are suitable for focusing sound at low and mid frequencies, as arrays with reasonable inter-element distances and apertures can be designed for these bands. However, very small inter-element distances are required for high frequencies, leading to non-realizable size requirements for the drivers of the array.

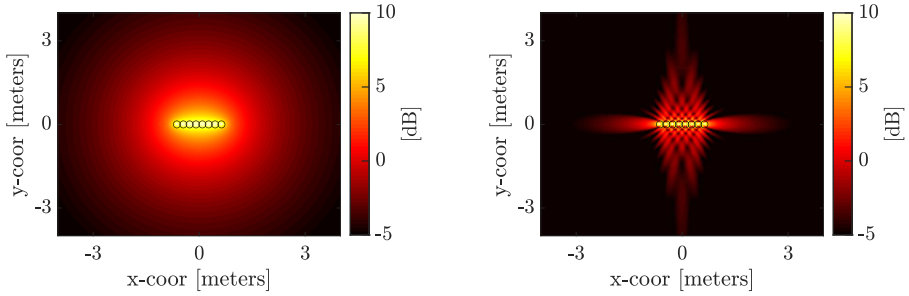

(a) $f = 80$ Hz **(b)** $f = 1750$ Hz

Figure 2.5: Magnitude of the pressure produced by a linear array of 8 point sources spaced by 18 cm radiating the same amplitude and phase at 2 different frequencies. Free-field propagation is assumed with a sound speed of $c = 343$ m/s.

Digital steering

Previously, we assumed that the same amplitude and phase was radiated by all the elements of the array. Now, we assume that the amplitude and the phase of the l-th element of the array is modified with a filter with frequency response $G_l(f) \in \mathbb{C}$. In this case, the pressure produced by the array in a point $\mathbf{r} = [x, y]$ is given by

$$p_{\text{ar}}(t, f, \mathbf{r}) = A(f) \sum_{l=0}^{L-1} G_l(f) \frac{e^{j2\pi f\left(t - \frac{1}{c}\|\mathbf{r}-\mathbf{r}_l\|\right)}}{\|\mathbf{r} - \mathbf{r}_l\|}. \tag{2.3}$$

We can see in (2.3) that the filters $G_l(f)$ influence the positions for which constructive and destructive interferences are produced. For example, let us assume that $G_l(f) = e^{-j2\pi f l\tau}$, i.e., a phase difference of $\phi_f = 2\pi f\tau$ radians is applied between consecutive sources in the array. This is equivalent to apply a delay $l\tau$ to the signals fed to the l-th element of the array. In Fig. 2.6, the magnitude of the pressure produced at a frequency $f = 400$ Hz by an array of $L = 8$ point sources is shown for two delays τ. It is clear from these results that the delay between sources directly influences the directional properties of the array. When all the elements are radiating without any delay between them, i.e., with $\tau = 0$, a narrow beam is created towards the on-axis direction of the array (as shown in Fig. 2.6a). However, the beam generated by the array is shifted when a delay is applied between

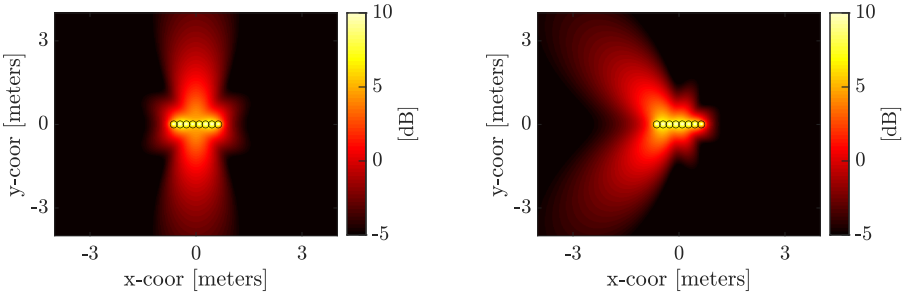

(a) $\tau = 0$ μs **(b)** $\tau = 310$ μs

Figure 2.6: Magnitude of the pressure produced at a frequency $f = 400$ Hz by a linear array of 8 point sources spaced by 18 cm radiating with a phase difference of $\phi_f = 2\pi f\tau$ between consecutive elements in the array for two values of τ. Free-field propagation is assumed with a sound speed of $c = 343$ m/s.

the sources. This effect can be seen in Fig. 2.6b, where we can see how a delay of 310 μs steers the beam towards a direction of approximately $\pi/4$ radians with respect to the on-axis direction. Then, the direction towards which an array of loudspeakers focuses sound can be changed digitally by applying different sets of filters $G_l(f)$. This is a great advantage with respect to directional loudspeakers, as they can only focus sound towards one direction and physical steering is required to change it. Moreover, thanks to the digital steering capabilities of the array, sound can be focused in multiple directions of the space using only one array of loudspeakers.

In the previous example we assumed that $G_l(f) = e^{-j2\pi fl\tau}$, which corresponds to the delay-and-sum beamformer [44] used by Druyvesteyn and Garas [1] for mid frequencies in their work on PSZ systems. This is the simpler method for focusing sound with an array of loudspeakers, as it only requires to apply a delay to the signal radiated by the elements of the array. It achieves good directivity when free-field propagation and point sources are assumed. However, for practical systems the directivity can be degraded by the effect of the electro-acoustic response of the loudspeakers and the reverberation of the room where the system is placed [45]. Then, alternative methods that take into account these factors in the design of the filters are required to obtain good performance for PSZ systems.

2.2.2 System model and formulation

Next, we study the system model proposed by Choi and Kim [9] for PSZ systems using loudspeaker array processing. This model considers an array of L loudspeakers and $M = M_\mathrm{b} + M_\mathrm{d}$ control points (as shown in Fig. 2.7), where M_b and M_d are the number of control points used to spatially sample the bright and dark zones, respectively. The system aims to render a given audio signal in the bright zone while keeping the interference in the dark zone as low as possible. To achieve it, the audio signal is filtered through a filter denoted by g_l prior to be fed to the l-th loudspeaker. In most works related to PSZ systems, g_l is defined as a Finite Impulse Response (FIR) filter, however, Widmark [46] proposed using Infinite Impulse Response (IIR) filters. In this work we consider FIR filters. It is worth notting that an alternative model to the one in Fig. 2.7 was presented by So and Choi [47]. In their model, subband filtering is used rather than broadband filtering prior to feed the input signal to the loudspeakers. This model will be discussed in detail in Chapter 4. From now on, we denote $\mathcal{B}$ and $\mathcal{D}$ as the sets of control points for the bright and dark zones, respectively.

In order to compute the optimal filters of the PSZ system, the model shown in Fig. 2.7 can be formulated in time, frequency, and modal domains. The time-domain formulation uses the impulse responses of the

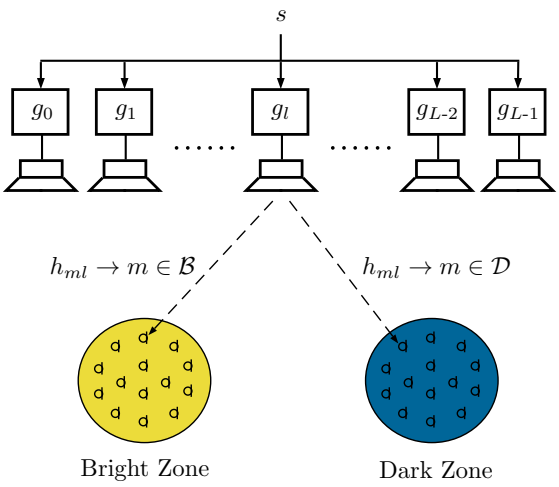

Figure 2.7: Model of a PSZ system using loudspeaker array processing.

elements of the model [39, 48, 49], the frequency-domain formulation uses frequency-domain responses [9, 38, 50], and the modal-domain uses the decomposition in spherical or cylindrical harmonics of the elements of the model [31, 32, 33]. This last formulation requires the use of spherical or circular arrays of loudspeakers with high number of elements, e.g, 57, 55, and 41 loudspeakers are used in [31, 32, 33], respectively. On the contrary, arrays with arbitrary geometry and lower number of elements can be used for the time and frequency domain formulations [9, 39, 47, 48, 49]. Then, in this work we focus on the time and frequency domain formulations, as they are more suitable than the modal-domain formulation for PSZ systems in practical scenarios. In this chapter, we review these two formulations.

In general, the design of the filters for the presented model does not consider the characteristics of the input audio signal, i.e., it is assumed that the input signal is a unit impulse [9, 39, 50, 51, 52]. The motivation is that a unit impulse has a flat spectrum, and then, the filters optimized with this assumption offer the desired directional properties in a broadband frequency range. An alternative model that takes into account the characteristics of the input audio signal in the optimization was proposed by Møller and Ostergaard [53]. Next, we describe the time and frequency domain formulations of the PSZ model assuming that the input signal is a unit impulse, i.e., $s(n) = \delta(n)$.

Time-domain formulation

Now, we describe the time-domain formulation of the model in Fig. 2.7, which was presented by Elliott and Cheer [54]. Let us start by defining g_l as the I_g-length real-valued FIR filter for the l-th loudspeaker. Also, let us define h_{ml} as the Room Impulse Response (RIR) between the l-th loudspeaker and the m-th control point, which is modelled as a real-valued FIR filter of length I_h. The RIR includes the electroacoustical response of the loudspeaker, the propagation delay between the loudspeaker and the control point, and the effect of the reflections of the room in which the system is placed. Then, we can define the cascade impulse response for the m-th control point as

$$x_m(n) = \sum_{l=0}^{L-1} h_{ml}(n) * g_l(n) = \sum_{l=0}^{L-1} \sum_{r=0}^{I_\mathrm{g}-1} h_{ml}(n-r) g_l(r). \tag{2.4}$$

The cascade impulse response includes the contributions of the filters g_l and the RIRs h_{ml}. Now, let us define a column vector of size $M\times 1$ containing the samples of the cascade response in time n for all control points as

$$\mathbf{x}_n = \begin{bmatrix} x_0(n) & \dots & x_{M-1}(n) \end{bmatrix}^T. \tag{2.5}$$

Also, let us define a vector of size $L\times 1$ containing the samples in time n of the filters for all loudspeakers as

$$\mathbf{g}_n = \begin{bmatrix} g_0(n) & \dots & g_{L-1}(n) \end{bmatrix}^T, \tag{2.6}$$

and a matrix of size $M\times L$ containing the RIR in time n between all loudspeakers and control points as

$$\mathbf{H}_n = \begin{bmatrix} h_{00}(n) & \dots & h_{0(L-1)}(n) \\ \vdots & \ddots & \vdots \\ h_{(M-1)0}(n) & \dots & h_{(M-1)(L-1)}(n) \end{bmatrix}. \tag{2.7}$$

Then, using (2.5) to (2.7) we can write

$$\mathbf{x}_n = \sum_{r=0}^{I_\mathrm{g}-1} \mathbf{H}_{n-r}\, \mathbf{g}_r. \tag{2.8}$$

Next, let us define a $M(I_\mathrm{h}+I_\mathrm{g}-1)\times 1$ vector containing the cascade impulse response in all time instants and in all control points as

$$\mathbf{x} = \begin{bmatrix} \mathbf{x}_0^T & \dots & \mathbf{x}_{I_\mathrm{g}+I_\mathrm{h}-2}^T \end{bmatrix}^T, \tag{2.9}$$

and a $LI_\mathrm{g}\times 1$ vector containing all the samples of the filters for all loudspeakers as

$$\mathbf{g} = \begin{bmatrix} \mathbf{g}_0^T & \dots & \mathbf{g}_{I_\mathrm{g}-1}^T \end{bmatrix}^T. \tag{2.10}$$

Similarly, let us define a block-toeplitz matrix of size $M(I_\mathrm{h}+I_\mathrm{g}-1)\times LI_\mathrm{g}$ containing shifted versions of $\mathbf{H}_n$ as

$$\mathbf{H} = \begin{bmatrix} \mathbf{H}_0^T & \dots & \mathbf{H}_{I_\mathrm{h}-1}^T & \mathbf{0}_{L\times M} & \dots & \mathbf{0}_{L\times M} \\ \mathbf{0}_{L\times M} & & & & & \\ \vdots & & & \mathit{Toeplitz} & & \\ \mathbf{0}_{L\times M} & & & & & \end{bmatrix}^T. \tag{2.11}$$

Finally, using (2.9) to (2.11) we can write

$$\mathbf{x} = \mathbf{H}\mathbf{g}. \tag{2.12}$$

Frequency-domain formulation

Next, we describe the frequency-domain formulation of the model in Fig. 2.7, which was presented by Choi and Kim [9]. Let us define $H_{ml}(f)$ as the Room Frequency Response (RFR) at frequency f between the l-th loudspeaker and the m-th control point, and $Q_l(f)$ as the frequency response at frequency f of the filter for the l-th loudspeaker[1]. Then, we can define the cascade frequency response for the m-th control point as

$$X_m(f) = \sum_{l=0}^{L-1} H_{ml}(f) Q_l(f). \tag{2.13}$$

It can be easily seen that there is a direct relation between the time and frequency domain formulations. In particular, the frequency response $H_{ml}(f)$ is the Discrete Time Fourier Transform (DTFT) of h_{ml} at frequency f. Let us define a vector of size $L\times 1$ containing the frequency responses at frequency f of the filters for all loudspeakers as

$$\bar{\mathbf{q}}_f = \begin{bmatrix} Q_0(f) & \dots & Q_{L-1}(f) \end{bmatrix}^T, \tag{2.14}$$

and the matrix of size $M\times L$ containing the room frequency responses between all the loudspeakers and all the control points as

$$\bar{\mathbf{H}}_f = \begin{bmatrix} H_{00}(f) & \dots & H_{0(L-1)}(f) \\ \vdots & \ddots & \vdots \\ H_{(M-1)0}(f) & \dots & H_{(M-1)(L-1)}(f) \end{bmatrix}. \tag{2.15}$$

Then, we can define the vector of size $M\times 1$ containing the cascade frequency responses for all the control points as

$$\bar{\mathbf{x}}_f = \bar{\mathbf{H}}_f \, \bar{\mathbf{q}}_f. \tag{2.16}$$

[1] $Q_l(f)$ is the frequency response of the filter used in the formulation, while $G_l(f)$ is the practical filter for the system obtained by applying certain transformations to $Q_l(f)$.

2.2.3 Filter optimization

The filters for the PSZ system are obtained by solving certain optimization problem, which can be defined using either the time or the frequency domain formulations presented in Section 2.2.2. Next, we describe these two types of optimizations.

Optimization using the time-domain formulation

The algorithms that employ the time-domain formulation for computing the filters of the system, as [39, 48, 49, 55], make use of the expressions presented in Section 2.2.2 to define a cost function $J(\mathbf{g})$. This cost function is designed such that certain conditions are fulfilled for the PSZ system. The optimal filters are then obtained as the ones minimizing $J(\mathbf{g})$, i.e.,

$$\mathbf{g}_{\text{opt}} = \arg\min_{\mathbf{g}} \left(J(\mathbf{g}) \right). \tag{2.17}$$

It is important to note that by solving this optimization we directly obtain all the filter coefficients for all loudspeakers, i.e., $g_l(n)$ for $0 \leq l < L$ and $0 \leq n < I_{\text{g}}$.

Optimization using the frequency-domain formulation

The algorithms that employ the frequency-domain formulation for computing the filters of the system, as [9, 38, 50], make use of the expressions presented in Section 2.2.2 for this formulation to define a cost function $J(\bar{\mathbf{q}}_f)$. Similarly to the time-domain case, the cost function is designed such that certain conditions are fulfilled for the PSZ system. The optimal frequency responses for the filters at frequency f are then obtained as the ones minimizing $J(\bar{\mathbf{q}}_f)$, i.e.,

$$\bar{\mathbf{q}}_{\text{opt},f} = \arg\min_{\bar{\mathbf{q}}_f} \left(J(\bar{\mathbf{q}}_f) \right). \tag{2.18}$$

In this case, solving the optimization provides the optimal coefficients $Q_l(f)$ for a single frequency. To compute the practical time-domain filters, i.e., $g_l(n)$ for $0 \leq l < L$ and $0 \leq n < I_{\text{g}}$, the following steps must be followed for each loudspeaker l [56, 57]:

1. Define a set of N equispaced control frequencies:

$$f_i = i\,\Delta_{\text{f}}, \quad -(N/2) + 1 \leq i \leq N/2, \tag{2.19}$$

where $i \in \mathbb{Z}$, and Δ_f is the frequency spacing between consecutive control frequencies. For a digital system operating at a sampling frequency f_s, it is defined as $\Delta_\mathrm{f} = f_\mathrm{s}/N$. The number of control frequencies N must be the same for all loudspeakers.

2. Compute the optimal frequency responses $Q_l(f)$ by solving (2.18) for the control frequencies (2.19).

3. Apply $e^{-j2\pi(f/f_\mathrm{s})\tau_\mathrm{d}}$ to $Q_l(f)$, being τ_d a modelling delay. This is equivalent to apply a circular delay τ_d to the N-point Inverse Discrete Fourier Transform (IDFT) of $Q_l(f)$. This step is not required for algorithms in which the target already includes the modelling delay.

4. Compute the N-point IDFT of $Q_l(f)$:

$$q_l = \mathcal{F}_N^{-1}\left\{Q_l\right\}. \tag{2.20}$$

5. Obtain the I_g-length impulse response g_l by windowing q_l:

$$g_l(n) = q_l(n)\, w(n), \tag{2.21}$$

where $w(n) = 0$ for $n < 0$ and $n \geq I_\mathrm{g}$.

Next, we discuss different aspects related to the previous method. An important point to take into account is that the time-domain optimization implies that the impulse responses of the filters are causal and of finite length. However, there is no guarantee that the estimated filters $Q_l(f)$ in the frequency domain correspond to finite length and causal impulse responses. Indeed, the estimated coefficients $Q_l(f)$ usually correspond to infinite length and non-causal responses because the RIRs are generally non-minimum phase impulse responses [58, 59]. Sampling the spectrum of such a response with a finite size IDFT produces that anti-causal components of the non-causal response appear at the end of the DFT period in q_l, due to the circularity of the DFT. To illustrate this phenomenon, we show in Fig. 2.8a an example of a non-causal impulse response, and in Fig. 2.8b the impulse response obtained after sampling the spectrum of the non-causal response with an IDFT of size $N = I_\mathrm{g}$. In this case, the anti-causal components of the original response appear at the end of the estimated response, which could produce artefacts in the reproduced signal. One possible solution to solve this limitation is to apply a window to

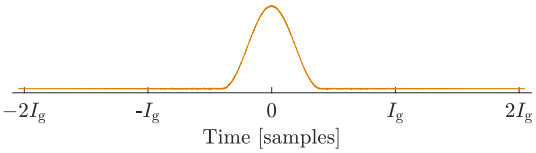

(a) Impulse response to estimate

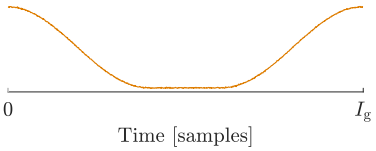

(b) Estimated q_l with $\tau_d = 0$

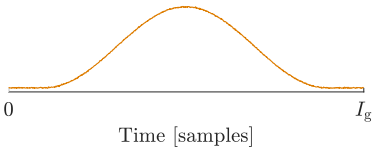

(c) Estimated q_l with $\tau_d = I_g/2$

Figure 2.8: Schematic to illustrate the effect of sampling the spectrum of a non-causal impulse response. The non-causal impulse response is shown in (a). The responses obtained by sampling the spectrum of the non-causal response with modelling delays τ_d=0 and τ_d=$I_g/2$ are shown in (b) and (c), respectively. The number of control frequencies for the sampling is N=I_g.

remove these components. However, this would degrade the performance, as these components have significant energy. A better solution is to add a circular delay $\tau_d = L_g/2$ to the estimated response, as in Fig. 2.8c. In that case, the anti-causal components of the original response are turned into causal components. Thus, this is the motivation to apply a circular modelling delay τ_d to compute the practical filters.

Another important aspect regarding the previous method is the selection of the number of control frequencies N. This aspect is especially important when we try to estimate a non-causal impulse response whose significant anti-causal and causal components can not be fitted in a period of I_g samples without overlapping, even if a modelling delay is used. In a number of publications, as [51, 60], the number of control frequencies is selected equal to the filter length, i.e., $N = I_g$. However, it is shown in [10] that this selection requires long filters to achieve good performance. The main reason is that with $N = I_g$ and low values of I_g, anti-causal components of significant energy appear in q_l in the interval 0 to I_g-1 and overlap with other causal components of significant energy. This overlapping produces a notable degradation in the performance. This effect can only be mitigated by increasing the filter length, since for long filter lengths the causal

and anti-causal components that overlap in the 0 to I_g-1 period have low energy, and then, the degradation is not significant. Alternatively, Simón Gálvez [10] proposed computing the optimal filters with a much larger number of control frequencies, i.e., $N \gg I_g$, and then truncating the computed responses to a length I_g. For $N \gg I_g$, it is less likely that anti-causal and causal components of significant energy overlap in q_l in the interval 0 to I_g-1. Then, as the causal and anti-causal components do not overlap, a window of length I_g can be used to keep the causal components only. To illustrate this, we present in Fig. 2.9a an example of a non-causal impulse response. We also show in Fig. 2.9b and Fig. 2.9c the responses q_l obtained when sampling the spectrum of the non-causal response with $N = I_g$ and $N = 2I_g$, respectively. We can clearly see that with $N = I_g$, the anti-causal components of the original response appear in the interval 0 to I_g-1, and overlap with some of the causal components. However, when sampling the spectrum with $N = 2I_g$, the anti-causal components appear in q_l outside the interval 0 to I_g-1, and do not overlap with causal components of significant energy. Then, these components can be easily removed by applying a window of length I_g. Ideally, we would like to keep both, the causal and

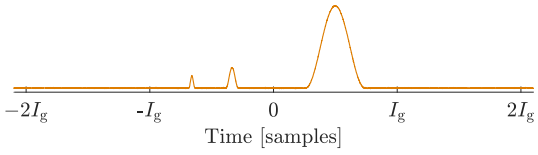

(a) Impulse response to estimate

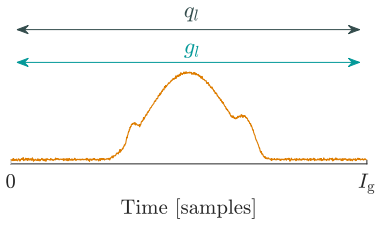

(b) Estimated q_l with $N = I_g$

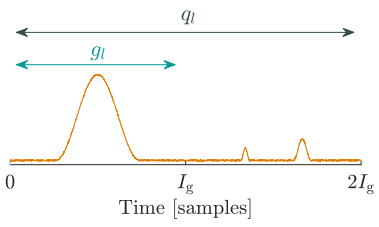

(c) Estimated q_l with $N = 2I_g$

Figure 2.9: Schematic to illustrate the effect of the IDFT size N when sampling the spectrum of a non-causal impulse response. The non-causal impulse response is shown in (a), the response obtained by sampling the spectrum of the original response with a number of points $N = I_g$ and $N = 2I_g$ in (b) and (c), respectively.

non-causal components, but this is not possible for the selected filter length I_g. Simón Gálvez [10] showed that for short filter lengths I_g, the performance with $N \gg I_g$ is notably better than with $N = I_g$, which indicates that removing the non-desired anti-causal components is a better option than using a response where the causal and anti-causal components overlap. Then, throughout this work, we will use $N = I_g + I_h - 1$, which has been observed to be large enough to achieve good performance, and then, a window of length I_g will be used to truncate the responses.

2.2.4 Review of algorithms

The design of the filters is a key aspect for a PSZ system, as it determines its performance. The algorithms used to calculate the optimal filters can be classified according to different criteria. On the one hand, the algorithms can be classified according to the aspects that are taken into account in the optimization: 1) energy cancellation algorithms, in which the energy of the cascade responses in each zone is controlled but their phase is not; and 2) soundfield synthesis algorithms, in which both the energy and the phase of the cascade responses are controlled. On the other hand, as discussed in Section 2.2.3, the algorithms can be classified according to the formulation used to define the optimization: 1) frequency-domain formulation; and 2) time-domain formulation. Next, we review the most relevant algorithms proposed in the literature, which are also listed in Table 2.1.

Several energy cancellation approaches that used the frequency-domain formulation were proposed in the literature. First, Choi and Kim [9] proposed the Acoustic Contrast Control (ACC) algorithm, which finds the filters that maximize the acoustic contrast. The acoustic contrast is the ratio between the mean energy of the cascade frequency responses in the bright and dark zones, and it is an indicator of the level of acoustic isolation between zones. The main drawback of the algorithm proposed by Choi and Kim [9] is that it requires the inversion of a matrix that might be ill-conditioned, and then, the computed filters offer poor robustness against perturbations. To solve this limitation, Shin et al. [38] proposed the Energy Difference Maximization (EDM) algorithm, which finds the filters that maximize the difference of the mean energies in the bright and dark zones, rather than their ratio. EDM does not require to compute any matrix inversion, so the robustness of the filters is not influenced by ill-conditioning problems. However, the cost function for EDM includes a tuning factor

Frequency-Domain	*Energy cancellation*	ACC [9, 61]
		EDM [38]
	Soundfield synthesis	PM [62]
		PC [63]
		wPM-F [50]
Time-Domain	*Energy cancellation*	BACC [54]
		BACC-RV [48]
		BACC-RD [55]
		BACC-RTE [49]
	Soundfield synthesis	wPM-T [39]
		VAST [64]

Table 2.1: Summary of the most relevant algorithms proposed in the literature to compute the filters of a PSZ system.

that has limited physical interpretation. It is shown in [61, 65] that EDM can obtain similar performance to ACC, but it is very sensitive to the selected tuning factor, and there is very little intuition on how to select it. Later, Elliott et al. [61] proposed a variation of the ACC algorithm, in which a constraint on the energy of the filters is included in the optimization. The energy constraint produces a regularization of the matrix that must be inverted, which mitigates the effect of the ill-conditioning problem and makes the filters more robust to perturbations. Furthermore, the constraint avoids feeding excessive electric power levels to the loudspeakers of the system [61]. This idea has been adopted in most of the algorithms proposed afterwards in the literature, in which a constraint on the energy of the filters is always included to increase their robustness to perturbations. This is a very important aspect for PSZ systems, as the filters must be robust enough to offer good performance in positions not explicitly considered by the algorithms but that are close to the control points. Also, the filters must be robust to changes in the environment, e.g., the perturbations

produced by the listeners when located within the zones. The formulation of ACC proposed by Elliott et al. [61] has been shown to provide very good isolation between the bright and dark zones. However, it does not offer control over the phase of the responses in the bright zone. Moreover, it is shown in [66] that non-uniform energy distributions can appear in the bright zone when using ACC. All these factors can lead to an uncomfortable listening experience to the user located in the bright zone.

Alternatively, several energy cancellation algorithms using the time-domain formulation were proposed in the literature. These algorithms obtain the filters directly by solving a single optimization, rather than computing their value for a set of discrete control frequencies. Elliott and Cheer [54] proposed the Broadband ACC (BACC) algorithm to compute the filters that minimize the ratio between the mean energy of the cascade impulse responses in the bright and dark zones (which can be interpreted as a time-averaged version of the acoustic contrast). Later, it was shown in [48, 67] that BACC leads to an uneven frequency response in the bright zone, meaning that the response is far from being flat and only presents significant energy in a narrow frequency band. Different algorithms were proposed to mitigate this effect, namely BACC with Response Variation constraint (BACC-RV) [48], BACC with Response Differential constraint (BACC-RD) [55], and BACC with Response Trend Estimation (BACC-RTE) [49]. These methods not only propose to minimize the time-averaged acoustic contrast, but also a term related to the variation of the responses across frequency in the bright zone. This additional term forces the filters to produce a flat response across frequency in the bright zone. A main drawback of these three algorithms is that the performance is very sensitive to the influence of the variation term in the optimization [51]. Then, a search must be carried out to find a suitable weighting factor that tunes the influence of this term in the optimal filters. Also, the performance of these approaches can be degraded in reverberant scenarios, where the room frequency responses present fluctuations across frequency due to the reflections. In these cases, targeting a flat response in the bright zone is a very restrictive condition that can only be achieved at the cost of degrading the isolation between zones. Then, ACC is preferred over its time-domain variations, because it does not target any specific response in the bright zone, and then, degradations in the acoustic contrast do not appear. For ACC, the frequency response in the bright zone can be modified by equalizing the input signals of the system [68].

Moreover, different soundfield synthesis algorithms using the frequency-domain formulation were proposed in the literature. First, Poletti [62] proposed the Pressure Matching (PM) algorithm, which finds the filters that minimize the Mean Squared Error (MSE) between the cascade frequency responses and some target frequency responses. In particular, the target is specified as a null response for the dark zone, and some response that leads to good listening experience for the bright zone. Then, more uniform energy distributions and suitable phase distributions can be achieved for the bright zone than with ACC [66]. However, this is at the cost of increasing the mean energy in the dark zone, which produces a reduction on the acoustic contrast. Simón Gálvez et al. [34] compared the performance of ACC and PM under anechoic conditions, and showed that PM can provide an acoustic contrast that is close to the one for ACC. Also, the authors concluded from a set of informal listening test that the audio quality of the sound reproduced in the bright zone was higher with PM than with ACC thanks to the control of the phase of the responses. Similar results were presented by Cheer et al. [11], in which the performance of both algorithms was compared in a car cabin. Moreover, thanks to the control of the phase and energy distributions in the bright zone, PM can be used to deliver stereo and other multi-channel programs in the bright zone, which can not be achieved with ACC. Also, Coleman et al. [63] proposed the Planarity Control (PC) algorithm, which is a similar approach to PM that aims to synthesize plane waves arriving from certain directions in the bright zone while maximizing the acoustic contrast. Chang and Jacobsen [50] proposed a variation of the PM algorithm called weighted Pressure Matching (wPM). This algorithm includes a weighting factor in the cost function for the optimization that allows to balance the solution. For example, a weighting factor that puts more effort in minimizing the MSE in the bright zone can synthesize the desired response for the bright zone with high accuracy at the cost of lower isolation between zones. On the contrary, a weighting factor that puts more effort in minimizing the MSE in the dark zone leads to acoustic contrast levels similar to those for ACC, but at the cost of decreasing the accuracy to synthesize the desired response in the bright zone. Even in this case, wPM still offers, to some extent, control over the energy and phase distributions in the bright zone [65]. Then, a trade-off between the interference level in the dark zone and the reproduction error in the bright zone can be obtained with wPM by properly selecting the weighting factor.

Later, Simón Gálvez et al. [39] proposed a variation of the wPM algorithm in which the time-domain formulation is used. This algorithm finds the filters that minimize the MSE between the cascade impulse responses and some target impulse responses. It also includes a weighting term that can be used to balance the solution. From now on, we will use the acronyms wPM-F and wPM-T to refer to wPM using the frequency and time domain formulations, respectively. It is shown in [39] that wPM-T outperforms wPM-F in anechoic room when short filters or modelling delays are considered, but at the cost of higher computational demands. Recently, Lee et al. [64] proposed the Variable Span Trade-off (VAST) algorithm, which is a generalization that has wPM-T and BACC as special cases.

From the previous discussion, it is clear that wPM, either with time or frequency domain formulations, is a good candidate for PSZ systems because it offers control over the energy in the dark zone and the response produced in the bright zone, so it can offer a trade-off between interference level in the dark zone and audio quality in the bright zone. In the remainder of this work, we will study and optimize the use of wPM for PSZ systems, either with time or frequency domain formulations. Later, we will review the wPM-F and wPM-T algorithms.

Finally, it is important to mention that all the algorithms described previously require some knowledge of the RIRs in the control points. The best performance is achieved when full knowledge of the RIRs is available, which can be obtained by measuring the RIRs between all the loudspeakers and control points using approaches as the swept-sine technique [69]. In some occasions, instead of measuring the RIRs, an acoustic model is used to estimate them, avoiding the measurement stage that can not be always carried out. In the literature, the free-field propagation model together with the position of the loudspeakers and control points has been considered to estimate the RIRs [7, 70]. Wallace and Cheer [71] compared the performance using measured RIRs and modelled RIRs with free-field assumption, and concluded that the performance with both methods is approximately equal above 1 kHz, but below this frequency the filters computed using measured RIRs significantly outperform the filters computed with modelled RIRs in terms of acoustic contrast. Since in this work we focus on filter optimizations for PSZ in low and mid frequencies, we will thus assume that full knowledge of the RIRs is available.

Weighted Pressure Matching with Freq.-Domain formulation (wPM-F)

Next, we review the wPM-F algorithm proposed by Chang and Jacobsen [50]. First, let us define $D_m(f)$ as the target frequency response at frequency f in the m-th control point. Also, let us define a vector of size $M\times 1$ with the target frequency responses in all control points as

$$\bar{\mathbf{d}}_f = \begin{bmatrix} D_0(f) & \dots & D_{M-1}(f) \end{bmatrix}^T. \tag{2.22}$$

Then, the wPM-F algorithm aims to find the filters at frequency f that minimize the following cost function

$$J(\bar{\mathbf{q}}_f) = \left\| \bar{\mathbf{W}}_f \left(\bar{\mathbf{H}}_f \, \bar{\mathbf{q}}_f - \bar{\mathbf{d}}_f \right) \right\|^2 + \bar{\beta}_f \left\| \bar{\mathbf{q}}_f \right\|^2, \tag{2.23}$$

where $\bar{\beta}_f \in \mathbb{R}^+$ is a regularization parameter that constrains the energy of the filters, and $\bar{\mathbf{W}}_f = \mathrm{diag}\left\{ \bar{w}_{0,f}, \dots, \bar{w}_{M-1,f} \right\}$ is a diagonal matrix of size $M\times M$ whose m-th diagonal element is defined as

$$\bar{w}_{m,f} = \begin{cases} \sqrt{\frac{\bar{\mu}_f}{M_\mathrm{d}}} & m \in \mathcal{D} \\ \sqrt{\frac{1-\bar{\mu}_f}{M_\mathrm{b}}} & m \in \mathcal{B} \end{cases}, \tag{2.24}$$

being $\bar{\mu}_f \in \mathbb{R}$ a weighting factor satisfying $0 \leq \bar{\mu}_f \leq 1$. We can see that the cost function (2.23) targets the minimization of the MSE between the cascade frequency responses and a selected target $\bar{\mathbf{d}}_f$. Usually, the elements of $\bar{\mathbf{d}}_f$ corresponding to the dark zone are selected as a null response, i.e., $D_m(f) = 0$ for $m \in \mathcal{D}$. Hence, the cost function aims to minimize the MSE with respect to a selected target response for the bright zone, and the energy of the cascade frequency response in the dark zone. The weighting parameter $\bar{\mu}_f$ produces a spatial weighting of the errors in the control points of the bright and dark zones, and it is used to balance the solution, e.g., high values of $\bar{\mu}_f$ put more effort in minimizing the mean energy in the dark zone whereas low values of $\bar{\mu}_f$ put more effort in minimizing the MSE with respect to the target response in the bright zone. Then, (2.23) offers a balanced solution between minimizing the mean energy in the dark zone and the MSE in the bright zone. The cost function (2.23) can be written as

$$J(\bar{\mathbf{q}}_f) = \bar{\mathbf{q}}_f^H \bar{\mathbf{H}}_f^H \bar{\mathbf{W}}_f^T \bar{\mathbf{W}}_f \bar{\mathbf{H}}_f \bar{\mathbf{q}}_f - 2\,\Re\left\{ \bar{\mathbf{q}}_f^H \bar{\mathbf{H}}_f^H \bar{\mathbf{W}}_f^T \bar{\mathbf{W}}_f \bar{\mathbf{d}}_f \right\} + \bar{\beta}_f \, \bar{\mathbf{q}}_f^H \bar{\mathbf{q}}_f, \tag{2.25}$$

where the term $\bar{\mathbf{d}}_f^H \, \bar{\mathbf{W}}_f^T \, \bar{\mathbf{W}}_f \, \bar{\mathbf{d}}_f$ has been omitted because it has no effect on the optimization. Since (2.23) is a quadratic cost function, it has a unique global minimum for $\bar{\beta}_f > 0$ at the point in which its gradient equals 0, i.e., $\nabla J(\bar{\mathbf{q}}_f) = \mathbf{0}$. The gradient of the cost function is given by [72]

$$\nabla J(\bar{\mathbf{q}}_f) = 2\,\bar{\mathbf{H}}_f^H \bar{\mathbf{W}}_f^T \bar{\mathbf{W}}_f \bar{\mathbf{H}}_f \bar{\mathbf{q}}_f - 2\,\bar{\mathbf{H}}_f^H \bar{\mathbf{W}}_f^T \bar{\mathbf{W}}_f \bar{\mathbf{d}}_f + 2\,\bar{\beta}_f\,\bar{\mathbf{q}}_f, \tag{2.26}$$

and then, the expression of the optimal filters can be written as [50]

$$\bar{\mathbf{q}}_{\mathrm{opt},f} = \left(\bar{\mathbf{H}}_f^H \bar{\mathbf{W}}_f^T \bar{\mathbf{W}}_f \bar{\mathbf{H}}_f + \bar{\beta}_f\,\mathbf{I}_L\right)^{-1} \bar{\mathbf{H}}_f^H \bar{\mathbf{W}}_f^T \bar{\mathbf{W}}_f \bar{\mathbf{d}}. \tag{2.27}$$

We can see in (2.27) that the constraint on the energy of the filters produces a regularization of the matrix that must be inverted to compute the filters. Then, the energy constraint makes the filters more robust against ill-conditioning problems. In particular, low regularization levels lead to high energy filters which obtain good performance in the control points, but bad performance in positions not controlled by the algorithm. On the contrary, higher regularization levels lead to filters with lower energy which do not offer as good performance in the control points, but offer better performance in positions not controlled by the algorithm.

It is important to mention that (2.23) is the cost function of a Least Squares (LS) problem. Then, the optimal filters are the solution of the following linear system of equations

$$\left(\bar{\mathbf{H}}_f^H \bar{\mathbf{W}}_f^T \bar{\mathbf{W}}_f \bar{\mathbf{H}}_f + \bar{\beta}_f\,\mathbf{I}_L\right) \bar{\mathbf{q}}_f = \bar{\mathbf{H}}_f^H \bar{\mathbf{W}}_f^T \bar{\mathbf{W}}_f \bar{\mathbf{d}}_f. \tag{2.28}$$

A regularization factor $\bar{\beta}_f > 0$ assures the existence of a unique solution, even if matrix $\bar{\mathbf{H}}_f$ of size $M \times L$ is rank deficient. A in-depth study of LS problems and their main properties can be found in [72].

Weighted Pressure Matching with Time-Domain formulation (wPM-T)

Now, we review the wPM-T algorithm proposed by Simón Gálvez et al. [39]. Let us define $d_m(n)$ as the real-valued FIR target impulse response of length $I_\mathrm{d} = I_\mathrm{h} + I_\mathrm{g} - 1$ in the m-th control point. Let us also define a vector of size $M \times 1$ containing the target for time n and for all control points as

$$\mathbf{d}_n = \begin{bmatrix} d_0(n) & \dots & d_{M-1}(n) \end{bmatrix}^T. \tag{2.29}$$

Moreover, let us define a vector of size $M I_\mathrm{d} \times 1$ containing the target for all control points and all time instants as

$$\mathbf{d} = \begin{bmatrix} \mathbf{d}_0^T & \dots & \mathbf{d}_{I_\mathrm{d}-1}^T \end{bmatrix}^T. \tag{2.30}$$

Then, the wPM-T algorithm aims to find the broadband filters $\mathbf{g}$ that minimize the following cost function

$$J(\mathbf{g}) = \|\mathbf{W}(\mathbf{H}\mathbf{g} - \mathbf{d})\|^2 + \beta \|\mathbf{g}\|^2, \tag{2.31}$$

where $\beta \in \mathbb{R}^+$ is a regularization factor and $\mathbf{W}$ is a weighting matrix. Cost function (2.31) aims the minimization of the MSE between the cascade impulse responses and a selected target $\mathbf{d}$. The elements of $\mathbf{d}$ corresponding to the dark zone are usually selected as a null response, i.e., $\mathbf{d}_m = \mathbf{0}$ for $m \in \mathcal{D}$. Hence, the cost function aims to minimize the MSE with respect to a selected target impulse response for the bright zone, and the energy of the cascade impulse response in the dark zone. The fundamental idea behind cost function (2.31) is the same as for cost function (2.23) for wPM-F, the only difference is that impulse responses instead of frequency responses are used. For the time domain formulation, $\mathbf{W}$ can include not only spatial, but also time and frequency weightings. This is an advantage of wPM-T with respect to wPM-F, as for example, time weighting can be used to reduce the pre-ringing levels [52]. However, in this work we only consider the spatial weighting. Then, let us define $\mathbf{W} = \mathbf{\Omega} \otimes \mathbf{I}_{I_\mathrm{d}}$, i.e., a block-diagonal matrix with diagonal blocks of size $M \times M$. In particular, let us define the diagonal blocks as $\mathbf{\Omega} = \mathrm{diag}\{w_0, \ldots, w_{M-1}\}$. It is easy to see that w_m is the weight given in the cost function to the error for the m-th control point, which can be defined as

$$w_m = \begin{cases} \sqrt{\frac{\mu}{M_\mathrm{d}}} & m \in \mathcal{D} \\ \sqrt{\frac{1-\mu}{M_\mathrm{b}}} & m \in \mathcal{B} \end{cases}, \tag{2.32}$$

where $\mu \in \mathbb{R}$ is a weighting factor satisfying $0 \leq \mu \leq 1$. Similarly to wPM-F, high values of μ put more effort in minimizing the mean energy in the dark zone while low values of μ put more effort in minimizing MSE with respect to the target response in the bright zone. The cost function (2.31) can be written as

$$J(\mathbf{g}) = \mathbf{g}^T\mathbf{H}^T\mathbf{W}^T\mathbf{W}\mathbf{H}\mathbf{g} - 2\,\mathbf{g}^T\mathbf{H}^T\mathbf{W}^T\mathbf{W}\mathbf{d} + \beta\,\mathbf{g}^T\mathbf{g}, \tag{2.33}$$

where the term $\mathbf{d}^T\mathbf{W}^T\mathbf{W}\mathbf{d}$ has been omitted because it has no effect on the optimization. By analogy with wPM-F, it is straight forward to show that the optimal filters that minimize (2.31) are given by

$$\mathbf{g}_\mathrm{opt} = \left(\mathbf{H}^T\mathbf{W}^T\mathbf{W}\mathbf{H} + \beta\,\mathbf{I}_{LI_\mathrm{g}}\right)^{-1}\mathbf{H}^T\mathbf{W}^T\mathbf{W}\mathbf{d}. \tag{2.34}$$

Again, adding a constraint on the energy of the filters produces a regularization of the matrix that must be inverted to compute the filters. It is worth mentioning that in the presented derivation β is a broadband regularization factor, i.e., the same regularization is applied to all frequencies. In [39], the authors propose a frequency-dependent regularization by replacing $\beta \mathbf{I}_{LI_\mathrm{g}}$ by $\beta \mathbf{R}_\mathrm{reg}$, where $\mathbf{R}_\mathrm{reg}$ is the correlation matrix of a FIR filter. Then, by properly designing the spectral shape of the filter a frequency-dependent regularization can be obtained.

Similarly to wPM-F, (2.31) is the cost function of a LS problem. However, in this case the number of unknown parameters of the system of linear equations is significantly larger. In particular, wPM-F has L unknown parameters for each frequency component whereas wPM-T has LI_g unknown parameters. This is the main drawback of wPM-T, since solving the LS problem requires significantly higher computational efforts than for wPM-F. In Chapter 3, we will study different exact and approximate methods to efficiently compute the optimal solution for wPM-T.

2.2.5 Control metrics

Next, we describe the metrics used in this work to evaluate the performance of PSZ systems.

First, let us consider the generic model shown in Fig. 2.10, in which s is the input signal and y_l is the signal fed to the l-th loudspeaker. In this model, the bright and dark zones are spatially sampled using two different grids of microphones, which represent the control and validation grids. The RIRs in the points of the control grid (control points) are denoted as h_{ml}, and are used by the presented algorithms to compute the optimal filters of the system. The RIRs in the points of the validation grid (validation points) are denoted as $h_{\mathrm{v},ml}$ and are used to evaluate the performance of the computed filters. Then, two different sets of RIRs are used to compute and to evaluate the filters. This is a common procedure for evaluating the performance of PSZ systems, because it allows to evaluate how robust the system is to perturbations [51].

Now, we present the metrics used to evaluate the performance. First, let us define $H_{\mathrm{v},ml}(f)$ as the room frequency response between the l-th loudspeaker and the m-th validation point, and $Y_l(f)$ as the frequency response of the signal fed to the l-th loudspeaker. Then, let us define the

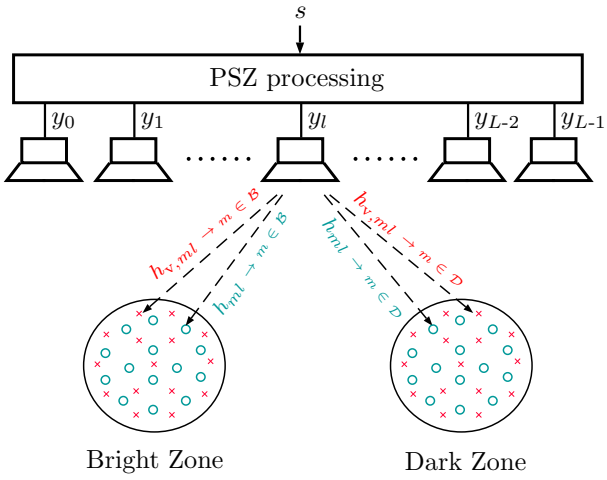

Figure 2.10: Model used for evaluating the performance of a PSZ system. The circle and cross markers denote control and validation points, respectively.

cascade frequency response in the m-th validation point as

$$X_{\mathrm{v},m}(f) = \sum_{l=0}^{L-1} H_{\mathrm{v},ml}(f) Y_l(f). \tag{2.35}$$

Also, we can define the mean energy in the validation points of the bright and dark zones at frequency f as

$$E_{\mathrm{b}}(f) = \frac{1}{M_{\mathrm{b}}} \sum_{m \in \mathcal{B}} \left| X_{\mathrm{v},m}(f) \right|^2, \tag{2.36}$$

and

$$E_{\mathrm{d}}(f) = \frac{1}{M_{\mathrm{d}}} \sum_{m \in \mathcal{D}} \left| X_{\mathrm{v},m}(f) \right|^2, \tag{2.37}$$

respectively. Moreover, let us define the Acoustic Contrast (AC) [9] as

$$C(f) = \frac{E_{\mathrm{b}}(f)}{E_{\mathrm{d}}(f)}, \tag{2.38}$$

and the Mean Squared Error (MSE) in the validation points of the bright zone as

$$\epsilon(f) = \frac{1}{M_\mathrm{b}} \sum_{m \in \mathcal{B}} \left| X_{\mathrm{v},m}(f) - S(f) D_{\mathrm{v},m}(f) \right|^2 , \tag{2.39}$$

where $D_{\mathrm{v},m}(f)$ is the target frequency response for the m-th validation point (which is indicated in each case), and $S(f)$ is the frequency response of the input signal. As we previously discussed, the acoustic contrast is a metric that is related to the level of acoustic isolation between zones, while the MSE is a metric that is related to the reproduction error and the audio quality in the bright zone. Then, these two metrics are fundamental for evaluating PSZ systems, as the acoustic contrast is an indicator of the level of interferences produced in the dark zone, and the MSE is an indicator of how good the listening experience is in the bright zone. Finally, let us define the Array Effort (AE) [61] as

$$\xi(f) = \frac{\sum_{l=0}^{L-1} |Y_l(f)|^2}{E_\mathrm{br}(f)}, \tag{2.40}$$

where $E_\mathrm{br}(f)$ is the energy required by a single reference loudspeaker l_r to produce the same energy in the validation points of the bright zone as the signals played by all the loudspeakers of the PSZ system, i.e.,

$$E_\mathrm{br}(f) = \frac{E_\mathrm{b}(f)}{\frac{1}{M_\mathrm{b}} \sum_{m \in \mathcal{B}} |S(f) H_{\mathrm{v},ml_\mathrm{r}}(f)|^2}. \tag{2.41}$$

Then, the array effort is an indicator of the energy required by the array of loudspeakers to produce a certain energy level in the bright zone.

In the model that we discussed in Section 2.2.2, we assumed that the input signal is a unit impulse, i.e., $S(f) = 1$, and that the signal fed to the loudspeakers is obtained by filtering the input signal with a FIR filter g_l, thus $Y_l(f) = G_l(f)S(f)$, where $G_l(f)$ is the frequency response of g_l at frequency f. Then, with these assumptions, the frequency content of the signal fed to the l-th loudspeaker is

$$Y_l(f) = G_l(f), \tag{2.42}$$

which is used in most of the performance evaluations of this work. However, we present generic equations for the metrics, which use Y_l instead of G_l, because these definitions are general enough to be used in Chapter 4, where we will use filter banks (i.e., time-variant systems) to process the signals of the PSZ system.

2.3 Performance evaluation

The performance of wPM with time and frequency domain formulations, i.e., wPM-T and wPM-F, was previously compared in several works. First, Simón Gálvez et al. [39] compared the performance of both algorithms in anechoic chamber for different filter lengths and modelling delays. They determined that both algorithms perform similarly when long filters and appropriated modelling delays are used, but wPM-T outperforms wPM-F for short filters or short modelling delays. Also, Vindrola et al. [60] compared the performance of the algorithms in anechoic chamber for filters of length 392 samples at a sampling frequency 2450 Hz. They concluded that both algorithms offer a very similar performance. However, the presented comparison is not fair, as the effect of the filter length is not taken into account. Moreover, Møller and Olsen [51] compared the performance of the algorithms in a reverberant environment with reverberation time $T_{60} = 0.6$ s for filters of length 256 samples at a sampling frequency 1.2 kHz. They concluded that wPM-T outperforms wPM-F in terms of acoustic contrast, but again, the comparison is not fair as they did not study whether wPM-T outperforms wPM-F for longer filters. To the best of our knowledge, there are no works in the literature that compare the performance of wPM-T and wPM-F in reverberant environment and that consider in the comparison the influence of the filter length, the modelling delay, and the regularization level. Thus, we present in this section such a comparison.

2.3.1 Setup and methodology

Setup

The experimental evaluations have been carried out in an office-like room at iTEAM-UPV. The room size is $7.2 \times 11.72 \times 2.65$ m and its reverberation time is $T_{60} = 500$ ms. The setup is formed by one bright and one dark zone, as shown in Fig. 2.11a. In each zone, two different grids of microphones are used for spatial sampling, such that the RIRs measured at the control and validation grids are used to compute the filters and to evaluate their performance, respectively. A linear array of 8 two-way JBL 305P MkII loudspeakers [73] with an inter-element distance of 0.18 m is used (see Fig. 2.11b). The RIRs were measured using the swept-sine technique [69] with a sampling frequency of 44100 Hz, and then downsampled to 6300 Hz, obtaining impulse responses of length $I_{\mathrm{h}} = 2330$. Two grids of

4×4 Brüel & Kjær microphones Type 4958 [74], previously calibrated with a Brüel & Kjær sound calibrator Type 4231 [75], were used to measure the RIRs at the control/validation points (as shown in Fig. 2.11c). The distance between the elements of the grid is 0.15 m.

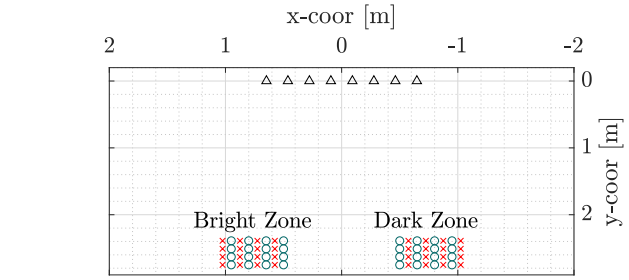

(a)

(b)

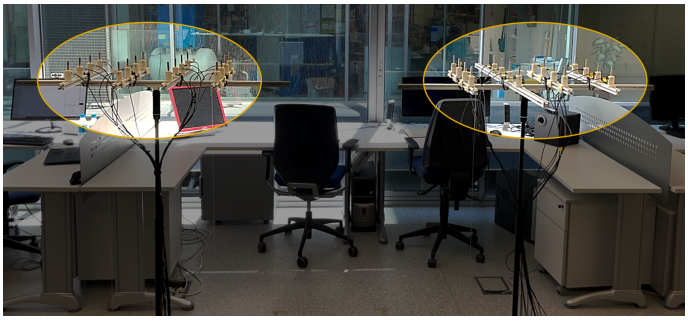

(c)

Figure 2.11: Setup used for the evaluations in (a), where ○ and × denote control and validation points, respectively, and ▲ denotes a loudspeaker. The walls are in $x = \pm 3.6$ m, $y = \pm 5.86$ m, and $z = \{0, 2.65\}$ m, and the loudspeakers and microphones are at a height of 1.56 m. The array of 8 loudspeakers is shown in (b). The two grids of 4×4 microphones used for measuring the RIRs in the control/validation points are shown in (c).

Methodology for computing the filters

First, let us select the target impulse response in the m-th control point as

$$d_m(n) = \begin{cases} h_{ml_\mathrm{r}}(n-\tau_\mathrm{d}) & m \in \mathcal{B} \\ 0 & m \in \mathcal{D} \end{cases}, \tag{2.43}$$

i.e., the RIR for the l_r-th loudspeaker and null response for the control points in the bright and dark zones, respectively. In particular, the reference loudspeaker is chosen as $l_\mathrm{r} = 3$ (as shown in Fig. 2.11b). The target (2.43) includes a modelling delay $\tau_\mathrm{d} \in \mathbb{N}$ whose value is indicated in each case. Now, we describe the methodology used to compute the optimal filters for the different algorithms:

- **wPM-T:** The filters g_l of length I_g are computed using (2.34), assuming that the target response d_m is given by (2.43). The weighting factor is set to $\mu = 0.5$. The regularization factor is selected as

$$\beta = \beta_0 \, u_\mathrm{avg}, \tag{2.44}$$

  where u_avg is the mean of the eigenvalues of matrix $\mathbf{H}^T\mathbf{W}^T\mathbf{W}\mathbf{H}$ in (2.34), and β_0 is the regularization factor relative to u_avg. Parameter β_0 is more meaningful than β, since it indicates the amount of regularization added to the matrix that we aim to invert with respect to the mean of its eigenvalues. The value of β_0 is indicated in each case.

- **wPM-F** The coefficients $Q_l(f)$ are computed for a set of $N{=}I_\mathrm{h}{+}I_\mathrm{g}{-}1$ control frequencies using (2.27), where $D_m(f)$ is selected as the DFT of $d_m(n)$ in (2.43). The coefficients $Q_l(f)$ are set to 0 for control frequencies below 80 Hz, to reduce the energy at low frequencies where high directivity can not be achieved. After that, an N-point IDFT is used to obtain the time-domain responses q_l, which are truncated using a window of size I_g to obtain the filters g_l (as described in Section 2.2.3). The selected window is indicated in each case. It is important to highlight that additional modelling delay is not added to q_l, as this response already includes the modelling delay τ_d due to the specified target. The weighting factor is set to $\bar{\mu}_f = 0.5$ for all frequencies. The regularization factor is selected as

$$\bar{\beta}_f = \bar{\beta}_{0,f} \, \bar{u}_{\mathrm{avg},f}, \tag{2.45}$$

where $\bar{u}_{\text{avg},f}$ is the mean of the eigenvalues of $\bar{\mathbf{H}}_f^H \bar{\mathbf{W}}_f^T \bar{\mathbf{W}}_f \bar{\mathbf{H}}_f$ in (2.27), and $\bar{\beta}_{0,f}$ is the regularization factor relative to $\bar{u}_{\text{avg},f}$. The value of $\bar{\beta}_{0,f}$ is indicated in each case.

Methodology for evaluating the filters

For evaluating the filters, the metrics described in Section 2.2.5 are computed for a set of 16384 equispaced frequencies with a resolution of 0.3845 Hz assuming that the input signal is a unit impulse. The target response for the m-th validation point used to evaluate the filters is selected as

$$d_{\text{v},m}(n) = \begin{cases} h_{\text{v},ml_\text{r}}(n - \tau_\text{d}) & m \in \mathcal{B} \\ 0 & m \in \mathcal{D} \end{cases}, \tag{2.46}$$

where h_{v,ml_r} is the RIR from the l_r-th loudspeaker to the m-th validation point. In Fig. 2.12, we show h_{v,ml_r} and $d_{\text{v},m}$ for the validation point $m = 0$ (in the bright zone) and with $\tau_\text{d} = 256$. The target frequency response $D_{\text{v},m}$ is computed as the DFT of $d_{\text{v},m}$. To improve the readability of the results, 1/3-octave band averaging [76] is used for all frequency-domain plots.

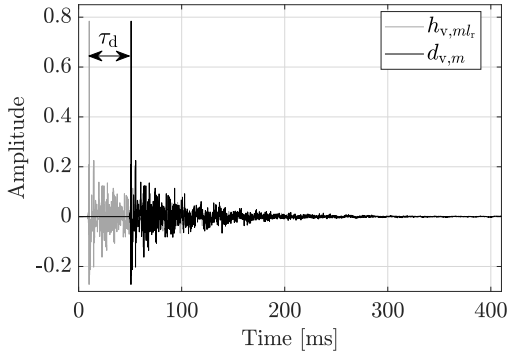

Figure 2.12: Room impulse response h_{v,ml_r} and target impulse response $d_{\text{v},m}$ for the validation point m=0 and a modelling delay τ_d=256 (40.6 ms).

2.3.2 Impulse response truncation for wPM-F

Previous works using wPM-F considered different window types for truncating the impulse responses obtained with the frequency domain optimization. In particular, Cheer et al. [11] and Simón Gálvez et al. [39] used a Hanning window, while Møller and Olsen [51] and Vindrola et al. [60] used

a rectangular window. However, the performance of the algorithm using these different windows was not compared in any of these works. This is an important aspect to study before comparing wPM-F and wPM-T, since the selected window influences the performance of wPM-F.

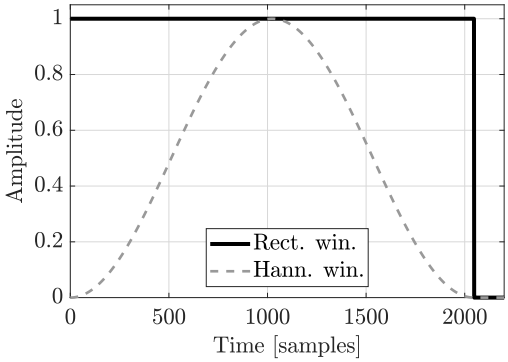

Figure 2.13: Impulse responses of rectangular and Hanning windows of length 2048 samples.

Then, we compare the performance of wPM-F using rectangular and Hanning windows for truncating q_l to obtain g_l. First, we show in Fig. 2.13 the impulse responses of rectangular and Hanning windows of length 2048 samples, to exemplify their time-domain properties. Next, we show in Fig. 2.14 the acoustic contrast, the MSE in the bright zone, and the array effort for wPM-F using both windows. We study the performance for filter lengths $I_\mathrm{g} = 512$ and $I_\mathrm{g} = 2048$ in the left and right columns of Fig. 2.14, respectively. The modelling delay is selected as $\tau_\mathrm{d} = I_\mathrm{g}/2$. For the rectangular window, the performance with two regularization factors $\bar{\beta}_{0,f} = 10^{-3}$ and $\bar{\beta}_{0,f} = 10^{-2}$ is included, while for the Hanning window the performance with $\bar{\beta}_{0,f} = 10^{-3}$ is shown. First, it is interesting to note that increasing the filter length from 512 to 2048 significantly improves the acoustic contrast and the MSE at frequencies below 800 Hz for all the studied windows and regularization factors. Also, we can see that for frequencies above 800 Hz the three metrics are very similar in all cases. This is because at these frequencies the wavelength is comparable with the size of the zones, so the optimization is less sensitive to parameters as the window type, the filter length and the regularization factor [68]. Moreover, we can clearly see the effect of the spatial aliasing for frequencies above 1.5 kHz, in which the acoustic contrast drops to values below 7 dB. Regarding the performance of

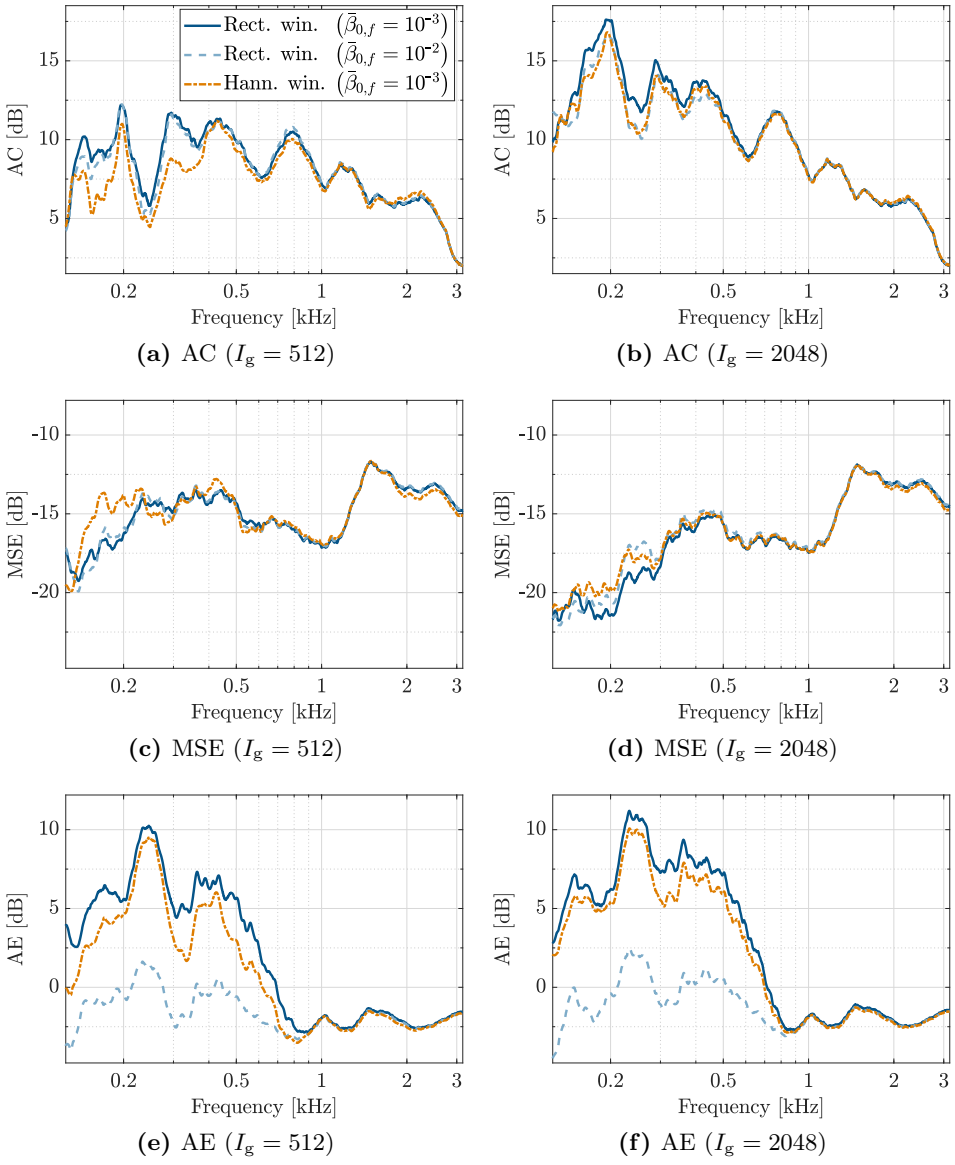

(a) AC ($I_\mathrm{g} = 512$) **(b)** AC ($I_\mathrm{g} = 2048$)

(c) MSE ($I_\mathrm{g} = 512$) **(d)** MSE ($I_\mathrm{g} = 2048$)

(e) AE ($I_\mathrm{g} = 512$) **(f)** AE ($I_\mathrm{g} = 2048$)

Figure 2.14: Acoustic contrast (a, b), MSE (c, d), and array effort (e, f) as a function of frequency for wPM-F with rectangular and Hanning windows. Filter lengths $I_\mathrm{g} = 512$ and $I_\mathrm{g} = 2048$ are considered with $\tau_\mathrm{d} = I_\mathrm{g}/2$. For the rectangular window we consider regularizations $\bar{\beta}_{0,f} = 10^{-3}$ and $\bar{\beta}_{0,f} = 10^{-2}$, and for the Hanning window $\bar{\beta}_{0,f} = 10^{-3}$.

the different windows in Fig. 2.14, the Hanning window offers worst acoustic contrast and MSE than the rectangular window at frequencies below 400 Hz for $\bar{\beta}_{0,f} = 10^{-3}$. In particular, degradations of up to 4 and 2 dB can be found for $I_\mathrm{g} = 512$ and $I_\mathrm{g} = 2048$, respectively. However, it is also important to notice that the Hanning window requires lower array effort than the rectangular window. For the rectangular window, increasing the regularization factor from $\bar{\beta}_{0,f} = 10^{-3}$ to $\bar{\beta}_{0,f} = 10^{-2}$ significantly reduces the array effort, at the cost of small degradations in the acoustic contrast and the MSE. For a filter length $I_\mathrm{g} = 512$, the acoustic contrast and the MSE obtained with the rectangular window with $\bar{\beta}_{0,f} = 10^{-2}$ are better than for the Hanning window with $\bar{\beta}_{0,f} = 10^{-3}$, while its array effort is significantly lower. For $I_\mathrm{g} = 2048$, the acoustic contrast and the MSE with the rectangular window with $\bar{\beta}_{0,f} = 10^{-2}$ and with the Hanning window with $\bar{\beta}_{0,f} = 10^{-3}$ are approximately equal, but again, with significantly lower array effort for the rectangular window. Then, these results show that using a rectangular window leads to better acoustic contrast and MSE than using a Hanning window, particularly at low frequencies. Also, the results show that increasing the filter length reduces the differences in the performance between the different windows.

Next, we study the impulse responses of the filters for wPM-F before and after truncation, i.e., q_l and g_l, respectively. We show in Fig. 2.15 the responses q_l and g_l for the reference loudspeaker, i.e., $l = 3$, obtained with $\bar{\beta}_{0,f} = 10^{-3}$ and for the cases in which rectangular and Hanning windows are used to truncate the filters. We include examples with $I_\mathrm{g} = 512$ and $\tau_\mathrm{d} = 256$, and $I_\mathrm{g} = 2048$ and $\tau_\mathrm{d} = 1024$. First, it is interesting to note that q_l in Fig. 2.15a and 2.15c include some components with significant energy at the end of the responses. As we discussed in Section 2.2.3, these components appear because the responses that we estimate are non-causal, and therefore, the circularity of the IDFT produces that the anti-causal components of these responses appear at the end of the period of the IDFT in q_l. Then, truncating the responses is required not only to obtain the desired length I_g, but also to remove these components (as they can deteriorate the quality of the audio rendered to the bright zone). Regarding the filters obtained after truncation, we can see that the rectangular window truncates the response q_l, but it preserves the amplitude of its components. On the contrary, the Hanning window not only truncates q_l, but also modifies its amplitude. This is the main difference between both windows, and the reason why the rectangular window outperforms the Hanning window. The

amplitude of the components of q_l for different time instants and loudspeakers is optimized such that their combination leads to high acoustic contrast and low MSE. However, when modifying the amplitude of the components of q_l with the Hanning window we are deviating from the optimal values, and the combination of the modified components for different time instants and loudspeakers leads to worse acoustic contrast and MSE (as shown in Fig. 2.14). Also, Fig. 2.15 shows that for $I_\mathrm{g} = 512$ the Hanning window significantly modifies the amplitude of components that are located at least 150 samples away from the main peak, which include components with im-

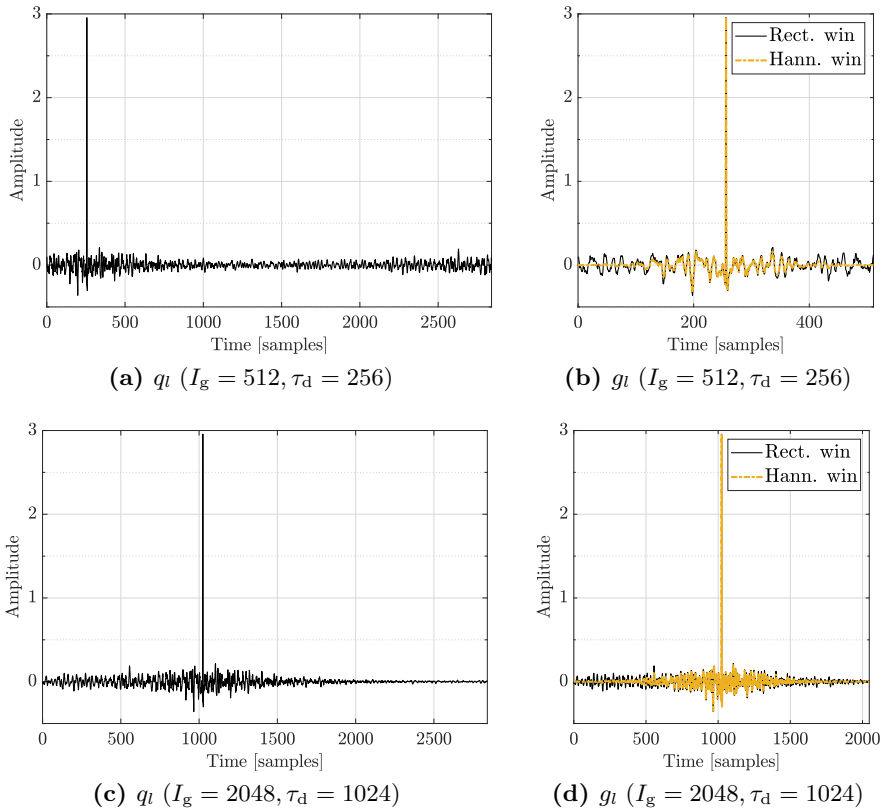

(a) q_l $(I_\mathrm{g} = 512, \tau_\mathrm{d} = 256)$ **(b)** g_l $(I_\mathrm{g} = 512, \tau_\mathrm{d} = 256)$

(c) q_l $(I_\mathrm{g} = 2048, \tau_\mathrm{d} = 1024)$ **(d)** g_l $(I_\mathrm{g} = 2048, \tau_\mathrm{d} = 1024)$

Figure 2.15: Impulse responses of the filters for wPM-F before and after truncation, i.e., q_l and g_l, respectively, for $l = 3$. The filters are computed with $I_\mathrm{g} = 512$ and $I_\mathrm{g} = 2048$, $\tau_\mathrm{d} = I_\mathrm{g}/2$, and $\bar{\beta}_{0,f} = 10^{-3}$. The impulse responses truncated with rectangular and Hanning windows are included.

portant energy levels. For $I_g = 2048$, the Hanning window significantly modifies the components that are located at least 500 samples away from the main peak, which are components with lower energy. Then, the differences between the filters truncated with both windows are less significant for long filters, which agrees with the results presented in Fig. 2.14.

In summary, we showed that better acoustic contrast and MSE can be achieved when using rectangular windows instead of Hanning windows to truncate the impulse responses obtained with wPM-F. Also, we showed that the differences between both windows are especially important when short filters are considered, while similar performance is obtained for long filters. In the remainder of this work, rectangular windows will be used to truncate the filters for wPM-F.

2.3.3 Influence of the regularization factor

The influence of the regularization factor on the performance is also an important aspect to consider before comparing the performance of the algorithms. Then, we study next the influence of the regularization factor on the performance of a PSZ system.

The acoustic contrast, the MSE in the bright zone, and the array effort as a function of the regularization factor β_0 for wPM-T are shown in Fig. 2.16, where a filter length $I_g = 2048$ and a modelling delay $\tau_d = 1024$ are considered. First, we can notice that the regularization factor and the array effort are directly related, since increasing the regularization factor decreases the array effort, i.e., the energy of the filters. This agrees with that discussed in Section 2.2.4, as the regularization factor constrains the energy of the filters in the cost function (2.31). Also, the results reveal that very low and very high regularization factors do not lead to the best achievable acoustic contrast and MSE. The motivation is that very low regularization factors obtain filters that offer good performance in those spatial positions that are taken into account in the optimization, i.e., the control points, but present bad performance in other positions within the zones that are not considered in the optimization, e.g., the validation points. Then, very low regularization factors lead to filters that present poor robustness against mismatches between the RIRs in the control and validations grids, and also, against perturbations on the environment, which in practice leads to bad performance for the PSZ system. Increasing the regularization factor strengthens the robustness of the filters to perturbations, and consequently, the perfor-

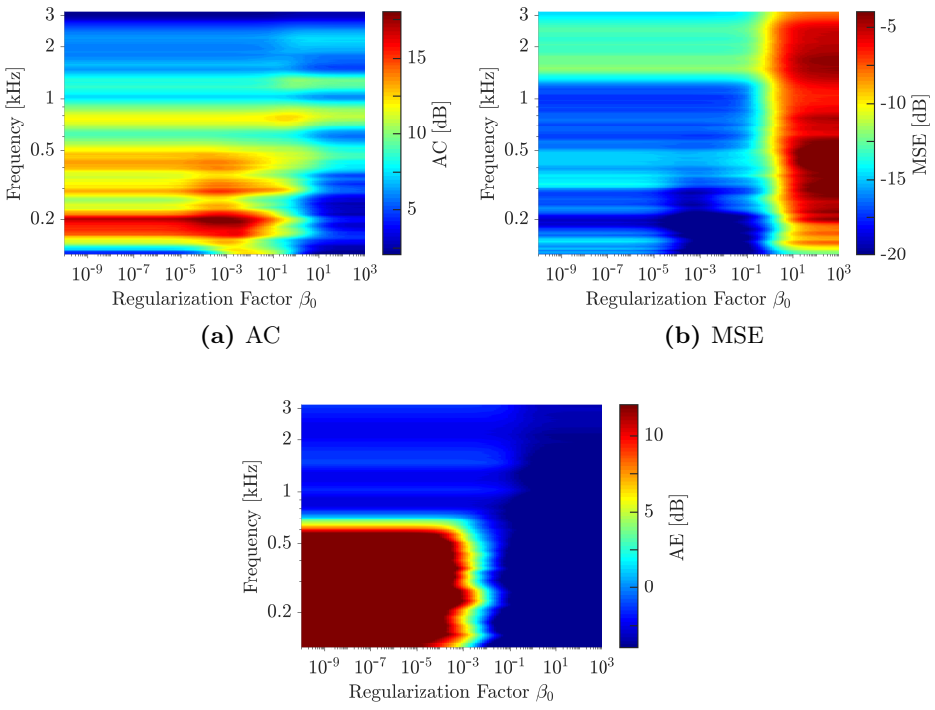

(a) AC **(b)** MSE **(c)** AE

Figure 2.16: Acoustic contrast (a, b), MSE (c, d), and array effort (e, f) as a function of frequency and the regularization factor β_0 for wPM-T. A filter length $I_g = 2048$ and a modelling delay $\tau_d = 1024$ are considered.

mance of the system in the validation points is improved. At some point, increasing the regularization factor does not longer improve the performance, and can even degrade it. This is because high regularization factors provide filters that present very low energy, but at the cost of degrading the acoustic contrast and the MSE. Then, the regularization factor must be high enough to obtain filters that are robust to perturbations, but also low enough to obtain filters with suitable energy levels that can offer good performance. The results in Fig. 2.16 suggest that regularization factors β_0 in the range 10^{-4} to 10^{-1} are adequate for the considered PSZ system. In particular, a regularization factor $\beta_0 = 10^{-3}$ offers a good compromise between acoustic contrast, MSE, and array effort.

2.3.4 Comparison of wPM-T and wPM-F

Next, we compare the performance of wPM-T and wPM-F in a reverberant environment, taking into account the influence of the filter length, the modelling delay, and the regularization level. We focus on the comparison of the performance of the algorithms, while their computational demands will be evaluated in Chapter 3. In the remainder of this section, a search is carried out to find the regularization factor $\bar{\beta}_{0,f}$ for each control frequency for wPM-F that leads to the same array effort as wPM-T with a regularization factor β_0 (with the same I_g and τ_d). Hence, we make sure that both algorithms present the same array effort, and then, the comparison between algorithms is fair, since differences in the acoustic contrast and the MSE are not produced because the algorithms present different effort levels.

Average performance per octave band

We compare the average acoustic contrast, MSE, and array effort in three octave bands for wPM-T and wPM-F. The average performance in the bands 125-250 Hz, 250-500 Hz, and 500-1000 Hz is shown in Fig. 2.17 to 2.19, respectively, as a function of the filter length. The performance with two regularization factors $\beta_0 = 10^{-3}$ and $\beta_0 = 10^{-1}$ is included in Fig. 2.17 to 2.19, and three modelling delays $\tau_\mathrm{d} = 64$ (10.2 ms) , $\tau_\mathrm{d} = 256$ (40.6 ms), and $\tau_\mathrm{d} = 1024$ (162.5 ms) are considered. In the evaluations, only the combinations of modelling delays and filter lengths fulfilling $I_\mathrm{g} > \tau_\mathrm{d}$ are considered.

First, we discuss some general considerations that are common to all the studied octave bands and algorithms. In general, Fig. 2.17 - 2.19 show that increasing the filter length improves the acoustic contrast and the MSE for all algorithms, modelling delays and regularizations. Then, PSZ systems usually need to use long filters to obtain good performance. However, increasing the filter length increases the computational efforts required to compute the optimal filters and to filter the input signals, and in some applications this is a critical aspect because high computational capabilities are not available. The presented results also show that, at some point, the performance converges and increasing the filter length does not longer offer performance improvements. Also, it is interesting to note that the required array effort is higher for short filters than for longer filters, while the acoustic contrast and the MSE are worse. This fact suggests that high

energy is required when using short filters, but still, the performance is not as good as with longer filters. Furthermore, the results show that, in general, increasing the modelling delay improves the acoustic contrast and the MSE. Then, in order to achieve very good performance a PSZ system must include a long modelling delay. Besides, it is interesting to note that, eventually, increasing the filter length without increasing the modelling delay or increasing the modelling delay without increasing the filter length does not lead to performance improvements. However, increasing both, the filter length and the modelling delay, improves the performance. This suggests that better performance is obtained when the filters have similar number of components before and after the main peak, i.e., for $\tau_{\mathrm{d}} \approx I_{\mathrm{g}}/2$. Unfortunately, this selection is not always possible because certain applications require low delay for the system (as discussed in Section 2.1.2). Nevertheless, increasing the regularization factor β_0 from 10^{-3} to 10^{-1} significantly reduces the array effort, but at the cost of worsening the acoustic contrast and the MSE.

Now, we focus on the results for the band 125-250 Hz in Fig. 2.17. In this case, we find very important differences between wPM-T and wPM-F, especially for short delays or short filters. For $\beta_0 = 10^{-3}$, wPM-F presents degradations of up to 4.5 dB for a modelling delay $\tau_{\mathrm{d}} = 64$, and degradations of around 1.5 and 0.5 dB for $\tau_{\mathrm{d}} = 256$ and $\tau_{\mathrm{d}} = 1024$, respectively. We can see in Fig. 2.17a and Fig. 2.17c that wPM-T offers significantly better acoustic contrast and MSE for $\tau_{\mathrm{d}} = 64$ and all the studied filter lengths. For $\tau_{\mathrm{d}} = 1024$, wPM-T offers better performance for short filters, e.g., it presents 2 dB higher acoustic contrast and 3.5 dB lower MSE for $I_{\mathrm{g}} = 1152$. These performance differences are reduced when the filter length is increased, e.g., the performance of both algorithms is very similar for $I_{\mathrm{g}} = 2048$ and $\tau_{\mathrm{d}} = 1024$. Also, the results in Fig. 2.17 indicate that increasing the regularization factor degrades more the performance of wPM-T than the performance of wPM-F, leading to smaller performance differences between both algorithms for high regularizations values. However, the average effort levels obtained for $\beta_0 = 10^{-1}$ are below 0 dB in all cases, while there are still significant acoustic contrast and MSE differences between both algorithms, particularly for short modelling delays or short filters. Then, all these results clearly indicate that, at low frequencies, wPM-T outperforms wPM-F when either short modelling delays or short filters are considered. These conclusions are aligned with those obtained in [39] for the comparison of both algorithms in anechoic conditions.

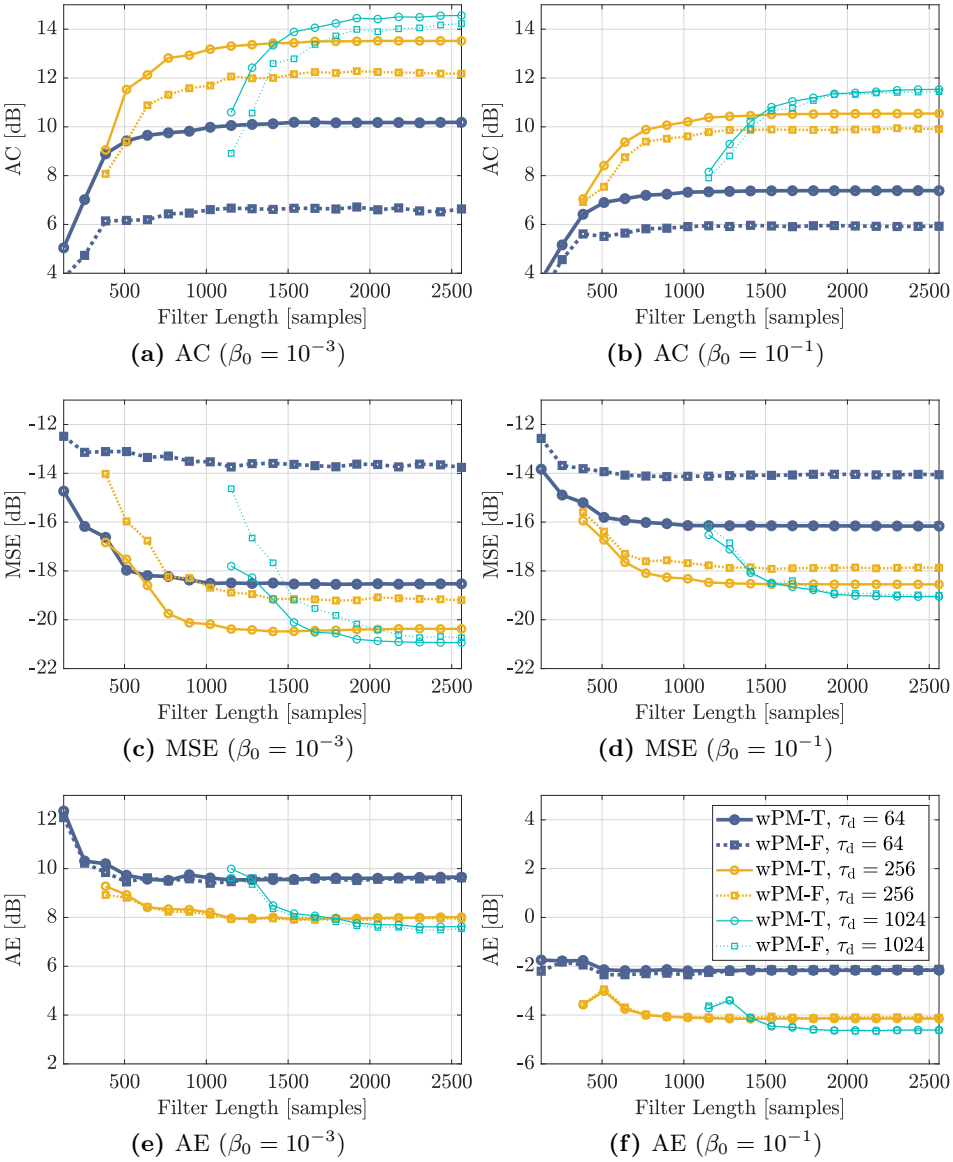

(a) AC ($\beta_0 = 10^{-3}$) **(b)** AC ($\beta_0 = 10^{-1}$)

(c) MSE ($\beta_0 = 10^{-3}$) **(d)** MSE ($\beta_0 = 10^{-1}$)

(e) AE ($\beta_0 = 10^{-3}$) **(f)** AE ($\beta_0 = 10^{-1}$)

Figure 2.17: Average acoustic contrast (a, b), MSE (c, d), and array effort (e, f) over 125-250 Hz as a function of the filter length for wPM-T and wPM-F. Three different modelling delays τ_d and two regularization factors β_0 are considered.

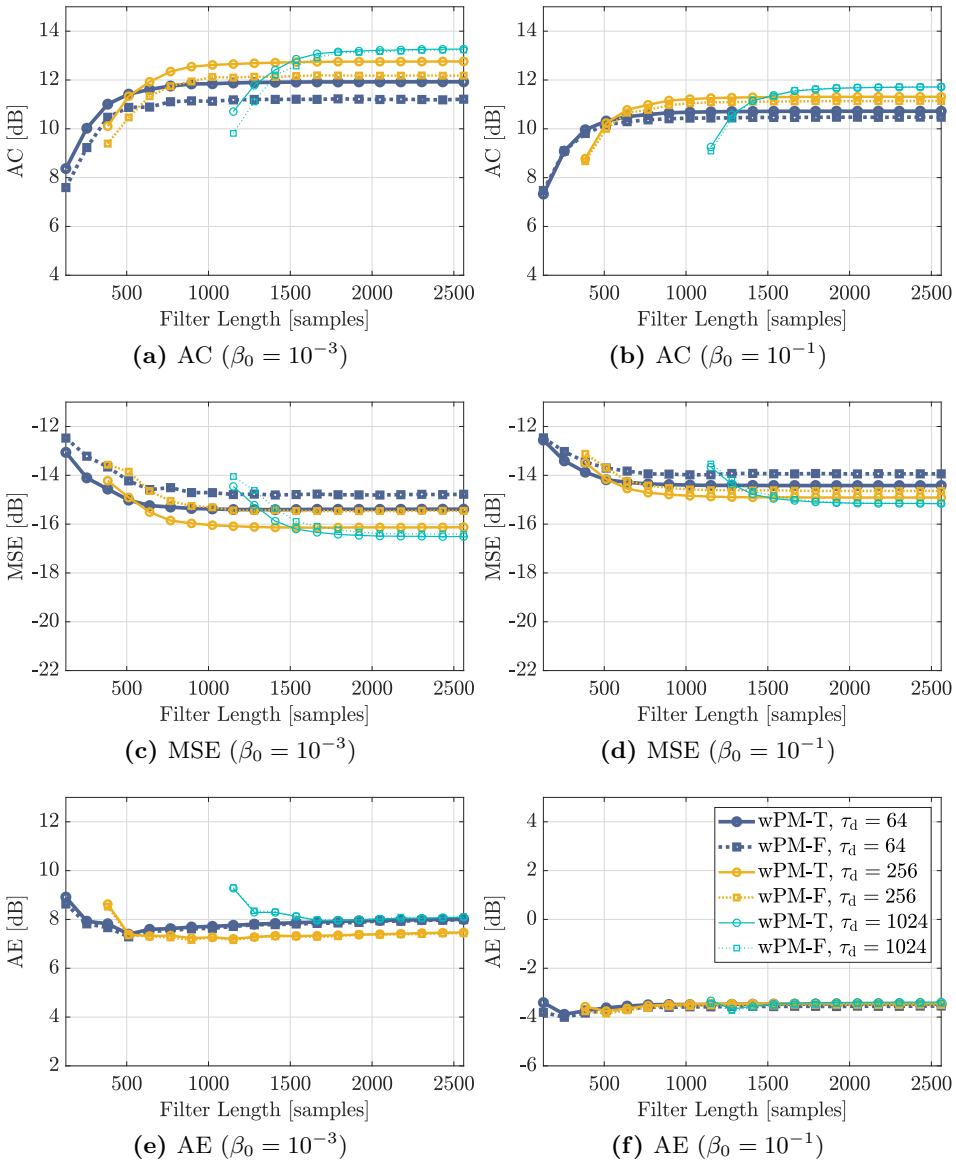

(a) AC ($\beta_0 = 10^{-3}$) **(b)** AC ($\beta_0 = 10^{-1}$)

(c) MSE ($\beta_0 = 10^{-3}$) **(d)** MSE ($\beta_0 = 10^{-1}$)

(e) AE ($\beta_0 = 10^{-3}$) **(f)** AE ($\beta_0 = 10^{-1}$)

Figure 2.18: Average acoustic contrast (a, b), MSE (c, d), and array effort (e, f) over 250-500 Hz as a function of the filter length for wPM-T and wPM-F. Three different modelling delays τ_d and two regularization factors β_0 are considered.

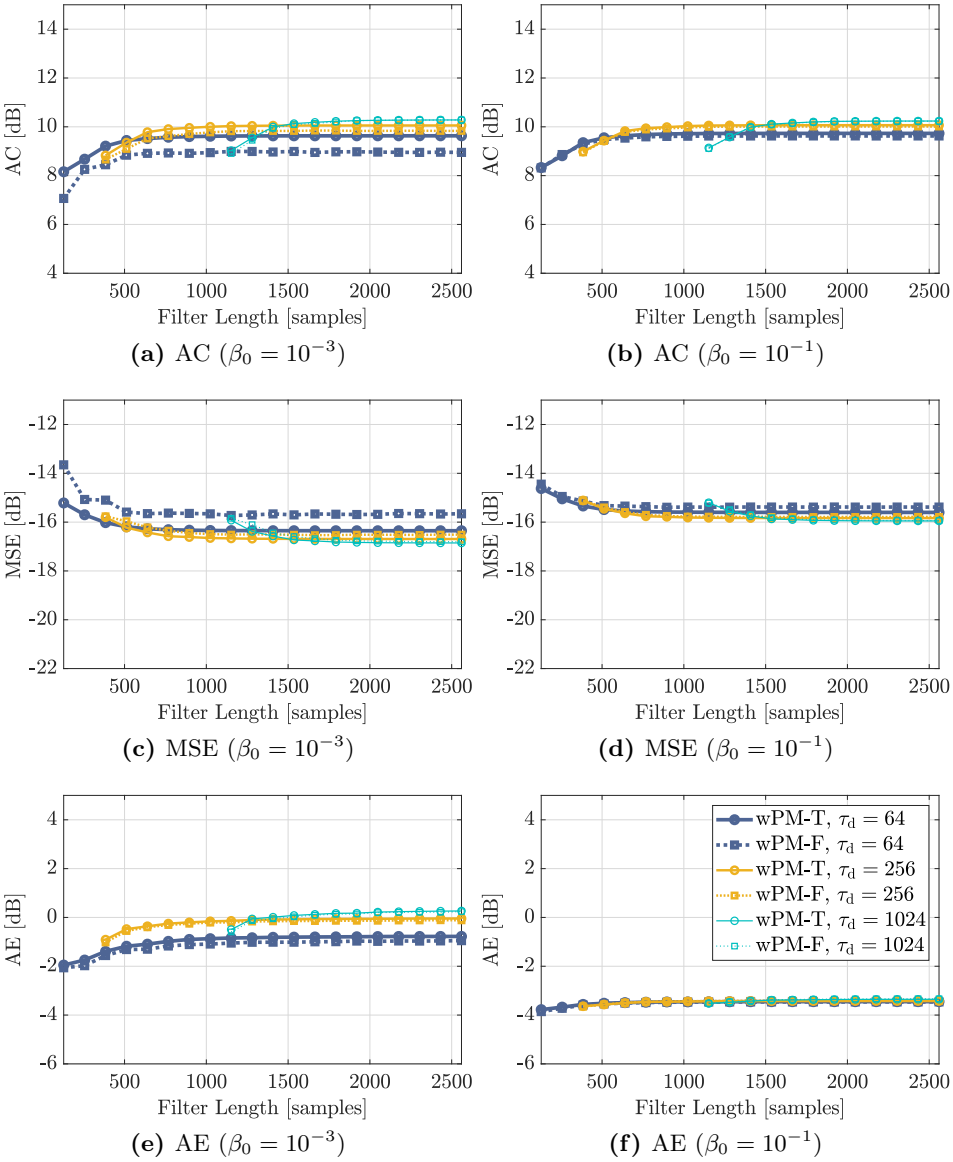

(a) AC ($\beta_0 = 10^{-3}$) **(b)** AC ($\beta_0 = 10^{-1}$)

(c) MSE ($\beta_0 = 10^{-3}$) **(d)** MSE ($\beta_0 = 10^{-1}$)

(e) AE ($\beta_0 = 10^{-3}$) **(f)** AE ($\beta_0 = 10^{-1}$)

Figure 2.19: Average acoustic contrast (a, b), MSE (c, d), and array effort (e, f) over 500-1000 Hz as a function of the filter length for wPM-T and wPM-F. Three different modelling delays τ_d and two regularization factors β_0 are considered.

Likewise, we focus now on the results for the bands 250-500 Hz and 500-1000 Hz in Fig. 2.18 and 2.19, respectively. In these results, we can see similar trends to the ones in Fig. 2.17, as for example, wPM-T presents better acoustic contrast and MSE than wPM-F for short delays or short filters. However, in these bands the performance differences between both algorithms are much smaller than for the band 125-250 Hz. In particular, the differences between both algorithms in these bands are lower than 1 dB in all the studied cases. These results also show that the higher the frequency, the lower the sensitivity of the performance to parameters such as the filter length, the modelling delay, and the regularization.

Performance as a function of frequency

Next, we compare the performance of wPM-T and wPM-F as a function of frequency. We show in Fig. 2.20 the acoustic contrast, the MSE, and the array effort for two regularization factors $\beta_0 = 10^{-3}$ and $\beta_0 = 10^{-1}$, and for three combinations of filter lengths and modelling delays: 1) $I_\mathrm{g} = 2048$ and $\tau_\mathrm{d} = 1024$; 2) $I_\mathrm{g} = 2048$ and $\tau_\mathrm{d} = 64$; 3) $I_\mathrm{g} = 1300$ and $\tau_\mathrm{d} = 1024$. These results lead to similar conclusions to those previously presented in Fig. 2.17 to 2.19. First, we can see in Fig. 2.20 that both algorithms offer very similar results for $I_\mathrm{g} = 2048$ and $\tau_\mathrm{d} = 1024$, indicating that both algorithms offer very similar performance when long filters and modelling delays are considered. For $\tau_\mathrm{d} = 1024$ and $I_\mathrm{g} = 1300$, wPM-T offers up to 3 dB higher acoustic contrast and 2 dB lower MSE for $\beta_0 = 10^{-3}$ at frequencies below 300 Hz, while similar performance is obtained for higher frequencies. The differences are reduced when increasing the regularization factor β_0 from 10^{-3} to 10^{-1}. These results confirm that, at low frequencies, wPM-T offers better performance than wPM-F for short filters, even if long modelling delays are considered. Moreover, we can see very significant differences between both algorithms for $\tau_\mathrm{d} = 64$ at frequencies below 250 Hz. In particular, wPM-F leads to degradations of up to 5 dB in the acoustic contrast and 6 dB in the MSE for $\beta_0 = 10^{-3}$. Again, the differences between both algorithms are reduced if the regularization factor is increased, but still, wPM-T offers up to 2.5 dB higher acoustic contrast and 3 dB lower MSE than wPM-F for $\beta_0 = 10^{-1}$. Then, we can confirm that wPM-T significantly outperforms wPM-F when short modelling delays are considered. Furthermore, to exemplify the frequency responses produced in the zones by both algorithms, we show in Fig. 2.21 the mean energy in the bright and dark zones as a function of frequency.

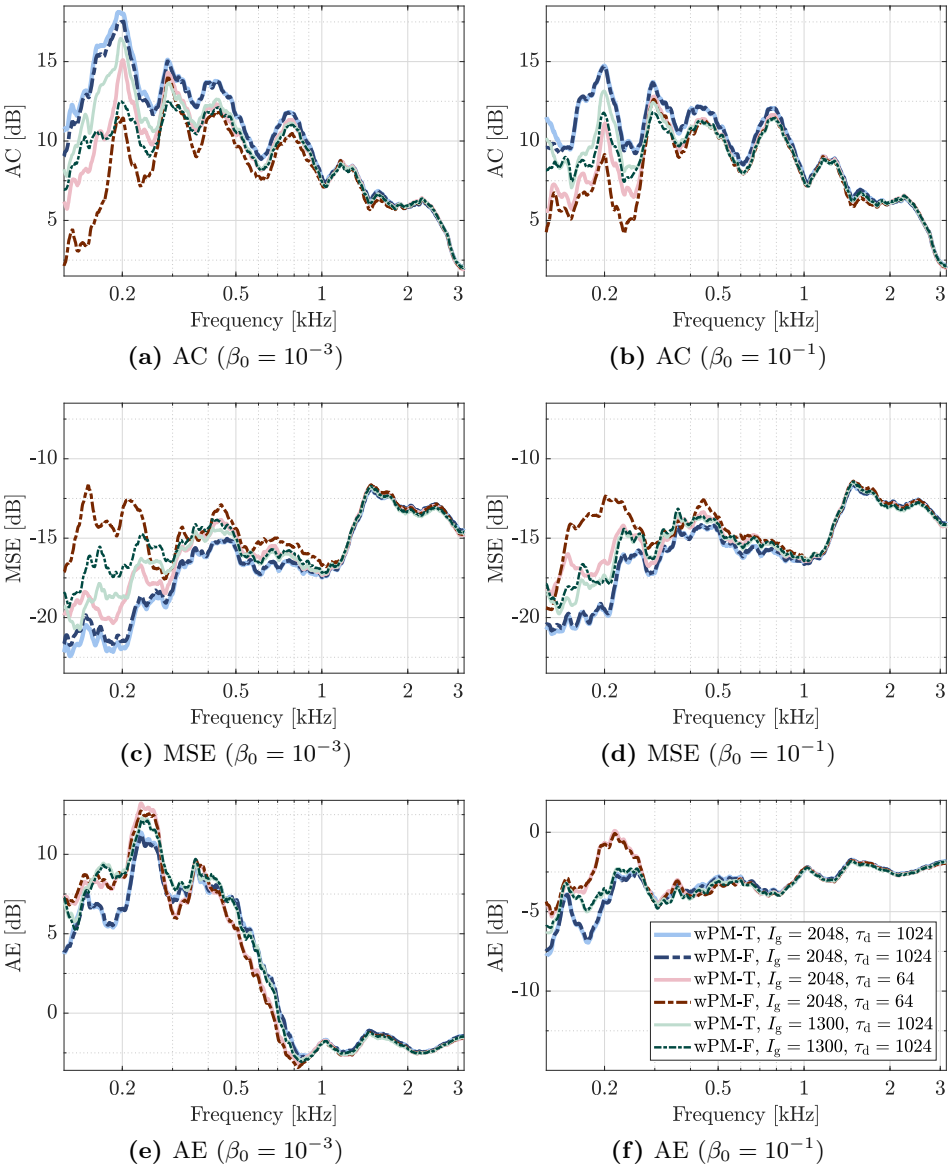

(a) AC ($\beta_0 = 10^{-3}$) **(b)** AC ($\beta_0 = 10^{-1}$)

(c) MSE ($\beta_0 = 10^{-3}$) **(d)** MSE ($\beta_0 = 10^{-1}$)

(e) AE ($\beta_0 = 10^{-3}$) **(f)** AE ($\beta_0 = 10^{-1}$)

Figure 2.20: Acoustic contrast (a, b), MSE (c, d), and array effort (e, f) as a function of frequency for wPM-T and wPM-F. Three different combinations of filter lengths I_g and modelling delays τ_d, and two different regularization factors β_0 are considered.

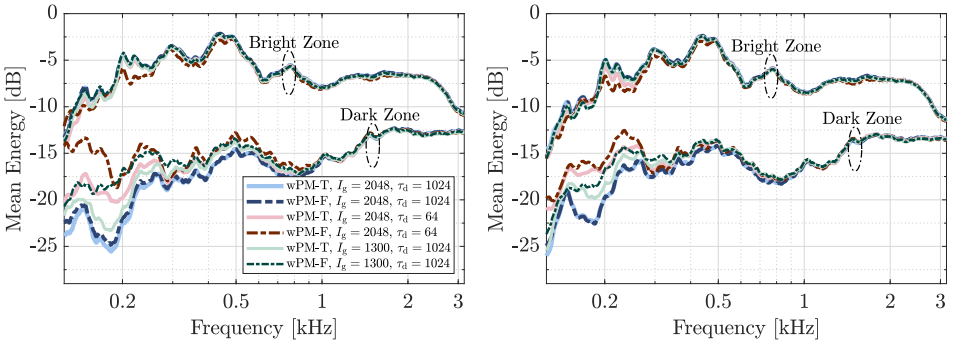

(a) $\beta_0 = 10^{-3}$ **(b)** $\beta_0 = 10^{-1}$

Figure 2.21: Mean energy in the bright and dark zones as a function of frequency for wPM-T and wPM-F with three different combinations of filter lengths I_g and modelling delays τ_d, and two different regularization factors β_0.

Impulse response of the filters

Finally, we study the impulse responses of the optimal filters of length $I_g = 2048$ for the reference loudspeaker $l = 3$, computed with modelling delays $\tau_d = 64$ and $\tau_d = 1024$, and with a regularization level $\beta_0 = 10^{-3}$. First, the impulse responses q_l obtained with wPM-F before windowing are shown in Fig. 2.22. These results show that several components of significant energy appear at the end of q_l for $\tau_d = 64$. This fact indicates that the frequency responses obtained through wPM-F correspond to time-domain responses with a high number of anti-causal components. These components can not be accommodated and turned into causal components for a modelling delay $\tau_d = 64$, so the windowed filters do not include them. On the contrary, for a modelling delay $\tau_d = 1024$, the anti-causal components of most significant energy are accommodated as causal components and are included in the windowed filters. Next, we show in Fig. 2.23a and Fig. 2.23b the impulse response of the filters g_l computed with wPM-T and wPM-F (after windowing). Moreover, we show in Fig. 2.23c the absolute value of the error between the filters for both algorithms. From these results, it is clear that both algorithms obtain more similar filters for high delays, while their differences are bigger when short delays are considered. The differences appear because wPM-T estimates the optimal

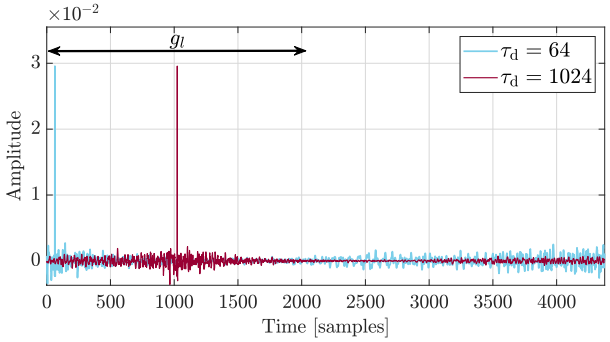

Figure 2.22: Impulse response q_l before windowing for wPM-F with $I_g = 2048$, $l = 3$, $\beta_0 = 10^{-3}$ and modelling delays $\tau_d = 64$ and $\tau_d = 1024$.

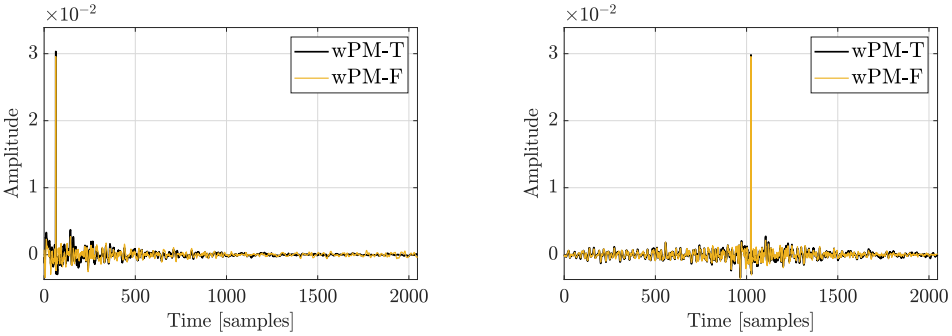

(a) $\tau_d = 64$ **(b)** $\tau_d = 1024$

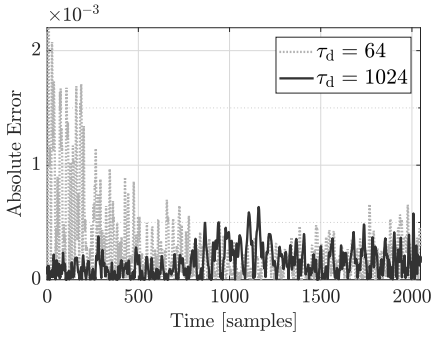

(c) Absolute error

Figure 2.23: Impulse response of the filters g_l for wPM-F and wPM-T with $I_g = 2048$, $l = 3$, $\beta_0 = 10^{-3}$ and two modelling delays $\tau_d = 64$ and $\tau_d = 1024$ in (a) and (b), respectively. Absolute error between the filters for both algorithms in (c).

causal filters of a given length, while wPM-F does not impose any causality constraint. This implies that wPM-T does not rely on the anti-causal components to optimize the performance of the system. However, wPM-F does rely on the anti-causal components to improve the performance, although these components are later suppressed by the truncation process. For suitable delays, the energy of the components suppressed by the truncation is very low, so the performance of wPM-F is similar to the one of wPM-T. For short delays, the energy of the components suppressed can be significant, which leads to important performance degradations for wPM-F and causes notable differences between both algorithms (as seen in Fig. 2.17 to Fig. 2.20).

2.4 Summary

In this chapter we reviewed the fundamental theory related to PSZ systems. First, we described the main goal and the requirements of PSZ systems, followed by a discussion on different approaches that can be used for these kinds of systems. Then, we considered the use of loudspeaker array processing for PSZ systems, which is the most suitable approach for focusing sound at low and mid frequencies. In particular, we studied a model in which a set of FIR filters is used to filter the audio signals that are fed to an array of loudspeakers. Also, we discussed the time and frequency domain formulations of this model, and the procedures required to obtain the filters of the system when these formulations are used. Later, we reviewed the most relevant algorithms proposed in the literature for computing the filters of a PSZ system using loudspeaker array processing. From this review, we concluded that weighted Pressure Matching (wPM), either with time or frequency domain formulations, is the most suitable algorithm for PSZ systems, as it allows to balance the interference level between zones and the audio quality of the signal rendered to the users. Then, we derived and discussed the expressions required to obtain the optimal filters with wPM using the time and frequency domain formulations, i.e., wPM-T and wPM-F, respectively. Finally, we presented novel experimental results for comparing the performance of wPM-T and wPM-F in a reverberant environment. The length of the filters, the modelling delay, and the regularization level were taken into account in the comparison. The presented results indicate that both algorithms show almost equal performance when long

filters and appropriate modelling delays are considered. However, wPM-T clearly outperforms wPM-F at low frequencies when either short filters or too short modelling delays are considered. Also, the effect of the regularization seems relevant, as increasing the regularization level leads to smaller differences between wPM-T and wPM-F, but at the cost of worsening the performance of both algorithms. In conclusion, wPM-T offers superior performance to wPM-F for systems in which short modelling delays or short filters are required. Also, it is important to mention that wPM-T requires higher computational efforts than wPM-F, which can be an important disadvantage for systems with limited computational capabilities. This aspect will be further studied in Chapter 3.

Chapter 3

Least Squares solvers for PSZ systems

We discussed and showed in Chapter 2 that wPM-T can outperform wPM-F for PSZ systems. The filters for wPM-T are computed by solving a Least Squares (LS) problem, which in some cases might involve a large number of unknown parameters. Hence, computing the optimal filters can be a computationally challenging task, which can be a serious limitation if the filters must be recalculated often. In this chapter, we first study the LS problem for wPM-T, and show that the matrices involved in the optimization have a block-toeplitz structure. Then, we review the state-of-the-art solvers for these kind of problems, including the generic solvers that do not consider the block-toeplitz structure, and the fast and superfast solvers that benefit from this structure to reduce the computational demands. Later, we show how to compute the optimal solution with three different solvers, namely: 1) a classic solver based on the Cholesky factorization [77]; 2) the Fast a Posteriori Error Sequential Technique (FAEST) [78]; and 3) the superfast solver proposed in [79]. Afterwards, the accuracy of these solvers and how it influences the performance of a PSZ system is experimentally evaluated. The evaluations show that the FAEST and superfast solvers are adequate for computing the filters for wPM-T when medium or high regularizations levels are used. Finally, the computational demands of the three solvers are compared. The results clearly indicate that the superfast solver and, to a lower extent, the FAEST solver can effectively lighten the computational efforts required by the Cholesky solver when long filters are considered.

3.1 Least Squares (LS) problem

We studied in Section 2.2.4 that the L optimal filters of length I_{g} for wPM-T are obtained by solving the following LS problem:

$$\mathbf{g}_{\mathrm{opt}} = \min_{\mathbf{g}} \left\{ \|(\mathbf{H}\mathbf{g} - \mathbf{d})\|^2 + \beta \|\mathbf{g}\|^2 \right\}, \tag{3.1}$$

where $\mathbf{g}_{\mathrm{opt}}$ is a $LI_{\mathrm{g}}\times 1$ vector, $\mathbf{H}$ is a $M(I_{\mathrm{h}}+I_{\mathrm{g}}-1)\times LI_{\mathrm{g}}$ block-toeplitz matrix defined in (2.11), and $\mathbf{d}$ is a $M(I_{\mathrm{h}}+I_{\mathrm{g}}-1)\times 1$ vector defined in (2.30). It is relevant to note that the weighting matrix $\mathbf{W}$ for wPM-T in (2.31) is omitted in (3.1). The solvers described in this chapter can be directly used for the case in which $\mathbf{W}$ is considered by replacing d_m by $w_m d_m$ to form $\mathbf{d}$ and h_{ml} by $w_m\, h_{ml}$ to form $\mathbf{H}$, since the weighting matrix selected for wPM-T is diagonal, i.e., $\mathbf{W} = \mathrm{diag}\,\{w_0, \ldots, w_{M-1}\} \otimes \mathbf{I}_{I_{\mathrm{d}}}$. We omit $\mathbf{W}$ here for the sake of simplicity on the notation. The solution for (3.1) is given by

$$\mathbf{g}_{\mathrm{opt}} = \left(\mathbf{H}^T\mathbf{H} + \beta\, \mathbf{I}_{LI_{\mathrm{g}}}\right)^{-1} \mathbf{H}^T\mathbf{d}, \tag{3.2}$$

which can be alternatively expressed as

$$\mathbf{g}_{\mathrm{opt}} = \mathbf{R}^{-1}\mathbf{c}, \tag{3.3}$$

where $\mathbf{R} = \mathbf{H}^T\mathbf{H} + \beta\, \mathbf{I}_{LI_{\mathrm{g}}}$ is a $LI_{\mathrm{g}}\times LI_{\mathrm{g}}$ matrix, and $\mathbf{c} = \mathbf{H}^T\mathbf{d}$ is a $LI_{\mathrm{g}}\times 1$ vector. Let us note that $\mathbf{R}$ is a symmetric block-toeplitz matrix that can be written as

$$\mathbf{R} = \begin{bmatrix} \mathbf{R}_0 & \mathbf{R}_1 & \cdots & \mathbf{R}_{I_{\mathrm{g}}-1} \\ \mathbf{R}_{-1} & & & \\ \vdots & & \mathit{Toeplitz} & \\ \mathbf{R}_{-(I_{\mathrm{g}}-1)} & & & \end{bmatrix}, \tag{3.4}$$

where $\mathbf{R}_n$ is a $L\times L$ matrix fulfilling $\mathbf{R}_n = \mathbf{R}_{-n}^T$, since $\mathbf{R}$ is symmetric. It is relevant to note that (3.1) can be otherwise expressed as

$$\mathbf{g}_{\mathrm{opt}} = \min_{\mathbf{g}} \left\{ \sum_{n=0}^{I_{\mathrm{d}}-1} \left\| \left(\overleftarrow{\mathbf{H}}_n \mathbf{g} - \mathbf{d}_n \right) \right\|^2 + \beta \|\mathbf{g}\|^2 \right\}, \tag{3.5}$$

where $\mathbf{d}_n$ is defined in (2.29) and $\overleftarrow{\mathbf{H}}_n$ is defined as

$$\overleftarrow{\mathbf{H}}_n = \begin{bmatrix} \mathbf{H}_n & \ldots & \mathbf{H}_{n-I_{\mathrm{g}}+1} \end{bmatrix}, \tag{3.6}$$

i.e., $\overleftarrow{\mathbf{H}}_n$ is a matrix of size $M \times LI_\mathrm{g}$ containing the RIRs for time instants n–I_g+1 to n (taking into account that $\mathbf{H}_n = \mathbf{0}_{M \times L}$ for $n < 0$). Problems of the form (3.5) are related to linear systems and arise in many fields, e.g., acoustics [80], astronomy [81], and image processing [82].

3.2 Literature review

Computing the solution for (3.1) can be a challenging task when large filter lengths I_g are considered. In this case, the computational complexity required to compute the optimal solution can be very high, as the number of unknown parameters in the system of linear equations, i.e., LI_g, is large. Many solvers with different computational requirements and accuracies have been proposed in the literature to solve (3.1), and there is an extensive literature related to this topic. The interested reader can find detailed discussions about this topic in [72, 83, 84, 85]. Usually, the term single-channel LS is used in the literature to refer to (3.1) when M=L=1, while multi-channel LS is used when $M \geq 1$ and $L \geq 1$ [72]. In this work, we are interested in the multi-channel case, since it is the one required to compute the filters for a PSZ system using wPM-T. An important consideration is that $\mathbf{H}$ and $\mathbf{R}$ are toeplitz matrices for the single-channel case, i.e., each descending diagonal from left to right is formed by a constant scalar value. For the multi-channel case, $\mathbf{H}$ and $\mathbf{R}$ are block-toeplitz matrices, in which each descending block-diagonal from left to right is formed by constant blocks of size $M \times L$ and $L \times L$, respectively [80]. Then, the solvers for single-channel LS can be generalized for multi-channel LS by replacing the scalar operations by their analogue matrix operations. The solvers are usually classified in three main categories [84]: 1) classic solvers; 2) fast solvers; and 3) superfast solvers.

3.2.1 Classic solvers

The classic solvers do not consider any particular structure for matrices $\mathbf{H}$ and $\mathbf{R}$ to solve (3.1), and require about $O\left((LI_\mathrm{g})^3\right)$ operations [84]. Some classic solvers employ factorizations of either $\mathbf{H}$ or $\mathbf{R}$ to compute the optimal solution $\mathbf{g}_\mathrm{opt}$. Among others, the Cholesky factorization, the QR factorization, and the LU factorization (which is the matrix form of Gaussian elimination) can be used to compute the optimal solution [77]. Also,

other classic solvers are based on computing recursively the optimal solution, e.g., the Recursive Least Squares (RLS) solver [84]. Let us define:

$$\widehat{\mathbf{g}}_i = \min_{\mathbf{g}} \left\{ \sum_{n=0}^{i} \left\| \left(\overleftarrow{\mathbf{H}}_n \mathbf{g} - \mathbf{d}_n \right) \right\|^2 + \beta \left\| \mathbf{g} \right\|^2 \right\}, \tag{3.7}$$

i.e., the optimal solution in the LS sense when considering $\overleftarrow{\mathbf{H}}_n$ and $\mathbf{d}_n$ for times up to i. The process of computing $\widehat{\mathbf{g}}_i$ from $\widehat{\mathbf{g}}_{i-1}$ is commonly called time-updating [86], since the elements $\overleftarrow{\mathbf{H}}_i$ and $\mathbf{d}_i$ for time i are used to update $\widehat{\mathbf{g}}_{i-1}$ to obtain $\widehat{\mathbf{g}}_i$. The RLS solver uses time-updating for computing recursively the optimal solution for (3.1), which is clear from (3.5) that is given by (3.7) when $i = I_\mathrm{d}-1$. An explicit set of equations can be derived for RLS to recursively compute $\widehat{\mathbf{g}}_i$ from $\widehat{\mathbf{g}}_{i-1}$ for $i = 0, \ldots, I_\mathrm{d}-1$ [83], such that the optimal solution is obtained for the last recursion as $\mathbf{g}_\mathrm{opt} = \widehat{\mathbf{g}}_{I_\mathrm{d}-1}$. Alternatively, the recursive methods in array form, as the square-root RLS solver [72], compute the recursions using elementary circular and hyperbolic rotations, which offer higher robustness to round-off errors in finite-size arithmetic than the explicit expressions for RLS [72].

3.2.2 Fast solvers

The fast solvers are those that consider the structure of matrices $\mathbf{H}$ and $\mathbf{R}$ to solve (3.1) [84]. In particular, $\mathbf{H}$ is a block-toeplitz matrix and $\mathbf{R}$ is a symmetric block-toeplitz matrix (which is positive-definite for $\beta > 0$). The fast solvers take advantage of the structure of the matrices to reduce the computational demands of the classic solvers to about $O\left((LI_\mathrm{g})^2\right)$. Let us point out that due to the block-toeplitz structure of $\mathbf{H}$, the following shifting property is fulfilled for (3.6):

$$\overleftarrow{\mathbf{H}}_n = \left[\mathbf{H}_n \quad \ldots \quad \left[\overleftarrow{\mathbf{H}}_{n-1} \right]_{(:,0:L(I_\mathrm{g}-1)-1)} \right], \tag{3.8}$$

i.e., $\overleftarrow{\mathbf{H}}_n$ can be seen as a shifted version of $\overleftarrow{\mathbf{H}}_{n-1}$, in which only L columns of $\overleftarrow{\mathbf{H}}_n$ are not present in $\overleftarrow{\mathbf{H}}_{n-1}$. Using (3.8), different variations of RLS can be derived to reduce the computational demands of each iteration [86]. Among others, the Fast Transversal Filters (FTF) [87] and the Fast a Posteriori Error Sequential Technique (FAEST) [88] are variations of the RLS solver that can efficiently time-update $\widehat{\mathbf{g}}_i$ from $\widehat{\mathbf{g}}_{i-1}$, leading to a cost $O\left((LI_\mathrm{g})^2\right)$. Similarly, an efficient variation of the square-root RLS solver, namely, the

Fast Array RLS (FARLS) solver [86], can be used to efficiently compute the recursions using elementary rotations. Again, the robustness to round-off errors in finite-size arithmetic of the array form FARLS is higher than that for FTF and FAEST. However, FTF and FAEST require less computations per iteration than FARLS [72]. So far, we have discussed fixed-order fast solvers that use time-updating. A conceptually different approach to solve (3.1) is the use of order-updating instead of time-updating. Order-updating is based on updating the optimal filters of a certain order $I-1$ to compute the optimal filters of order I [72]. For systems of equations involving symmetric block-toeplitz matrices, order-updating can be efficiently performed using the fast Levinson-Durbin solver [85]. This method starts by computing the optimal filters of order 0, and recursively applies order-updating until the filters of the desired order I are obtained. Then, since $\mathbf{R}$ is a symmetric block-toeplitz matrix, the optimal solution $\mathbf{g}_{\text{opt}}$ in (3.1) can be computed with the Levinson-Durbin solver with $O\left((LI_{\text{g}})^2\right)$ operations by recursively iterating from order 0 to order $I_{\text{g}}-1$. Alternatively, the optimal solution can be obtained with a fast solver based on the Schur algorithm [89, 90], which exploits the block-toeplitz structure of $\mathbf{R}$ to compute its Cholesky factorization with $O\left((LI_{\text{g}})^2\right)$ operations [91].

3.2.3 Superfast solvers

The superfast solvers, also known as asymptotically fast solvers, are those requiring less than $O\left((LI_{\text{g}})^2\right)$ operations to solve (3.1) [84]. Commonly, these solvers require $O\left(LI_{\text{g}} \log_2^u I_{\text{g}}\right)$, with $u \geq 1$, because are based on the use of the Fast Fourier Transform (FFT). One of these solvers is the Generalized Schur algorithm [92], which is a variation of the Schur Algorithm, whose recursions can be efficiently implemented using the FFT. This algorithm requires $O\left(LI_{\text{g}} \log_2^2 I_{\text{g}}\right)$ operations to solve (3.1). An interesting idea that can be used to relax the computational demands is to reformulate (3.2) by using a circulant extension matrix $\mathbf{H}_{\text{e}}$ of matrix $\mathbf{H}$. Based on this idea, Schneider and Habets [52] proposed the Iterative DFT-Domain Inverse (IDI) solver, which is a superfast solver that iteratively finds an approximate solution for (3.1). Each iteration of the IDI solver only involves FFTs, so it requires $O\left(PLI_{\text{g}} \log_2 I_{\text{g}}\right)$ operations to approximately compute $\mathbf{g}_{\text{opt}}$, where P is the number of iterations. Recently, Poletti and Teal [79] showed that the inverse matrix required to compute $\mathbf{g}_{\text{opt}}$ can be expressed as an infinite series if the circulant extention $\mathbf{H}_{\text{e}}$ is used to reformulate (3.2).

Then, the authors in [79] proposed a superfast solver to approximately compute $\mathbf{g}_{\text{opt}}$ by approximating the infinite series by its P-th partial sum. The most relevant aspect of the proposed solver is that each of the elements of the P-th order partial sum can be computed efficiently using FFTs. Hence, the superfast solver proposed in [79] requires $O\left(PLI_{\text{g}} \log_2 I_{\text{g}}\right)$ operations to compute the P-th order approximation of the optimal solution.

An important aspect to point out is that the computational reductions obtained by the fast and superfast solvers with respect to the classic solvers are at the cost of higher sensitivity to round-off errors in finite-size arithmetic [72]. Most of the fast and superfast solvers discussed previously obtain the exact optimal solution $\mathbf{g}_{\text{opt}}$ if exact arithmetic is considered. However, their higher sensitivity to round-off errors can make the algorithms diverge in some practical cases (especially when matrix $\mathbf{R}$ is ill-conditioned). Similarly, the approximate superfast solvers [52, 79] may not converge to the optimal solution $\mathbf{g}_{\text{opt}}$ if matrix $\mathbf{R}$ is ill-conditioned. This is an interesting point to study, as the lower robustness of the fast and superfast solvers could degrade the performance of wPM-T for PSZ system.

In the remainder of this chapter we study and compare three different solvers, one from each category previously described, for computing the optimal solution for (3.1). Particularly, we study the classic solver based on the Cholesky factorization, the fast FAEST solver, and the superfast solver proposed by Poletti and Teal [79]. These three solvers are described next. Later, their accuracy and computational demands are compared and some relevant conclusions are summarized.

3.3 Cholesky solver

Next, we study how to compute the optimal solution for (3.1) using the Cholesky factorization. Let us note that $\mathbf{R} = \mathbf{H}^T\mathbf{H} + \beta\,\mathbf{I}_{LI_{\text{g}}}$ is a symmetric positive-definite matrix for $\beta > 0$. Then, using the Cholesky factorization [77], we can express matrix $\mathbf{R}$ as

$$\mathbf{R} = \mathbf{L}\mathbf{L}^T \tag{3.9}$$

where $\mathbf{L}$ is a $LI_{\text{g}} \times LI_{\text{g}}$ lower triangular matrix. Using (3.9) we can write the optimal solution (3.3) as

$$\mathbf{g}_{\text{opt}} = \left(\mathbf{L}\mathbf{L}^T\right)^{-1}\mathbf{c} = \left(\mathbf{L}^T\right)^{-1}\mathbf{L}^{-1}\mathbf{c}. \tag{3.10}$$

Making use of the previous expression, and by defining the auxiliary vector $\mathbf{y} = \mathbf{L}^{-1}\mathbf{c}$, the optimal solution $\mathbf{g}_{\text{opt}}$ can be computed by solving the two following systems of linear equations:

$$\mathbf{L}\mathbf{y} = \mathbf{c}, \tag{3.11}$$

$$\mathbf{L}^T\mathbf{g}_{\text{opt}} = \mathbf{y}. \tag{3.12}$$

The systems in (3.11) and (3.12) can be solved using forward and backward substitution [77], respectively, because $\mathbf{L}$ is a lower triangular matrix.

The steps required to compute the optimal solution with the Cholesky solver are summarized in Algorithm 3.1, and a detailed count of operations is included in Appendix A.1.1. There, we can see that the dominant operation is the Cholesky factorization, which requires about $O\left((LI_{\text{g}})^3/3\right)$ operations.

Algorithm 3.1: Compute (3.1) with a Cholesky solver.

Compute $\mathbf{R} = \mathbf{H}^T\mathbf{H} + \beta\mathbf{I}_{LI_{\text{g}}}$;
Compute $\mathbf{c} = \mathbf{H}^T\mathbf{d}$;
Compute Cholesky factorization $\mathbf{R} = \mathbf{L}\mathbf{L}^T$;
Solve the triangular linear system $\mathbf{L}\mathbf{y} = \mathbf{c}$;
Solve the triangular linear system $\mathbf{L}^T\mathbf{g}_{\text{opt}} = \mathbf{y}$;

3.4 Fast a Posteriori Error Sequential Technique

The Fast a Posteriori Error Sequential Technique (FAEST) is a variation of RLS that was proposed by Carayannis et al. [78] to efficiently compute the optimal solution of LS problems of the form (3.5) that fulfil (3.8). In particular, Carayannis et al. [78] proposed the FAEST solver for the single-channel case, and later, Kalouptsidis et al. [88] extended the FAEST solver for the multi-channel case. Similarly to RLS, FAEST is based on time-updating, i.e., computing $\widehat{\mathbf{g}}_i$ from $\widehat{\mathbf{g}}_{i-1}$, to solve (3.1). Then, the optimal solution $\mathbf{g}_{\text{opt}}$ is obtained with FAEST after I_{d} iterations, i.e., $\mathbf{g}_{\text{opt}} = \widehat{\mathbf{g}}_{I_{\text{d}-1}}$. The main advantage of FAEST is that it exploits the shifting property (3.8) to reduce the number of operations required by RLS for time-updating the filters. The steps required to compute the optimal solution with FAEST are summarized in Algorithm 3.2, where the following elements are used:

Algorithm 3.2: Compute (3.1) with a FAEST solver.

Initialize: $\mathbf{G}_{-1} = \mathbf{0}_{LI_\mathrm{g}\times M}$ $\quad \mathbf{\Psi}^\mathrm{f}_{-1} = \mathbf{\Psi}^\mathrm{b}_{-1} = \mathbf{0}_{LI_\mathrm{g}\times L}$ $\quad \widehat{\mathbf{g}}_{-1} = \mathbf{0}_{LI_\mathrm{g}\times 1}$
$\mathbf{\Gamma}_{-1} = \mathbf{I}_M$ $\quad \mathbf{\Omega}^\mathrm{f}_{-1} = \mathbf{\Omega}^\mathrm{b}_{-1} = \beta\,\mathbf{I}_L$

for $n = 0, ..., I_\mathrm{d} - 1$ **do**

Update auxiliary variables:

$$\mathbf{E}^\mathrm{f}_n = \mathbf{H}_n - \overleftarrow{\mathbf{H}}_{n-1}\mathbf{\Psi}^\mathrm{f}_{n-1};$$
$$\mathbf{R}^\mathrm{f}_n = \mathbf{\Gamma}_{n-1}\mathbf{E}^\mathrm{f}_n;$$
$$\mathbf{G}^\mathrm{e}_n = \begin{bmatrix}\mathbf{0}_{L\times M}\\ \mathbf{G}_{n-1}\end{bmatrix} + \begin{bmatrix}\mathbf{I}_L\\ -\left(\mathbf{\Psi}^\mathrm{f}_{n-1}\right)\end{bmatrix}\left(\mathbf{\Omega}^\mathrm{f}_{n-1}\right)^{-1}\left(\mathbf{E}^\mathrm{f}_n\right)^T;$$
$$\mathbf{G}_n = [\mathbf{G}^\mathrm{e}_n]_{(0:LI_\mathrm{g}-1,:)} + \mathbf{\Psi}^\mathrm{b}_{n-1}\,[\mathbf{G}^\mathrm{e}_n]_{(LI_\mathrm{g}:L(I_\mathrm{g}+1)-1,:)};$$
$$(\mathbf{\Gamma}^\mathrm{e}_n)^{-1} = (\mathbf{\Gamma}_{n-1})^{-1} + \mathbf{E}^\mathrm{f}_n\,[\mathbf{G}^\mathrm{e}_n]_{(0:L-1,:)};$$
$$(\mathbf{\Gamma}_n)^{-1} = (\mathbf{\Gamma}^\mathrm{e}_n)^{-1} - \mathbf{E}^\mathrm{b}_n\,[\mathbf{G}^\mathrm{e}_n]_{(LI_\mathrm{g}:L(I_\mathrm{g}+1)-1,:)};$$
$$\mathbf{E}^\mathrm{b}_n = \beta\,[\mathbf{G}^\mathrm{e}_n]^T_{(LI_\mathrm{g}:L(I_\mathrm{g}+1)-1,:)}\,\mathbf{\Omega}^\mathrm{b}_{n-1};$$
$$\mathbf{R}^\mathrm{b}_n = \mathbf{\Gamma}_n\mathbf{E}^\mathrm{b}_n;$$
$$\mathbf{\Omega}^\mathrm{f}_n = \mathbf{\Omega}^\mathrm{f}_{n-1} + \left(\mathbf{E}^\mathrm{f}_n\right)^T\mathbf{R}^\mathrm{f}_n;$$
$$\mathbf{\Omega}^\mathrm{b}_n = \mathbf{\Omega}^\mathrm{b}_{n-1} + \left(\mathbf{E}^\mathrm{b}_n\right)^T\mathbf{R}^\mathrm{b}_n;$$
$$\mathbf{\Psi}^\mathrm{f}_n = \mathbf{\Psi}^\mathrm{f}_{n-1} + \mathbf{G}_{n-1}\mathbf{R}^\mathrm{f}_n;$$
$$\mathbf{\Psi}^\mathrm{b}_n = \mathbf{\Psi}^\mathrm{b}_{n-1} + \mathbf{G}_n\mathbf{R}^\mathrm{b}_n;$$

Update estimate:

$$\mathbf{e}_n = \mathbf{d}_n - \overleftarrow{\mathbf{H}}_n\widehat{\mathbf{g}}_{n-1};$$
$$\mathbf{r}_n = \mathbf{\Gamma}_n\mathbf{e}_n;$$
$$\widehat{\mathbf{g}}_n = \widehat{\mathbf{g}}_{n-1} + \mathbf{G}_n\mathbf{r}_n;$$

end

Compute the optimal solution: $\mathbf{g}_\mathrm{opt} = \widehat{\mathbf{g}}_{I_\mathrm{d}-1}$

- $\mathbf{G}_n$ is the $LI_\mathrm{g}\times M$ normalized gain for time n.
- $\mathbf{G}_n^\mathrm{e}$ is the $L(I_\mathrm{g}+1)\times M$ extended and normalized gain for time n.
- $\mathbf{\Gamma}_n$ is the $M\times M$ conversion factor for time n.
- $\mathbf{\Gamma}_n^\mathrm{e}$ is the $M\times M$ extended conversion factor for time n.
- $\mathbf{\Psi}_n^\mathrm{b}$ and $\mathbf{\Psi}_n^\mathrm{f}$ are the $LI_\mathrm{g}\times L$ backward and forward propagation filters, respectively, for time n.
- $\mathbf{\Omega}_n^\mathrm{b}$ and $\mathbf{\Omega}_n^\mathrm{f}$ are $L\times L$ auxiliary backward and forward variables, respectively, for time n.
- $\mathbf{E}_n^\mathrm{b}$ and $\mathbf{E}_n^\mathrm{f}$ are the $M\times L$ a priori backward and forward errors, respectively, for time n.
- $\mathbf{R}_n^\mathrm{b}$ and $\mathbf{R}_n^\mathrm{f}$ are the $M\times L$ a posteriori backward and forward errors, respectively, for time n.
- $\mathbf{e}_n$ and $\mathbf{r}_n$ are the $M\times 1$ a priori and a posteriori estimation errors, respectively, for time n.

Detailed derivations of the expressions for FAEST can be found in [72, 93]. The operation count for multi-channel FAEST, which is included in Appendix A.1.2, indicates that it requires $O\left(L^2 I_\mathrm{g}\right)$ operations per iteration. Then, FAEST requires about $O\left((LI_\mathrm{g})^2\right)$ operations to solve (3.1).

3.5 Superfast solver

Next, we review the superfast solver recently proposed by Poletti and Teal [79] to approximately compute the optimal solution for (3.1) when $\beta > 0$. In their work, Poletti and Teal propose the superfast solver for both the single-channel and the multi-channel case. This solver relates the optimal filters obtained with the time and frequency domain formulations of the LS problem, i.e., the filters obtained with wPM-T and wPM-F, and then, an approximate solution for (3.1) is obtained using this relation. We think that this relation is very illustrative, and it can be helpful to understand the performance differences between wPM-T and wPM-F shown in Section 2.3.4. Then, we do include the derivations required to obtain the expressions for

the superfast solver, as they are useful to show the relation between the filters obtained with both algorithms.

First, let us consider the following LS problem:

$$\bar{\mathbf{q}}_{\text{opt},f} = \min_{\bar{\mathbf{q}}_f} \left\{ \left\| \left(\bar{\mathbf{H}}_f \bar{\mathbf{q}}_f - \bar{\mathbf{d}}_f \right) \right\|^2 + \beta \left\| \bar{\mathbf{q}}_f \right\|^2 \right\}, \tag{3.13}$$

where $\bar{\mathbf{H}}_f$ and $\bar{\mathbf{d}}_f$ are defined in (2.15) and (2.22), respectively. The LS problem in (3.13) is based on using the frequency-domain formulation to compute the optimal frequency responses of the filters for each frequency individually. In particular, we can see that (3.13) leads to the optimal filter coefficients at frequency f for wPM-F, i.e., (2.27), if we consider that $\beta = \beta_f$ and that no weighting matrix is used. The optimal solution for (3.13) can be written as

$$\bar{\mathbf{q}}_{\text{opt},f} = \left(\bar{\mathbf{H}}_f^H \bar{\mathbf{H}}_f + \beta \, \mathbf{I}_L \right)^{-1} \bar{\mathbf{H}}_f^H \bar{\mathbf{d}}_f. \tag{3.14}$$

We studied in Section 2.2.3 that in order to compute the time-domain filters of length I_g from the optimal frequency responses obtained with (3.14), the following steps must be carried out:

1. Compute the optimal frequency responses $\bar{\mathbf{q}}_{\text{opt},f}$ for a set of I_d equispaced control frequencies. Then, let us define

$$\bar{\mathbf{q}}_{\text{opt}} = \left[\bar{\mathbf{q}}_{\text{opt},f_0}^T \quad \dots \quad \bar{\mathbf{q}}_{\text{opt},f_{I_\text{d}-1}}^T \right]^T, \tag{3.15}$$

   which is a vector of size $LI_\text{d} \times 1$ containing $\bar{\mathbf{q}}_{\text{opt},f}$ for a set of I_d control frequencies f_k, being f_k the frequency of the k-th frequency bin for a I_d-point DFT.

2. Obtain the I_d-length impulse responses by applying an I_d-point IDFT to the optimal frequency responses in $\bar{\mathbf{q}}_{\text{opt}}$. Thus, let us define a $LI_\text{d} \times LI_\text{d}$ matrix $\mathbf{F}_L$ as

$$\mathbf{F}_L = \begin{bmatrix} \Phi_{I_\text{d}}^{(0,0)} \, \mathbf{I}_L & \dots & \Phi_{I_\text{d}}^{(0,I_\text{d}-1)} \, \mathbf{I}_L \\ \vdots & \ddots & \vdots \\ \Phi_{I_\text{d}}^{(I_\text{d}-1,0)} \, \mathbf{I}_L & \dots & \Phi_{I_\text{d}}^{(I_\text{d}-1,I_\text{d}-1)} \, \mathbf{I}_L \end{bmatrix}, \tag{3.16}$$

   where $\Phi_{I_\text{d}}^{(k,n)} = \frac{1}{\sqrt{I_\text{d}}} e^{-j\frac{2\pi kn}{I_\text{d}}}$ is the coefficient for the n-th time index and the k-th frequency bin of a I_d-point DFT. Then, $\mathbf{F}_L$ and $\mathbf{F}_L^H$ can

be used to compute the I_d-point DFTs and IDFTs, respectively, of L signals that are interleaved in a column vector of size $LI_\mathrm{d}\times 1$.

3. Truncate the impulse responses of length I_d to a length I_g to obtain the filters. Consequently, let us define

$$\mathbf{T} = \begin{bmatrix} \mathbf{I}_{LI_\mathrm{g}} & \mathbf{0}_{LI_\mathrm{g}\times L(I_\mathrm{d}-I_\mathrm{g})} \end{bmatrix}, \tag{3.17}$$

which is a $LI_\mathrm{g}\times LI_\mathrm{d}$ matrix that can be used to truncate a set of L impulse responses of length I_d to a length I_g.

Hence, we can define the $LI_\mathrm{g}\times 1$ vector $\mathbf{g}_\mathrm{fd}$ containing the estimated filters using the previous steps as

$$\mathbf{g}_\mathrm{fd} = \mathbf{T}\,\mathbf{F}_L^H\,\bar{\mathbf{q}}_\mathrm{opt}. \tag{3.18}$$

We showed in Section 2.3.4 that the performance of $\mathbf{g}_\mathrm{fd}$ is degraded with respect to $\mathbf{g}_\mathrm{opt}$, especially for short filters or short modelling delays. This is caused by the truncation of the impulse responses obtained from the optimal frequency responses. Poletti and Teal [79] showed that the optimal solution $\mathbf{g}_\mathrm{opt}$ for (3.1) can be related to $\mathbf{g}_\mathrm{fd}$, and proposed the superfast solver to approximate $\mathbf{g}_\mathrm{opt}$ from $\mathbf{g}_\mathrm{fd}$, i.e., to approximate the filters for wPM-T from the filters for wPM-F. Next, we review this solver.

Let us define a $MI_\mathrm{d}\times LI_\mathrm{d}$ block-diagonal matrix $\bar{\mathbf{H}}$ containing the room frequency responses for I_d control frequencies as

$$\bar{\mathbf{H}} = \mathrm{diag}\left\{ \bar{\mathbf{H}}_{f_0} \quad \dots \quad \bar{\mathbf{H}}_{f_{I_\mathrm{d}-1}} \right\}. \tag{3.19}$$

Now, let us define a $MI_\mathrm{d}\times LI_\mathrm{d}$ matrix $\mathbf{H}_\mathrm{e}$ as

$$\mathbf{H}_\mathrm{e} = \mathbf{F}_M^H\,\bar{\mathbf{H}}\,\mathbf{F}_L, \tag{3.20}$$

which using (3.16) and (3.19) can be alternatively defined as

$$\mathbf{H}_\mathrm{e} = \begin{bmatrix} \mathbf{H}_0 & \mathbf{0}_{\mathrm{M}\times\mathrm{L}} & \dots & \mathbf{0}_{\mathrm{M}\times\mathrm{L}} & \mathbf{H}_{I_\mathrm{h}\text{-}1} & \dots & \mathbf{H}_1 \\ \vdots & & & & & & \\ \mathbf{H}_{I_\mathrm{h}\text{-}1} & & & & & & \\ \mathbf{0}_{\mathrm{M}\times\mathrm{L}} & & & \mathit{Toeplitz} & & & \\ \vdots & & & & & & \\ \mathbf{0}_{\mathrm{M}\times\mathrm{L}} & & & & & & \end{bmatrix}. \tag{3.21}$$

It is easy to see that $\mathbf{H}_{\mathrm{e}}$ is a circulant extension of $\mathbf{H}$ in (2.11), and then, it can be partitioned as

$$\mathbf{H}_{\mathrm{e}} = \begin{bmatrix} \mathbf{H} & \mathbf{E} \end{bmatrix}, \tag{3.22}$$

where $\mathbf{E}$ is a matrix of size $MI_{\mathrm{d}} \times L\,(I_{\mathrm{d}}-I_{\mathrm{g}})$. Now, we can express

$$\mathbf{H} = \mathbf{H}_{\mathrm{e}}\mathbf{T}^{T}, \tag{3.23}$$

where $\mathbf{T}$ is defined in (3.17). Furthermore, using (3.20) and (3.23) we can express $\mathbf{H}$ as

$$\mathbf{H} = \mathbf{F}_{M}^{H}\,\bar{\mathbf{H}}\,\mathbf{F}_{L}\mathbf{T}^{T}. \tag{3.24}$$

A key aspect for the derivation of the superfast solver is that the optimal solution for (3.1) can be computed as

$$\mathbf{g}_{\mathrm{opt}} = \left(\mathbf{H}^{T}\mathbf{H} + \beta\,\mathbf{I}_{LI_{\mathrm{g}}}\right)^{-1}\mathbf{H}^{T}\mathbf{d}, \tag{3.25}$$

or alternatively as

$$\mathbf{g}_{\mathrm{opt}} = \mathbf{H}^{T}\left(\mathbf{H}\mathbf{H}^{T} + \beta\,\mathbf{I}_{MI_{\mathrm{d}}}\right)^{-1}\mathbf{d}, \tag{3.26}$$

for any $\beta > 0$, since (3.25) and (3.26) are equivalent for $\beta > 0$ [79]. Then, using (3.24) and (3.26), we can write the optimal solution for (3.1) as

$$\mathbf{g}_{\mathrm{opt}} = \mathbf{T}\mathbf{F}_{L}^{H}\bar{\mathbf{H}}^{H}\left(\bar{\mathbf{H}}\mathbf{F}_{L}\mathbf{T}^{T}\mathbf{T}\mathbf{F}_{L}^{H}\bar{\mathbf{H}}^{H} + \beta\,\mathbf{I}_{MI_{\mathrm{d}}}\right)^{-1}\mathbf{F}_{M}\mathbf{d}, \tag{3.27}$$

where we took into account that $\mathbf{F}_{M}^{-1} = \mathbf{F}_{M}^{H}$ and $\mathbf{H}^{T} = \mathbf{H}^{H}$, since $\mathbf{F}_{M}$ is a unitary matrix and $\mathbf{H}$ is a real matrix. The term $\mathbf{T}^{T}\mathbf{T}$ can be expressed as

$$\mathbf{T}^{T}\mathbf{T} = \mathbf{I}_{LI_{\mathrm{d}}} - \mathbf{\Psi}, \tag{3.28}$$

in which $\mathbf{\Psi}$ is a $LI_{\mathrm{d}} \times LI_{\mathrm{d}}$ matrix that is defined as

$$\mathbf{\Psi} = \begin{bmatrix} \mathbf{0}_{LI_{\mathrm{g}}} & \mathbf{0}_{LI_{\mathrm{g}} \times L(I_{\mathrm{d}}-I_{\mathrm{g}})} \\ \mathbf{0}_{L(I_{\mathrm{d}}-I_{\mathrm{g}}) \times LI_{\mathrm{g}}} & \mathbf{I}_{L(I_{\mathrm{d}}-I_{\mathrm{g}})} \end{bmatrix}. \tag{3.29}$$

Then, using (3.28) we can write (3.27) as

$$\mathbf{g}_{\mathrm{opt}} = \mathbf{T}\mathbf{F}_{L}^{H}\bar{\mathbf{H}}^{H}\left(\bar{\mathbf{H}}\bar{\mathbf{H}}^{H} - \bar{\mathbf{H}}\mathbf{F}_{L}\mathbf{\Psi}\mathbf{F}_{L}^{H}\bar{\mathbf{H}}^{H} + \beta\,\mathbf{I}_{MI_{\mathrm{d}}}\right)^{-1}\mathbf{F}_{M}\mathbf{d}. \tag{3.30}$$

Now, let us define

$$\mathbf{A} = \bar{\mathbf{H}}\bar{\mathbf{H}}^H + \beta\,\mathbf{I}_{MI_\mathrm{d}}, \tag{3.31}$$

$$\mathbf{B} = \mathbf{F}_L \boldsymbol{\Psi}\, \mathbf{F}_L^H, \tag{3.32}$$

$$\mathbf{U} = \bar{\mathbf{H}}, \tag{3.33}$$

$$\mathbf{V} = \bar{\mathbf{H}}^H, \tag{3.34}$$

so we can express (3.30) as

$$\mathbf{g}_\mathrm{opt} = \mathbf{T}\mathbf{F}_L^H \mathbf{V} \left(\mathbf{A} - \mathbf{U}\mathbf{B}\mathbf{V}\right)^{-1} \mathbf{F}_M \mathbf{d}. \tag{3.35}$$

We can use Woodbury matrix identity [77] to write (3.35) as

$$\mathbf{g}_\mathrm{opt} = \mathbf{T}\mathbf{F}_L^H \mathbf{V} \left(\mathbf{A}^{-1} + \mathbf{A}^{-1}\mathbf{U}\left(\mathbf{I}_{LI_\mathrm{d}} - \mathbf{B}\mathbf{V}\mathbf{A}^{-1}\mathbf{U}\right)^{-1} \mathbf{B}\mathbf{V}\mathbf{A}^{-1}\right) \mathbf{F}_M \mathbf{d}. \tag{3.36}$$

Moreover, let us define

$$\bar{\mathbf{H}}^\dagger = \mathbf{V}\mathbf{A}^{-1}, \tag{3.37}$$

which from (3.31) and (3.34) can be re-written as

$$\bar{\mathbf{H}}^\dagger = \bar{\mathbf{H}}^H \left(\bar{\mathbf{H}}\bar{\mathbf{H}}^H + \beta\,\mathbf{I}_{MI_\mathrm{d}}\right)^{-1}, \tag{3.38}$$

i.e., $\bar{\mathbf{H}}^\dagger$ is the $LI_\mathrm{d} \times MI_\mathrm{d}$ right pseudoinverse matrix of $\bar{\mathbf{H}}$. Since $\bar{\mathbf{H}}$ is a block-diagonal matrix, $\bar{\mathbf{H}}^\dagger$ is also a block-diagonal matrix defined as

$$\bar{\mathbf{H}}^\dagger = \mathrm{diag}\left\{\bar{\mathbf{H}}_{f_0}^\dagger, \ldots, \bar{\mathbf{H}}_{f_{I_\mathrm{d}-1}}^\dagger\right\}, \tag{3.39}$$

where $\bar{\mathbf{H}}_f^\dagger$ is the $L \times M$ right pseudoinverse of $\bar{\mathbf{H}}_f$, i.e.,

$$\bar{\mathbf{H}}_f^\dagger = \bar{\mathbf{H}}_f^H \left(\bar{\mathbf{H}}_f \bar{\mathbf{H}}_f^H + \beta\,\mathbf{I}_M\right)^{-1}. \tag{3.40}$$

The pseudoinverse $\bar{\mathbf{H}}_f^\dagger$ can be alternatively written for $\beta > 0$ [79] as

$$\bar{\mathbf{H}}_f^\dagger = \left(\bar{\mathbf{H}}_f^H \bar{\mathbf{H}}_f + \beta\,\mathbf{I}_L\right)^{-1} \bar{\mathbf{H}}_f^H. \tag{3.41}$$

Next, using (3.33) and (3.37), we can write (3.36) as

$$\mathbf{g}_\mathrm{opt} = \mathbf{T}\mathbf{F}_L^H \left(\mathbf{I} + \bar{\mathbf{H}}^\dagger \bar{\mathbf{H}} \left(\mathbf{I}_{LI_\mathrm{d}} - \mathbf{B}\bar{\mathbf{H}}^\dagger \bar{\mathbf{H}}\right)^{-1} \mathbf{B}\right) \bar{\mathbf{H}}^\dagger \mathbf{F}_M \mathbf{d}. \tag{3.42}$$

Moreover, we can define a matrix $\bar{\mathbf{\Lambda}}$ of size $LI_{\mathrm{d}} \times LI_{\mathrm{d}}$ as

$$\bar{\mathbf{\Lambda}} = \bar{\mathbf{H}}^{\dagger}\bar{\mathbf{H}} = \mathrm{diag}\left\{\bar{\mathbf{\Lambda}}_{f_0}, \dots, \bar{\mathbf{\Lambda}}_{f_{I_{\mathrm{d}}-1}}\right\}, \tag{3.43}$$

where $\bar{\mathbf{\Lambda}}_f = \bar{\mathbf{H}}_f^{\dagger}\bar{\mathbf{H}}_f$ is a matrix of size $L \times L$. Then, we can write (3.42) as

$$\mathbf{g}_{\mathrm{opt}} = \mathbf{T}\mathbf{F}_L^H \left(\mathbf{I} + \bar{\mathbf{\Lambda}}\left(\mathbf{I}_{LI_{\mathrm{d}}} - \mathbf{B}\bar{\mathbf{\Lambda}}\right)^{-1}\mathbf{B}\right)\bar{\mathbf{H}}^{\dagger}\mathbf{F}_M\mathbf{d}. \tag{3.44}$$

Now, from (2.30) and (3.16), we can express $\mathbf{F}_M\mathbf{d}$ as

$$\mathbf{F}_M\mathbf{d} = \left[\bar{\mathbf{d}}_{f_0}^T \quad \dots \quad \bar{\mathbf{d}}_{f_{I_{\mathrm{d}}-1}}^T\right]^T, \tag{3.45}$$

where $\bar{\mathbf{d}}_f$ is defined in (2.22). Then, using (3.39) and (3.45), we can write

$$\bar{\mathbf{H}}^{\dagger}\mathbf{F}_M\mathbf{d} = \left[\left(\bar{\mathbf{H}}_{f_0}^{\dagger}\bar{\mathbf{d}}_{f_0}\right)^T \quad \dots \quad \left(\bar{\mathbf{H}}_{f_{I_{\mathrm{d}}-1}}^{\dagger}\bar{\mathbf{d}}_{f_{I_{\mathrm{d}}-1}}\right)^T\right]^T, \tag{3.46}$$

and taking into account (3.14), (3.15), and (3.41), we can express

$$\bar{\mathbf{q}}_{\mathrm{opt}} = \bar{\mathbf{H}}^{\dagger}\mathbf{F}_M\mathbf{d}, \tag{3.47}$$

which holds for $\beta > 0$. Next, using (3.47), we can write (3.44) as

$$\mathbf{g}_{\mathrm{opt}} = \mathbf{T}\mathbf{F}_L^H \left(\mathbf{I} + \bar{\mathbf{\Lambda}}\left(\mathbf{I}_{LI_{\mathrm{d}}} - \mathbf{B}\bar{\mathbf{\Lambda}}\right)^{-1}\mathbf{B}\right)\bar{\mathbf{q}}_{\mathrm{opt}}, \tag{3.48}$$

which using (3.18) can be expressed as

$$\mathbf{g}_{\mathrm{opt}} = \mathbf{g}_{\mathrm{fd}} + \mathbf{T}\mathbf{F}_L^H\bar{\mathbf{\Lambda}}\left(\mathbf{I}_{LI_{\mathrm{d}}} - \mathbf{B}\bar{\mathbf{\Lambda}}\right)^{-1}\mathbf{B}\,\bar{\mathbf{q}}_{\mathrm{opt}}. \tag{3.49}$$

We can see in (3.49) that the optimal solution $\mathbf{g}_{\mathrm{opt}}$ for the LS problem formulated in time-domain can be expressed as the sum of the truncated filters $\mathbf{g}_{\mathrm{fd}}$ and a correction term. The correction term compensates for the degradation that appears for $\mathbf{g}_{\mathrm{fd}}$ due to the truncation of the filters. Computing the correction term in (3.49) requires the inversion of a matrix of size $LI_{\mathrm{d}} \times LI_{\mathrm{d}}$, which is even more computationally demanding than computing the optimal solution with (3.2). However, the inverse in (3.49) can be defined using Neumann series [79, 94] as

$$\left(\mathbf{I}_{LI_{\mathrm{d}}} - \mathbf{B}\bar{\mathbf{\Lambda}}\right)^{-1} = \sum_{p=0}^{\infty}\left(\mathbf{B}\bar{\mathbf{\Lambda}}\right)^p. \tag{3.50}$$

It is proven in [79] that the summation in the previous expression converges, since all the eigenvalues of matrix $\mathbf{B}\bar{\mathbf{\Lambda}}$ are less than one. Also, the authors in [79] showed that the convergence rate for the summation is governed by the regularization parameter β, and pointed out that higher regularizations require lower number of iterations to converge. Now, using (3.50), we can write the optimal solution (3.49) as

$$\mathbf{g}_{\text{opt}} = \mathbf{g}_{\text{fd}} + \mathbf{T}\mathbf{F}_L^H \bar{\mathbf{\Lambda}} \left\{ \sum_{p=0}^{\infty} \left(\mathbf{B}\bar{\mathbf{\Lambda}} \right)^p \right\} \mathbf{B}\, \bar{\mathbf{q}}_{\text{opt}}. \tag{3.51}$$

Next, let us define

$$\bar{\mathbf{r}}_p = \begin{cases} \mathbf{B}\, \bar{\mathbf{q}}_{\text{opt}} & p = 0 \\ \mathbf{B}\bar{\mathbf{\Lambda}}\bar{\mathbf{r}}_{p-1} & p > 0 \end{cases}, \tag{3.52}$$

which is a $LI_{\text{d}} \times 1$ vector that can be computed recursively. Then, we can write the optimal solution (3.51) as

$$\mathbf{g}_{\text{opt}} = \mathbf{g}_{\text{fd}} + \mathbf{T}\mathbf{F}_L^H \bar{\mathbf{\Lambda}} \left(\sum_{p=0}^{\infty} \bar{\mathbf{r}}_p \right). \tag{3.53}$$

The previous expression to compute the optimal solution is not feasible, as it includes an infinite series. However, an approximation of (3.53) can be obtained by replacing the infinite series by its P-th partial sum. Hence, the P-th order approximation of (3.53) can be written as

$$\mathbf{g}_{\text{ap},P} = \mathbf{g}_{\text{fd}} + \mathbf{T}\mathbf{F}_L^H \bar{\mathbf{\Lambda}} \left(\sum_{p=0}^{P} \bar{\mathbf{r}}_p \right). \tag{3.54}$$

It is shown in [79] that approximation (3.54) tends monotonically with P to the optimal exact solution (3.53). Then, the order of the approximation (3.54) is directly related to the accuracy of the estimation. For low orders P, the approximation (3.54) is closer to the truncated filters $\mathbf{g}_{\text{fd}}$ obtained with the frequency-domain LS problem than to the optimal solution $\mathbf{g}_{\text{opt}}$. For high orders P, the correction term in (3.54) can compensate to a great degree the degradations that appear for $\mathbf{g}_{\text{fd}}$ due to truncation, and then, the approximation is closer to the optimal solution $\mathbf{g}_{\text{opt}}$. The main advantage of (3.54) is that it can be computed very efficiently, because pre-multiplication

by $\mathbf{B} = \mathbf{F}_L \mathbf{\Psi} \mathbf{F}_L^H$ is equivalent to transform L frequency responses to the time-domain, set to zero their first I_g samples, and transform back to the frequency domain. This process can be performed with DFTs and IDFTs of size I_d, consequently, pre-multiplication by $\mathbf{B}$ can be efficiently computed using the FFT algorithm.

The steps required to approximate (3.1) with the superfast solver are summarized in Algorithm 3.3, and a detailed operation count is included in Appendix A.1.3. Hence, the superfast solver requires about $O\left(PLI_\mathrm{g} \log_2 I_\mathrm{g}\right)$ operations for computing the P-th order approximation of (3.1).

Algorithm 3.3: Compute the P-th order approximation of (3.1) with the superfast solver [79].

Compute the frequency-domain solution:

for $k = 0, \ldots, I_\mathrm{d}-1$ **do**
- $\bar{\mathbf{H}}_{f_k}^{\dagger} = \left(\bar{\mathbf{H}}_{f_k}^H \bar{\mathbf{H}}_{f_k} + \beta\, \mathbf{I}_L\right)^{-1} \bar{\mathbf{H}}_{f_k}^H$;
- $\bar{\mathbf{\Lambda}}_{f_k} = \bar{\mathbf{H}}_{f_k}^{\dagger} \bar{\mathbf{H}}_{f_k}$;
- $\bar{\mathbf{q}}_{\mathrm{opt},f_k} = \bar{\mathbf{H}}_{f_k}^{\dagger} \bar{\mathbf{d}}_{f_k}$;

end

Form $\bar{\mathbf{q}}_\mathrm{opt}$ using $\bar{\mathbf{q}}_{\mathrm{opt},f_k}$;

$\mathbf{g}_\mathrm{fd} = \mathbf{T} \mathbf{F}_L^H \bar{\mathbf{q}}_\mathrm{opt}$;

Compute the correction terms:

Form $\bar{\mathbf{\Lambda}}$ using $\bar{\mathbf{\Lambda}}_{f_k}$;

for $p = 0, \ldots, P$ **do**
- **if** $p > 0$ **then**
  - $\bar{\mathbf{r}}_p = \mathbf{B} \bar{\mathbf{\Lambda}} \bar{\mathbf{r}}_{p-1}$;
- **else**
  - $\bar{\mathbf{r}}_p = \mathbf{B}\, \bar{\mathbf{q}}_\mathrm{opt}$;
- **end**

end

Compute the time-domain approximation:

$\mathbf{g}_{\mathrm{ap},P} = \mathbf{g}_\mathrm{fd} + \mathbf{T} \mathbf{F}_L^H \bar{\mathbf{\Lambda}} \left(\sum_{p=0}^{P} \bar{\mathbf{r}}_p\right)$;

3.6 Performance evaluation

Next, we evaluate the performance of the Cholesky, the FAEST, and the superfast [79] solvers. First, we compare the accuracy of the different solvers to compute the optimal filters for wPM-T. Later, we study the influence of the different solvers on the performance of a PSZ system. Finally, we compare the computational complexity of the three solvers.

3.6.1 Setup and methodology

Setup

The setup described in Section 2.3.1 is used for the evaluations of this chapter, i.e., a linear array of 8 two-way loudspeakers and single bright and dark zones in a office-like room with reverberation time $T_{60} = 500$ ms. We consider that the system is operating at a sampling frequency of 6300 Hz.

Methodology for computing the filters

The filters for wPM-T are computed by solving (3.1) with the Cholesky, the FAEST, and the superfast solvers, which are detailed in Algorithms 3.1 to 3.3, respectively. We select the target impulse response in the m-th control point for wPM-T as

$$d_m(n) = \begin{cases} h_{ml_\mathrm{r}}(n - \tau_\mathrm{d}) & m \in \mathcal{B} \\ 0 & m \in \mathcal{D} \end{cases}, \tag{3.55}$$

where $l_\mathrm{r} = 3$ is the reference loudspeaker, and $\tau_\mathrm{d} \in \mathbb{N}$ is a modelling delay whose value is indicated in each case. The regularization factor is selected as

$$\beta = \beta_0 \, u_\mathrm{avg}, \tag{3.56}$$

where u_avg is the mean of the eigenvalues of matrix $\mathbf{H}^T\mathbf{H}$, and β_0 is the regularization factor relative to u_avg. Different values β_0 are evaluated.

Methodology for evaluating the filters

First, the accuracy of the solvers for computing the optimal filters will be studied. The Cholesky solver has shown the highest accuracy to solve (3.1), whereas the other two solvers have shown higher sensitivity to factors as the regularization level. Then, we will focus on evaluating the accuracy of the

FAEST and the superfast solver. The filters obtained with the Cholesky solver, which we denote as $\mathbf{g}_{\text{ref}}$, are taken as a reference to evaluate the accuracy. The metric used to evaluate the accuracy is the Normalized Mean Squared Error (NMSE) of the filters computed with either the FAEST or the superfast solver with respect to the reference filters, which is given by

$$\varepsilon = \frac{\left\|\mathbf{g} - \mathbf{g}_{\text{ref}}\right\|^2}{\left\|\mathbf{g}_{\text{ref}}\right\|^2}. \tag{3.57}$$

To evaluate how the different solvers influence the performance of a PSZ system, the metrics described in Section 2.2.5 are computed for a set of 16384 equispaced frequencies with a resolution of 0.3845 Hz. The target response for the m-th validation point is selected as

$$d_{\text{v},m}(n) = \begin{cases} h_{\text{v},ml_{\text{r}}}(n - \tau_{\text{d}}) & m \in \mathcal{B} \\ 0 & m \in \mathcal{D} \end{cases}. \tag{3.58}$$

where $h_{\text{v},ml_{\text{r}}}$ is the RIR from the l_{r}-th loudspeaker to the m-th validation point.

3.6.2 Accuracy of solvers

First, we evaluate the accuracy of the FAEST and superfast solvers described in Sections 3.4 and 3.5, respectively. For the evaluations, let us consider four sets of filter lengths and modelling delays: 1) $I_{\text{g}} = 512$ and $\tau_{\text{d}} = 64$; 2) $I_{\text{g}} = 512$ and $\tau_{\text{d}} = 256$; 3) $I_{\text{g}} = 2048$ and $\tau_{\text{d}} = 64$; and 4) $I_{\text{g}} = 2048$ and $\tau_{\text{d}} = 1024$.

FAEST

The NMSE with respect to the reference filters for FAEST is shown in Fig. 3.1 as a function of the regularization factor. We include results for the four combinations of filter lengths and modelling delays previously discussed. In general, we can see that the NMSE is very similar and follows similar trends for the different filter lengths and delays. It is interesting to note that the higher the regularization factor, the lower the NMSE. The motivation is that higher regularization factors make the solver less sensitive to the round-off errors produced by the finite-size arithmetic. In particular, the NMSE is below –30 dB for $\beta_0 \geq 10^{-13}$ and it is about –280 dB for $\beta_0 = 10^{-1}$, which indicates that the solver presents very good accuracy because this error is very close to the IEEE 754 64-bit floating-point precision

[95]. For $\beta_0 < 10^{-13}$, FAEST diverges due to the round-off errors and it can not obtain a suitable set of filters for wPM-T. Then, FAEST seems a good option for computing the optimal filters when extremely low regularization factors are not needed.

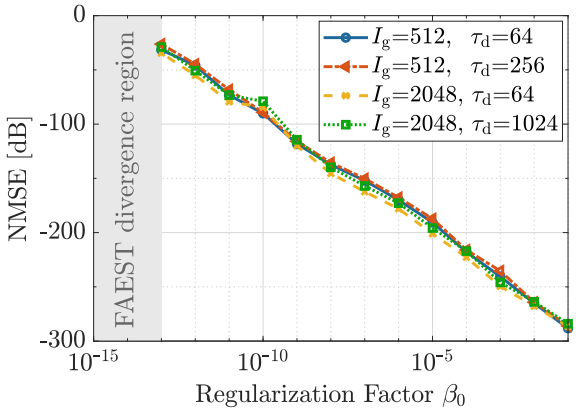

Figure 3.1: NMSE for the filters computed with FAEST with respect to the reference filters as a function of the regularization factor. Four combinations of filter lengths I_g and modelling delays τ_d are considered. The grey area shows the regularization factors for which FAEST diverges.

Superfast

The NMSE with respect to the reference filters for the superfast solver is shown in Fig. 3.2 as a function of the approximation order P and the regularization factor β_0. The NMSE for the four considered combinations of filter lengths and modelling delays is shown in Fig. 3.2a to Fig. 3.2d. Approximation orders P in the range 1 to 10^5, and regularization factors β_0 in the range 10^{-8} to 10^{-1} are evaluated. The results in Fig. 3.2 show similar trends for the different filter lengths and modelling delays that are considered. Overall, the results indicate that increasing the regularization factor reduces the NMSE, i.e., improves the accuracy of the solver. This is because the initial estimate $\mathbf{g}_{fd}$ for the superfast solver is more similar to $\mathbf{g}_{opt}$ for high regularizations levels (as shown in Section 2.3.4), and then, lower correction levels are required to obtain an accurate approximation. Also, the results show that increasing the approximation order monotonically decreases the NMSE, with a decaying rate that is directly related to the regularization factor. In particular, the higher the regularization factor,

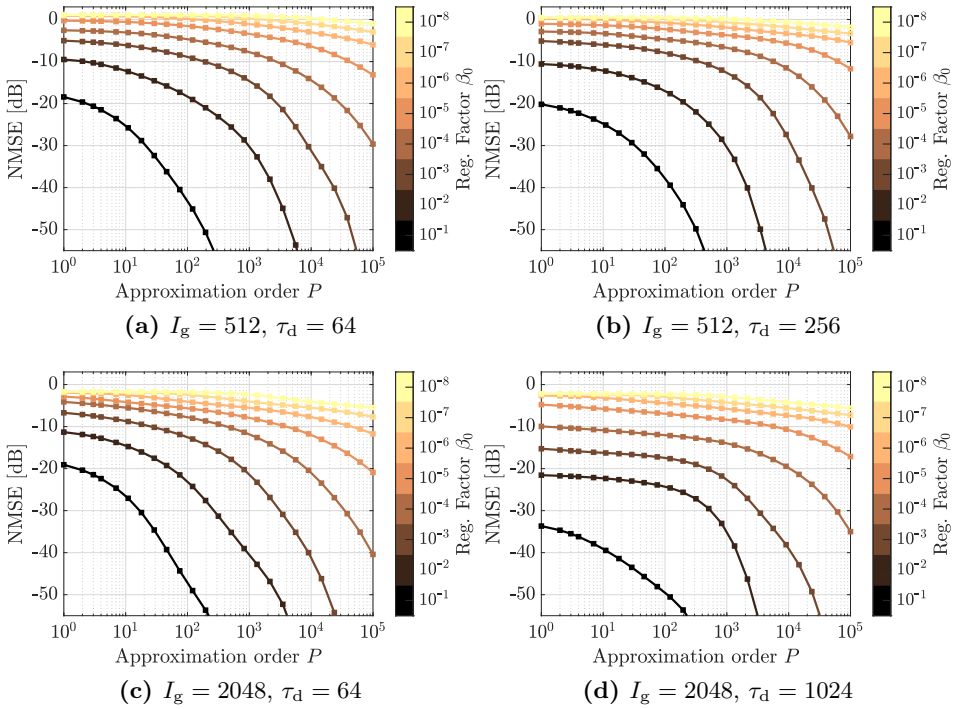

(a) $I_\mathrm{g} = 512$, $\tau_\mathrm{d} = 64$ **(b)** $I_\mathrm{g} = 512$, $\tau_\mathrm{d} = 256$

(c) $I_\mathrm{g} = 2048$, $\tau_\mathrm{d} = 64$ **(d)** $I_\mathrm{g} = 2048$, $\tau_\mathrm{d} = 1024$

Figure 3.2: NMSE for the filters computed with the superfast solver [79] with respect to the reference filters as a function of the approximation order and the regularization factor. Four combinations of filter lengths I_g and modelling delays τ_d are considered.

the higher the decaying rate. This is motivated by the fact that the infinite series in (3.53) converges faster for high regularization factors (as shown in [79]). Then, low approximation orders can accurately estimate the optimal solution when high regularizations factors are considered. For example, the NMSE is below –50 dB for $\beta_0 = 10^{-1}$ and $P = 300$, and for $\beta_0 = 10^{-2}$ and $P = 4000$. It is relevant that the decaying rate for the NMSE is very low for $\beta_0 \leq 10^{-5}$, leading to values that are generally above –20 dB for all the studied approximation orders. Then, we can conclude that the superfast solver is a good option to compute the filters when medium and high regularizations factors are considered, however, it requires large approximation orders to accurately compute the optimal filters for low regularization levels. Finally, we can note from Fig. 3.1 and Fig. 3.2 that FAEST obtains

notably higher accuracy than the superfast solver, which follows from the fact that FAEST is an exact solver while the superfast solver is an approximate solver.

3.6.3 Performance of solvers for PSZ

Next, we evaluate how the accuracy of the solvers influences the performance of a PSZ system. The four combinations of filter lengths and modelling delays considered in the previous section are evaluated in this section. We present in Fig. 3.3 the average acoustic contrast and MSE in the band 125-250 Hz for the Cholesky, the FAEST, and the superfast solvers. We consider regularization factors $\beta_0 = 10^{-1}$, $\beta_0 = 10^{-3}$, and $\beta_0 = 10^{-5}$, in Fig. 3.3a-b, 3.3c-d, and 3.3e-f, respectively. In Fig. 3.3, the x-axis represents the approximation order for the superfast solver, which has no influence on the Cholesky and FAEST solvers. We focus on the band 125-250 Hz because it is the range where the PSZ system is more sensitive to the design of the filters (as shown in Section 2.3.4), so we are especially interested on studying the performance of the solvers for wPM-T in this band.

First, let us note that in Fig. 3.3 the Cholesky and FAEST solvers lead to the same acoustic contrast and MSE in all cases. Also, it is interesting to notice that increasing the regularization factor β_0 from 10^{-5} to 10^{-3} improves the performance, but increasing it from 10^{-3} to 10^{-1} degrades the performance. Then, the PSZ system does not benefit from a regularization factor significantly lower or higher than $\beta_0 = 10^{-3}$. These results agree with those presented in Section 2.3.3, which revealed that the regularization factor for practical PSZ systems must be selected high enough to make the filters robust to perturbations, but taking into account that too high regularization factors also degrade the performance. In Section 3.6.2, we determined that the FAEST solver diverges for $\beta_0 < 10^{-13}$, so this solver is not a good option for very low regularizations. However, in practice the filters must not be computed with such low regularizations, as they lead to poor robustness to perturbations. Then, the FAEST solver seems a good option for computing the wPM-T filters for practical PSZ systems, in which extremely low regularization factors are not used.

Regarding the superfast solver, we can see in Fig. 3.3 that its performance is directly related to the approximation order. In particular, increasing the approximation order approaches its acoustic contrast and MSE to those for the Cholesky solver. Also, the results show that increasing the

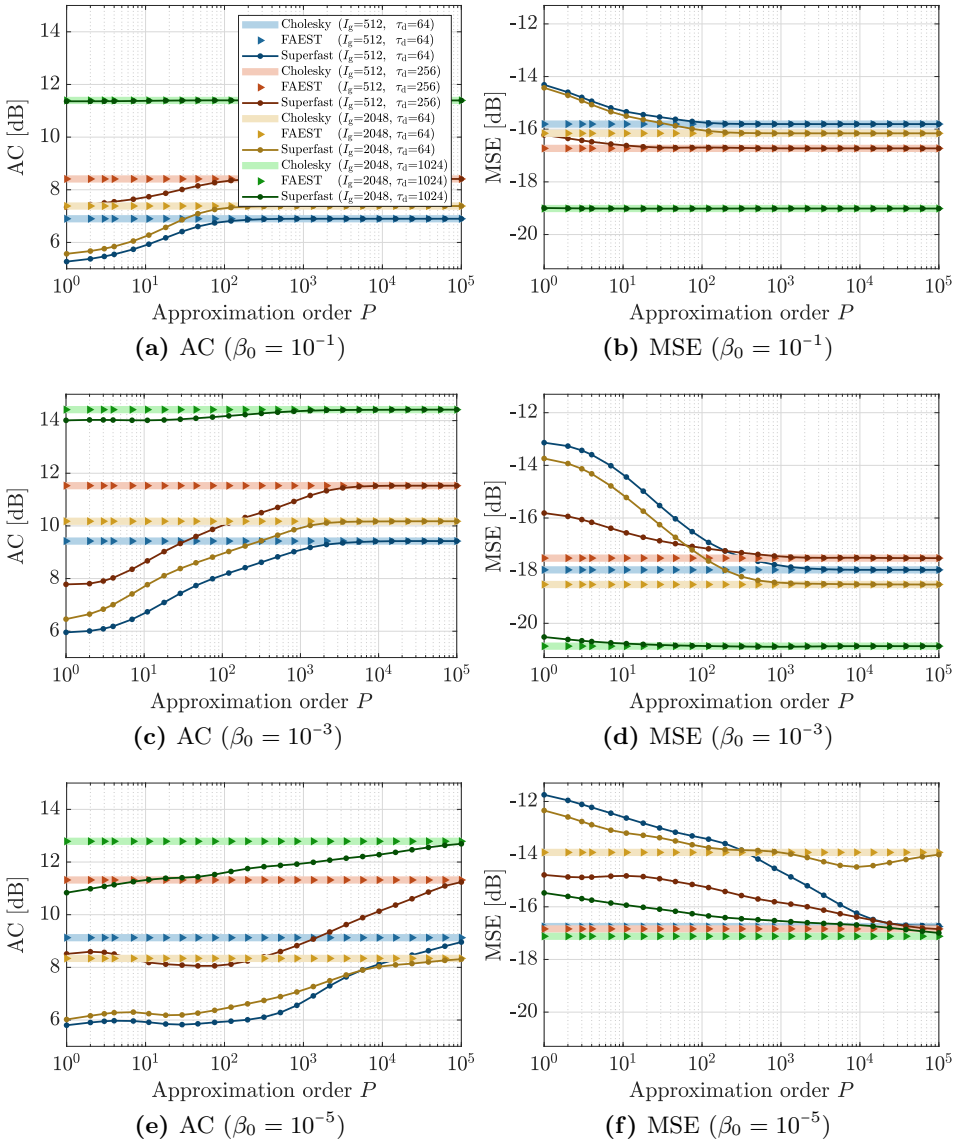

(a) AC ($\beta_0 = 10^{-1}$) **(b)** MSE ($\beta_0 = 10^{-1}$)

(c) AC ($\beta_0 = 10^{-3}$) **(d)** MSE ($\beta_0 = 10^{-3}$)

(e) AC ($\beta_0 = 10^{-5}$) **(f)** MSE ($\beta_0 = 10^{-5}$)

Figure 3.3: Average acoustic contrast (a, c, e), and MSE (b, d, f) over 125-250 Hz for wPM-T using the Cholesky, the FAEST, and the superfast [79] solvers. The x-axis represents the approximation order for the superfast solver. Three different regularization factors β_0 and four combinations of filter lengths I_g and modelling delays τ_d are considered.

regularization level reduces the order required by the superfast solver to converge to the Cholesky solver, which agrees with the accuracy results presented in Section 3.6.2. Moreover, it is interesting to note that lower approximation orders are required for $I_g = 2048$ and $\tau_d = 1024$ than for the other configurations. This is because wPM-T and wPM-F offer very similar performance when long filters and appropriated modelling delays are considered, so in this case the approximation obtained with the superfast solver is accurate even for low orders. However, the use of wPM-T is not essential in this case, since very similar performance can be achieved with wPM-F (see Section 2.3.4). Then, we are more interested in the performance of the superfast solver for the other configurations involving either short filters or short modelling delays, i.e., for the cases in which wPM-T clearly outperforms wPM-F. The results for these configurations show that the convergence is achieved at about $P = 100$ for $\beta_0 = 10^{-1}$, and at about $P = 2000$ for $\beta_0 = 10^{-3}$. For $\beta_0 = 10^{-5}$, the superfast solver requires very high orders of about $P = 10^5$ to converge. Then, it is clear that good performance is achieved with reasonable approximation orders for moderately high regularization factors, but very high orders are required for low regularizations levels. However, we discussed in Section 3.6.2 that the filters for practical PSZ systems must be computed with moderately high regularization factors to assure the robustness of the system. Particularly, the results in Section 3.6.2 indicated that $\beta_0 = 10^{-3}$ is an appropriated choice for the considered PSZ system. Hence, an approximation order P of about 2000 for the superfast solver is a reasonable selection for the considered PSZ system. Then, the superfast solver can be a good option to compute the filters in practical systems because it can obtain approximately equal performance than the Cholesky solver with reasonable approximation orders. It is important to highlight that the required approximation order is scenario dependent.

3.6.4 Computational complexity

Finally, we evaluate the computational complexity of the studied solvers to compute the wPM-T filters for a system with 8 loudspeakers. We show in Fig. 3.4a and 3.4b the number of FLOPs and the computation time, respectively, required by each solver as a function of the filter length. For the superfast solver, we consider three approximation orders, i.e., $P = 2000$, $P = 4000$, and $P = 8000$. For comparison purposes, the computational

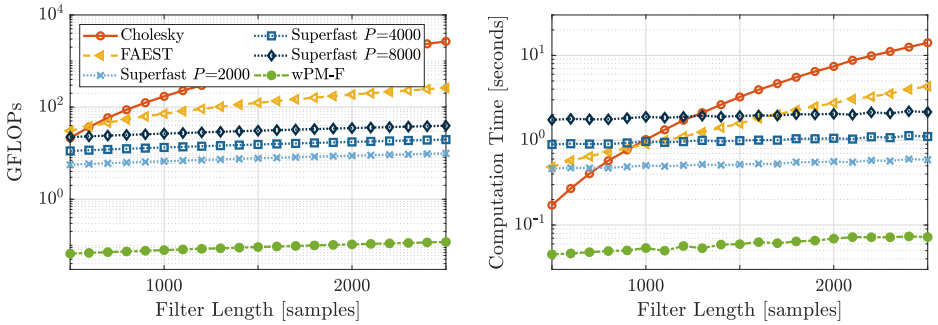

(a) FLOPs **(b)** Computation time

Figure 3.4: Number of FLOPs and computation time in (a) and (b), respectively, required by the Cholesky, the FAEST, and the superfast [79] solvers to compute the optimal filters for wPM-T. For comparison purposes, we also include the computational complexity for wPM-F.

efforts required by wPM-F are also included. The operation count for the different solvers can be found in Appendix A.1. To measure the computation time, the solvers were implemented with C language, as described in Appendix A.1, and ran from MATLAB R2018a using *mex* functions [96] on an Intel Core i7-7700 processor at 3.60 GHz. The measurement was computed as the mean over 50 executions. First, it is relevant to note that wPM-F is significantly less computationally demanding than wPM-T (with any of the considered solvers). For short filters, the Cholesky solver requires similar number of FLOPs to the other solvers, but for longer filters it requires significanly more FLOPs. FAEST can efficiently reduce the computational demands of the Cholesky solver for filters longer than about $I_{\mathrm{g}} = 750$. For example, for $I_{\mathrm{g}} = 2500$, FAEST requires about 10 times less FLOPs than the Cholesky solver. Regarding the superfast solver, the results reveal that it requires lower number of FLOPs than the Cholesky and the FAEST solvers for all the considered approximation orders and filter lengths. In particular, the superfast solver with $P = 2000$ requires about 270 and 27 times less FLOPs than the Cholesky and the FAEST solvers, respectively, for $I_{\mathrm{g}} = 2500$. The computation time measurements in Fig. 3.4b show slightly different trends to those in Fig. 3.4a, especially for the superfast solver. Particularly, the results indicate that the computational improvements offered by the superfast solver with respect to the other solvers appear for larger filter lengths than those expected from the

FLOPs estimation. This may be produced because other computational aspects than the number of FLOPs have a significant influence on the running time of the superfast solver, e.g., memory access and displacements. In any case, for the considered approximation orders, the superfast solver [79] offers important computational reductions when long filters are considered. Then, we can conclude that the superfast solver, and to a lower extent the FAEST solver, can lighten the computational demands required to compute the filters for wPM-T, especially when long filters are considered.

3.7 Summary

In this chapter, we discussed and evaluated different solvers for computing the optimal filters for wPM-T. First, we studied the Least Squares problem related to wPM-T, and reviewed the state-of-the-art solvers for this kind of problem. Next, we studied how to compute the optimal solution with three different solvers, which were suitably selected as good representatives of the main families of solvers: 1) a classic solver based on the Cholesky factorization; 2) the Fast a Posteriori Error Sequential Technique (FAEST); and 3) the superfast solver proposed by Poletti and Teal [79]. Later, the accuracy of the solvers, their influence on the performance of a PSZ system, and their computational demands were experimentally evaluated. The Cholesky solver presents the highest accuracy and the lowest sensitivity to aspects as the regularization factor or the round-off errors that appear in finite-size arithmetic. However, it requires very high computational demands to obtain the optimal solution. The presented results show that FAEST can reduce to a great extent the computational requirements of the Cholesky solver when long filters are considered. Also, FAEST achieves great accuracy and leads to the same performance as the Cholesky solver if reasonable regularization factors for a practical PSZ system are considered. Still, FAEST diverges when extremely low regularization factors are used due to the round-off errors. For the superfast solver [79], which is an approximate solver, the approximation order required to get similar performance to the Cholesky solver decreases by increasing the regularization factor. The evaluation results show that the superfast solver can obtain good performance with reasonable approximation orders for the regularization factors typically considered for practical PSZ systems. Still, it is important to note that the required approximation order is scenario-specific, so it has

to be determined in each case. The presented results also indicate that the superfast solver can notably reduce the computational requirements of the Cholesky and FAEST solvers when reasonable approximation orders and long filters are considered. Then, the superfast solver seems a good candidate to compute the wPM-T filters for practical PSZ systems in reverberant environments, since it can obtain good accuracy and affordable computational demands. In any case, we also showed that the computational complexity for wPM-T with any of the considered solvers is notably higher than for wPM-F.

Chapter 4

Subband filtering for PSZ systems

An important aspect of PSZ systems in real-world scenarios is that long broadband filters must be used due to the room reverberation [97]. This can be a serious limitation when real-time filtering is needed but the available computational capabilities in the system are limited [98]. Also, some PSZ systems present strong latency requirements, e.g., systems used together with other audiovisual content or systems used for bidirectional telecommunication applications. We showed in Chapter 2 that wPM-T is better suited than wPM-F for these kind of systems, as it leads to significantly better performance for short system delays (especially at low frequencies). However, wPM-T requires a high computational effort for computing the filters of the system, as shown in Chapter 3. This is not a major limitation for static PSZ systems, where the filters can be computed offline. Nevertheless, for dynamic PSZ systems, the filters must be recalculated regularly to adapt to changes in the position of the users or in the environment, among others [53]. In this case, the high computational demands of wPM-T can be an important limitation. Then, it seems that neither wPM-F nor wPM-T are good approaches for dynamic PSZ systems, as one requires low computational demands for computing the filters but presents bad performance for short system delays, and the other presents good performance for short system delays but at the cost of high computational demands. Consequently, PSZ systems would benefit from an alternative approach that offers good performance for short system delays and that requires low computational demands.

The computational demands of a PSZ system can be reduced using filter bank structures [99], since the signals can be processed independently in the subbands of the filter bank at a lower sampling rate. Moreover, PSZ systems may benefit from applying different signal processing techniques in each subband of the filter bank, because the signals and impulse responses handled by the system do not have the same properties across all the spectrum. So and Choi [47] proposed using multi-stage Quadrature Mirror Filters (QMF) for PSZ systems. The proposed approach can effectively reduce the computational requirements of the system, however, it presents bad performance in the edges of the subbands. This is caused by the high aliasing levels of the QMF structure, which is a critically-sampled filter bank. In this chapter, we propose using a Generalized Discrete Fourier Transform (GDFT) filter bank [100] together with a set of subband filters to filter the input signals of the PSZ system. Previous studies showed the effectiveness of oversampled GDFT filter banks to perform acoustic echo cancellation [100] and room equalization [101], among others. In addition, we propose a subband formulation for PSZ that makes use of the subband decomposition algorithm presented in [102]. The proposed formulation has the main advantage that allows us to formulate an independent optimization for each subband of the filter bank. To compute the subband filters, we propose the weighted Pressure Matching with Subband-Domain Formulation (wPM-S) algorithm, which applies a wPM criterion in time-domain in each subband.

In this chapter, we first review the basic filter bank theory that is of concern for this work. Then, the decomposition of a signal in its subband components proposed in [102] is studied. In order to reduce the computational demands of this method, alternative expressions for computing the subband components are presented. Afterwards, we propose a subband formulation for PSZ systems that employs a GDFT filter bank, which is later used to propose the wPM-S algorithm. The proposed algorithm is experimentally evaluated in a real room with $T_{60} = 500$ ms. First, the influence of the configuration of the filter bank in the performance of the proposed algorithm is studied. Also, the proposed algorithm is compared with wPM-T, wPM-F, and with the algorithm proposed in [47]. Afterwards, the versatility of the proposed algorithm to select different filter lengths, loudspeaker configurations, and LS solvers in each subband is evaluated. Finally, the computational complexity of the algorithms is compared.

4.1 Filter bank theory

A common phenomenon in many signal processing systems is that the signals handled by the system do not have the same properties across all the spectrum. Then, it is convenient to apply different signal processing techniques to different portions of the spectrum. This can be achieved with the use of filter banks. Filter banks are structures which split the input signal into a set of subbands signals, such that each subband can be independently processed, and then, the processed signals are combined to obtain the output of the system [103]. The subband signals can be decimated before applying the specific subband processing because each subband signal only occupies a portion of the spectrum of the broadband signal [104]. This is one of the main advantages of filter banks, because the subband signals can be processed at a lower sampling rate, leading to computational and memory savings. Once the subband signals are processed, they must be interpolated to preserve the sampling rate of the input signal. Filter banks have been extensively used in a wide range of applications, e.g., audio coding [105, 106], image processing [107, 108], pattern recognition [109, 110], and digital communications [111, 112]. In the context of audio signal processing, the computational savings offered by filter banks are of special interest in applications where the input signal needs to be processed using high order filters. In that case, the high order filters can be replaced by a set of shorter subband filters in the subbands of the filter bank. This approach is usually called subband filtering, and it has been used in applications such as room equalization [101, 113], echo cancellation [114, 115], and active noise control [116, 117], among others. In this work, we study the use of subband filtering for PSZ systems. Systems using filter banks are usually called multirate systems, as they are formed by components operating at different sampling rates. Extensive works regarding the main fundamentals of filter bank theory and multirate signal processing can be found in [99, 118, 119, 120]. In this section, we briefly review the basic properties of filter banks that are relevant to this work.

4.1.1 Basic multirate operations

The basic building blocks used in multirate systems are the decimator and the interpolator, as they can alter the sampling rate of the signals [99]. We use $(\cdot)_{\downarrow R}$ and $(\cdot)_{\uparrow R}$ to denote decimation and interpolation, respectively.

(a) Decimator **(b)** Interpolator

Figure 4.1: Block diagram of a decimator and an interpolator in (a) and (b), respectively.

The decimator, shown in Fig. 4.1a, reduces the sampling rate of an input signal by a factor $R \in \mathbb{N}$. Then, it only retains in the output signal $y(n)$ every R-th sample of the input signal $x(n)$, i.e.,

$$y(n) = (x(n))_{\downarrow R} = x(nR). \tag{4.1}$$

This operation can be alternatively expressed in the z-domain as [99]

$$Y(z) = \frac{1}{R} \sum_{i=0}^{R-1} X(z^{1/R} \Phi_R^i), \tag{4.2}$$

where $z = e^{j\omega}$ for $0 \leq \omega < 2\pi$, $\Phi_R^i = e^{-j\frac{2\pi i}{R}}$, and $X(z)$ and $Y(z)$ are the z-transforms of $x(n)$ and $y(n)$, respectively. In (4.2), $X(z^{1/R})$ represents the spectrum of $X(z)$ stretched by a factor R. Then, the spectrum of the decimated signal $Y(z)$ is formed by superimposing R copies of $X(z^{1/R})$, each one shifted by multiples of 2π. If the input signal is not properly band limited, spectral overlapping appears between the different copies of the input signal. This phenomenon is commonly known as aliasing [119], which produces an undesired and uncontrolled modification of the original spectrum. This effect is illustrated in Fig. 4.2, where the left and right columns present examples of decimation without and with aliasing, respectively. To avoid aliasing, filters are generally used prior to decimation to make sure that the input signal is band limited. In the following sections, we will show that the aliasing produced by the decimator is a key aspect for the design of filter banks.

The interpolator, shown in Fig. 4.1b, increases the sampling rate of an input signal by a factor $R \in \mathbb{N}$. Thus, it inserts $R - 1$ zeros between consecutive samples of the input signal, i.e.,

$$y(n) = (x(n))_{\uparrow R} = \begin{cases} x\left(\frac{n}{R}\right) & \text{if } n = rR \\ 0 & \text{otherwise} \end{cases}, \quad r \in \mathbb{Z}, \tag{4.3}$$

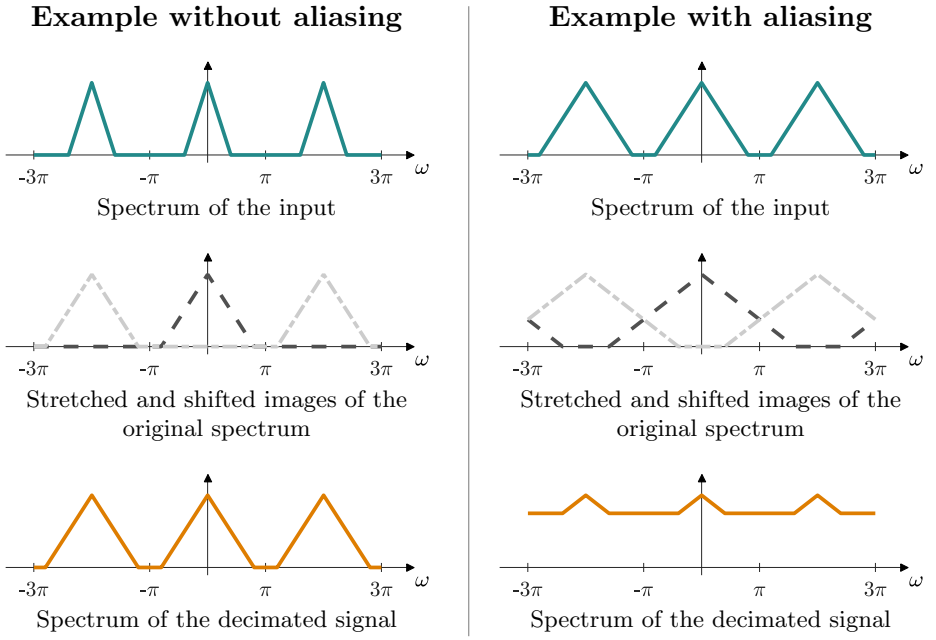

Figure 4.2: Schematic to illustrate the effect of the decimation operation in the spectrum of an input signal. The cases without and with aliasing are illustrated in the left and right columns, respectively. A decimation factor $R = 2$ is considered.

which in the z-domain can be expressed as [99]

$$Y(z) = X(z^R). \tag{4.4}$$

In the previous expression, $X(z^R)$ represents the spectrum of $X(z)$ compressed by a factor R. Due to the compression of the frequency axis and to the periodicity of the spectrum, undesired copies of $X(z)$ can appear in the spectrum of $Y(z)$ [119]. These undesired copies can be suppressed by filtering the signal at the output of the interpolator.

The decimator (4.1) and the interpolator (4.3) are linear time-varying systems. However, a system formed by a decimator followed by an interpolator, both with the same sampling factor R, is a linear R-periodically time-varying system [118].

4.1.2 Filter bank analysis

We show in Fig. 4.3 the basic block diagram of a filter bank with $K \in \mathbb{N}$ subbands and resampling factor $R \in \mathbb{N}$ [99]. The filter bank structure is formed by the analysis and synthesis filter banks, and between them, the subband processing blocks are placed. In the analysis filter bank, a band-pass filter u_k followed by a decimator is used in each subband to compute the subband signals $\widetilde{x}_k$. The band-pass filter assures that the input signal x is properly band limited and the decimator reduces the sampling rate of the subband signals. The signals at the output of the analysis filter bank are processed using the subband filters c_k, and then, are fed to the synthesis filter bank. In the synthesis filter bank, an interpolator followed by a band-pass filter v_k is used in each subband, and then, the outputs of all subbands are combined to obtain the output signal y. The interpolator increases the sampling rate of the subband signals to match the original sampling rate, and the band-pass filter removes any undesired copies of the spectrum of the subband signals. Usually, the band-pass filters in the analysis and synthesis filter banks are called analysis and synthesis filters, respectively. The analysis and synthesis filters can be either FIR or IIR filters, in this work we focus in the FIR case. Usually, the signal processing required by the analysis and synthesis filter banks can be efficiently implemented using polyphase networks [121].

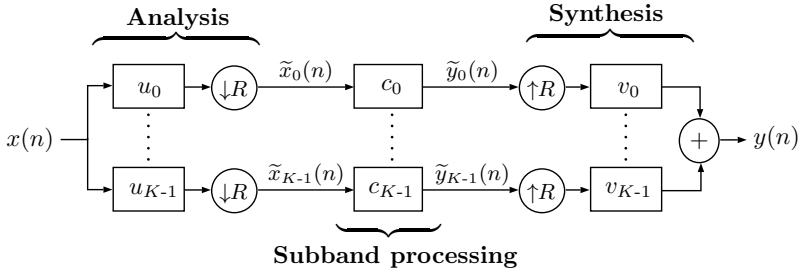

Figure 4.3: Block diagram of a filter bank with subband processing.

Now, we derive the expressions of the signals in the filter bank shown in Fig. 4.3. First, let us denote x as the input signal to the filter bank, and $X(z)$ as its z-transform. Also, let us denote $\widetilde{x}_k$ as the k-th subband signal in Fig. 4.3, i.e., the signal at the output of the k-th subband of the analysis

filter bank. Using (4.2), we can write the z-transform of $\widetilde{x}_k$ as

$$\widetilde{X}_k(z) = \frac{1}{R}\sum_{i=0}^{R-1} U_k(z^{1/R}\Phi_R^i)X(z^{1/R}\Phi_R^i), \tag{4.5}$$

where U_k is the transfer function of the analysis filter in the k-th subband. Moreover, let use define the signal after the subband processing stage in the k-th subband as $\widetilde{y}_k(n) = \widetilde{x}_k(n) * c_k(n)$, where c_k is the impulse response of the subband processing block for the k-th subband. Now, if we denote the transfer function of c_k as $C_k(z)$, we can define the z-transform of $\widetilde{y}_k$ as $\widetilde{Y}_k(z) = \widetilde{X}_k(z)C_k(z)$, which using (4.5) can be written as

$$\widetilde{Y}_k(z) = \frac{1}{R}\sum_{i=0}^{R-1} U_k(z^{1/R}\Phi_R^i)X(z^{1/R}\Phi_R^i)C_k(z). \tag{4.6}$$

In addition, the signal at the output of the filter bank is denoted as y and its z-transform can be defined as

$$Y(z) = \sum_{k=0}^{K-1} \widetilde{Y}_k(z^R)V_k(z), \tag{4.7}$$

which using (4.6) can be re-written as

$$Y(z) = \frac{1}{R}\sum_{i=0}^{R-1}\sum_{k=0}^{K-1} U_k(z\Phi_R^i)C_k(z^R)V_k(z)X(z\Phi_R^i). \tag{4.8}$$

Next, we analyse different properties of filter banks that are related to the previous expressions.

Aliasing in the subbands

We previously defined the subband signal in the k-th subband in (4.5), where $U_k(z)X(z)$ is the signal at the output of the analysis filter for the k-th subband and before the decimator. As we discussed in Section 4.1.1, aliasing can appear after decimation if $U_k(z)X(z)$ is not properly band-limited. To further study this aspect, let us write (4.5) as

$$\widetilde{X}_k(z) = \frac{1}{R}U_k(z^{1/R})X(z^{1/R}) + \frac{1}{R}\sum_{i=1}^{R-1} U_k(z^{1/R}\Phi_R^i)X(z^{1/R}\Phi_R^i), \tag{4.9}$$

where the second term is the aliasing component that appears in the subbands after decimation. Now, we can re-write (4.9) as

$$\widetilde{X}_k(z) = \frac{U_k(z^{1/R})}{R}\left(X(z^{1/R}) + \sum_{i=1}^{R-1}\frac{U_k(z^{1/R}\Phi_R^i)X(z^{1/R}\Phi_R^i)}{U_k(z^{1/R})}\right). \quad (4.10)$$

Since $U_k^{-1}(z) = U_k^*(z)/\left|U_k(z)\right|^2$, (4.10) can be expressed as

$$\widetilde{X}_k(z) = \frac{U_k(z^{1/R})}{R}\left(X(z^{1/R}) + \sum_{i=1}^{R-1}\frac{U_k^*(z^{1/R})U_k(z^{1/R}\Phi_R^i)X(z^{1/R}\Phi_R^i)}{\left|U_k(z^{1/R})\right|^2}\right). \quad (4.11)$$

From (4.11), we can see that the aliasing is completely removed in the subbands if the analysis filters are designed such that

$$U_k^*(z)U_k(z\Phi_R^i) = 0, \quad \text{for} \begin{cases} 0 \le k < K \\ 1 \le i < R \end{cases}, \quad (4.12)$$

i.e., if the spectrum of the analysis filters do not overlap for shifts of $2\pi i/R$. Then, aliasing can be avoided (or at least minimized) if the analysis filters are properly designed band-pass filters. From now on, we refer to $U_k(z\Phi_R^i)$ for $1 \le i < R$ as the images of the analysis filter $U_k(z)$.

Input-output relation

Next, we derive the input-output relation for the generic filter bank shown in Fig. 4.3. The input-output relation is the transfer function that relates the input and the output of the filter bank when no processing is performed in the subbands [122], i.e., when $C_k(z) = 1\,\forall k$. From (4.8), and taking into account that $C_k(z) = 1$, we can write the input-output relation as

$$Y(z) = \frac{1}{R}\sum_{i=0}^{R-1}\sum_{k=0}^{K-1}U_k(z\Phi_R^i)V_k(z)X(z\Phi_R^i). \quad (4.13)$$

Now, let us define the distortion transfer function of the filter bank [118] as

$$T(z) = \frac{1}{R}\sum_{k=0}^{K-1}U_k(z)V_k(z), \quad (4.14)$$

and the gain of the i-th aliasing component [122] as

$$A_i(z) = \frac{1}{R}\sum_{k=0}^{K-1} U_k(z\Phi_R^i)V_k(z), \quad \text{for } 1 \leq i < R. \tag{4.15}$$

Then, using (4.13) to (4.15), we can re-write the input-output relation as

$$Y(z) = T(z)X(z) + \sum_{i=1}^{R-1} A_i(z)X(z\Phi_R^i). \tag{4.16}$$

From the previous expression, we can see that the input-output relation gives us an inside about how well the filter bank is able to reconstruct the input signal when no processing is performed in the subbands. By inspecting (4.16), we can notice that the phase and the amplitude of the input signal are altered by $T(z)$, and that the aliasing gain terms $A_i(z)$ produce undesired additive components in the output. For the case without subband processing, the filter bank preserves the magnitude and the phase of the input signal when the distortion transfer function has constant magnitude and linear phase at all frequencies, i.e., $T(z) = \rho_{\mathrm{f}}\, z^{-\tau_{\mathrm{f}}}$. In addition, for the case without subband processing, the output of the filter bank is alias free if $A_i(z) = 0$, for $1 \leq i < R$. At this point, it is important to clarify that a filter bank with alias-free input-output relation is not necessarily a filter bank without aliasing in the subbands [118]. This is because the analysis and synthesis filters can be designed such that aliasing is cancelled out at the output of the filter bank, but it is still present in the subbands. According to the properties of the input-output relation, we classify the filter banks in two main categories:

- **Perfect-Reconstruction (PR)**: filter banks that have distortionless transfer function and alias-free output [118], i.e.,

$$\begin{aligned} T(z) &= \rho_{\mathrm{f}}\, z^{-\tau_{\mathrm{f}}}, \\ A_i(z) &= 0, \quad \text{for } 1 \leq i < R, \end{aligned} \tag{4.17}$$

  where ρ_{f} and τ_{f} are arbitrary scaling and delay components, respectively. These filter banks can not achieve very low aliasing levels in the subbands, however, the analysis and synthesis filters can be designed such that the effect of the aliasing in the subbands is cancelled

at the output of the filter bank (when no subband processing is considered). When the PR conditions (4.17) are met and there is not subband processing, the filter bank is a Linear Time-Invariant (LTI) system, since $Y(z) = \rho_{\mathrm{f}} X(z)\, z^{-\tau_{\mathrm{f}}}$. Among others, QMF are PR filter banks [123].

- **Near Perfect-Reconstruction (NPR)**: filter banks in which low aliasing in the subbands is achieved at the cost of relaxing the perfect reconstruction conditions [124], i.e.,

$$\begin{aligned} T(z) &\approx \rho_{\mathrm{f}}\, z^{-\tau_{\mathrm{f}}}, \\ A_i(z) &\approx 0, \quad \text{for } 1 \leq i < R, \\ U_k^*(z) U_k(z\Phi_R^i) &\approx 0, \quad \text{for } \begin{cases} 0 \leq k < K \\ 1 \leq i < R \end{cases}. \end{aligned} \tag{4.18}$$

  Then, negligible aliasing in the subbands, with low distortion and low aliasing at the output of the filter bank are obtained. In this case, the filter bank is a linear R-periodically time-varying system [118]. Properly designed GDFT filter banks are NPR filter banks [125].

Effect of subband processing in the output signal

Now, we study the influence of the subband processing stage in Fig. 4.3 in the output of the filter bank. First, let us assume that the analysis and synthesis filters are conjugated and delayed versions of each other, i.e., $V_k(z) = U_k^*(z) z^{-\tau_{\mathrm{f}}}$. This is a reasonable assumption that is fulfilled by most filter banks, e.g., QMF, cosine modulated, and GDFT filter banks [122]. If the previous assumption is considered, the expression for the output of the filter bank (4.8) can be written as

$$Y(z) = \frac{1}{R} \sum_{i=0}^{R-1} \sum_{k=0}^{K-1} U_k(z\Phi_R^i) C_k(z^R) U_k^*(z) X(z\Phi_R^i) z^{-\tau_{\mathrm{f}}}, \tag{4.19}$$

which can be re-written as

$$\begin{aligned} Y(z) = &\left(\frac{1}{R} \sum_{k=0}^{K-1} U_k(z) U_k^*(z) C_k(z^R) \right) X(z) z^{-\tau_{\mathrm{f}}} + \\ &\sum_{i=1}^{R-1} \left(\frac{1}{R} \sum_{k=0}^{K-1} U_k^*(z) U_k(z\Phi_R^i) C_k(z^R) \right) X(z\Phi_R^i) z^{-\tau_{\mathrm{f}}}. \end{aligned} \tag{4.20}$$

The second term in (4.20) represents the aliasing at the output of the filter bank when subband processing is considered. In this case, even if the gain of the aliasing terms is 0, i.e., $A_i(z) = 0$, the aliasing at the output of the filter bank may not be suppressed, due to the effect of the subband processing blocks. In particular, aliasing at the output of the filter bank is avoided only if (4.12) is fulfilled, i.e., if there is no aliasing in the subbands. Later on, we will show that (4.12) can not be strictly fulfilled by any set of finite length analysis filters. Still, some filter banks can approximately fulfill (4.12), i.e.,

$$U_k^*(z)U_k(z\Phi_R^i) \approx 0, \quad \text{for} \quad \begin{cases} 0 \leq k < K \\ 1 \leq i < R \end{cases}. \tag{4.21}$$

If the previous assumption is fulfilled, we can assume that the aliasing in the subbands is negligible, and then, (4.20) can be approximated as

$$Y(z) \approx \left(\frac{1}{R} \sum_{k=0}^{K-1} U_k(z)U_k^*(z)C_k(z^R) \right) X(z)z^{-\tau_\mathrm{f}}. \tag{4.22}$$

Hence, filter banks with very low aliasing levels in the subbands, i.e., (4.21), can obtain negligible aliasing at the output of the filter bank, even if subband processing is used. Consequently, filter banks with low aliasing levels in the subbands are better suited for systems with subband processing [122]. In general, PR filter banks do not offer low aliasing levels in the subbands, thus, NPR filter banks, which fulfil (4.21), are preferred when subband processing is used. Finally, it is important to note that any filter bank with subband processing and finite length analysis and synthesis filters is not a LTI system, as (4.22) only holds approximately. In that case, the system becomes a linear R-periodically time-varying system.

4.1.3 Design considerations

Next, we discuss different aspects regarding the design of filter banks.

Subband types

Filter banks can be designed with uniform and non-uniform subbands. For the uniform case, the analysis and synthesis filters have the same bandwidth for all subbands, while different bandwidths are selected for each subband in the non-uniform case [126]. Filter banks with non-uniform subbands can

be achieved by appending multiple analysis stages with uniform subbands in a tree structure [127]. In this work, we focus on filter banks with uniform subbands, which is the relevant case for this study. According to the portion of the spectrum assigned to each subband, we can classify the subbands as:

- **Single-sided (SS) subbands**: The analysis and synthesis filters are single-sided band-pass filters, i.e., with complex coefficients. Then, the subband signals are complex signals containing information from either the positive or negative sides of the spectrum. If ideal filters are assumed, the magnitude of the frequency response of the analysis and synthesis filters in the k-th subband is

$$\left|U_k(e^{j\omega})\right| = \left|V_k(e^{j\omega})\right| = \begin{cases} 1 & \text{if } \frac{2\pi k}{K} \leq \omega \leq \frac{2\pi(k+1)}{K} \\ 0 & \text{otherwise} \end{cases}, \tag{4.23}$$

  where K is the number of SS subbands in the filter bank. For example, SS subbans are used in GDFT filter banks [128].

- **Double-sided (DS) subbands**: The analysis and synthesis filters are double-sided band-pass filters, i.e., with real coefficients. Thus, if the input signal is real, the subband signals are real and contain information from both, the positive and negative sides of the spectrum. If ideal filters are assumed, the magnitude of the frequency response of the analysis and synthesis filters in the k-th subband is

$$\left|U_k(e^{j\omega})\right| = \left|V_k(e^{j\omega})\right| = \begin{cases} 1 & \text{if } \frac{\pi k}{K_{\text{ds}}} \leq |\omega| \leq \frac{\pi(k+1)}{K_{\text{ds}}} \\ 0 & \text{otherwise} \end{cases}, \tag{4.24}$$

  where K_{ds} is the number of DS subbands in the filter bank. For example, DS subbans are used in cosine modulated filter banks [99].

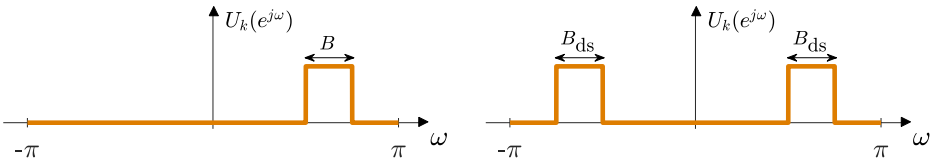

(a) Single-sided **(b)** Double-sided

Figure 4.4: Spectrum of single-sided (SS) and double-sided (DS) analysis filters in (a) and (b), respectively.

We show in Fig. 4.4a-b examples of the spectrum of SS and DS analysis filters, respectively. We assume that the bandwidth of the DS subbands is equal to the bandwidth of the SS subbands, i.e., $B_{\text{ds}} = B$. Then, each DS subband can be seen as the combination of two SS subbands. Thus, it is obvious that the number of DS subbands is half the number of SS subbands, i.e, $K_{\text{ds}} = K/2$. Moreover, as the portion of the spectrum occupied by a DS subband is twice the portion occupied by a SS subband, the resampling factor for the DS case is limited to $R_{\text{ds}} \leq K_{\text{ds}} = K/2$, while for the SS case to $R \leq K$. Also, let us note that if the SS subbands are designed such that the subbands in the positive and negative sides of the spectrum have hermitian symmetry, only $K/2$ subbands must be processed.

We previously studied that aliasing in the subbands is avoided if the spectrum of the analysis filters does not overlap with its images, i.e., if (4.12) is fulfilled. An important difference regarding aliasing in the subbands can be found between SS and DS subbands. For SS subbands, (4.12) is fulfilled if $R \leq K$ and $B \leq \frac{2\pi}{R}$ (at least, if ideal band-pass filters are considered). For DS subbands, (4.12) is not fulfilled in all cases, even if $R_{\text{ds}} \leq K_{\text{ds}}$ and $B_{\text{ds}} \leq \frac{\pi}{R_{\text{ds}}}$ [100]. To exemplify this phenomenon, we show in Fig. 4.5 the spectrum of the analysis filters and their images for a filter bank with DS subbands, $K_{\text{ds}} = 4$, $R_{\text{ds}} = 3$, and $B_{\text{ds}} = \frac{\pi}{K_{\text{ds}}}$. Also, we show in Fig. 4.6 the spectrum of the analysis filters and their images for a filter bank with SS subbands, $K = 8$, $R = 6$, and $B = \frac{2\pi}{K}$. It is clear that spectral overlap does not appear in any case for the SS subbands in

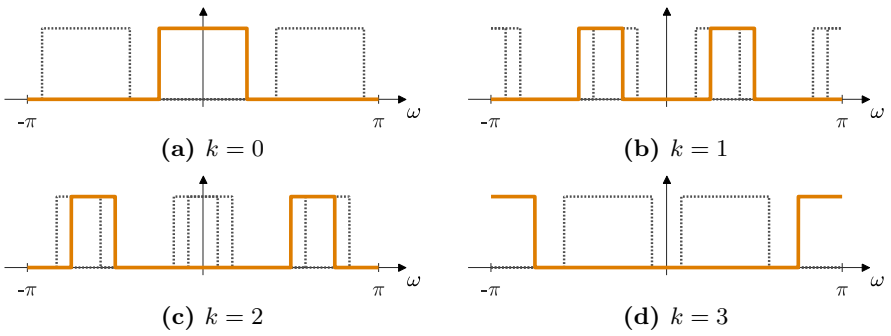

Figure 4.5: Spectrum of the analysis filter $U_k(e^{j\omega})$ in solid lines and its images $U_k(e^{j\omega}\Phi^i_{R_{\text{ds}}})$ in dotted lines for each DS subband of a filter bank with $K_{\text{ds}} = 4$, $R_{\text{ds}} = 3$, and $B_{\text{ds}} = \frac{\pi}{K_{\text{ds}}}$.

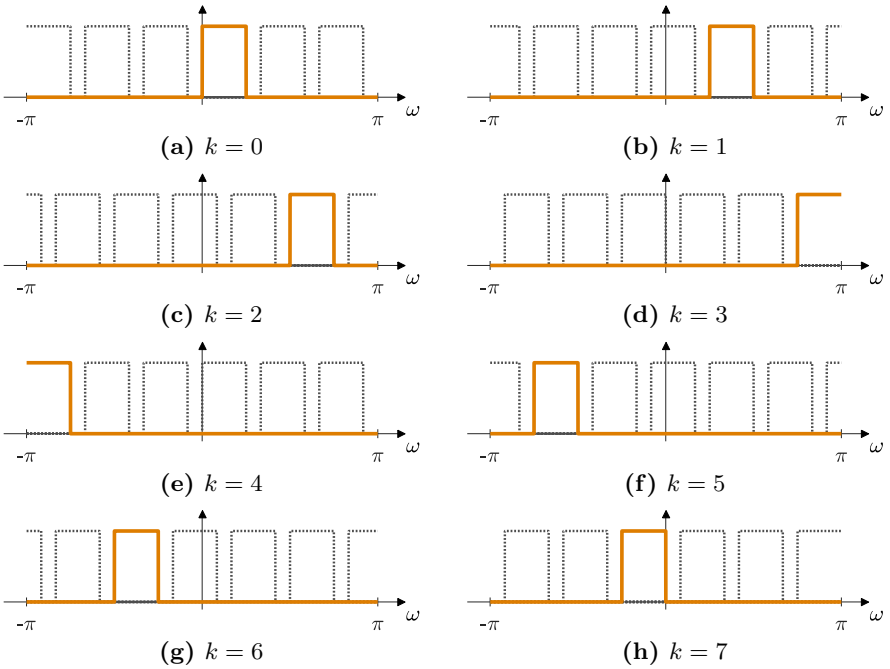

Figure 4.6: Spectrum of the analysis filter $U_k(e^{j\omega})$ in solid lines and its images $U_k(e^{j\omega}\Phi_R^i)$ in dotted lines for each SS subband of a filter bank with $K = 8$, $R = 6$, and $B = \frac{2\pi}{K}$.

Fig. 4.6. For the DS subbands in Fig. 4.5, spectral overlap does not occur for subbands $k = 0$ and $k = 3$, but it does for $k = 1$ and $k = 2$. Then, high levels of aliasing appear in these subbands. We showed in Section 4.1.2 that high aliasing in the subbands is a serious limitation for subband processing systems, then, single-sided subbands are preferred for these systems.

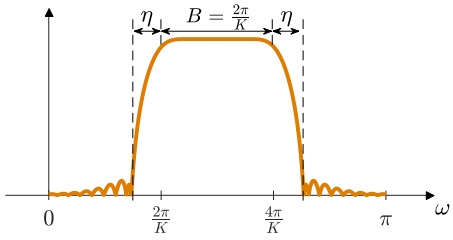

Figure 4.7: Frequency response of a finite length band-pass filter.

Resampling factor

The resampling factor R is a key aspect in the design of the filter bank. Next, we focus on the selection of the resampling factor for filter banks with SS subbands, which is the case that is relevant to this work.

Previously, we considered that the magnitude of the frequency response of the analysis filters is given by (4.23), i.e., with a passband with bandwidth $B = 2\pi/K$ and a stopband with infinite attenuation. However, infinite length filters are required to fulfil (4.23), which is not feasible for practical systems. Hence, (4.23) must be relaxed for finite length filters as

$$\left|U_k(e^{j\omega})\right| \approx \begin{cases} 1 & \frac{2\pi k}{K} - \eta \leq \omega \leq \frac{2\pi(k+1)}{K} + \eta \\ 0 & \text{otherwise} \end{cases}. \tag{4.25}$$

This response has a passband with bandwidth $B = 2\pi/K$, and a transition bandwidth η between the passband and the stopband (as shown in Fig. 4.7). Moreover, the passband of the filter is not completely flat and the attenuation in the stopband is not infinite. Consequently, (4.12) can not be strictly fulfilled, and then, the aliasing in the subbands can not be exactly 0. However, (4.21) can be fulfilled if the passband of the analysis filters only overlaps with the stopband of their images. In this case, we can assume that the aliasing in the subbands is negligible. To clarify this aspect, we show in Fig. 4.8 the spectrum of a practical analysis filter and its images for the second subband of a filter bank with $K = 8$ and two different resampling factors. We can see in Fig. 4.8a that, for $R = 5$, the passband of the analysis filter only overlaps with the stopbands of its images, then, very low aliasing levels appear in the subbands. However, the passband of the analysis filter overlaps with the transition bandwidth of its images for $R = 8$ (as shown in Fig. 4.8b), which leads to significant aliasing levels in the subbands. Then, it is clear at this point that the selected resampling factor heavily influences the level of aliasing in the subbands of the filter bank. It can be proven that the aliasing in the subbands is negligible when $R \leq \lfloor 2\pi / (B + \eta) \rfloor$, or equivalently, when $R \leq \lfloor K / (1 + (\eta K/(2\pi))) \rfloor$ [102]. Filter bank configurations that do not fulfil the previous condition present high aliasing levels in the subbands.

The ratio between the number of subbands and the resampling factor, i.e., K/R, is defined as the oversampling ratio of the filter bank [122]. Filter banks with $K/R > 1$ are oversampled filter banks [128], while filter banks with $K/R = 1$ are critically-sampled filter banks [99]. Oversampled

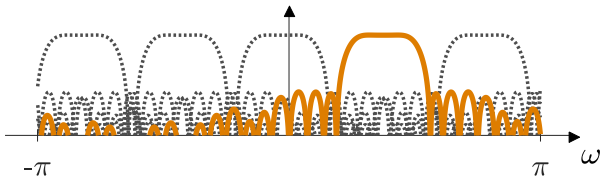

(a) $R = 5$

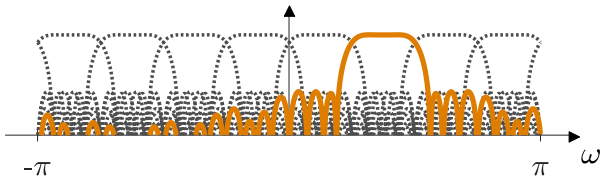

(b) $R = 8$

Figure 4.8: Spectrum of a finite length analysis filter $U_k(e^{j\omega})$ and its images $U_k(e^{j\omega}\Phi_R^i)$ for the second subband of a filter bank with $K = 8$ subbands, and for two resampling factors R.

filter banks do not reduce the sampling rate of the subband signals as much as critically-sampled filter banks, which leads to higher computational requirements to process the subband signals. However, oversampled filter banks, with a proper selection of R, can assure negligible aliasing in the subbands, while critically-sampled filter banks usually present higher aliasing levels. Then, oversampled filter banks are preferred for systems with subband filtering.

4.1.4 Generalized Discrete Fourier Transform filter bank

Next, we discuss the main properties of Generalized Discrete Fourier Transform (GDFT) filter banks, which use single-sided subbands [128]. The main advantage of GDFT filter banks is that the NPR conditions (4.18) can be fulfilled by properly designing the analysis and synthesis filters, and by selecting a suitable resampling factor [100]. Consequently, negligible aliasing in the subbands can be obtained. This is the motivation for using GDFT filter banks in this work for the subband formulation of PSZ systems.

In Fig. 4.9, we show the block diagram of a GDFT filter bank with K subbands and resampling factor $R \leq K$, where u_k and v_k denote the analysis and synthesis filters for the k-th subband, respectively. In this work, we

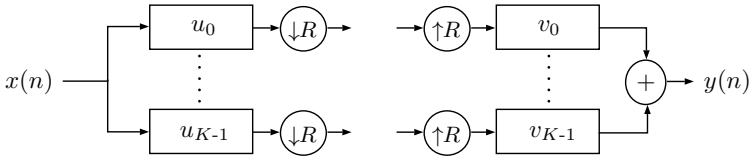

Figure 4.9: Block diagram of a GDFT filter bank.

focus on the case with even number of subbands[1]. The analysis filters are single-sided responses (i.e., with complex coefficients), and are obtained by modulating a real-valued low-pass prototype filter $p(n)$ of length I_p as

$$u_k(n) = p(n)e^{j\frac{2\pi}{K}\left(k+\frac{1}{2}\right)n}, \tag{4.26}$$

for $0 \leq n < I_\mathrm{p}$ and $0 \leq k < K$. The prototype filter $p(n)$, whose frequency response is denoted as $P(e^{j\omega})$, should be designed to fulfil

$$\left|P(e^{j\omega})\right| \approx \begin{cases} 1 & -\left(\frac{\pi}{K}+\eta\right) \leq \omega \leq \frac{\pi}{K}+\eta \\ 0 & \text{otherwise} \end{cases}. \tag{4.27}$$

In particular, the aliasing in the subbands is avoided if the prototype filter fulfills [102]

$$R \leq \left\lfloor \frac{K}{(1+(\eta K/(2\pi)))} \right\rfloor. \tag{4.28}$$

The synthesis filters are time-reversed and conjugated versions of the analysis filters, i.e.,

$$v_k(n) = u_k^*(I_\mathrm{p}{-}1{-}n). \tag{4.29}$$

Moreover, the analysis and synthesis filters in the positive and negative spectrum are complex conjugates, i.e.,

$$u_k(n) = u_{K-1-k}^*(n), \forall k, \tag{4.30}$$

$$v_k(n) = v_{K-1-k}^*(n), \forall k. \tag{4.31}$$

Then, if the input signal x is real-valued, only $K/2$ subbands must be processed, as the other subbands are their complex conjugates. In that case, the system in Fig. 4.9 can be simplified to the one shown in Fig. 4.10.

[1]For a GDFT filter bank, K can be either even or odd. For K even, the $K/2$ subbands in the positive and negative spectrum are complex conjugates. For K odd, the $(K\text{–}1)/2$ subbands in the positive and negative spectrum are complex conjugates and the subband in the center of the spectrum is unique.

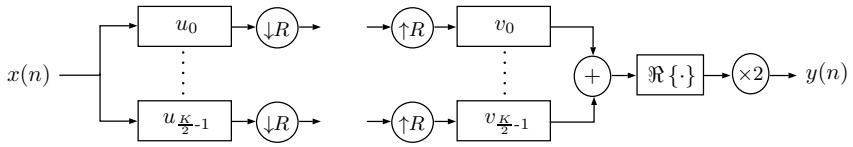

Figure 4.10: Block diagram of a GDFT filter bank with real inputs.

Finally, an important aspect of GDFT filter banks is that a computationally efficient implementation using polyphase structures is possible for any oversampling ratio fulfilling $K/R \geq 1$ [125].

4.2 Subband decomposition

In this section, we study how a Finite Impulse Response (FIR) $a(n)$ (as in Fig. 4.11a) can be approximated by a filter bank with a set of FIR subband components $a_k(n)$ inserted between the analysis and synthesis filter banks (as in Fig. 4.11b). The set of operations required to compute the subband components a_k that make the systems in Fig. 4.11a and 4.11b equivalent is called subband decomposition. We review hereafter the algorithm proposed in [102] to perform the subband decomposition of FIR systems using GDFT filter banks. Also, we propose a novel expression to compute the subband components with lower computational demands than those required by the expression proposed in [102].

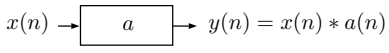

(a)

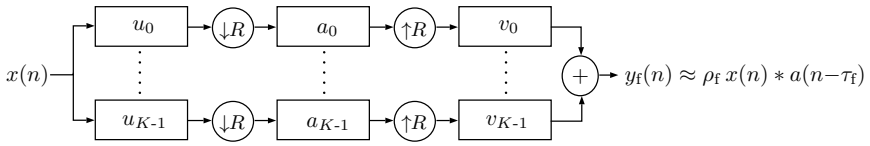

(b)

Figure 4.11: Diagram of a FIR filter $a(n)$ and its subband approximation using a filter bank in (a) and (b), respectively.

4.2.1 Sufficient conditions

Next, we review the sufficient conditions, presented in [102], required to perform the subband decomposition of a FIR system. For an input signal $X(z)$, we can write the output of the FIR system in Fig. 4.11a as

$$Y(z) = A(z)X(z), \tag{4.32}$$

where $A(z)$ is the transfer function of the FIR system. Ideally, we would like to compute the subband components in Fig. 4.11b that lead to

$$Y_{\mathrm{f}}(z) = \rho_{\mathrm{f}}\, A(z)X(z)z^{-\tau_{\mathrm{f}}}, \tag{4.33}$$

where τ_{f} is the delay produced by the filter bank, and ρ_{f} is an arbitrary amplitude scaling. If (4.33) is fulfilled, it means that the output of the system in Fig. 4.11b is a delayed and scaled version of the output of the system in Fig. 4.11a, and then, we can consider that both systems are equivalent. It is shown in [102] that equality (4.33) is only achieved when ideal analysis and synthesis filters, i.e., with infinite length, are considered. For finite length filters, the equality can only be assumed approximately. The authors in [102] showed that the approximation error can be negligible if the following conditions are fulfilled:

1. Negligible phase and amplitude distortion, i.e.,

$$T(z) = \sum_{k=0}^{K-1} U_k(z)V_k(z) \approx \rho_{\mathrm{f}}\, z^{-\tau_{\mathrm{f}}}. \tag{4.34}$$

2. Negligible aliasing level in the subbands, i.e.,

$$U_k^*(z)U_k(z\Phi_R^i) \approx 0, \quad \text{for} \quad \begin{cases} 0 \leq k \leq K-1 \\ 1 \leq i \leq R-1 \end{cases}. \tag{4.35}$$

It is easy to see that the previous conditions are the same as the ones for Near Perfect-Reconstruction in (4.18), which are fulfilled for properly designed GDFT filter banks. In particular, (4.34) is fulfilled if the prototype filter is a root-Nyquist filter [102]. Regarding (4.35), high oversampling ratios K/R and high values of I_{p} assure low aliasing levels in the subbands, but require higher computational efforts to process the subband signals.

Therefore, a compromise between K/R and I_p must be reached such that (4.35) is fulfilled while benefiting from a reduction on the computational complexity.

Finally, we present two metrics that will be used later on to determine if a specific filter bank configuration fulfils conditions (4.34) and (4.35). First, let us define the Reconstruction Error (RE) [100] as

$$\mathrm{RE} = \frac{1}{2\pi} \int_0^{2\pi} \left| T(e^{j\omega}) - \rho_\mathrm{f}\, e^{-j\omega\tau_\mathrm{f}} \right|^2 d\omega, \tag{4.36}$$

which is a metric that indicates how well a filter bank fulfills condition (4.34). Next, let us define the Alias-To-Signal Ratio (ASR) as

$$\mathrm{ASR} = \frac{\frac{1}{R-1} \sum_{k=0}^{K-1} \sum_{i=1}^{R-1} \int_0^{2\pi} \left| U_k^*(e^{j\omega}) U_k(e^{j\omega} \Phi_R^i) \right|^2 d\omega}{\sum_{k=0}^{K-1} \int_0^{2\pi} \left| U_k(e^{j\omega}) \right|^2 d\omega}, \tag{4.37}$$

which is the ratio between the energy of the aliasing terms and the energy of the analysis filters. It is easy to see that the ASR is a metric that is directly related to condition (4.35). Then, the smaller the RE and ASR, the better the approximation between the systems in Fig. 4.11a and 4.11b.

4.2.2 Optimal subband components

Next, we review the subband decomposition proposed in [102]. At this point, it is important to highlight the difference between the subband components and the subband signals. On the one hand, the subband component a_k is the FIR filter that is inserted in the k-th subband between the analysis and the synthesis filter banks, such that the overall response of the filter bank is approximately equivalent to a FIR system a of length I_a. On the other hand, the subband signal $\widetilde{a}_k$ is the signal present at the output of k-th subband of the analysis filter bank when it is fed with a, i.e.,

$$\widetilde{a}_k(n) = \left(u_k(n) * a(n) \right)_{\downarrow R}, \tag{4.38}$$

which is a signal of length $I_{\widetilde{\mathrm{a}},k} = \lceil (I_\mathrm{a}+I_\mathrm{p}-1)/R \rceil$. Both $\widetilde{a}_k$ and a_k are complex-valued because GDFT filter banks use single-sided subbands.

The authors in [102] showed that for a GDFT filter bank fulfilling (4.34) and (4.35), the subband components a_k that make the systems in Fig. 4.11a and Fig. 4.11b approximately equivalent are given by

$$a_{\text{opt},k}(n) = \underset{a_k(n)}{\arg\min} \left\{ \sum_{n\in\mathbb{Z}} \left| \widetilde{\delta}_k(n) * a_k(n) - \widetilde{a}_k(n) \right|^2 \right\}. \tag{4.39}$$

where $\widetilde{\delta}_k(n)$ is the subband signal in the k-th subband when a unit impulse $\delta(n)$ is fed to the filter bank, i.e.,

$$\widetilde{\delta}_k(n) = \left(u_k(n) * \delta(n)\right)_{\downarrow R}, \tag{4.40}$$

which is a signal of length $I_{\widetilde{\delta},k} = \lceil I_\text{p}/R \rceil$. In (4.39), the optimal subband components a_k are those that minimize the Mean Squared Error (MSE) between the subband signal $\widetilde{a}_k$ and the convolution of the subband signal $\widetilde{\delta}_k$ and the subband component a_k. We can interpret (4.39) as a de-convolution problem, in which we aim to remove the contribution of $\widetilde{\delta}_k$ from $\widetilde{a}_k$ to obtain the optimal subband components a_k. As a_k results from the de-convolution of a signal of length $I_{\widetilde{\text{a}},k}$ and a signal of length $I_{\widetilde{\delta},k}$, its length is

$$I_{\text{a},k} = I_{\widetilde{\text{a}},k} - I_{\widetilde{\delta},k} + 1 = \left\lceil \frac{I_\text{a} + I_\text{p} - 1}{R} \right\rceil - \left\lceil \frac{I_\text{p}}{R} \right\rceil + 1. \tag{4.41}$$

Now, in order to obtain the optimal solution (4.39), let us define a $I_{\text{a},k}\times 1$ vector containing all the samples of a_k as

$$\mathbf{a}_k = \begin{bmatrix} a_k(0) & \dots & a_k(I_{\text{a},k}-1) \end{bmatrix}^T. \tag{4.42}$$

Similarly, let us define a $I_{\widetilde{\text{a}},k}\times 1$ vector containing all the samples of $\widetilde{a}_k$ as

$$\widetilde{\mathbf{a}}_k = \begin{bmatrix} \widetilde{a}_k(0) & \dots & \widetilde{a}_k(I_{\widetilde{\text{a}},k}-1) \end{bmatrix}^T, \tag{4.43}$$

and a $I_{\widetilde{\text{a}},k}\times I_{\text{a},k}$ toeplitz matrix containing shifted copies of $\widetilde{\delta}_k$ as

$$\widetilde{\mathbf{\Delta}}_k = \begin{bmatrix} \widetilde{\delta}_k(0) & \dots & \widetilde{\delta}_k(I_{\widetilde{\delta},k}-1) & 0 & \dots & 0 \\ 0 & & & & & \\ \vdots & & \multicolumn{3}{c}{\textit{Toeplitz}} & \\ 0 & & & & & \end{bmatrix}^T. \tag{4.44}$$

Then, we can re-write the optimization problem(4.39) as

$$\mathbf{a}_{\text{opt},k} = \arg\min_{\mathbf{a}_k} \left\{ \left\| \widetilde{\mathbf{\Delta}}_k \mathbf{a}_k - \widetilde{\mathbf{a}}_k \right\|^2 \right\}, \tag{4.45}$$

whose optimal solution is given by [102]

$$\mathbf{a}_{\text{opt},k} = \left(\widetilde{\mathbf{\Delta}}_k^H \widetilde{\mathbf{\Delta}}_k \right)^{-1} \widetilde{\mathbf{\Delta}}_k^H \widetilde{\mathbf{a}}_k. \tag{4.46}$$

Finally, it is important to note that, if a is formed by real coefficients, the subband components a_k only need to be computed for $K/2$ subbands, due to the hermitian symmetry of the subbands in the GDFT filter bank.

4.2.3 Efficient computation

If (4.46) is used to compute the subband components, we must compute the inverse of $K/2$ complex matrices if a has real coefficients, and the inverse of K complex matrices if a has complex coefficients. Next, we derive a novel expression that only requires to compute the inverse of one real matrix. We start by re-writing $\mathbf{\Delta}_k$ as

$$\widetilde{\mathbf{\Delta}}_k = \mathbf{T}_k \mathbf{P} \mathbf{E}_k, \tag{4.47}$$

where $\mathbf{T}_k$ and $\mathbf{E}_k$ are diagonal matrices of size $I_{\widetilde{\mathrm{a}},k} \times I_{\widetilde{\mathrm{a}},k}$ and $I_{\mathrm{a},k} \times I_{\mathrm{a},k}$, respectively, which are defined as

$$\mathbf{T}_k = \text{diag}\left(\left[e^{j\frac{2\pi R}{K}\left(k+\frac{1}{2}\right)0}, \ldots, e^{j\frac{2\pi R}{K}\left(k+\frac{1}{2}\right)\left(I_{\widetilde{\mathrm{a}},k}-1\right)} \right] \right), \tag{4.48}$$

$$\mathbf{E}_k = \text{diag}\left(\left[e^{-j\frac{2\pi R}{K}\left(k+\frac{1}{2}\right)0}, \ldots, e^{-j\frac{2\pi R}{K}\left(k+\frac{1}{2}\right)\left(I_{\mathrm{a},k}-1\right)} \right] \right). \tag{4.49}$$

In (4.47), $\mathbf{P}$ is $I_{\widetilde{\mathrm{a}},k} \times I_{\mathrm{a},k}$ toeplitz matrix that is defined as

$$\mathbf{P} = \begin{bmatrix} p_{\downarrow R}(0) & \ldots & p_{\downarrow R}(I_{\widetilde{\delta},k}-1) & 0 & \ldots & 0 \\ 0 & & & & & \\ \vdots & & Toeplitz & & & \\ 0 & & & & & \end{bmatrix}^T, \tag{4.50}$$

where $p_{\downarrow R} = (p(n))_{\downarrow R}$ is the decimated prototype filter. Now, we can use (4.47) to re-write (4.46) as

$$\mathbf{a}_{\text{opt},k} = \left(\mathbf{E}_k^H \mathbf{P}^T \mathbf{T}_k^H \mathbf{T}_k \mathbf{P} \mathbf{E}_k \right)^{-1} \mathbf{E}_k^H \mathbf{P}^T \mathbf{T}_k^H \widetilde{\mathbf{a}}_k, \tag{4.51}$$

which can be finally expressed as

$$\mathbf{a}_{\mathrm{opt},k} = \mathbf{E}_k^H \left(\mathbf{P}^T\mathbf{P}\right)^{-1} \mathbf{P}^T \mathbf{T}_k^H \widetilde{\mathbf{a}}_k. \tag{4.52}$$

Equation (4.52) has the key property that the real matrix $\left(\mathbf{P}^T\mathbf{P}\right)^{-1}\mathbf{P}^T$ is common to all subbands, so only one real matrix must be inverted for computing all the subband components.

In Appendix A.3.1, we present the Floating Point Operations (FLOPs) count for the expression proposed by [102] and for the novel expression (4.52) proposed in this work. We show in Fig. 4.12 the FLOPs required by both approaches to compute the subband components of a real FIR system a as a function of its length I_a. The computational requirements are shown for different filter bank configurations, i.e, for different resampling factors R and prototype filter lengths I_p. The results show that the higher the resampling factor, the lower the computational demands of the subband decomposition. This is motivated by the fact that for high values of R the

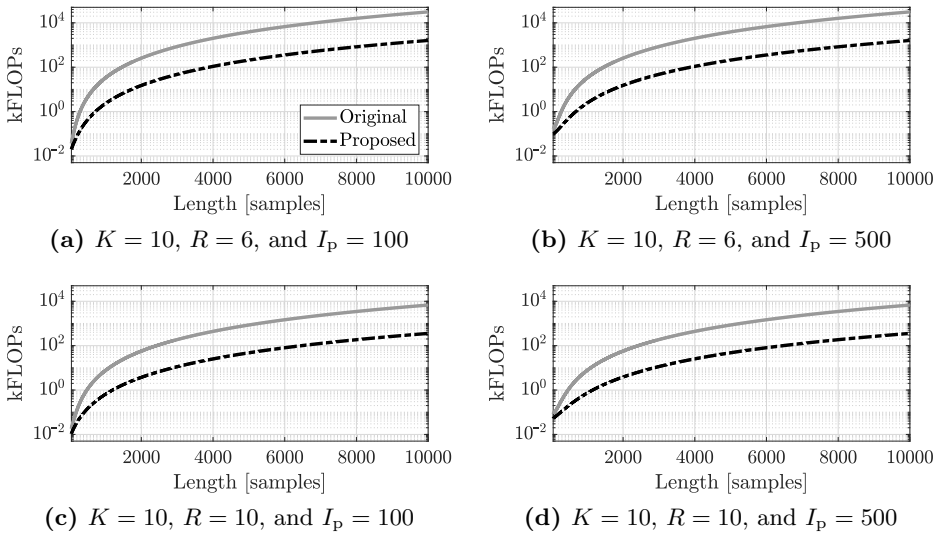

(a) $K = 10$, $R = 6$, and $I_\mathrm{p} = 100$ **(b)** $K = 10$, $R = 6$, and $I_\mathrm{p} = 500$

(c) $K = 10$, $R = 10$, and $I_\mathrm{p} = 100$ **(d)** $K = 10$, $R = 10$, and $I_\mathrm{p} = 500$

Figure 4.12: Number of FLOPs required to compute the subband decomposition of a FIR system a as a function of its length I_a for different filter bank configurations. The FLOPs required by the original expression in [102] are plotted with solid lines, and dashed-dotted lines are used for the proposed expression in (4.52).

length of the subband components (4.41) is low. Also, the results reveal that the length of the prototype filter does not have an important influence on the computational requirements. Finally, we can see that the proposed expression requires approximately $2K$ times less FLOPs than the original expression. Then, the proposed expression can significantly reduce the computational demands required to compute the subband decomposition.

4.3 Optimization of subband filters for PSZ

In previous chapters, we have considered a system model in which the input signal is filtered by a FIR broadband filter g_l before being fed to the l-th loudspeaker (as shown in Fig. 4.13). In this section, we study the use of subband filtering for PSZ systems. Then, rather than using a broadband filter g_l for each loudspeaker, a set of FIR subband filters $g_{l,k}$ is used.

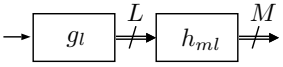

Figure 4.13: System model for a PSZ system using broadband filtering.

4.3.1 Previous works

The authors in [47] first used subband filtering for PSZ systems. In their work, they propose to perform the filtering required by the system in the subbands of structure formed by appending multiple QMF stages. Moreover, they compute the required subband filters by formulating independent optimization problems for each subband using the subband signals obtained by feeding the RIRs to the analysis filter bank. The system model proposed in [47] is shown in Fig. 4.14 for two QMF stages, i.e., with 3 subbands. In Fig. 4.14, u_{lp} and u_{hp} are the low and high-pass analysis filters, respectively, and v_{lp} and v_{hp} are the low and high-pass synthesis filters, respectively. In this structure, the sampling rate at which the k-th subband operates is $R_k \in \mathbb{N}$ times lower than at the input of the filter bank, where

$$R_k = \begin{cases} 2^{(K-1)} & \text{for } 0 \leq k \leq 1 \\ \\ 2^{(K-k)} & \text{for } 1 < k < K \end{cases}. \tag{4.53}$$

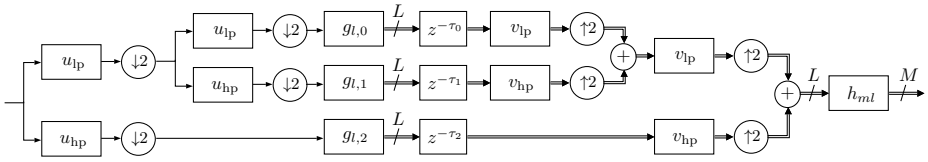

Figure 4.14: System model proposed in [47] for a PSZ system with multi-stage QMF structures. A structure with 2 stages is shown.

Also, the multi-stage structure produces a delay in the system of

$$\tau_{\mathrm{f}} = \left(2^{(K-1)}-1\right)(I_{\mathrm{p}}-1)\,, \tag{4.54}$$

where I_{p} is the length of the analysis and synthesis filters. Since all the subbands do not operate at the same sampling frequency, a delay τ_k must be applied at the output of the subband filters in the k-th subband to align the signals of all subbands at the output. In particular, this delay is selected as

$$\tau_k = \begin{cases} 0 & \text{for } 0 \leq k \leq 1 \\ \\ (R_k-1)\,(I_{\mathrm{p}}-1) & \text{for } 1 < k < K \end{cases}, \tag{4.55}$$

It is important to note that QMF structures are critically-sampled, and then, high levels of aliasing appear in the subbands. We previously showed in Section 4.1.2 that aliasing at the output of the filter bank can not be suppressed if high levels of aliasing are present in the subbands for systems using subband filtering. Moreover, the independence between the subbands assumed by the authors in [47] to formulate the optimization problems can only be assumed when certain conditions, as low aliasing levels in the subbands, are fulfilled [102]. Then, the proposed model with tree-QMF structure is not suitable for PSZ systems, as we will show that the aliasing in the subbands degrades the performance of the system.

4.3.2 System model

Next, we propose to use a GDFT filter bank with K subbands and resampling factor R to perform the filtering operation required by the PSZ system. We show in Fig. 4.15 the proposed model, where the filtering required by the PSZ system is performed in the subbands of the filter bank.

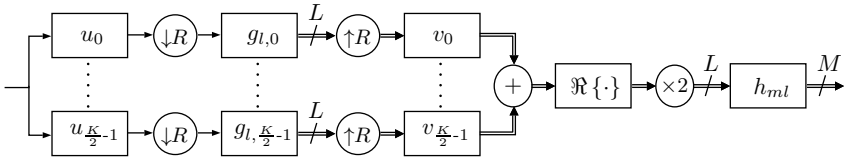

Figure 4.15: Proposed system model for a PSZ system using subband filtering with GDFT filter banks.

Since GDFT filter banks can achieve very low aliasing in the subbands, the proposed model overcomes the limitations of the model presented in [47]. Also, the proposed model is more versatile than the broadband model, since different configurations can be used for each subband, e.g., different sets of loudspeakers and filter lengths.

It is important to note that the subband filters $g_{l,k}$ are complex-valued (contrary to the broadband filters g_l, which are real-valued), but the input signal only needs to be processed in $K/2$ subbands due to the hermitian symmetry of the GDFT filter bank (for K even[2]). Also, a key aspect is that the GDFT filter bank produces an additional delay in the system of

$$\tau_{\mathrm{f}} = I_{\mathrm{p}} - 1, \tag{4.56}$$

where I_{p} is the length of the prototype filter used in the filter bank.

4.3.3 Formulation

Next, we propose a formulation for the model in Fig. 4.15. Let us denote $h_{ml,k}$ as the complex-valued k-th subband component of h_{ml} obtained with the subband decomposition described in Section 4.2. Particularly, we need to replace the generic response a used in Section 4.2 by response h_{ml}, and use (4.52) to obtain the subband component $h_{ml,k}$ of length

$$I_{\mathrm{h},k} = \left\lceil \frac{I_{\mathrm{h}} + I_{\mathrm{p}} - 1}{R} \right\rceil - \left\lceil \frac{I_{\mathrm{p}}}{R} \right\rceil + 1. \tag{4.57}$$

Let us define the alternative system model shown in Fig. 4.16, in which each subband includes the subband filters $g_{l,k}$ and the subband components of the RIR $h_{ml,k}$. The authors in [102] showed that the models in

[2]For the odd case the signal must be filtered with $((K\text{-}1)/2) + 1$ subband filters for each loudspeaker.

Fig. 4.15 and 4.16 are approximately equivalent if conditions (4.34) and (4.35) are fulfilled. Hence, the model in Fig. 4.16 can be used to compute the filters required by the model in Fig. 4.15. The main advantage of the model in Fig. 4.16 is that the subsystems for each subband can be considered independent, and then, the optimization problem can be formulated independently for each subband.

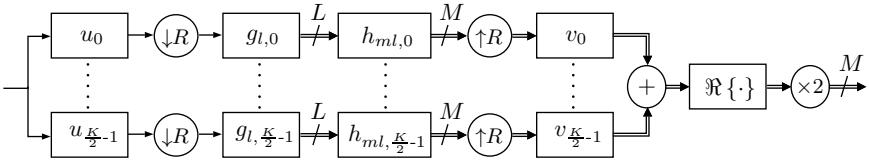

Figure 4.16: System model with the subband filters and the subband components of the RIRs.

In Fig. 4.16, the subsystem in each subband can be formulated in either time or frequency domains. We focus on the time-domain formulation because it leads to better performance when either short filters or short modelling delays are considered (as shown in Section 2.3.4). For the sake of simplicity on the notation, we assume that all subbands use the same set of L loudspeakers. Now, let us define $g_{l,k}$ as the $I_{\mathrm{g},k}$-length subband filter for the l-th loudspeaker and the k-th subband. Then, we can define the cascade impulse response in the m-th control point for the k-th subband as

$$x_{m,k}(n) = \sum_{l=0}^{L-1} h_{ml,k}(n) * g_{l,k}(n) = \sum_{l=0}^{L-1} \sum_{r=0}^{I_{\mathrm{g},k}-1} h_{ml,k}(n-r) g_{l,k}(r). \tag{4.58}$$

Also, let us define a $M\times 1$ vector of the samples of the cascade impulse response in time n for the k-th subband and for all control points as

$$\dot{\mathbf{x}}_{n,k} = \Big[x_{0,k}(n) \ \ldots \ x_{M-1,k}(n) \Big]^T. \tag{4.59}$$

Similarly, let us define a $L\times 1$ vector of the samples of the subband filters in time n for the k-th subband and for all loudspeakers as

$$\dot{\mathbf{g}}_{n,k} = \Big[g_{0,k}(n) \ \ldots \ g_{L-1,k}(n) \Big]^T, \tag{4.60}$$

and a $M \times L$ matrix containing the subband components of the RIRs in time n for the k-th subband and for all loudspeakers and control points as

$$\dot{\mathbf{H}}_{n,k} = \begin{bmatrix} h_{00,k}(n) & \dots & h_{0(L-1),k}(n) \\ \vdots & \ddots & \vdots \\ h_{(M-1)0,k}(n) & \dots & h_{(M-1)(L-1),k}(n) \end{bmatrix}. \tag{4.61}$$

Then, using (4.59) to (4.61) we can write

$$\dot{\mathbf{x}}_{n,k} = \sum_{r=0}^{I_{\mathrm{g},k}-1} \dot{\mathbf{H}}_{n-r,k}\, \dot{\mathbf{g}}_{r,k}. \tag{4.62}$$

Next, let us define a $M(I_{\mathrm{h},k}+I_{\mathrm{g},k}-1)\times 1$ vector with the cascade impulse responses in all time instants and control points for the k-th subband as

$$\dot{\mathbf{x}}_k = \left[\dot{\mathbf{x}}_{0,k}^T \ \dots \ \dot{\mathbf{x}}_{I_{\mathrm{g},k}+I_{\mathrm{h},k}-1,k}^T\right]^T, \tag{4.63}$$

and a $LI_{\mathrm{g},k}\times 1$ vector of the filters for subband k as

$$\dot{\mathbf{g}}_k = \left[\dot{\mathbf{g}}_{0,k}^T \ \dots \ \dot{\mathbf{g}}_{I_{\mathrm{g},k}-1,k}^T\right]^T. \tag{4.64}$$

Also, let us define a $M\,(I_{\mathrm{h},k}+I_{\mathrm{g},k}-1)\times LI_{\mathrm{g},k}$ block-toeplitz matrix $\dot{\mathbf{H}}_k$ as

$$\dot{\mathbf{H}}_k = \begin{bmatrix} \dot{\mathbf{H}}_{0,k}^T & \dots & \dot{\mathbf{H}}_{I_{\mathrm{h},k}-1,k}^T & \mathbf{0}_{L\times M} & \dots & \mathbf{0}_{L\times M} \\ \mathbf{0}_{L\times M} & & & & & \\ \vdots & & & Toeplitz & & \\ \mathbf{0}_{L\times M} & & & & & \end{bmatrix}^T. \tag{4.65}$$

Finally, using (4.63) to (4.65) we can write

$$\dot{\mathbf{x}}_k = \dot{\mathbf{H}}_k\, \dot{\mathbf{g}}_k. \tag{4.66}$$

4.3.4 Weighted Pressure Matching with Subband-Domain Formulation (wPM-S)

Now, we propose the weighted Pressure Matching with Subband-Domain Formulation (wPM-S) algorithm to compute the subband filters $g_{l,k}$. The proposed algorithm uses the subband formulation presented in Section 4.3.3,

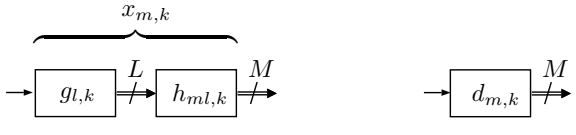

Figure 4.17: Subsystem and target for the k-th subband in (a) and (b), respectively.

and it is based on applying the wPM criterion individually to the subsystems in each subband.

First, we need to select the complex-valued FIR target $d_{m,k}$ of length $I_{\mathrm{d},k} = I_{\mathrm{h},k}+I_{\mathrm{g},k}-1$ for each subband k and for each control point m. In particular, we propose to define a broadband target d_m, and then, use the subband decomposition described in Section 4.2 to obtain the subband components $d_{m,k}$. Now, let us define

$$\dot{\mathbf{d}}_{n,k} = \begin{bmatrix} d_{0,k}(n) & \dots & d_{M-1,k}(n) \end{bmatrix}^T, \tag{4.67}$$

which is $M\times 1$ vector containing the target in time instant n for the k-th subband and all control points. Similarly, let us define a $MI_{\mathrm{d},k}\times 1$ vector containing the target for all time instants and all control points as

$$\dot{\mathbf{d}}_k = \begin{bmatrix} \dot{\mathbf{d}}_{0,k}^T & \dots & \dot{\mathbf{d}}_{I_{\mathrm{d},k}-1,k}^T \end{bmatrix}^T. \tag{4.68}$$

Once the target is defined, the aim of wPM-S is to find the subband filters $g_{l,k}$ that minimize the MSE between the subsystems in Fig. 4.17a and Fig. 4.17b, i.e., the MSE between the cascade impulse response $x_{m,k}$ and a selected target $d_{m,k}$ for each control point m. Then, the optimal subband filters are the ones that minimize the cost function

$$J\left(\dot{\mathbf{g}}_k\right) = \left\| \dot{\mathbf{W}}_k \left(\dot{\mathbf{H}}_k \dot{\mathbf{g}}_k - \dot{\mathbf{d}}_k \right) \right\|^2 + \dot{\beta}_k \left\| \dot{\mathbf{g}}_k \right\|^2, \tag{4.69}$$

where $\dot{\beta}_k \in \mathbb{R}^+$ is the regularization factor for the k-th subband, and $\dot{\mathbf{W}}_k$ is a weighting matrix that can include time, frequency, and spatial weighting. However, we only consider the spatial weighting in this work. Then, let us define the weighting matrix as $MI_{\mathrm{d},k}\times MI_{\mathrm{d},k}$ block-diagonal matrix

$\dot{\mathbf{W}}_k = \dot{\mathbf{\Omega}}_k \otimes \mathbf{I}_{I_{\mathrm{d},k}}$ formed by blocks $\dot{\mathbf{\Omega}}_k = \mathrm{diag}\{\dot{w}_{0,k}, \ldots, \dot{w}_{M-1,k}\}$ of size $M \times M$, where $\dot{w}_{m,k}$ is the weight given in the cost function to the error for the m-th control point, i.e.,

$$\dot{w}_{m,k} = \begin{cases} \sqrt{\frac{\dot{\mu}_k}{M_\mathrm{d}}} & m \in \mathcal{D} \\ \sqrt{\frac{1-\dot{\mu}_k}{M_\mathrm{b}}} & m \in \mathcal{B} \end{cases}, \tag{4.70}$$

where $\dot{\mu}_k \in \mathbb{R}$ is a weighting factor satisfying $0 \leq \dot{\mu}_k \leq 1$ for the k-th subband. Now, let us re-write (4.69) as

$$J\left(\dot{\mathbf{g}}_k\right) = \dot{\mathbf{g}}_k^H \dot{\mathbf{H}}_k^H \dot{\mathbf{W}}_k^T \dot{\mathbf{W}}_k \dot{\mathbf{H}}_k \dot{\mathbf{g}}_k - 2\,\Re\left\{\dot{\mathbf{g}}_k^H \dot{\mathbf{H}}_k^H \dot{\mathbf{W}}_k^T \dot{\mathbf{W}}_k \dot{\mathbf{d}}_k\right\} + \dot{\beta}_k\, \dot{\mathbf{g}}_k^H \dot{\mathbf{g}}_k, \tag{4.71}$$

in which the term $\dot{\mathbf{d}}_k^H \dot{\mathbf{W}}_k^T \dot{\mathbf{W}}_k \dot{\mathbf{d}}_k$ has been omitted because has not effect on the optimization. The gradient of (4.71) is given by [72]

$$\nabla J\left(\dot{\mathbf{g}}_k\right) = 2\,\dot{\mathbf{H}}_k^H \dot{\mathbf{W}}_k^T \dot{\mathbf{W}}_k \dot{\mathbf{H}}_k \dot{\mathbf{g}}_k - 2\,\dot{\mathbf{H}}_k^H \dot{\mathbf{W}}_k^T \dot{\mathbf{W}}_k \dot{\mathbf{d}}_k + 2\,\dot{\beta}_k\, \dot{\mathbf{g}}_k. \tag{4.72}$$

Since (4.69) is a quadratic cost function, it has a unique global minimum for $\dot{\beta}_k > 0$ at the point in which its gradient equals 0, i.e., $\nabla J\left(\dot{\mathbf{g}}_k\right) = \mathbf{0}$. Then, the optimal filters are given by

$$\dot{\mathbf{g}}_{\mathrm{opt},k} = \left(\dot{\mathbf{H}}_k^H \dot{\mathbf{W}}_k^T \dot{\mathbf{W}}_k \dot{\mathbf{H}}_k + \dot{\beta}_k \mathbf{I}_{LI_{\mathrm{g},k}}\right)^{-1} \dot{\mathbf{H}}_k^H \dot{\mathbf{W}}_k^T \dot{\mathbf{W}}_k \dot{\mathbf{d}}_k. \tag{4.73}$$

As the length of the subband filters is approximately R times smaller than the length of the broadband filters, solution (4.73) requires the inversion of a matrix that is approximately R times smaller than the matrix that needs to be inverted with wPM-T, leading to important computational savings (as we will show in Section 4.4). It is important to mention that wPM-S requires the subband decomposition of the RIRs, which could require additional computational load. However, using the proposed expression (4.52), only one matrix inversion is required to compute the subband components for all the control points, loudspeakers, and subbands, so its computational cost is not significant. Moreover, although we have assumed that the same set of loudspeakers is used in all subbands, different sets of loudspeakers can be used for each subband. Finally, we have assumed that the same criterion is used to obtain the optimal filters for all subbands (in our case wPM), however, the subband formulation allows us to use different algorithms for

different subbands (as for example ACC, which could be beneficial for very low frequencies [49]). In conclusion, wPM-S can not only offer a reduction of the computational cost with respect to wPM-T, but also greater versatility, as it allows to use different setups for different subbands.

4.4 Performance evaluation

Next, the proposed wPM-S algorithm is experimentally evaluated and compared with wPM-T, wPM-F, and with the approach proposed in [47].

4.4.1 Setup and methodology

Setup

The setup described in Section 2.3.1 is used for the evaluations of this chapter, i.e., a linear array of 8 two-way loudspeakers and single bright and dark zones in a office-like room with reverberation time $T_{60} = 500$ ms. We consider that the system is operating at a sampling frequency of 6300 Hz, and that the length of the RIRs is $I_\mathrm{h} = 2330$.

Methodology for computing the filters

In order to compute the optimal filters, let us select the target impulse response in the m-th control point as

$$d_m(n) = \begin{cases} h_{ml_\mathrm{r}}(n - \tau_\mathrm{d}) & m \in \mathcal{B} \\ 0 & m \in \mathcal{D} \end{cases}, \tag{4.74}$$

where $l_\mathrm{r} = 3$ is the reference loudspeaker, and $\tau_\mathrm{d} \in \mathbb{N}$ is a modelling delay whose value is indicated in each case. Now, we describe the methodology used to compute the optimal filters for the different algorithms:

- **wPM-T:** The filters g_l of length I_g are computed using (2.34) and assuming that the target response d_m is given by (4.74). The regularization factor is selected as

$$\beta = \beta_0 u_\mathrm{avg}, \tag{4.75}$$

  where u_avg is the mean of the eigenvalues of $\mathbf{H}^T\mathbf{W}^T\mathbf{W}\mathbf{H}$ in (2.34), and β_0 is the regularization factor relative to u_avg. The value of β_0 is indicated in each case.

- **wPM-F:** The optimal filter coefficients $Q_l(f)$ are computed for a set of $N = I_\mathrm{h}+I_\mathrm{g}-1$ control frequencies using (2.27), where $D_m(f)$ is selected as the DFT of $d_m(n)$ in (4.74). The coefficients $Q_l(f)$ are set to 0 for control frequencies below 80 Hz. After that, an N-point IDFT is used to obtain the time-domain responses q_l, which are truncated using a rectangular window of size I_g to obtain the filters g_l (as described in Section 2.2.2). A search is carried out to find the regularization factor $\bar{\beta}_f$ for each control frequency that leads to the same array effort as the other algorithms with which it is compared.

- **wPM-Q:** The subband filters $g_{l,k}$ are computed using the model proposed in [47]. It is worth noting that a frequency-domain ACC criterion is used in [47] in each subband, however, we use a time-domain wPM criterion to make a fair comparison between the different algorithms. The target in the m-th control point for the k-th subband is selected as the output of the k-th subband of the analysis filter bank in Fig. 4.14 when it is fed with d_m in (4.74). The regularization factor in the k-th subband is selected as $\dot{\beta}_k = \beta/R_k^2$, where R_k is defined in (4.53) and β is obtained using (4.75) for a given β_0. When a broadband filter of length I_g is considered, we assume that the length of the equivalent subband filters for the k-th subband is selected as

$$I_{\mathrm{g},k} = \left\lceil \frac{I_\mathrm{g}}{R_k} \right\rceil, \quad \text{for } 0 \leq k < K, \tag{4.76}$$

  The analysis and synthesis filters of the QMF structure are computed with `firpr2chfb` MATLAB's function with a passband edge of 0.46.

- **wPM-S:** The subband filters $g_{l,k}$ are computed using (4.73). The target $d_{m,k}$ is obtained by computing the subband decomposition of d_m in (4.74), as described in Section 4.2. The regularization factor in the subbands is selected as $\dot{\beta}_k = \beta$, where β is obtained using (4.75) for a given β_0. When a broadband filter of length I_g is considered, we assume that the length of the equivalent subband filters for the k-th subband is selected as

$$I_{\mathrm{g},k} = \left\lceil \frac{I_\mathrm{g}}{R} \right\rceil, \quad \text{for } 0 \leq k < K/2. \tag{4.77}$$

  The prototype filter for the GDFT filter bank is computed with the method described in Appendix B.

Moreover, equal effort is used in all cases to minimize the error in the bright zone and the energy in the dark zone, i.e., $\mu = \bar{\mu}_f = \dot{\mu}_k = 0.5$. For the sake of simplicity, in some cases we will indicate I_g rather $I_{\mathrm{g},k}$ in the evaluations for wPM-S and wPM-Q. The interested reader can obtain $I_{\mathrm{g},k}$ using (4.76) and (4.77) for wPM-Q and wPM-S, respectively.

Methodology for evaluating the filters

Up to this point, we have considered that the PSZ system is fed with a unit impulse $\delta(n)$ for computing the metrics in Section 2.2.5. However, filter banks are linear R-periodically time-varying systems, and then, using a unit impulse for evaluating their performance is not a good choice. To compute the metrics in this section, we feed the PSZ system with a signal s of length 6300 samples (i.e., 1 second) from a gaussian sample distribution with mean $\mu_s = 0$ and variance $\sigma_s^2 = 1$. By using this signal instead of the unit impulse, we evaluate the time-variability of the filter bank. The metrics described in Section 2.2.5 are computed for a set of 32768 equispaced frequencies with a resolution of 0.1923 Hz. Finally, it is important to consider that the filter bank introduces an additional delay τ_f in the system. Then, the target response for the m-th validation point used to evaluate the filters is selected as

$$d_{\mathrm{v},m}(n) = \begin{cases} h_{\mathrm{v},ml_\mathrm{r}}(n-\tau) & m \in \mathcal{B} \\ 0 & m \in \mathcal{D} \end{cases}. \tag{4.78}$$

where $h_{\mathrm{v},ml}$ is the RIR from the l_r-th loudspeaker to the m-th validation point, and $\tau \in \mathbb{N}$ is the total system delay. For wPM-T and wPM-F we use $\tau = \tau_\mathrm{d}$, while $\tau = \tau_\mathrm{d} + \tau_\mathrm{f}$ is used for wPM-Q and wPM-S. If not stated otherwise, a 1/3-octave band averaging [76] is used for the frequency-domain plots to improve the readability of the results.

4.4.2 Influence of the filter bank configuration

Next, we study the influence of the configuration of the GDFT filter bank on the performance of a PSZ system using wPM-S. In particular, we evaluate configurations with different number of subbands K, resampling factors R, and prototype filter lengths I_p. We show in Fig. 4.18, as an example, the magnitude of the spectrum of the analysis filters for two configurations whose prototype filter is computed using the method described in Appendix B.

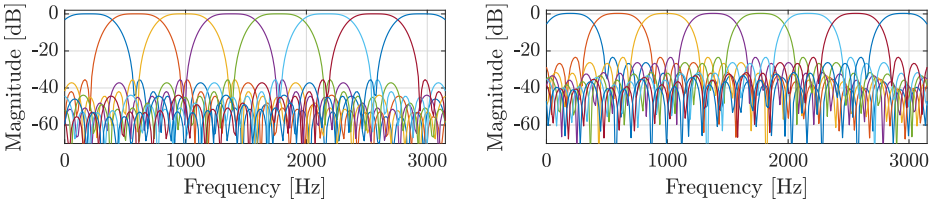

(a) Oversampled, $R = 10$ **(b)** Critically-sampled, $R = 16$

Figure 4.18: Magnitude of the frequency response of the analysis filters in the positive spectrum for a GDFT filter bank with $I_\mathrm{p} = 45$, $K = 16$, and resampling factors $R = 10$ and $R = 16$ in (a) and (b), respectively.

First, we present in Fig. 4.19 the Reconstruction Error (RE) and the Alias-To-Signal Ratio (ASR) for a number of filter bank configurations. The results show that the higher the prototype filter length I_p and the oversampling ratio K/R, the lower the RE and the ASR. Then, long prototype filters and high oversampling ratios assure minor magnitude and phase distortions, and negligible aliasing in the subbands. Also, we can see that for the same prototype filter length and similar oversampling ratio, a smaller number of subbands K leads to lower RE and ASR. It is worth noting that long prototype filters lead to high delay τ_f for the filter bank. Moreover, high values of K/R do not reduce the sampling frequency in the

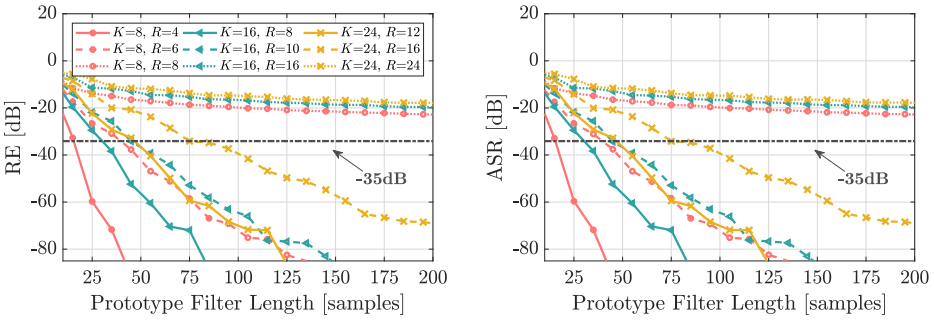

(a) Reconstruction Error (RE) **(b)** Alias-To-Signal Ratio (ASR)

Figure 4.19: RE and ASR for different GDFT filter bank configurations in (a) and (b), respectively. The gray dash-dotted line indicates a reference of -35 dB.

subbands as much as values of K/R close to 1, and then, higher computational demands are needed for subband filtering. Hence, it is important to find a balance such that low enough RE and ASR are obtained for the filter bank, as well as reasonable computational demands and delays.

Next, we study the performance of wPM-S with different filter bank configurations. For computing the filters, we consider $I_{\mathrm{g}} = 1024$, $\tau_{\mathrm{d}} = 512$, and $\beta_0 = 10^{-3}$, and (4.77) is used to compute $I_{\mathrm{g},k}$ for each configuration. In Fig. 4.20, the average acoustic contrast and MSE over 125-1500 Hz for

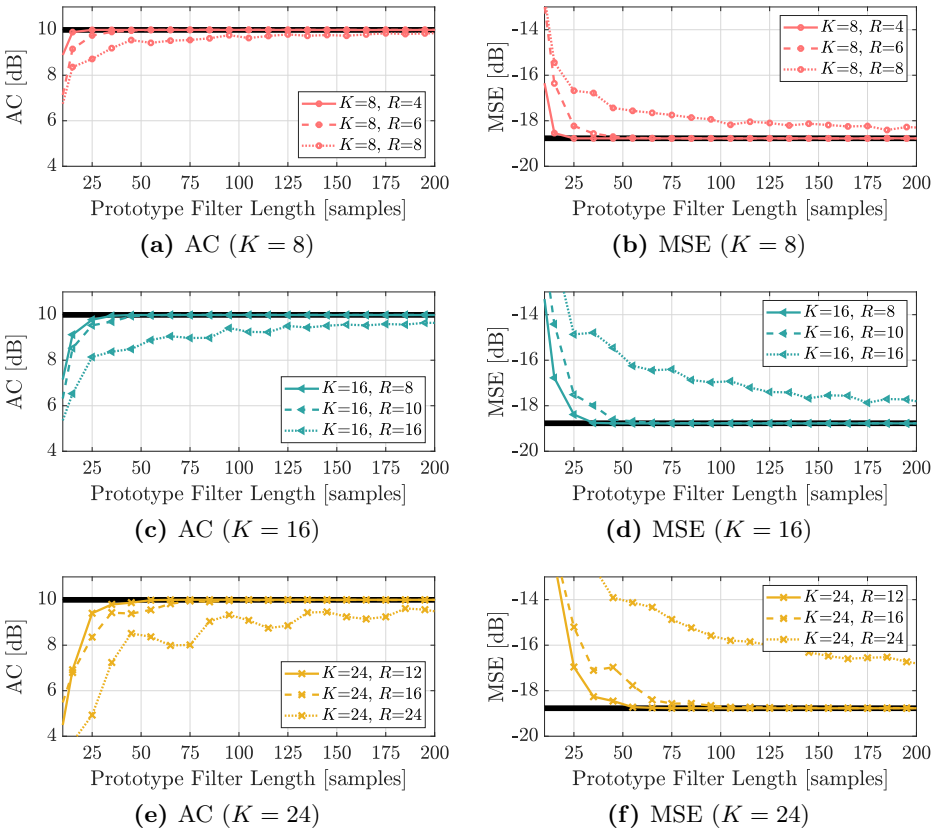

(a) AC ($K = 8$) **(b)** MSE ($K = 8$)

(c) AC ($K = 16$) **(d)** MSE ($K = 16$)

(e) AC ($K = 24$) **(f)** MSE ($K = 24$)

Figure 4.20: Average acoustic contrast and MSE over 125-1500 Hz for wPM-S with different GDFT filter bank configurations, considering $I_{\mathrm{g}} = 1024$, $\tau_{\mathrm{d}} = 512$, and $\beta_0 = 10^{-3}$. The thick black line represents the performance for wPM-T with $I_{\mathrm{g}} = 1024$, $\tau_{\mathrm{d}} = 512$, and $\beta_0 = 10^{-3}$.

wPM-S are shown for the different configurations. Also, we include in Fig. 4.20 the performance of broadband filters computed with wPM-T for $I_{\mathrm{g}} = 1024$, $\tau_{\mathrm{d}} = 512$, and $\beta_0 = 10^{-3}$, which is used here as reference. By inspecting Fig. 4.20, and comparing it with Fig. 4.19, we can see a direct relation between the performance of wPM-S and the RE and ASR of the filter bank. Particularly, the performance of wPM-S converges to the one for wPM-T when configurations with low values of RE and ASR are used. This was expected, as we studied in Section 4.3.3 that the model used to formulate the wPM-S algorithm is a good approximation of the broadband model if conditions (4.34) and (4.35) are fulfilled, and the RE and the ASR are directly related to these conditions. We can see that the MSE does not completely converge to the reference for the critically-sampled cases, i.e., $K = R$. This is produced because these configurations present high RE and ASR, so critical sampling is not a good choice for a PSZ system. In general, the results in Fig. 4.20 show that the performance of wPM-S converges to the one for wPM-T when the RE and the ASR are below -35 dB. Then, we can assume that conditions (4.34) and (4.35) are fulfilled, and consequently, that wPM-S obtains good performance, if the RE and the ASR of the filter bank are upper-bounded to -35 dB. This is a very important finding, since it indicates that we can improve aspects such as the computational demands or the delay of the filter bank at the cost of higher RE and ASR, as long as the -35 dB upper-bound is met.

In order to further study the influence of the configuration of the filter bank on the performance of wPM-S, we present in Fig. 4.21 the acoustic contrast and the MSE as a function of frequency for two different configurations. Specifically, we study an oversampled configuration with $I_{\mathrm{p}} = 45$, $K = 16$, and $R = 10$, that meets the -35 dB upper-bound for the RE and the ASR, and the critically-sampled configuration with $I_{\mathrm{p}} = 45$, $K = 16$, and $R = 16$, which does not meet the upper-bound. The bandwidth of the subbands is 393.75 Hz for both configurations. We consider $I_{\mathrm{g}} = 1024$, $\tau_{\mathrm{d}} = 512$, and $\beta_0 = 10^{-3}$. The results show that the critically-sampled configuration presents worst performance than the oversampled one, especially at frequencies near the transitions between subbands, i.e., 393.75, 787.5, 1181.3, 1575, 1968.8, 2362.5, 2756.3, and 3150 Hz. In particular, degradations of up to 5 and 7 dB in the acoustic contrast and the MSE, respectively, appear for the critically-sampled case. Then, we can see that a filter bank configuration with high RE and ASR degrades the performance of the PSZ system, especially in the transitions between subbands.

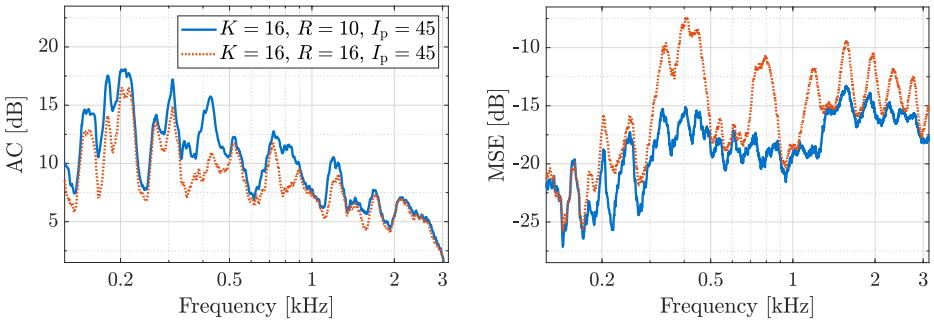

(a) AC **(b)** MSE

Figure 4.21: Acoustic contrast and MSE as a function of frequency in (a) and (b), respectively, for wPM-S with $I_p = 45$, $K = 16$, and resampling factors $R = 10$ and $R = 16$, considering $I_g = 1024$, $\tau_d = 512$, and $\beta_0 = 10^{-3}$. We use 1/10 octave band averaging [76] in the plots.

Finally, we show in Fig. 4.22 the computational demands of a PSZ system that uses the studied filter bank configurations, considering $I_g = 1024$ and $L = 8$. The number of FLOPs required to compute the optimal wPM-S filters using a Cholesky solver and to filter a frame of 10 ms (63 samples) are shown in Fig. 4.22a and 4.22b, respectively, for the different filter bank configurations. The operation counts used to obtain the results in Fig. 4.22 can

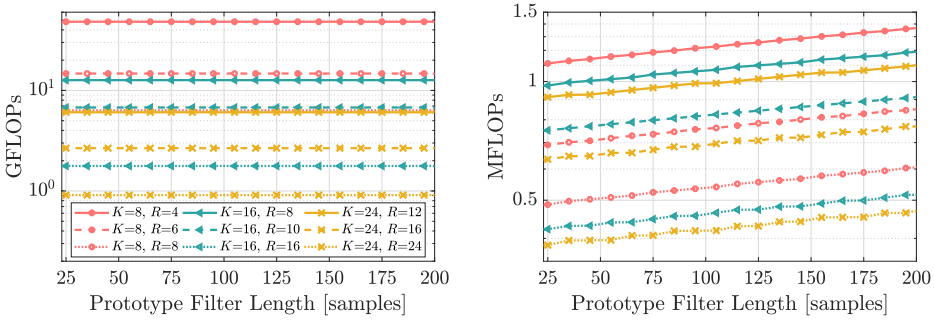

(a) Computing the filters for wPM-S. **(b)** Filtering a frame of 10 ms.

Figure 4.22: Number of FLOPs required to compute the optimal wPM-S filters and to filter a signal of 10 ms in (a) and (b), respectively, for different GDFT filter bank configurations. We consider $I_g = 1024$ and $L = 8$.

be found in Appendix A. The results show that the filter bank configuration has a significant influence in the computational demands of the system. We can see some similar trends in Fig. 4.22a and 4.22b. For example, the closer K/R is to 1, the lower the computational demands. Moreover, increasing the number of subbands reduces the computational requirements. Also, selecting a longer prototype filter increases the computational requirements for filtering the input signals, but it does not significantly influence the number of FLOPs required to compute the subband filters.

In conclusion, the configuration of the filter bank has a important influence on the performance and the computational demands of the PSZ system. We showed that subband filtering can obtain as good performance as broadband filtering if the RE and the ASR are upper-bounded to -35 dB. Furthermore, our findings reveal that very low computational demands are required if filter banks with short prototype filters, high number of subbands, and values of K/R close to 1 are used. However, low values of RE and ASR can not be achieved in this case. Then, we need to vary the filter bank parameters if we want to meet the RE and ASR upper-bound. For example, increasing the length of the prototype filter can reduce the RE and the ASR, but at the cost of increasing the delay τ_{f} introduced by the filter bank and the computational efforts required for subband filtering. Then, the configuration of the filter bank must be selected taking into account the performance and delay requirements of the system, and the available computational capabilities. From now on, we will use the filter bank configuration with $I_{\mathrm{p}} = 45$, $K = 16$, and $R = 10$, which fulfils the upper-bound for the RE and the ASR, and leads to a good compromise between performance, computational demands and delay.

4.4.3 Comparison of subband filters

Now, we compare wPM-S and wPM-Q, i.e., the algorithms that use subband filters. For wPM-S, we use a GDFT filter bank with $I_{\mathrm{p}} = 45$, $K = 16$, and $R = 10$, whose spectrum is shown in Fig. 4.18a. For wPM-Q, we use 3 QMF stages, i.e., $K = 4$ subbands, and analysis and synthesis filters of length $I_{\mathrm{p}} = 100$. We select this configuration for wPM-Q because it presents a maximum resampling factor comparable to the one selected for wPM-S. The transition between the non-uniform subbands of the multi-stage QMF structure are located in 393.7, 787.5, and 1575 Hz. The spectrum of the analysis filters for a QMF stage are shown in Fig. 4.23.

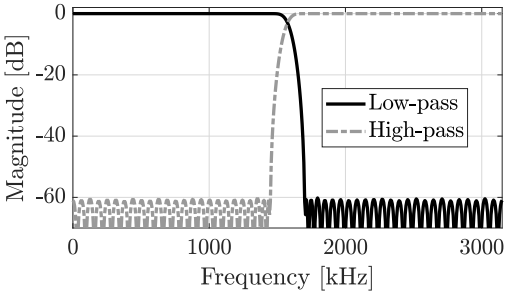

Figure 4.23: Magnitude of the frequency response of the low-pass and high-pass analysis filters of length $I_\mathrm{p} = 100$ for a single QMF stage. The filters are computed with *firpr2chfb* MATLAB's function with a passband edge of 0.46.

Next, evaluation results showing the acoustic contrast, the MSE, and the array effort for wPM-S and wPM-Q are presented in Fig. 4.24. For the evaluations, we consider $I_\mathrm{g} = 1024$, $\tau_\mathrm{d} = 512$, and two regularization factors β_0. The values of $I_{\mathrm{g},k}$ are obtained with (4.76) and (4.77) for wPM-Q and wPM-S, respectively. In Fig. 4.24, we use 1/10 instead of 1/3 octave band averaging to determine with higher precision the frequencies where degradations appear. The results show that the performance of both algorithms is similar for a number of frequencies, but wPM-Q performs worse than wPM-S in those frequencies that are close to the transition between the subbands of the multi-stage QMF structure. For example, for $\beta_0 = 10^{-1}$, wPM-Q presents 4 dB worse acoustic contrast and MSE than wPM-S near 400 Hz, and also, 4 dB higher array effort. Similar results can be found for $\beta_0 = 10^{-3}$. The degradations for wPM-Q are caused by its high aliasing levels in the subbands, as critical sampling is used in this case. The effect of aliasing in the performance of wPM-Q could be mitigated if longer analysis and synthesis filters were used, but this would lead to higher delay for the system. In particular, the multi-stage QMF structure with $I_\mathrm{p} = 100$ produces a delay of $\tau_\mathrm{f} = 693$ samples (110 ms), while the GDFT filter bank with $I_\mathrm{p} = 45$ produces a delay of $\tau_\mathrm{f} = 44$ samples (6.9 ms), i.e., 15.75 times shorter. Then, the proposed wPM-S algorithm is preferred to wPM-Q for PSZ systems, not only because it does not suffer performance degradation in the transition between the subbands, but also, because it leads to significantly lower system delay.

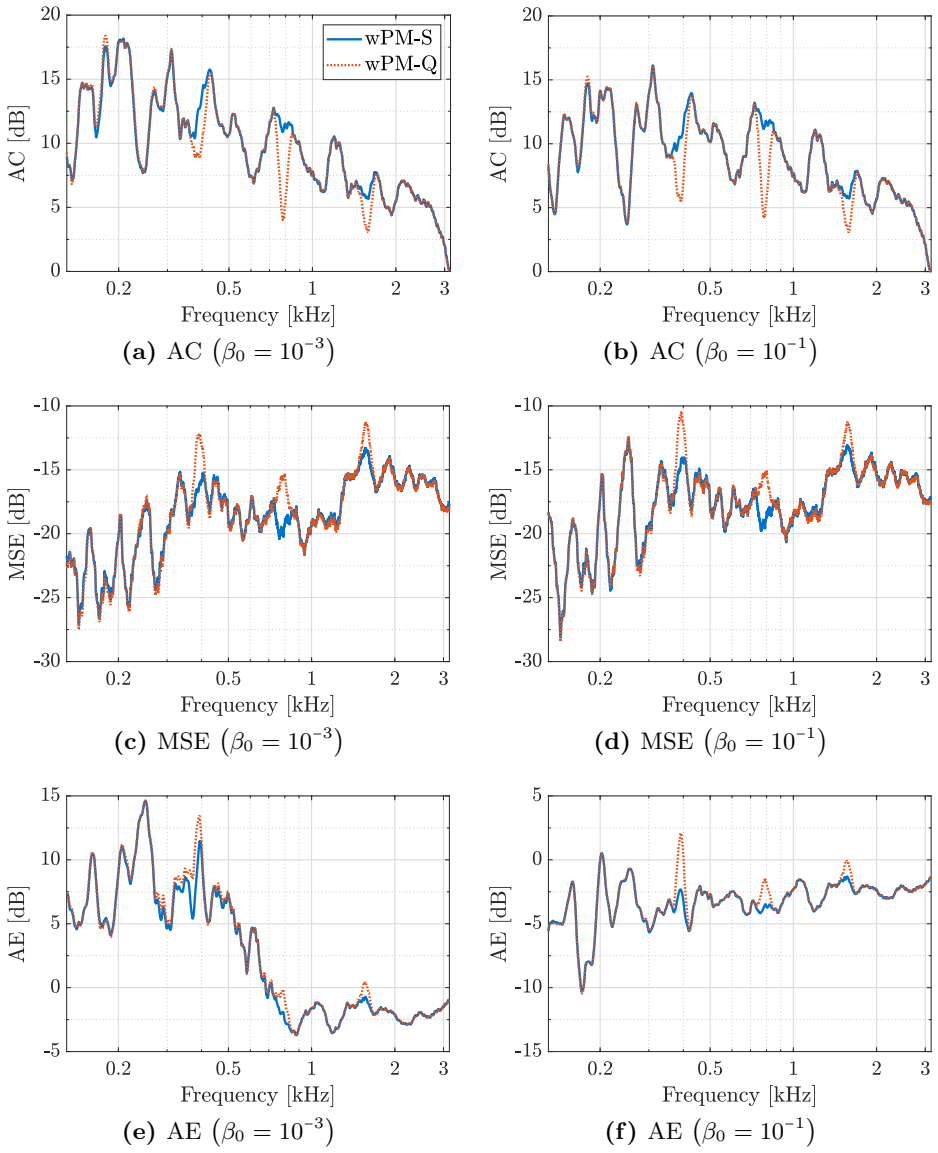

(a) AC $(\beta_0 = 10^{-3})$ **(b)** AC $(\beta_0 = 10^{-1})$

(c) MSE $(\beta_0 = 10^{-3})$ **(d)** MSE $(\beta_0 = 10^{-1})$

(e) AE $(\beta_0 = 10^{-3})$ **(f)** AE $(\beta_0 = 10^{-1})$

Figure 4.24: Acoustic contrast (a, b), MSE (c, d), and array effort (e, f) as a function of frequency for wPM-S and wPM-Q. We consider $I_{\mathrm{g}} = 1024$, $\tau_{\mathrm{d}} = 512$, and two values of β_0 . We use 1/10 octave band averaging [76] in the plots.

4.4.4 Comparison of broadband and subband filters

Next, we evaluate the performance of the subband filters computed with wPM-S, and the broadband filters computed with wPM-T and wPM-F. For wPM-S, we consider a GDFT filter bank with $I_\mathrm{p} = 45$, $K = 16$, and $R = 10$.

The performance of wPM-T and wPM-S is compared in Fig. 4.25 to Fig. 4.27 for $\beta_0 = 10^{-1}$, $\beta_0 = 10^{-3}$, and $\beta_0 = 10^{-5}$, respectively. We include results for a filter length $I_\mathrm{g} = 512$ with modelling delays $\tau_\mathrm{d} = 64$ and $\tau_\mathrm{d} = 256$ in the left-column of the figures, and for $I_\mathrm{g} = 2048$ with $\tau_\mathrm{d} = 64$ and $\tau_\mathrm{d} = 1024$ in the right-column. For wPM-S, the length of the equivalent subband filters is obtained with (4.77). The results in Fig. 4.25 and Fig. 4.26 show that the performance of both algorithms is approximately equal for $\beta_0 = 10^{-1}$ and $\beta_0 = 10^{-3}$, respectively. However, Fig. 4.27 reveals that wPM-S outperforms wPM-T for $\beta_0 = 10^{-5}$, especially for short modelling delays. For example, wPM-S presents about 1.5 dB higher acoustic contrast and 4 dB lower MSE than wPM-T for frequencies below 200 Hz, $I_\mathrm{g} = 2048$, $\tau_\mathrm{d} = 64$, and $\beta_0 = 10^{-5}$. These improvements appear because the subband decomposition of the RIRs adds some small random errors to the wPM-S optimization, which makes the filters more robust to perturbations and to mismatches between the RIRs in the control and validation points. Then, wPM-S presents higher robustness than wPM-T to perturbations, and it is less sensitive to the regularization factor selection. Similar trends were reported by Gaubitch and Naylor [101] in the context of room equalization using GDFT filter banks. From the presented results, we can conclude that nearly equal performance is achieved with broadband filters computed with wPM-T and with subband filters computed with wPM-S for mid and high regularization levels. Furthermore, wPM-S outperforms wPM-T when low regularization factors are considered. Finally, it is important to highlight that the system delay is $\tau = \tau_\mathrm{d}$ for wPM-T, while it is $\tau = \tau_\mathrm{d} + \tau_\mathrm{f}$ for wPM-S. As a consequence, even if the same modelling delay is selected for both algorithms, wPM-S leads to an additional delay for the system, which for the selected filter bank configuration is $\tau_\mathrm{f} = 44$ samples (6.9 ms). Consequently, wPM-T is preferred to wPM-S for PSZ system that present very strong delay requirements, but wPM-S may be beneficial for systems in which the delay only needs to be moderately short, e.g., between 10 and 20 ms.

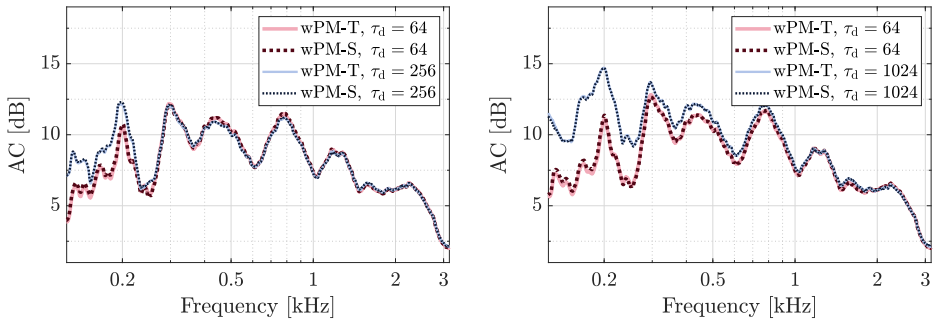

(a) AC ($I_g = 512$, $I_{g,k} = 52$)

(b) AC ($I_g = 2048$, $I_{g,k} = 205$)

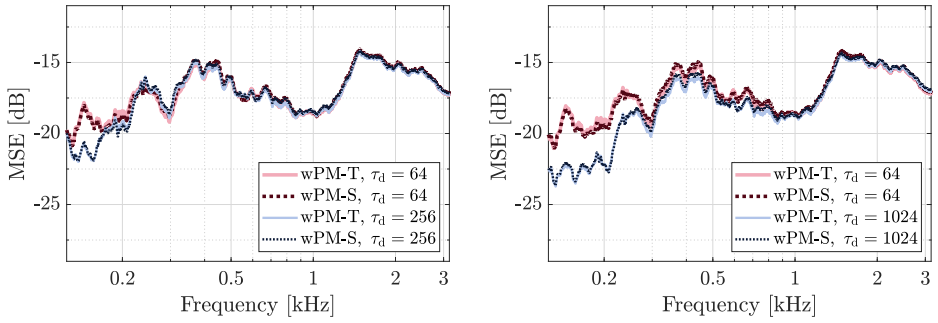

(c) MSE ($I_g = 512$, $I_{g,k} = 52$)

(d) MSE ($I_g = 2048$, $I_{g,k} = 205$)

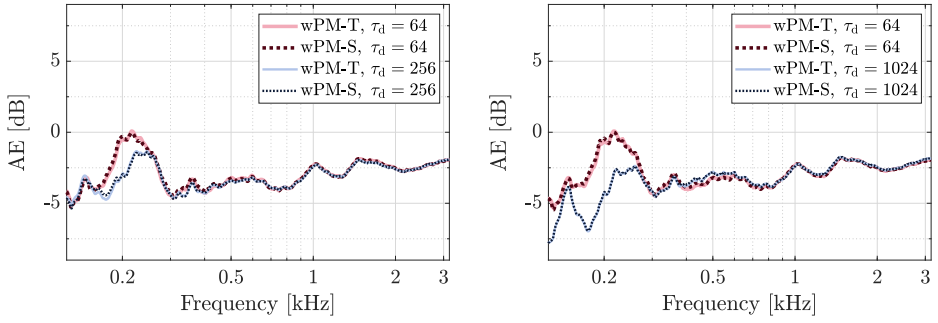

(e) AE ($I_g = 512$, $I_{g,k} = 52$)

(f) AE ($I_g = 2048$, $I_{g,k} = 205$)

Figure 4.25: Acoustic contrast (a, b), MSE (c, d), and array effort (e, f) as a function of frequency for wPM-S and wPM-T. We include results for a filter length $I_g = 512$ with modelling delays $\tau_d = 64$ and $\tau_d = 256$ in the left-column, and for $I_g = 2048$ with $\tau_d = 64$ and $\tau_d = 1024$ in the right-column. A regularization factor $\beta_0 = 10^{-1}$ is used. For wPM-S, $I_{g,k}$ is computed using (4.77).

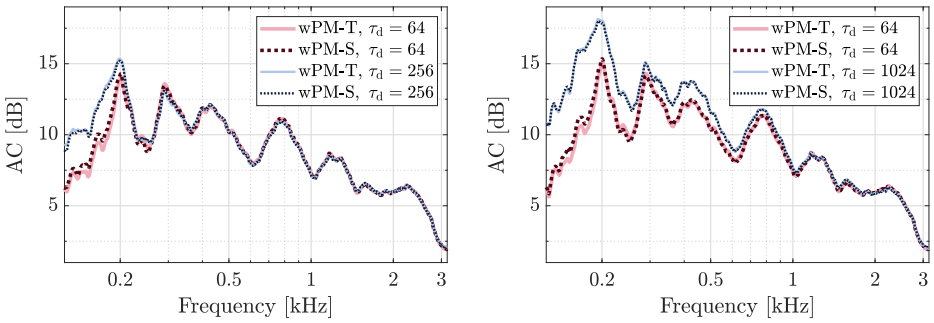

(a) AC ($I_g = 512$, $I_{g,k} = 52$) **(b)** AC ($I_g = 2048$, $I_{g,k} = 205$)

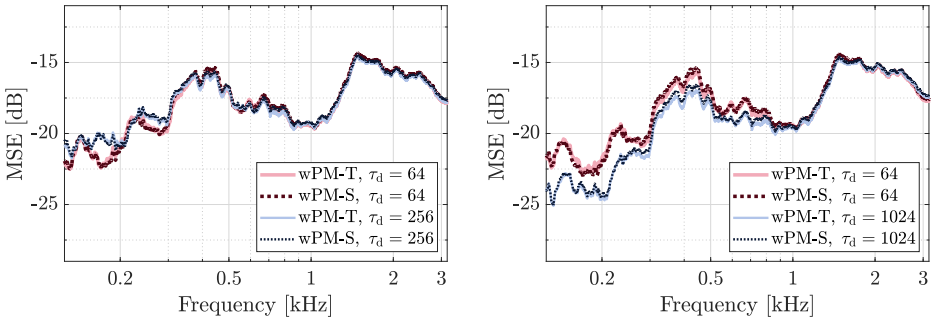

(c) MSE ($I_g = 512$, $I_{g,k} = 52$) **(d)** MSE ($I_g = 2048$, $I_{g,k} = 205$)

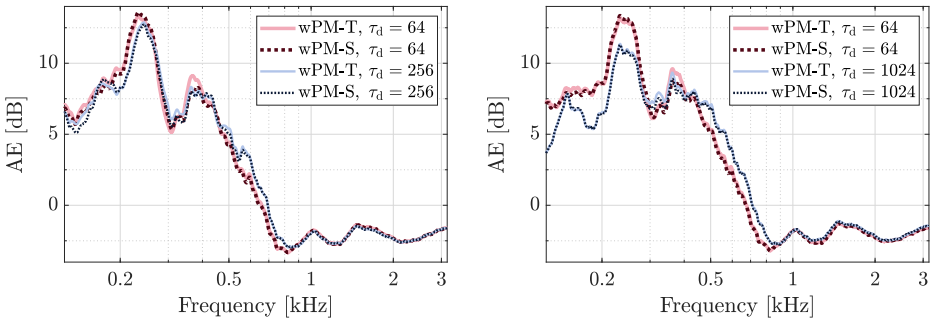

(e) AE ($I_g = 512$, $I_{g,k} = 52$) **(f)** AE ($I_g = 2048$, $I_{g,k} = 205$)

Figure 4.26: Acoustic contrast (a, b), MSE (c, d), and array effort (e, f) as a function of frequency for wPM-S and wPM-T. We include results for a filter length $I_g = 512$ with modelling delays $\tau_d = 64$ and $\tau_d = 256$ in the left-column, and for $I_g = 2048$ with $\tau_d = 64$ and $\tau_d = 1024$ in the right-column. A regularization factor $\beta_0 = 10^{-3}$ is used. For wPM-S, $I_{g,k}$ is computed using (4.77).

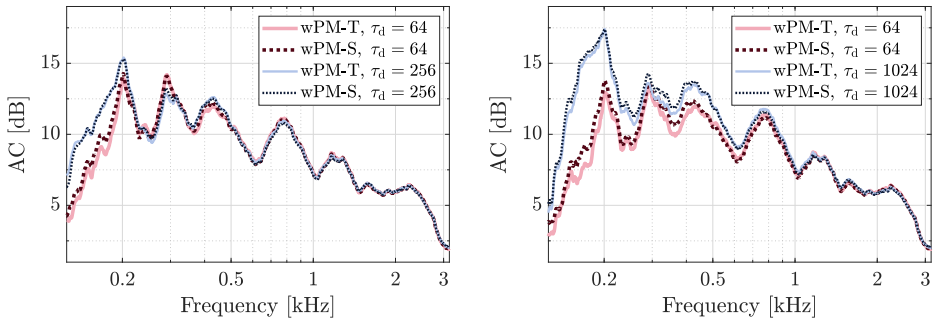

(a) AC ($I_g = 512$, $I_{g,k} = 52$)

(b) AC ($I_g = 2048$, $I_{g,k} = 205$)

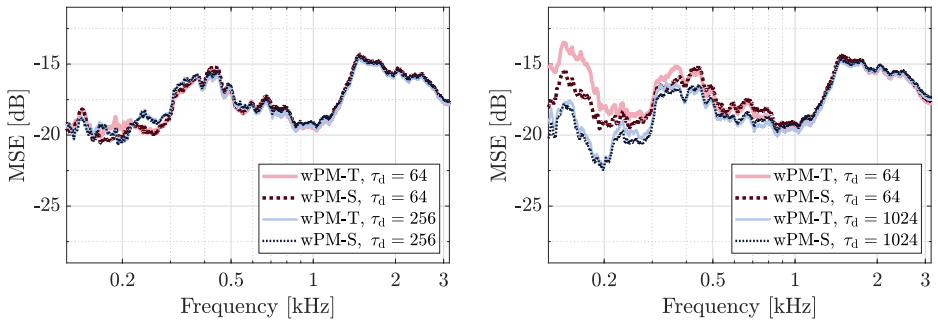

(c) MSE ($I_g = 512$, $I_{g,k} = 52$)

(d) MSE ($I_g = 2048$, $I_{g,k} = 205$)

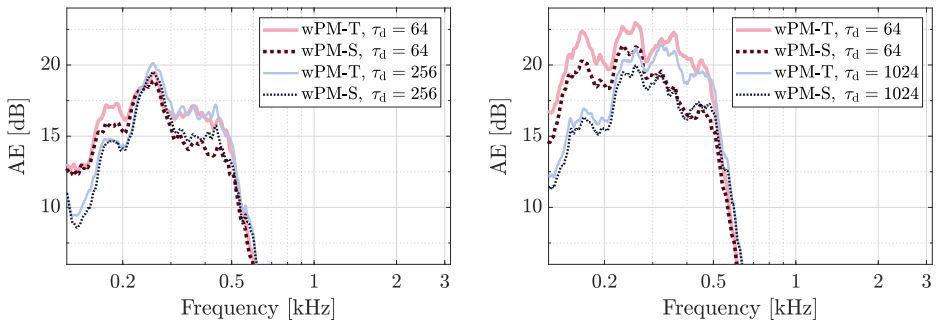

(e) AE ($I_g = 512$, $I_{g,k} = 52$)

(f) AE ($I_g = 2048$, $I_{g,k} = 205$)

Figure 4.27: Acoustic contrast (a, b), MSE (c, d), and array effort (e, f) as a function of frequency for wPM-S and wPM-T. We include results for a filter length $I_g = 512$ with modelling delays $\tau_d = 64$ and $\tau_d = 256$ in the left-column, and for $I_g = 2048$ with $\tau_d = 64$ and $\tau_d = 1024$ in the right-column. A regularization factor $\beta_0 = 10^{-5}$ is used. For wPM-S, $I_{g,k}$ is computed using (4.77).

Next, we compare the performance of wPM-S and wPM-F. We showed in Section 2.3.4 that the performance of wPM-F is good when long filters, long modelling delays, and high regularization factors are considered, so the use of wPM-S in those cases is not particularly interesting. Then, we focus next on the case with short modelling delays, in which wPM-S may be a good alternative to wPM-F. The performance of both algorithms is shown in Fig. 4.28 for $I_g = 2048$, $\tau_d = 64$, and $\beta_0 = 10^{-3}$. The results indicate that wPM-S clearly outperforms wPM-F for frequencies below 300 Hz, e.g., wPM-F presents 5 dB worse acoustic contrast and MSE around 180 Hz. To determine whether wPM-S still outperforms wPM-F when the additional

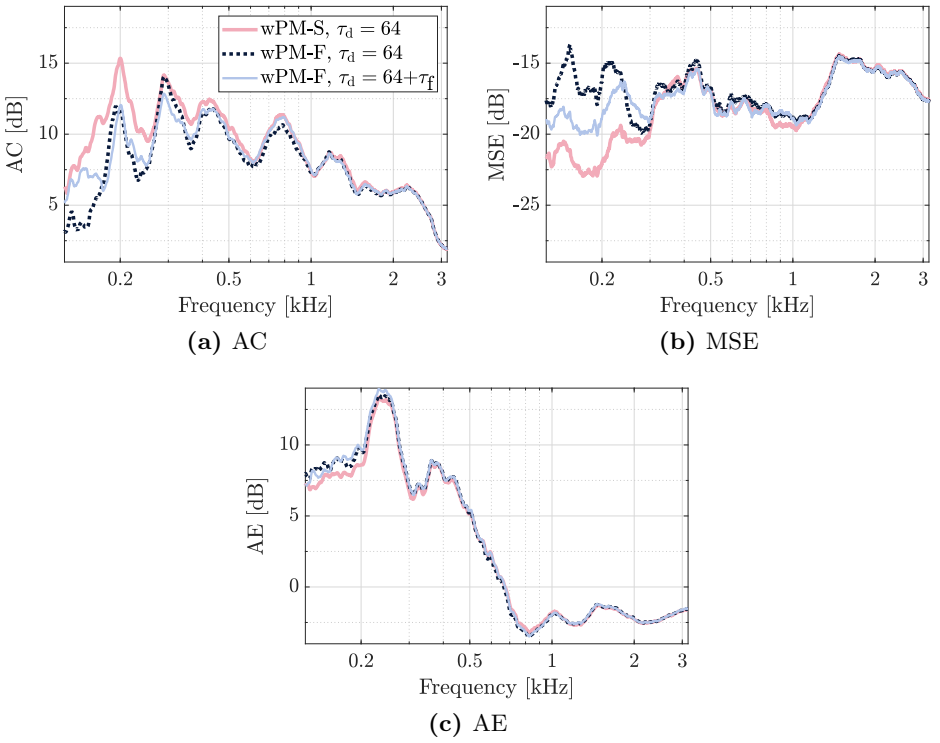

(a) AC **(b)** MSE

(c) AE

Figure 4.28: Acoustic contrast (a, b), MSE (c, d), and array effort (e, f) as a function of frequency for wPM-S and wPM-F. A filter length $I_g = 2048$, a modelling delay $\tau_d = 64$, and a regularization factor $\beta_0 = 10^{-3}$ are used. For wPM-S, $I_{g,k}$ is computed using (4.77). We also include the case with $\tau_d = 64+\tau_f$ for wPM-F, being $\tau_f = 44$.

delay produced by the filter bank is considered, we also include in Fig. 4.28 the performance of wPM-F with $\tau_\mathrm{d} = 64+\tau_\mathrm{f}$. Increasing the modelling delay from $\tau_\mathrm{d} = 64$ to $\tau_\mathrm{d} = 64+\tau_\mathrm{f}$ improves the performance of wPM-F. Still, it presents worse performance than wPM-S for frequencies below 300 Hz, e.g., wPM-F presents 3 dB lower acoustic contrast and 2.5 dB higher MSE around 180 Hz. Then, we can conclude that wPM-S outperforms wPM-F when short modelling delays are considered.

4.4.5 Subband-dependent configuration for wPM-S

Next, we evaluate the versatility provided by wPM-S to use different configurations in each subband of the filter bank. We consider the cases in which different filter lengths $I_{\mathrm{g},k}$, number of loudspeakers L, and solvers are considered in each subband. For the evaluations, we consider a GDFT filter bank with $I_\mathrm{p} = 45$, $K = 16$, and $R = 10$, a regularization factor $\beta_0 = 10^{-3}$, and a modelling delay $\tau_\mathrm{d} = 64$.

Filter length configuration

The length of the filters of a PSZ system is related, among others, with the reverberation time of the environment, which is frequency dependent (being usually higher for lower frequencies [129]). Also, the performance is not very sensitive to the filter length selection for frequencies whose wavelength is comparable with the size of the zones. For wPM-T and wPM-F, the frequencies with strongest filter length requirements determine the length of the filter that must be used for all the operation bandwidth. However, the versatility of wPM-S allows us to use different filter lengths in each subband. Then, the length of the subband filters can be selected for each subband according to the particular requirements in that subband.

Subband index (k)	0 - 1	2 - 7
Filter length ($I_{\mathrm{g},k}$)	205	30

Table 4.1: Filter length $I_{\mathrm{g},k}$ used in each subband for wPM-S with subband dependent filter-length. This configuration is denoted as $I_{\mathrm{g},k}$-SBD.

We show in Table 4.1 the subband-dependent filter length configuration for wPM-S considered next, which we denote as $I_{\mathrm{g},k}$-SBD. This configuration employs a filter length $I_{\mathrm{g},k} = 205$ for subbands 0 and 1, and $I_{\mathrm{g},k} = 30$ for subbands 2 to 7. The performance of wPM-S is shown in Fig. 4.29

for: 1) $I_{g,k} = 205$ in all subbands; 2) $I_{g,k} = 30$ in all subbands; and 3) the $I_{g,k}$-SBD configuration shown in Table 4.1. These results show that reducing the filter length from $I_{g,k} = 205$ to $I_{g,k} = 30$ produces an important degradation for frequencies below 800 Hz, with differences in the acoustic contrast and the MSE of about 3 dB. Also, $I_{g,k} = 30$ requires higher array effort than $I_{g,k} = 205$ in these frequencies. Then, long filters are needed to obtain good performance at low frequencies in this scenario. It is interesting to note that decreasing the filter length from $I_{g,k} = 205$ to $I_{g,k} = 30$ does not significantly influence the performance for frequencies above 800 Hz, which indicates that long filters are not required in these frequencies. Moreover,

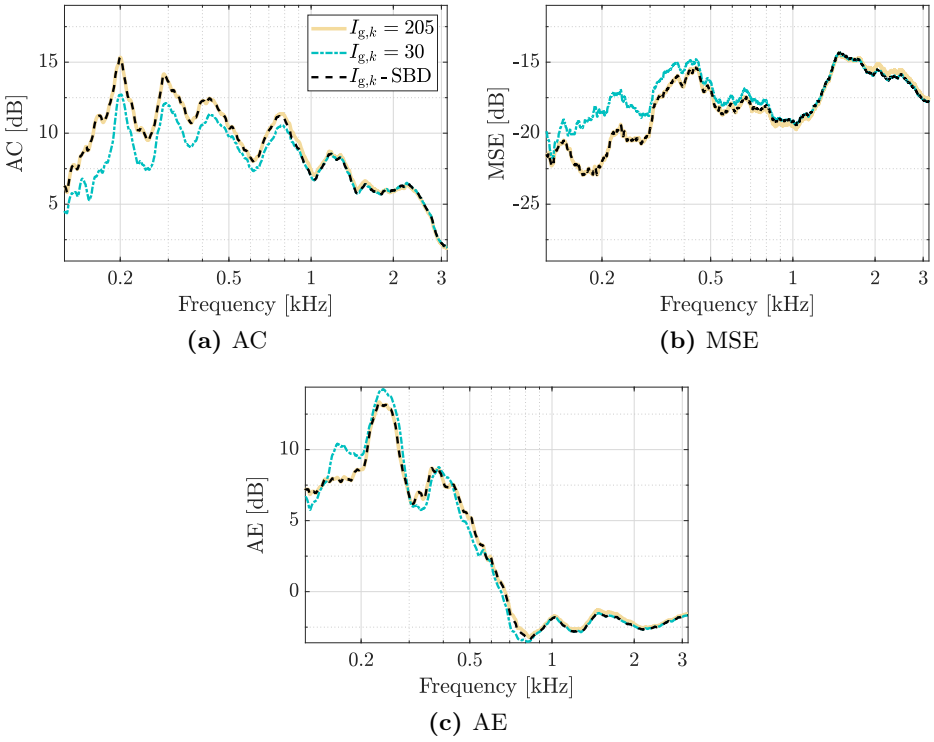

(a) AC **(b)** MSE

(c) AE

Figure 4.29: Acoustic contrast (a), MSE (b), and array effort (c) as a function of frequency for wPM-S with different subband filter lengths $I_{g,k}$. We include two configurations where $I_{g,k} = 205$ and $I_{g,k} = 30$ are used in all the subbands, and the configuration $I_{g,k}$-SBD shown in Table 4.1. The filters are computed assuming $\beta_0 = 10^{-3}$ and $\tau_d = 64$.

it is relevant to note that $I_{g,k} = 30$ presents a slightly better performance than $I_{g,k} = 205$ for frequencies above 2 kHz, which is produced because the longer filters are less robust to perturbations at higher frequencies. This means that $I_{g,k} = 205$ performs better than $I_{g,k} = 30$ if evaluated in the control points, but $I_{g,k} = 30$ is more robust to the mismatches between the RIRs in the control and validation points at high frequencies, and then, it performs better if evaluated in the validation points. Finally, Fig. 4.29 shows that the performance with $I_{g,k}$-SBD is almost identical to the performance with $I_{g,k} = 205$ in all subbands, since reducing the filter length in subbands 2 to 7 does not notably influence the performance of the system. Then, the versatility of wPM-S to select different filter lengths in different subbands is one of its main advantages, because it allows to use long filters only in those subbands that have stronger filter length requirements, and short filters in the other subbands that are less sensitive to the filter length selection.

Loudspeaker configuration

We noted in Section 2.2.1 that the ability of an array of loudspeakers to focus sound in certain directions at a given frequency is directly related to its inter-element distance and its aperture. This indicates that a PSZ system may benefit from using different configurations of loudspeakers in different frequencies to obtain good performance. This can be achieved with wPM-S, since its versatility allows us to use different sets of loudspeakers in each subband, as studied in Section 4.3.4. We show in Fig. 4.30 the sets of loudspeakers considered next for the evaluations.

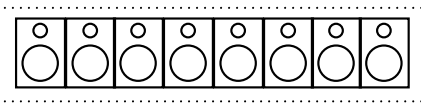

(a) Set $\mathcal{L}_{\text{all}}$ of 8 loudspeakers

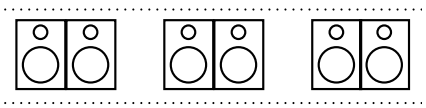

(b) Subset $\mathcal{L}_1$ of 6 loudspeakers

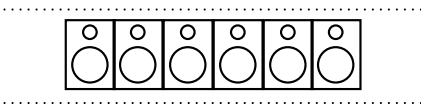

(c) Subset $\mathcal{L}_2$ of 6 loudspeakers

Figure 4.30: Sets of loudspeakers evaluated with wPM-S.

Subband index (k)	0 - 1	2 - 7
Set of loudspeakers	$\mathcal{L}_1$	$\mathcal{L}_2$

Table 4.2: Set of loudspeakers used in each subband for wPM-S with subband-dependent loudspeaker selection, where sets $\mathcal{L}_1$ and $\mathcal{L}_2$ are shown in Fig. 4.30b-c, respectively. This configuration is denoted as $\mathcal{L}$-SBD.

We show in Table 4.2 the subband-dependent loudspeaker configuration for wPM-S considered next, which we denote as $\mathcal{L}$-SBD. This configuration employs the subset $\mathcal{L}_1$ of 6 loudspeakers shown in Fig. 4.30b in subbands 0 and 1, and the subset $\mathcal{L}_2$ of 6 loudspeakers shown in Fig. 4.30c in subbands 2 to 7. The performance of wPM-S is shown in Fig. 4.31 using: 1) the set $\mathcal{L}_{\text{all}}$ of all available loudspeakers in all subbands; 2) the set $\mathcal{L}_1$ in all subbands; 3) the set $\mathcal{L}_2$ in all subbands; and 4) the $\mathcal{L}$-SBD configuration shown in Table 4.2. In the evaluations, we assume that a filter length $I_{\text{g},k} = 205$ is used in all cases. The results reveal that the overall best performance is achieved when all the available loudspeakers are used in all subbands. Even so, $\mathcal{L}_1$ can achieve similar performance to $\mathcal{L}_{\text{all}}$ for frequencies below 800 Hz, but noticeable worse performance for higher frequencies. For example, $\mathcal{L}_1$ leads to 2.5 dB worse acoustic contrast and MSE than $\mathcal{L}_{\text{all}}$ at frequencies near 1200 Hz. This degradation is produced by the spatial aliasing, which appears at lower frequencies for $\mathcal{L}_1$ due to its longer inter-element distance (see Fig. 4.30b). On the contrary, the performance of $\mathcal{L}_{\text{all}}$ and $\mathcal{L}_2$ is quite similar for frequencies above 500 Hz, with differences lower than 1 dB. However, $\mathcal{L}_2$ presents worse performance for frequencies below 500 Hz, because it presents a shorter array aperture (see Fig. 4.30c). Moreover, we can observe in Fig. 4.31 that the performance achieved with $\mathcal{L}$-SBD is broadly similar to the one with $\mathcal{L}_{\text{all}}$ in all the studied frequency range, with some degradations of up to 1 dB in a small subset of frequencies. Thus, we can conclude that, according to the desired performance and to the available computational capabilities, the flexibility of wPM-S allows us to select the most convenient set of loudspeakers for each subband. Finally, it is important to mention that the versatility of wPM-S is particularly beneficial for cases where multiple arrays of loudspeakers are used in the system, since each array can be selected to operate only in the subbands in which it has suitable directional properties.

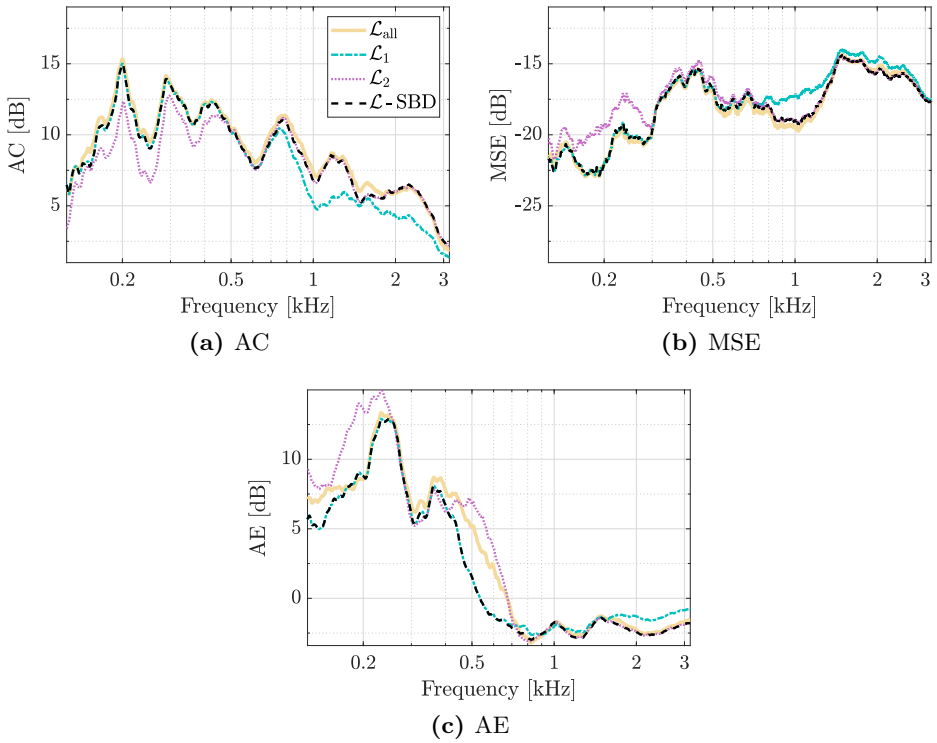

(a) AC **(b)** MSE **(c)** AE

Figure 4.31: Acoustic contrast (a), MSE (b), and array effort (c) as a function of frequency for wPM-S with different loudspeaker configurations. We include results for the cases in which the sets of loudspeakers shown in Fig. 4.30, i.e., $\mathcal{L}_{\text{all}}$, $\mathcal{L}_1$, and $\mathcal{L}_1$, are used in all subbands, and for the configuration $\mathcal{L}$-SBD shown in Table 4.2. The filters are computed assuming $I_{\text{g},k} = 205$, $\beta_0 = 10^{-3}$, and $\tau_{\text{d}} = 64$.

Solver configuration

So far, we have assumed that a Cholesky solver is used to compute the exact optimal subband filters for wPM-S. However, the PSZ system could benefit from using different solvers in each subband. In particular, the superfast solver [79] seems a good option when dealing when long filters in certain subbands. Next, we evaluate the use of the superfast solver to compute the subband filters for wPM-S using different approximation orders in each subband.

We show in Table 4.3 the subband-dependent solver configuration for wPM-S, which we denote as P-SBD. This configuration employs the superfast solver to compute the subband filters with an approximation order $P = 2000$ in subband 0, and $P = 10$ in subbands 1 to 7. The performance

Subband index (k)	0	1 - 7
Approximation order (P)	2000	10

Table 4.3: Approximation order in each subband for wPM-S using the superfast solver [79]. This configuration is denoted as P-SBD.

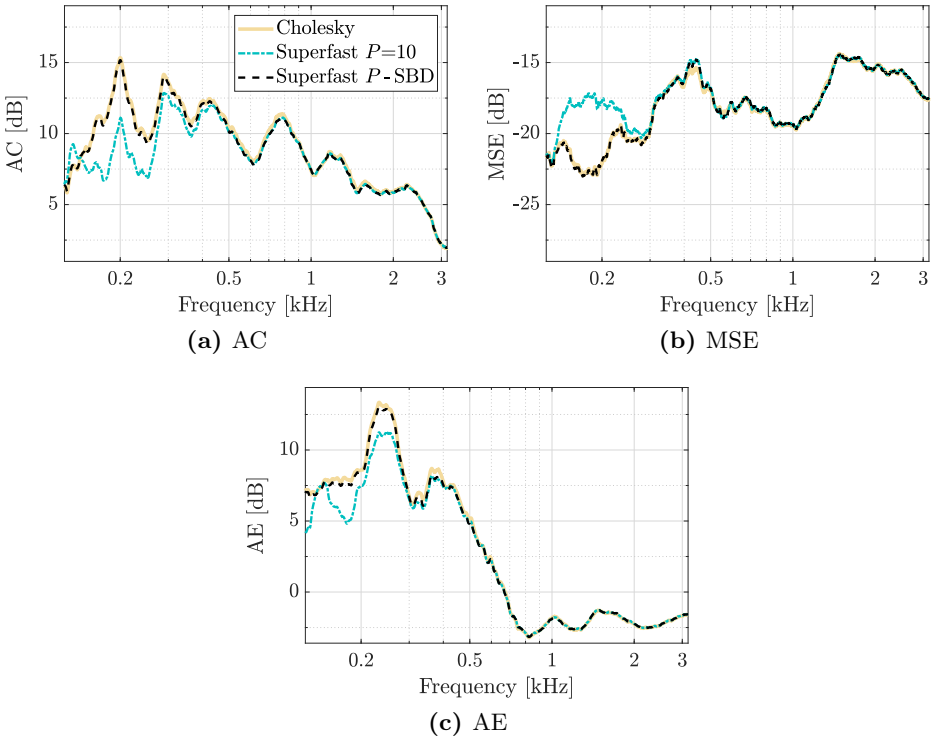

(a) AC **(b)** MSE **(c)** AE

Figure 4.32: Acoustic contrast (a), MSE (b), and array effort (c) as a function of frequency for wPM-S with different solvers. We include the cases in which the Cholesky solver and the superfast solver [79] with $P = 10$ are used in all subbands, and the configuration P-SBD shown in Table 4.3. The filters are computed assuming $I_{g,k} = 205$, $\beta_0 = 10^{-3}$, and $\tau_d = 64$.

of wPM-S is shown in Fig. 4.32 using: 1) the Cholesky solver in all subbands; 2) the superfast solver with $P = 10$ in all subbands; and 3) the P-SBD configuration shown in Table 4.3. We assume that a filter length $I_{\mathrm{g},k} = 205$ and the $L = 8$ available loudspeakers are used in all subbands. In Fig. 4.32, the overall best performance is achieved when the Cholesky solver is used in all subbands. The superfast solver with $P = 10$ offers almost identical performance to the Cholesky solver for frequencies above 350 Hz, but worse performance for lower frequencies, e.g., it presents 4 dB lower acoustic contrast and higher MSE than the Cholesky solver for frequencies around 200 Hz. This fact indicates that the superfast solver can accurately approximate the optimal filters with low orders P at mid and high frequencies, whereas high orders are required for low frequencies. The motivation is that the initial estimate for the superfast solver is very close to the optimal solution for mid and high frequencies, but it is quite different for low frequencies. Moreover, we can observe in Fig. 4.32 that the performance achieved with P-SBD is almost identical to the one with the Cholesky solver. Then, the versatility of wPM-S allows us to decrease the approximation order for the superfast solver in the mid and high-frequency subbands with negligible performance degradations.

4.4.6 Computational complexity

Next, we compare the computational complexity of wPM-T, wPM-F, and wPM-S for a PSZ system with $L = 8$ loudspeakers. We show in Fig. 4.33a and 4.33b the number of FLOPs and the computation time, respectively, required to compute the optimal filters as a function of the filter length for the following cases:

1. wPM-T with the Cholesky solver.
2. wPM-T with the superfast solver [79] and $P = 2000$.
3. wPM-F with the Cholesky solver for each frequency bin.
4. wPM-S with the Cholesky solver (the same filter length and number of loudspeakers are used in all subbands).
5. wPM-S with the Cholesky solver and config. $I_{\mathrm{g},k}$-SBD in Table 4.1.
6. wPM-S with the Cholesky solver and config. $\mathcal{L}$-SBD in Table 4.2.
7. wPM-S with the superfast solver [79] and config. P-SBD in Table 4.3.

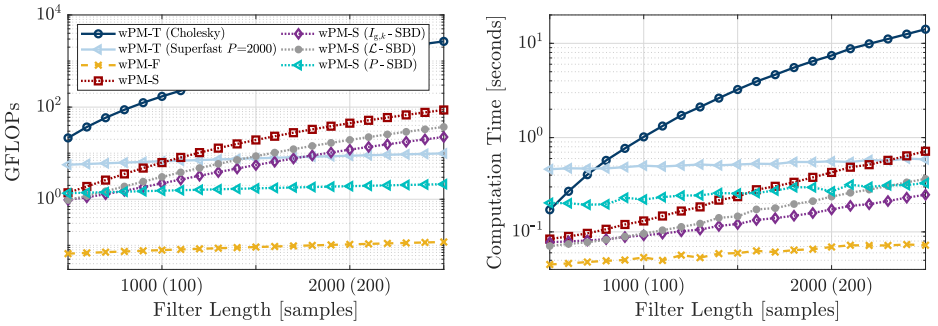

(a) FLOPs **(b)** Computation time

Figure 4.33: Number of FLOPs and computation time and in (a) and (b), respectively, required to compute the optimal filters for wPM-T, wPM-F, and wPM-S as a function of the filter length. In the x-axis, we use the notation I_{g} ($I_{\mathrm{g},k}$), where I_{g} is the length of the broadband filters and $I_{\mathrm{g},k}$ is the length of the equivalent subband filters (obtained with (4.77)).

In the evaluations, when a specific filter length I_{g} is considered for wPM-T and wPM-F, (4.77) is used to obtain the length $I_{\mathrm{g},k}$ of the equivalent subband filters for wPM-S. Moreover, for $I_{\mathrm{g},k}$-SBD the filter length in the x-axis is only used in subbands 0 and 1, whereas $I_{\mathrm{g},k} = 30$ is used in the other subbands. The operation count for the different algorithms can be found in Appendix A. In order to measure the computation time, the different algorithms were implemented with C language, as described in Appendix A, and ran from MATLAB R2018a using *mex* functions [96] on an Intel Core i7-7700 processor at 3.60 GHz. The measurement was computed as the mean over 50 executions. It is worth mentioning that the number of FLOPs and the computation time required to compute the subband components of the RIRs and the target responses for wPM-S are taken into account in Fig. 4.33a and 4.33b, respectively.

The results in Fig. 4.33a indicate that wPM-F is less computationally demanding than wPM-T and wPM-S in all cases. Also, we can see that wPM-S without subband-dependent configuration requires lower number of FLOPs than wPM-T for filter lengths smaller than 1000, however, wPM-T with the superfast solver requires less FLOPs for longer filters. The results in Fig. 4.33a show that all the subband-dependent configurations can effectively reduce the number of FLOPs required by wPM-S. Specifically,

$\mathcal{L}$-SBD reduces by a factor of 2 the number of FLOPs required by wPM-S, and presents computational savings with respect to wPM-T for filter lengths smaller than 1500. Similarly, $I_{\mathrm{g},k}$-SBD reduces by a factor of 3 the number of FLOPs required by wPM-S, and presents computational savings with respect to wPM-T for filter lengths smaller than 1750. Moreover, P-SBD leads to very significant computational improvements and requires lower number of FLOPs than wPM-T with any of the considered solvers for all the studied filter lengths. In particular, wPM-S with P-SBD requires about 4.5 times less FLOPs than wPM-T with the superfast solver. The computation time measurements in Fig. 4.33b show slightly different trends to those in Fig. 4.33a, particularly in the cases in which the superfast solver is involved. This may be produced because other computational aspects than the number of FLOPs have a significant influence on the running time of the superfast solver, e.g., memory access and displacements. We can see in Fig. 4.33b that $I_{\mathrm{g},k}$-SBD is the configuration of wPM-S that lowest computation time exhibits. It presents substantially lower computation time than wPM-T with any of the considered solvers for all the studied filter lengths. For example, it exhibits about 5.5 and 2.5 times less computation time than wPM-T with the superfast solver for filter lengths 1000 and 2500, respectively. Moreover, let us note that the superfast solver with $P = 2000$ may not be suitable to compute the filters for wPM-T when low regularization factors are considered. For instance, we showed in Section 3.6.3 that values of P of about 10^5 are required to obtain a good approximation of the filters for $\beta_0 = 10^{-5}$. Then, in this case the computational savings offered by wPM-S with respect to wPM-T are even more significant, since the computational demands of the superfast solver are approximately 50 times higher for $P = 10^5$ than for $P = 2000$. All these facts indicate that wPM-S with a proper subband-dependent configuration can offer substantial computational complexity savings with respect to wPM-T.

An important aspect for PSZ systems is the computational complexity required to filter the input audio signals, as real-time operation is usually needed. Next, we compare the computational demands of broadband filtering (for wPM-T and wPM-F) and subband filtering with a GDFT filter bank with $I_{\mathrm{p}} = 45$, $K = 16$, and $R = 10$ (for wPM-S). We show in Fig. 4.34 the number of FLOPs required by a system with $L = 8$ loudspeakers to filter an input signal of 63 samples (i.e., a frame of 10 ms). We consider the broadband filtering based on the FFT [130], and the polyphase implementation of the GDFT filter bank [100] for subband filtering. We also

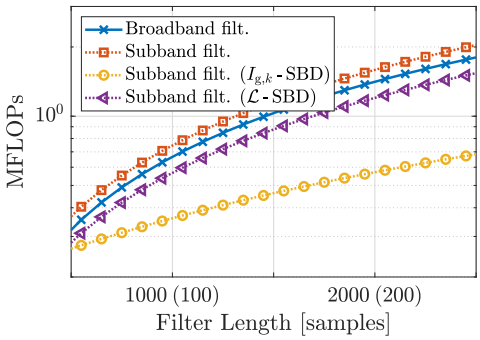

Figure 4.34: Number of FLOPs to filter a frame of 10 ms (63 samples) using broadband and subband filtering as a function of the filter length. In the x-axis, we use the notation I_{g} ($I_{\mathrm{g},k}$), where I_{g} is the length of the broadband filters and $I_{\mathrm{g},k}$ is the length of the equivalent subband filters (obtained with (4.77)).

include in Fig. 4.34 the results for subband filtering using the configurations $I_{\mathrm{g},k}$-SBD and $\mathcal{L}$-SBD shown in Table 4.1 and 4.2, respectively. The results show that subband filtering requires slightly higher number of FLOPs than broadband filtering when the same configuration is used in all subbands. However, subband filtering with $\mathcal{L}$-SBD, and specially, with $I_{\mathrm{g},k}$-SBD is capable of reducing the number of FLOPs required by broadband filtering. Particularly, subband filtering with $I_{\mathrm{g},k}$-SBD requires about 2.6 times less FLOPs than broadband filtering for a filter length of 2500.

From these results, we can conclude that the versatility provided by wPM-S is a clear advantage for PSZ systems. We showed that reducing the filter length, the number of loudspeakers, and the approximation order in certain subbands does not produce noticeable degradations in the performance of wPM-S, and leads to very important computational savings. Particularly, wPM-S with an appropriated subband-dependent configuration can present significantly lower computational complexity than wPM-T. Still, wPM-S requires higher computational efforts than wPM-F, although it notably outperforms wPM-F for short system delays. The suitability of an algorithm for a PSZ system depends on its specific requirements and available capabilities. For example, wPM-S is a good candidate for dynamic systems requiring low latency, as it presents lower computational demands than wPM-T and better performance than wPM-F for short system delays.

4.5 Summary

In this chapter, we proposed using subband filtering with a GDFT filter bank for PSZ systems. In this regard, we presented a novel subband formulation of the PSZ problem that makes use of the subband decomposition algorithm proposed in [102], which is further optimized in this work to reduce the required number of matrix inversions. The main advantage of the presented subband formulation is that it allows us to formulate independent optimization problems for each subband of the filter bank. We proposed the wPM-S algorithm to compute the optimal subband filters, which is based on formulating a time-domain optimization for each subband using the wPM criterion. The proposed algorithm was experimentally evaluated in a room with reverberation time $T_{60} = 500$ ms.

First, we studied the influence of the configuration of the filter bank on wPM-S. We experimentally determined that good performance is achieved when the RE and the ASR of the filter bank are below -35 dB. In particular, long prototype filters, low number of subbands, and high oversampling factors, assure low RE and ASR, but also lead to systems with long delays and high computational demands. Hence, the configuration of the filter bank must be selected taking into account the performance and delay requirements of the system, and the available computational capabilities.

Next, we compared wPM-S with the algorithm proposed in [47], which also makes use of subband filtering. The evaluation results showed that wPM-S outperforms the algorithm in [47], since this presents bad performance in the edges of the subbands due to its high aliasing levels. Also, the system delay for wPM-S is much shorter than for the algorithm in [47].

Later, we compared the performance of wPM-T, wPM-F, and wPM-S. The evaluation results indicated that wPM-S and wPM-T offer almost equal performance for moderately high regularization factors, although wPM-S presents an additional delay in the system that is introduced by the filter bank. Also, we showed that wPM-S outperforms wPM-T for low regularization factors. The motivation is that wPM-S offers higher robustness to perturbations thanks to the small random errors produced by the subband decomposition of the RIRs. Furthermore, we determined that wPM-S presents better performance than wPM-F when short modelling delays are considered, even when the additional delay produced by the filter bank is considered for wPM-F. All these results indicate that, although wPM-T

is preferred for systems requiring extremely low delays, wPM-S is a good alternative to wPM-T, and is preferred to wPM-F, for systems with more relaxed delay requirements, e.g, for system delays between 10 and 20 ms.

Afterwards, we considered the versatility offered by wPM-S to use different configurations in each subband. First, we evaluated wPM-S with different filter lengths in each subband, and showed that the performance is not degraded if short filters are used in the high-frequency subbands. Furthermore, we evaluated the performance of wPM-S with different sets of loudspeakers in each subband. The results revealed that reducing the number of loudspeakers in certain subbands may not produce significant degradations in the performance of the system. Moreover, we investigated the use of the superfast solver [79] to compute the filters for wPM-S with different approximation orders in each subband. The results indicated that good performance is obtained even if low approximation orders are selected for the high-frequency subbands, however, high orders are required in the low-frequency subbands. Then, PSZ systems benefit from the versatility offered by wPM-S, which allows to select shorter filters, lower number of loudspeakers, and lower approximation orders in certain subbands with negligible performance degradation.

Finally, the computational complexity of wPM-S was evaluated and compared with wPM-T and wPM-F. First, we showed that the computational savings offered by wPM-S are minor when the same filter length, the same set of loudspeakers, and the same solver are used in all subbands. However, very important computational savings are obtained when the versatility of wPM-S is exploited to use suitable configurations in each subband. In that case, wPM-S requires substantially lower computational efforts than wPM-T to compute the filters, even when the superfast solver [79] is used for wPM-T. Still, wPM-S presents higher computational complexity than wPM-F. Moreover, subband filtering requires lower computational efforts than broadband filtering when proper filter lengths are selected for each subband. From these results, we can conclude that wPM-S is a good alternative to wPM-T and wPM-F for PSZ systems, since it presents better performance than wPM-F for short system delays and it requires lower computational efforts than wPM-T.

Chapter 5

Weighted Pressure Matching with windowed targets

In Chapter 2 we reviewed the state-of-the-art algorithms to compute the filters for PSZ systems, and concluded that weighted Pressure Matching (wPM) is a good candidate for these systems because it can offer a trade-off between reproduction error in the bright zone and acoustic contrast. The selection of the target responses for the bright zone is a key point for wPM, since different targets can lead to different levels of acoustic contrast. However, this is an aspect that, to the best of our knowledge, has not been previously studied in the literature. The most usual approach in reverberant environments is to select the target for the bright zone as the Room Impulse Response (RIR) produced by one of the loudspeakers of the system [39, 52, 57, 60, 131]. This approach aims to synthesize all the direct and reverberant components of the RIR in the bright zone while minimizing the energy in the dark zone. The late reverberation components, however, can be assumed to be diffuse for frequencies above the Schroeder frequency. We will show that there is no set of filters that can achieve high energy differences for the diffuse reverberant components in the bright and dark zones. Therefore, trying to synthesize these components in the bright zone while minimizing their energy in the dark zone does not give the best overall performance. Then, we propose a variation of the approach used to select the targets for wPM, in which the target impulse responses for the bright zone are windowed. By windowing the targets, we can control

which reverberant components are synthesized and which are minimized in the bright zone. We present experimental evaluations that indicate that windowing the target for the bright zone can lead to acoustic contrast improvements with respect to the case without windowing. In general, it seems that the optimal window length is frequency and scenario dependent, but the improvements that can be obtained are more significant for mid-high frequencies. Moreover, the results show that the higher the room reverberation, the higher the performance improvements obtained by windowing the target. The wPM algorithm can be formulated in time-domain [39], frequency-domain [50], and subband-domain (as proposed in Chapter 4). For the evaluations, because of its simplicity for the comparison of the different targets, we will use the frequency-domain formulation of wPM, i.e., wPM-F. Nevertheless, our findings can be generalized to the other formulations of wPM.

In this chapter, we first review the target selection for wPM, and then, we propose the novel selection in which the target in the bright zone is windowed. Afterwards, the proposed target selection is experimentally evaluated in a room with reverberation time $T_{60} = 500$ ms. Finally, experimental evaluations for the proposed approach in a damped room with reverberation time $T_{60} = 180$ ms are presented.

5.1 Target selection

The target selected for the bright zone heavily influences the performance of wPM, however, this is an aspect that has not been extensively studied in the PSZ related literature. Some works, as [132, 133], proposed selecting the target in the bright zone as the response produced by a plane wave arriving from a certain direction. However, this target is very restrictive, because it not only aims to cancellate all the reverberation components in the bright zone, but also, it targets the equalization of the response of the loudspeakers. The performance can be heavily degraded when using such a restrictive target, especially in reverberant environments, because in this case low error in the bright zone can only be achieved at the cost of important degradations in the acoustic contrast. The most common approach in reverberant environments is to select the target impulse responses for the bright zone as the delayed RIRs from one of the loudspeakers of the system to all of the control points in the bright zone [39, 52, 57, 60, 131]. Next, we

review this approach, and later, we propose an alternative method in which the targets for the bright zone are windowed. It is important to mention that, although we will evaluate the performance of the different targets using wPM-F, we present expressions for the impulse response of the targets, i.e., $d_m(n)$, rather than their frequency response, i.e., $D_m(f)$. This is because the expressions for the impulse responses are more meaningful for our study. In any case, the expressions for the target impulse responses $d_m(n)$ presented next can be directly used with the three formulations of wPM by applying the following procedures:

- For wPM-F, the vector $\bar{\mathbf{d}}_f$ in (2.22) is formed using the DFT of d_m.
- For wPM-T, the vector $\mathbf{d}_m$ in (2.29) is formed using d_m.
- For wPM-S, the vector $\dot{\mathbf{d}}_{m,k}$ in (4.67) is formed using the subband components of d_m.

Also, it is important to mention that in this chapter the target response for the dark zone is always selected as a null response, i.e., $d_m(n)$=0 for $m \in \mathcal{D}$.

5.1.1 Non-windowed targets

Next, we review the approach used in [39, 52, 57, 60, 131] to select the target response for the bright zone. This approach is based on choosing the target for the bright zone as the delayed RIRs from one of the loudspeakers to all of the control points in the bright zone, i.e.,

$$d_m(n) = h_{ml_\mathrm{r}}(n - \tau_\mathrm{d}), \quad \text{for } m \in \mathcal{B}, \tag{5.1}$$

where $l_\mathrm{r} \in \{0, \ldots, L-1\}$ is the index of the reference loudspeaker, and τ_d is the modelling delay. We present in Fig. 5.1 an schematic to illustrate the main idea behind the target (5.1). In the schematic, we show an example of the RIRs between the reference loudspeaker and one control point in the bright and dark zones, and also, the targets that we aim to achieve at these control points using the target (5.1). It is clear that with (5.1) we want to synthesize the direct propagation component and all the reverberant components in the bright zone while minimizing the energy of all the components in the dark zone.

5.1.2 Windowed targets

Now, we present the proposed approach to select the targets for the bright zone. First, let us define

$$w_{I_\mathrm{w}}(n) = \begin{cases} \text{window values} & \text{for } -I_\mathrm{w} < n < I_\mathrm{w} \\ 0 & \text{otherwise} \end{cases}, \tag{5.2}$$

which is a generic window function of length $2I_\mathrm{w}-1$ centered on $n = 0$. For the sake of simplicity, from now on we are going to refer to the length of the window as I_w, i.e., the number of positive-time samples of the window. Next, we alternatively propose to define the target impulse response in the control points of the bright zone as

$$d_m(n) = \begin{cases} w_{I_\mathrm{w}}(n-\tau_\mathrm{d}-\tau_{ml_\mathrm{r}})\, h_{ml_\mathrm{r}}(n-\tau_\mathrm{d}) & \text{if } I_\mathrm{w} < \infty \\ h_{ml_\mathrm{r}}(n-\tau_\mathrm{d}) & \text{otherwise} \end{cases}, \quad \text{for } m \in \mathcal{B}, \tag{5.3}$$

in which the window w_{I_w} is time-shifted such that its center is located on $n = \tau_\mathrm{d}+\tau_{ml_\mathrm{r}}$, being τ_{ml_r} the propagation delay corresponding to the direct propagation component of h_{ml_r}. First, it is relevant to note that the targets in (5.1) and (5.3) are equivalent when $I_\mathrm{w} = \infty$. However, (5.3) has the advantage that, by selecting the window length, we can choose the reverberant components that we want to synthesize and which should be suppressed in the bright zone. Then, when selecting a window length that removes certain reverberant components, we are aiming to achieve dereverberation in the bright zone. We present in Fig. 5.2 a schematic to illustrate this effect. There, we show an example of the RIRs between the reference loudspeaker and one control point in the dark and bright zones, and also, the targets that we aim to achieve at these control points using a window of length I_w. In the schematic we can see that, for time instants within the window, we seek to synthesize the direct propagation component and some early reflections in the bright zone while minimizing the energy in the dark zone. However, for time instants after the end of the window we want to minimize the energy of the reverberant components both in the bright and dark zones.

So far, it is not clear whether windowing the target responses in the bright zone will lead to performance improvements. Next, we give some intuition to better understand why the performance may be improved. First, let us note that usually the early part of the RIRs is formed by the direct

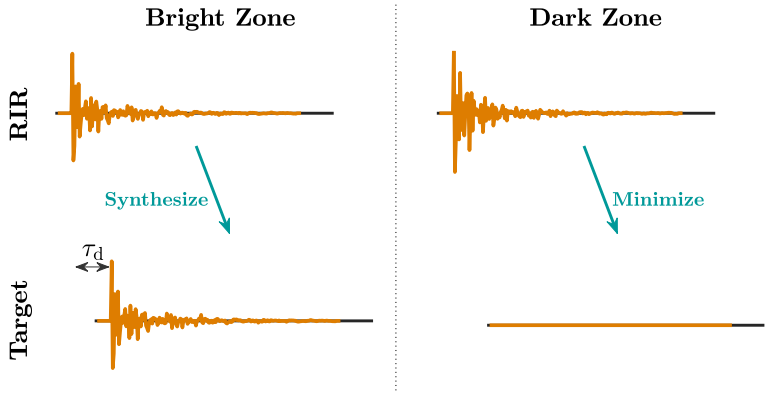

Figure 5.1: Schematic to illustrate the target selection used in [39, 52, 57, 60, 131]. The upper plots represent the RIRs between the reference loudspeaker and one control point in the bright and dark zones, and the lower plots represent the selected targets at these control points.

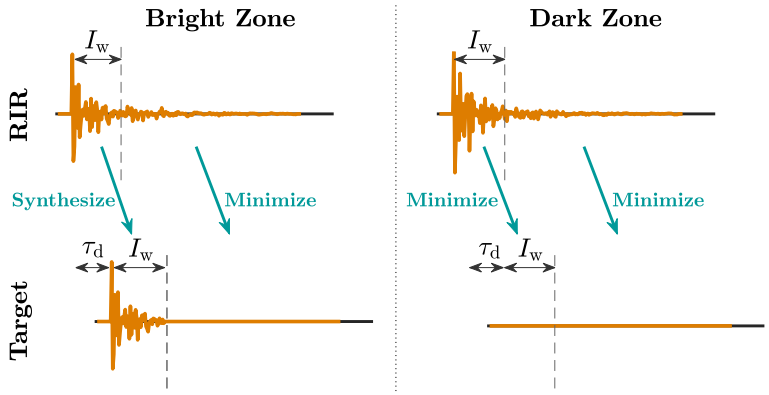

Figure 5.2: Schematic to illustrate the proposed target selection. The upper plots represent the RIRs between the reference loudspeaker and one control point in the bright and dark zones, and the lower plots represent the windowed targets at these control points using a window of length I_w.

propagation component and some sparse early reflections [134]. However, the later part of the RIRs is formed by a large number of contributions from waves arriving from all directions, so these components can be considered diffuse, especially above the Schroeder frequency [129]. Now, let us denote $\bar{\mathbf{H}}_{b,f}$ and $\bar{\mathbf{H}}_{d,f}$ as the matrices containing the room frequency responses at

frequency f between all loudspeakers and control points in the bright and dark zones, respectively, which can be decomposed as

$$\bar{\mathbf{H}}_{\mathrm{b},f} = \bar{\mathbf{H}}_{\mathrm{b},f}^{\mathrm{dir}} + \bar{\mathbf{H}}_{\mathrm{b},f}^{\mathrm{early}} + \bar{\mathbf{H}}_{\mathrm{b},f}^{\mathrm{diff}}, \tag{5.4}$$

$$\bar{\mathbf{H}}_{\mathrm{d},f} = \bar{\mathbf{H}}_{\mathrm{d},f}^{\mathrm{dir}} + \bar{\mathbf{H}}_{\mathrm{d},f}^{\mathrm{early}} + \bar{\mathbf{H}}_{\mathrm{d},f}^{\mathrm{diff}}, \tag{5.5}$$

where $\bar{\mathbf{H}}_{\mathrm{b},f}^{\mathrm{dir}}$, $\bar{\mathbf{H}}_{\mathrm{b},f}^{\mathrm{early}}$, and $\bar{\mathbf{H}}_{\mathrm{b},f}^{\mathrm{diff}}$, are the frequency responses at frequency f related to the direct propagation components, the early reflections, and the late diffuse components of the RIRs in the bright zone, respectively. Similarly, $\bar{\mathbf{H}}_{\mathrm{d},f}^{\mathrm{dir}}$, $\bar{\mathbf{H}}_{\mathrm{d},f}^{\mathrm{early}}$, and $\bar{\mathbf{H}}_{\mathrm{d},f}^{\mathrm{diff}}$, are the frequency responses at frequency f related to the direct propagation components, the early reflections, and the late diffuse components of the RIRs in the dark zone, respectively. From the ACC algorithm [61], we know that the maximum acoustic contrast that can be achieved between the diffuse components in the bright and dark zones is given by the highest eigenvalue of matrix

$$\left(\left(\bar{\mathbf{H}}_{\mathrm{d},f}^{\mathrm{diff}}\right)^{H} \bar{\mathbf{H}}_{\mathrm{d},f}^{\mathrm{diff}}\right)^{-1} \left(\bar{\mathbf{H}}_{\mathrm{b},f}^{\mathrm{diff}}\right)^{H} \bar{\mathbf{H}}_{\mathrm{b},f}^{\mathrm{diff}}. \tag{5.6}$$

It is important to note that the diffuse reverberation components can be assumed to be of similar energy but uncorrelated between the different control points [129], and then, we can assume that [45]

$$\left(\bar{\mathbf{H}}_{\mathrm{b},f}^{\mathrm{diff}}\right)^{H} \bar{\mathbf{H}}_{\mathrm{b},f}^{\mathrm{diff}} \approx \sigma\mathbf{I}, \tag{5.7}$$

$$\left(\bar{\mathbf{H}}_{\mathrm{d},f}^{\mathrm{diff}}\right)^{H} \bar{\mathbf{H}}_{\mathrm{d},f}^{\mathrm{diff}} \approx \sigma\mathbf{I}, \tag{5.8}$$

where σ is the energy of the diffuse field in the room. Therefore, using (5.6) to (5.8), we determine that the maximum acoustic contrast that can be achieved between the diffuse components in the bright and dark zones is approximately 1 (in linear units). This is an important fact, since it reveals that there is no set of filters that is able to provide significant energy differences between the diffuse components in the bright and dark zones. Thus, selecting a target that tries to synthesize all of the reverberant components in the bright zone, including the diffuse components, is not a wise choice, because the previous derivation indicates that the diffuse components can not be synthesized in the bright zone and at the same time suppressed in the dark zone. Then, it seems a better option to select a target that aims to suppress the diffuse components both in the bright

and dark zones. This can be achieved with the proposed target (5.3) by properly selecting the window length I_{w}. Later, we will present evaluation results that show that improvements in the performance can be achieved by windowing the target, i.e., aiming the minimization of the energy of the late reverberant components in both zones.

Finally, let us point out that windowing has been previously used in the context of PSZ systems in [37, 66, 135]. In these works, the authors proposed to window the RIRs used to form matrix $\bar{\mathbf{H}}_f$ in (2.15) for wPM-F. The effect of windowing in these cases is similar to regularization, as it makes the filters more robust to inaccuracies in the RIRs. The approach previously proposed is conceptually different, since no windowing is applied to the RIRs used to form matrix $\bar{\mathbf{H}}_f$, but windowing is instead applied to the targets for the bright zone used to form $\bar{\mathbf{d}}_f$ in (2.22) for wPM-F.

5.2 Kurtosis as a measure of diffuseness

Previously, we discussed that the proposed target selection may lead to performance improvements because it allows us to minimize the energy of the diffuse reverberant components in the bright and dark zones. Then, an important point is to determine when we can consider that the RIRs are diffuse, since this will allow us to choose a suitable window length I_{w} to compute the target (5.3).

The Kurtosis of a Probability Density Function (PDF) of a random variable x is defined as [136]

$$K_x = \frac{\mathbb{E}\left\{(x-\mu_x)^4\right\}}{\sigma_x^4} - 3, \tag{5.9}$$

where μ_x and σ_x are the mean value and the standard deviation of x, respectively. The Kurtosis is a measure of the tailedness of the probability distribution, e.g., the Kurtosis of a Gaussian PDF is 0. Jeong [137] showed that the diffuseness of the late reverberation is closely related to the Kurtosis of the RIRs. Particularly, Jeong [137] demonstrated that the early part of the RIRs, containing the direct propagation component and strong deterministic reflections, is unlikely to have a Gaussian distribution, so it presents high Kurtosis levels. However, the late diffuse components of the RIRs present Kurtosis values close to 0. The motivation is that the reflec-

tion density is high for the diffuse part of the RIRs, which makes it more likely to follow a Gaussian PDF. Then, in this work we use the Kurtosis of the RIRs to determine their diffuseness. In particular, we estimate the average Kurtosis of all the RIRs of the system as

$$K_h(n) = \frac{1}{ML} \sum_{\forall m, \forall l} \left(\frac{\frac{1}{I_\mathrm{s}} \sum_{r=0}^{I_\mathrm{s}-1} \left(h_{ml}(n+r) - \mu_{ml}^{(n)} \right)^4}{\left(\sigma_{ml}^{(n)} \right)^4} - 3 \right), \tag{5.10}$$

where I_s is the segment length used to estimate the Kurtosis of the RIRs in time n, and $\mu_{ml}^{(n)}$ and $\sigma_{ml}^{(n)}$ are the mean value and the standard deviation of h_{ml}, respectively, over the interval $n, \ldots, n+I_\mathrm{s}-1$. Let us note that we consider that all the RIRs h_{ml} are aligned before computing the Kurtosis, such that their direct propagation component is located at sample index $n = 0$. In the following sections, we will show empirically that the Kurtosis of the RIRs is a good indicator for the selection of the window length for the target (5.3).

5.3 Performance evaluation in an office-like room

In this section, the proposed target selection is experimentally evaluated in an office-like room. The room is not acoustically treated, and it includes common office furniture, e.g., tables, chairs, cabinets, shelves, etc. We selected this room for the experiments to evaluate the performance of the proposed approach in a realistic environment.

5.3.1 Setup and methodology

Setup

The setup described in Section 2.3.1 is used for the evaluations of this section, i.e., a linear array of 8 two-way loudspeakers and single bright and dark zones in a office-like room with reverberation time $T_{60} = 500$ ms. We consider that the system is operating at a sampling frequency of 6300 Hz, and that the length of the RIRs is $I_\mathrm{h} = 2330$.

Methodology for computing the filters

The filters of length $I_\mathrm{g} = 2048$ are computed using wPM-F. In particular, the frequency responses $Q_l(f)$ are computed for a set of $N = I_\mathrm{h}+I_\mathrm{g}-1$ control frequencies using (2.27). The coefficients $Q_l(f)$ are set to 0 for control frequencies below 80 Hz. After that, an N-point IDFT is used to obtain the time-domain responses q_l, which are truncated using a rectangular window of size I_g to obtain the filters g_l (as described in Section 2.2.3). The weighting factor is set to $\bar{\mu}_f = 0.5$ for all frequencies, if not indicated otherwise. The regularization factor $\bar{\beta}_f$ is selected for each control frequency such that the array effort is upper bounded to a certain maximum value AE_max, which is indicated in each case.

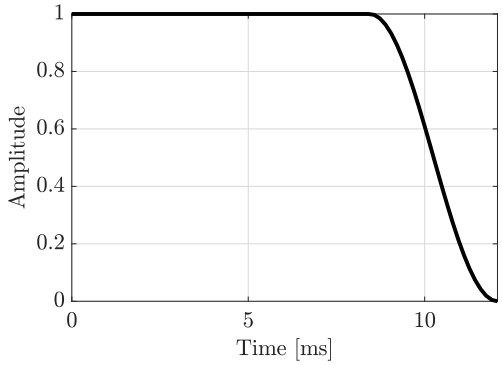

Figure 5.3: Example of the causal part of a Tukey window with $I_\mathrm{w} = 76$ (12 ms) and cosine fraction $\alpha = 0.3$.

For computing the filters, the target impulse response d_m for the m-th control point in the bright zone is computed using the proposed approach, i.e., using (5.3), where the reference loudspeaker is selected as l_r=3 and the modelling delay is $\tau_\mathrm{d} = 1024$. Moreover, in (5.3) we select w_{I_w} as a Tukey window [138] with cosine fraction α=0.3, whose length I_w is indicated in each case. We show in Fig. 5.3 an example of the causal part of a Tukey window with I_w=76 (12 ms). We select a Tukey window because it does not modify the amplitude of the first early-reflections of the target and it leads to a smooth transition between the reverberant and null components. Other types of window have also been investigated, but gave similar results. Furthermore, for $I_\mathrm{w} < \infty$ we apply an octave band equalization to the target to obtain the same energy per octave band in the bright zone as for the

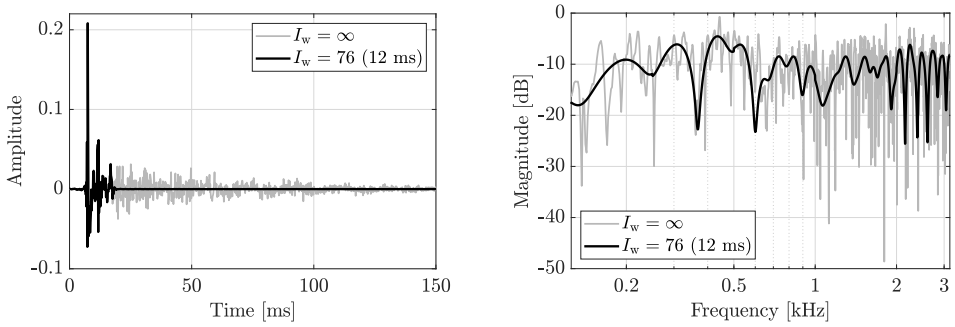

Figure 5.4: Target impulse response and target frequency response in (a) and (b), respectively, in the 0-th control point of the bright zone for two window lengths. The modelling delay is not considered in (a).

case with $I_\mathrm{w} = \infty$. The motivation is that the energy of the targets is not equal for different window lengths, so the equalization is required to obtain the same energy for the target no matter which window length is used. We show in Fig. 5.4a and 5.4b examples of target impulse and frequency responses, respectively, in the bright zone with $I_\mathrm{w} = 76$ and $I_\mathrm{w} = \infty$.

Methodology for evaluating the filters

For evaluating the filters, the metrics described in Section 2.2.5 are computed for a set of 16384 equispaced frequencies with a resolution of 0.3845 Hz assuming that the input signal is a unit impulse. The target response $d_{\mathrm{v},m}$ in the m-th validation point is selected using (5.3) but replacing h_{ml_r} by $h_{\mathrm{v},ml_\mathrm{r}}$. An important point is that the same criterion is used to compute and to evaluate the filters, meaning that whenever a window w_{I_w} is employed to obtain the target d_m that is used to compute the filters, the same window w_{I_w} is employed to obtain the target $d_{\mathrm{v},m}$ that is used to evaluate those filters. To improve the readability of the results, 1/3-octave band averaging [76] is used for all frequency-domain plots.

5.3.2 Kurtosis of RIRs

Before evaluating the performance of the proposed approach, we study the Kurtosis of the measured RIRs in the office-like room. We show in

Fig. 5.5 the average Kurtosis of the RIRs, which is computed with (5.10) considering a segment length $I_\mathrm{s} = 126$, i.e., 20 ms, as suggested in [137]. We can observe that the Kurtosis exhibits high values for the early part of the RIRs, where the direct propagation component and the early reflections are located, and drops to values below 3 after about 18 ms. This fact indicates that the RIRs start to behave randomly following a Gaussian PDF after 18 ms, so the reverberant components for this scenario can be assumed approximately diffuse after this time.

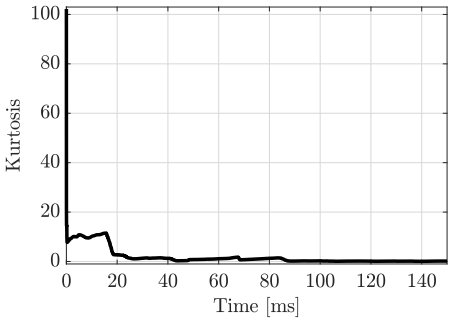

Figure 5.5: Average Kurtosis of the RIRs in the office-like room.

5.3.3 Evaluation of windowed targets

Next, we evaluate the performance of the windowed targets proposed in (5.3). In particular, we study the effect on the performance of the window length I_w used to compute the target. Let us highlight that the proposed approach is equivalent to the non-windowed target in (5.1) if $I_\mathrm{w} = \infty$.

We show in Fig. 5.6 the performance of the proposed approach as a function of the window length I_w and frequency in terms of: acoustic contrast (in Fig. 5.6a-b), MSE in the bright zone (in Fig. 5.6c-d), and array effort (in Fig. 5.6e-f). In Fig. 5.6, the metrics in the left and right columns are computed with effort constraints $\mathrm{AE}_\mathrm{max} = 10$ dB and $\mathrm{AE}_\mathrm{max} = 0$ dB, respectively. First, we can see that the performance for both effort constraints is equal for frequencies above 800 Hz. These results agree with those in Chapters 2 to 4, which indicated that the optimization is less sensitive to the regularization factor for frequencies whose wavelength is comparable with the size of the zones. For frequencies below 800 Hz, the performance is different for the two effort constraints, however, the effect of the window length in the performance is similar in both cases. Then, the

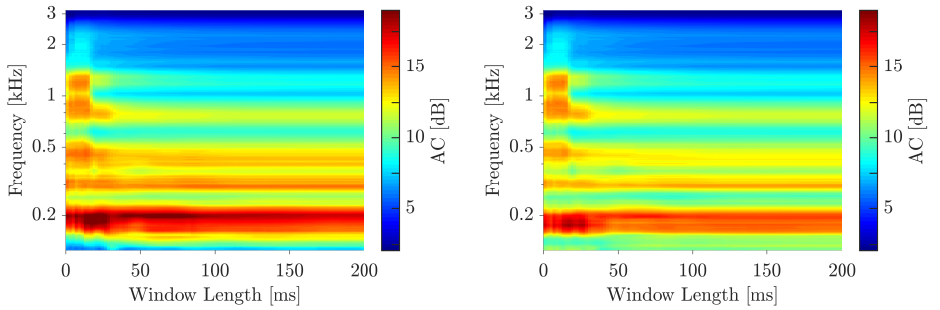

(a) AC (AE_{max} = 10 dB)

(b) AC (AE_{max} = 0 dB)

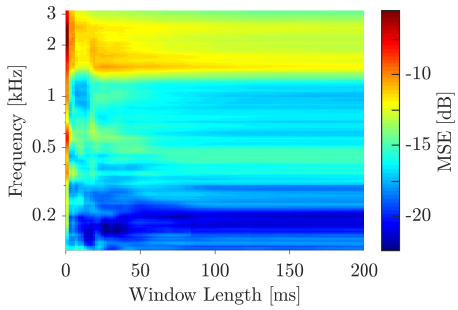

(c) MSE (AE_{max} = 10 dB)

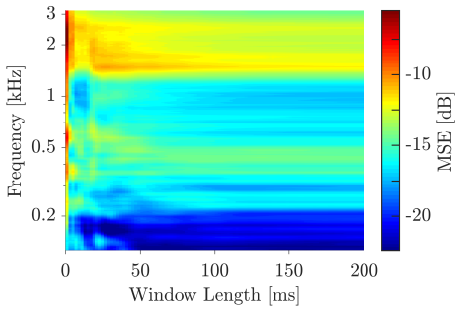

(d) MSE (AE_{max} = 0 dB)

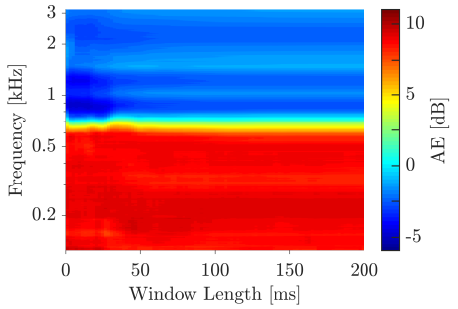

(e) AE (AE_{max} = 10 dB)

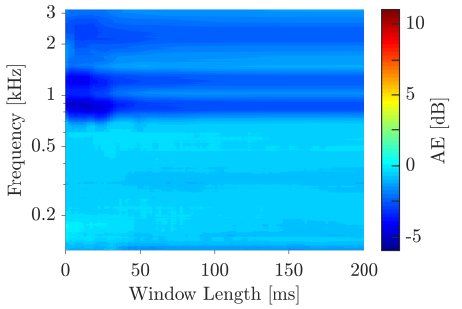

(f) AE (AE_{max} = 0 dB)

Figure 5.6: Performance of the proposed target selection in (5.3) as a function of the window length and frequency in terms of: acoustic contrast in (a, b), MSE in the bright zone in (c, d), and array effort in (e, f). For the left-column figures AE_{max}=10 dB is selected, and AE_{max}=0 dB for the right-column figures.

following analysis is valid for the two studied constraints. We can see in Fig. 5.6c-d that very short windows (of 1 ms or less) lead to an MSE that is at least 10 dB worse than for longer windows, while the acoustic contrast is similar (in Fig. 5.6a-b). This degradation appears because very short windows aim to suppress the first early reflections, and also, to equalize the response of the reference loudspeaker in the bright zone, which is too restrictive and leads to important errors in the bright zone. Also, we can see that, in general, short windows of about 6 to 18 ms present a significantly higher acoustic contrast than longer windows. It is interesting to note that there exists a close relation between Fig. 5.5 and Fig. 5.6. Particularly, the acoustic contrast in Fig. 5.6a-b starts to deteriorate for window lengths greater than about 18 ms and the Kurtosis of the RIRs also drops 18 ms after the arrival of the direct propagation components. Hence, this reveals that improvements in the acoustic contrast may appear if the selected window removes from the target for the bright zone the reverberant components that present approximately diffuse behaviour. Furthermore, these results indicate that the Kurtosis provides a useful metric to select the window length I_{w} for computing the windowed target (5.3). Moreover, Fig. 5.6 shows that the improvements in the acoustic contrast obtained with short windows are not at the cost of substantially higher MSE for frequencies in the range 150-200 Hz, 400-500 Hz, and 800-1500 Hz. However, the improvements in the acoustic contrast for short windows are at the cost of worse MSE for frequencies 200-400 Hz, 500-800 Hz, and 1500-3150 Hz. For these frequency bands, higher acoustic contrast may be achieved for long windows by tuning the weighting parameter $\bar{\mu}_f$ for wPM-F. Therefore, at this point it is not yet clear if real improvements in the performance are achieved with short windows in all the studied frequencies.

To fairly determine which window length is able to provide higher acoustic contrast, we must compare their performance for the case in which their MSE is equal. In that case, improvements in the acoustic contrast for one window length compared to another are not at the cost of higher MSE. With that aim, we compare next the performance of the following configurations:

- Windowed Target (WT): $I_{\mathrm{w}} = 76$ (12 ms) and $\bar{\mu}_f = 0.5$.
- Full Target (FT): $I_{\mathrm{w}} = \infty$ and $\bar{\mu}_f = 0.5$.
- Full Target with Frequency Dependent $\bar{\mu}_f$ (FT-FD): $I_{\mathrm{w}} = \infty$ and $\bar{\mu}_f$ selected as shown in Fig. 5.7 to achieve the same MSE as WT.

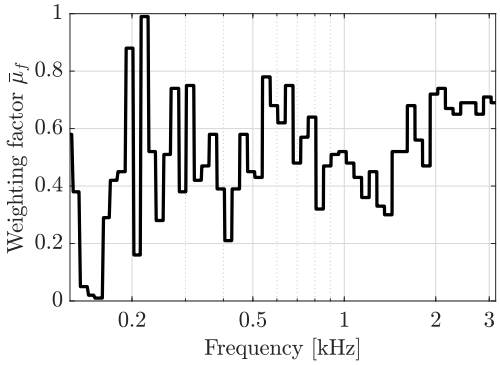

Figure 5.7: Weighting factor $\bar{\mu}_f$ selected for FT-FD.

The performance of the three configurations is shown in Fig. 5.8 as a function of frequency in terms of: acoustic contrast (in Fig. 5.8a), MSE in the bright zone (in Fig. 5.8b), and array effort (in Fig. 5.8c). We only present results for $\mathrm{AE}_{\max} = 10$ dB because we can see in Fig. 5.6 that the effect of the window length on the performance is similar for different effort constraints. In Fig. 5.8, we see that WT can offer higher acoustic contrast than FT and also lower or equal MSE in certain frequency bands, e.g., 150-200 Hz, 400-500 Hz, and 800-1500 Hz. This means that a longer window cannot offer better performance than $I_{\mathrm{w}} = 76$ for these frequencies, neither in terms of acoustic contrast nor in terms of MSE (even if we tune $\bar{\mu}_f$). Next, if we compare WT and FT-FD, we can see that WT leads to higher acoustic contrast for all the studied frequencies except for the bands 125-150 Hz and 280-300 Hz, where FT-FD presents slightly better acoustic contrast. For example, WT leads to almost 6 dB better acoustic contrast than FT-FD around 1 kHz, and 4 dB better contrast around 180 Hz. Also, the MSE is almost the same for WT and FT-FD, as expected, and is broadly similar for FT, although slightly higher or lower for different frequencies. Moreover, the array effort required by WT is lower than for FT and FT-FD for frequencies above 700 Hz. From these results, we can conclude that windowing the target response with a short window of length $I_{\mathrm{w}} = 76$ (12 ms) leads to significantly better acoustic contrast than the case without windowing for most of the studied frequencies. This indicates that targeting the minimization of the energy of the diffuse reverberant components in the bright and dark zones can lead to great improvements in the performance for this scenario.

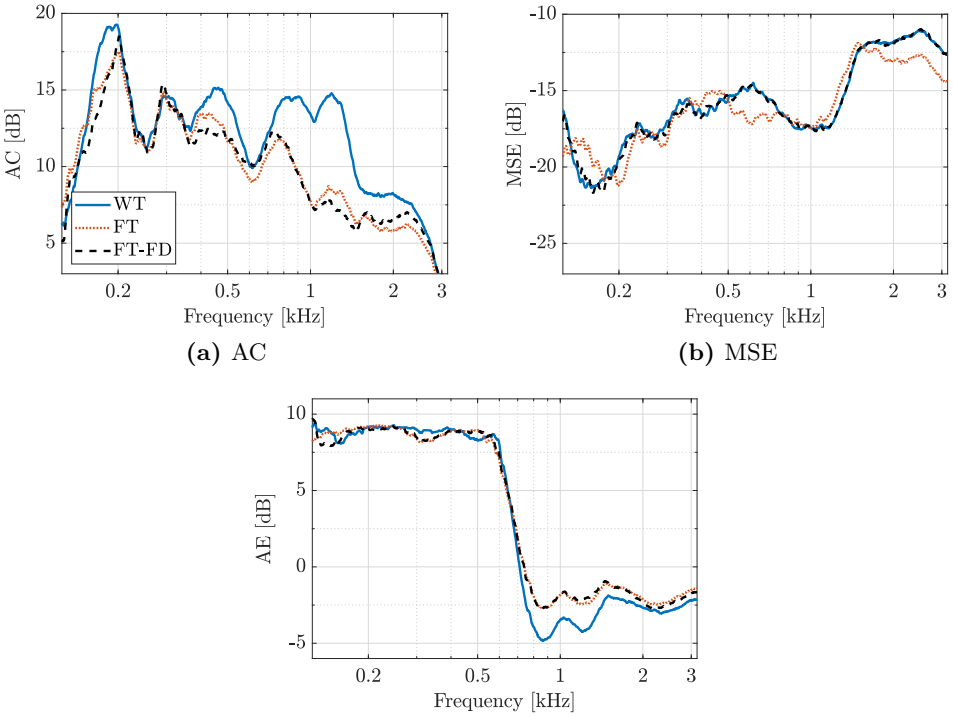

(a) AC **(b)** MSE

(c) AE

Figure 5.8: Performance for three different configurations as a function of frequency in terms of: acoustic contrast in (a), MSE in the bright zone in (b), and array effort in (c). An effort constraint $\mathrm{AE}_{\max} = 10$ dB is considered.

Next, we study the energy of the cascade impulse responses that are obtained with the filters for configurations WT and FT, i.e., with window lengths $I_{\mathrm{w}} = 76$ and $I_{\mathrm{w}} = \infty$, respectively. Let us define the cascade impulse response in the m-th validation point for a given set of filters g_l as

$$x_{\mathrm{v},m}(n) = \sum_{l=0}^{L-1} g_l(n) * h_{\mathrm{v},ml}(n). \tag{5.11}$$

We show in Fig. 5.9 the energy per sample of the cascade impulse responses in six validations points for configurations WT and FT. In particular, the energy in three validation points in the bright and dark zones is shown in the

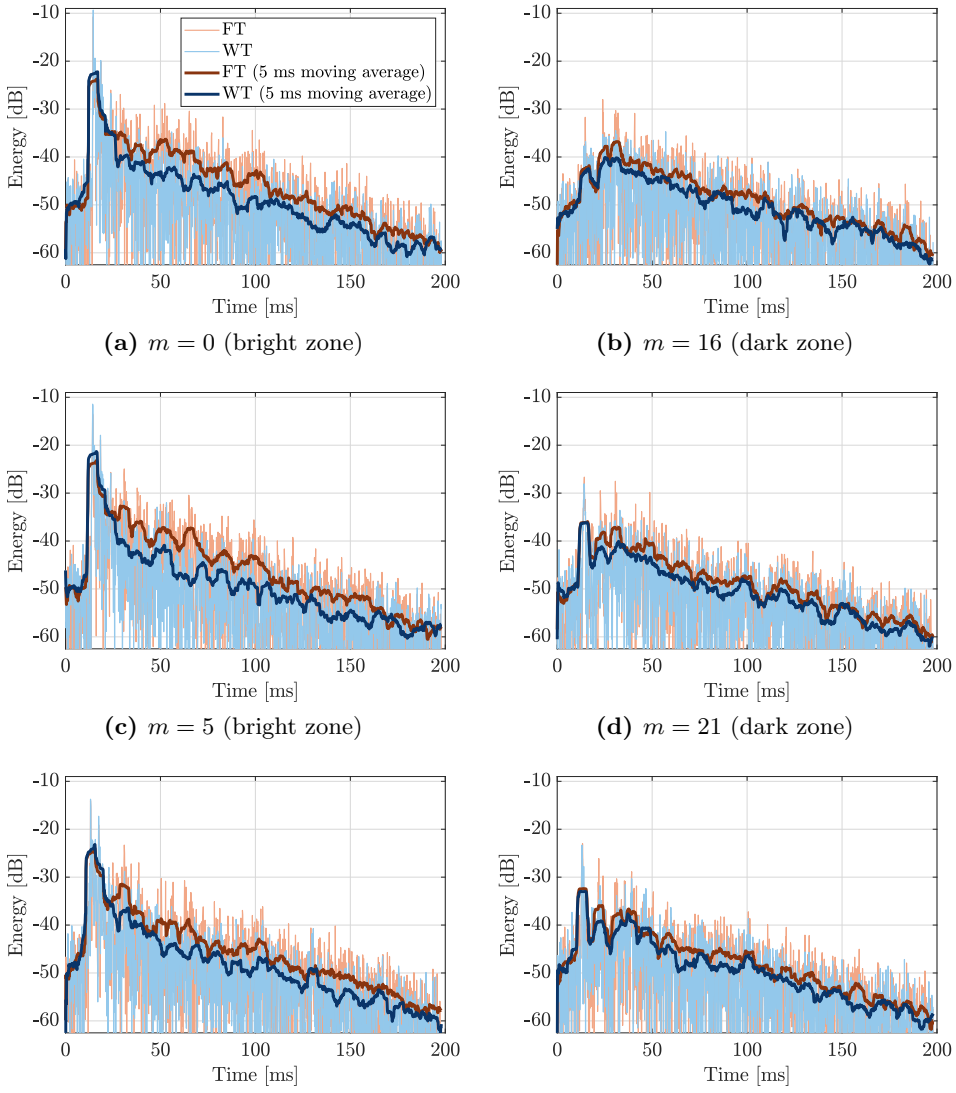

(a) $m = 0$ (bright zone)

(b) $m = 16$ (dark zone)

(c) $m = 5$ (bright zone)

(d) $m = 21$ (dark zone)

(e) $m = 15$ (bright zone)

(f) $m = 31$ (dark zone)

Figure 5.9: Energy of the cascade impulse response for configurations WT and FT, i.e., with $I_\mathrm{w} = 76$ and $I_\mathrm{w} = \infty$, respectively. The energy for three validation points in the bright and dark zones is shown in the left and right columns, respectively. The 32 samples (5 ms) moving average of the energy is included to improve the readability of the results. An effort constraint $\mathrm{AE}_\mathrm{max} = 10$ dB is considered.

left and right columns of Fig. 5.9, respectively. To improve the readability of the results, we also include in Fig. 5.9 the 32 samples (5 ms) moving average of the energy. An effort constraint $\mathrm{AE}_{\max} = 10$ is considered. Also, it is worth noting that, for the sake of simplicity on the visualization, we do not include in the figures all the time instants before the propagation peak in which the response has near 0 energy and that are produced by the modelling delay. The results show that the energy in the bright zone is similar for both configurations in the time instants near the arrival of the direct propagation component, being slightly higher for WT due to the equalization applied to the target. However, WT leads to lower energy in the bright zone than FT for times between 12 ms and 200 ms after the arrival of the direct component, mainly because WT aims the suppression of the reverberant components in the bright zone in those times. Moreover, we can see that WT also leads to lower energy than FT in the dark zone for most times between 12 ms and 200 ms after the arrival of the direct component. These facts indicate that the improvements obtained with windowed targets are not achieved because we force the cancellation of some sparse high-energy early-reflections, but because we target the cancellation of the diffuse reverberant tail in the bright and dark zones.

Finally, we show in Fig. 5.10 and 5.11 the impulse responses of the filters g_l of length $I_\mathrm{g} = 2048$ for FT and WT, respectively, and for all the loudspeakers of the system. An effort constraint $\mathrm{AE}_{\max} = 10$ is considered. The most significant difference between the two sets of filters is their energy distribution along the loudspeakers. For FT, it is clear that the filter for $l = 3$, i.e., the reference loudspeaker, presents significantly higher energy than the filters for the other loudspeakers. The motivation is that in this case we want to synthesize the response produced by loudspeaker $l = 3$ in the control points of the bright zone, so it is reasonable that the greatest contribution of the array comes from this loudspeaker. For WT, the energy of the filters is more uniform along the loudspeakers. In this case, we do not want to synthesize exactly the response produced by loudspeaker $l = 3$ in the control points of the bright zone, but a modified version which does not include all the reverberation components. Then, the filters for all loudspeakers present more similar energy levels than for FT, since the contributions from all the loudspeakers are required to suppress some of the reverberant components in the bright zone.

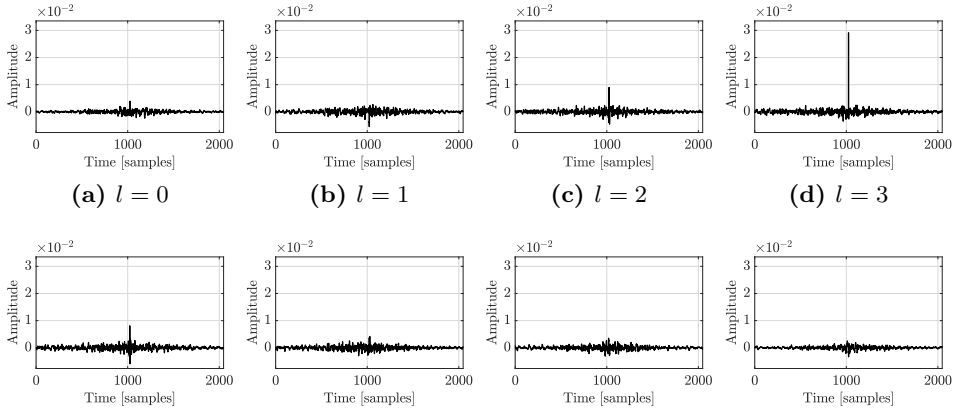

(a) $l = 0$ **(b)** $l = 1$ **(c)** $l = 2$ **(d)** $l = 3$

(e) $l = 4$ **(f)** $l = 5$ **(g)** $l = 6$ **(h)** $l = 7$

Figure 5.10: Impulse response of the filters g_l for configuration FT, i.e., with $I_\mathrm{w} = \infty$, and for all the loudspeakers of the system. An effort constraint $\mathrm{AE}_\mathrm{max} = 10$ dB is considered.

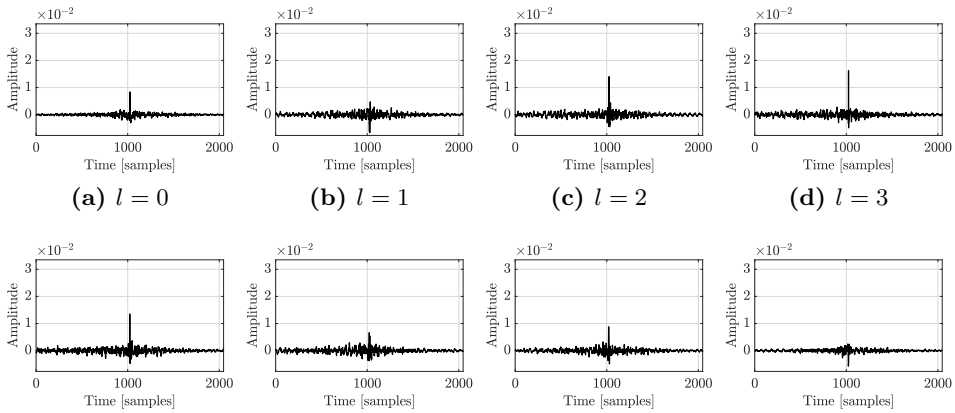

(a) $l = 0$ **(b)** $l = 1$ **(c)** $l = 2$ **(d)** $l = 3$

(e) $l = 4$ **(f)** $l = 5$ **(g)** $l = 6$ **(h)** $l = 7$

Figure 5.11: Impulse response of the filters g_l for configuration WT, i.e., with $I_\mathrm{w} = 76$ (12 ms), and for all the loudspeakers of the system. An effort constraint $\mathrm{AE}_\mathrm{max} = 10$ dB is considered.

(a)

(b)

Figure 5.12: Setup used to measure the RIRs without perturbations in (a), and to measure the RIRs with the perturbations produced by two persons within the zones in (b).

5.3.4 Robustness to perturbations

We now evaluate whether the improvements obtained by windowing the target are robust to perturbations in the environment. To this end, we present evaluation results where the filters are computed with the RIRs measured at the control points without any perturbation (as in Fig. 5.12a) and evaluated using the RIRs measured at the control points when perturbations in the RIRs, due to two people located within the zones, are present (as in Fig. 5.12b). The control filters are those calculated without any perturbations, as in Section 5.3.3, but now the performance, as shown in Fig. 5.13, has been calculated after these perturbations in the RIRs. For comparison purposes, we also include in Fig. 5.13 the performance of the filters when evaluated without perturbations (as in Section 5.3.3). We can see that the perturbations have generally decreased the acoustic contrast and increased the MSE in the bright zone with respect to the case without perturbations. However, the acoustic contrast is still significantly larger for the windowed target than it is without the window, and the MSE is also again broadly similar in the two cases. We can thus conclude that the performance improvements obtained by selecting a short window are robust to perturbations in the environment.

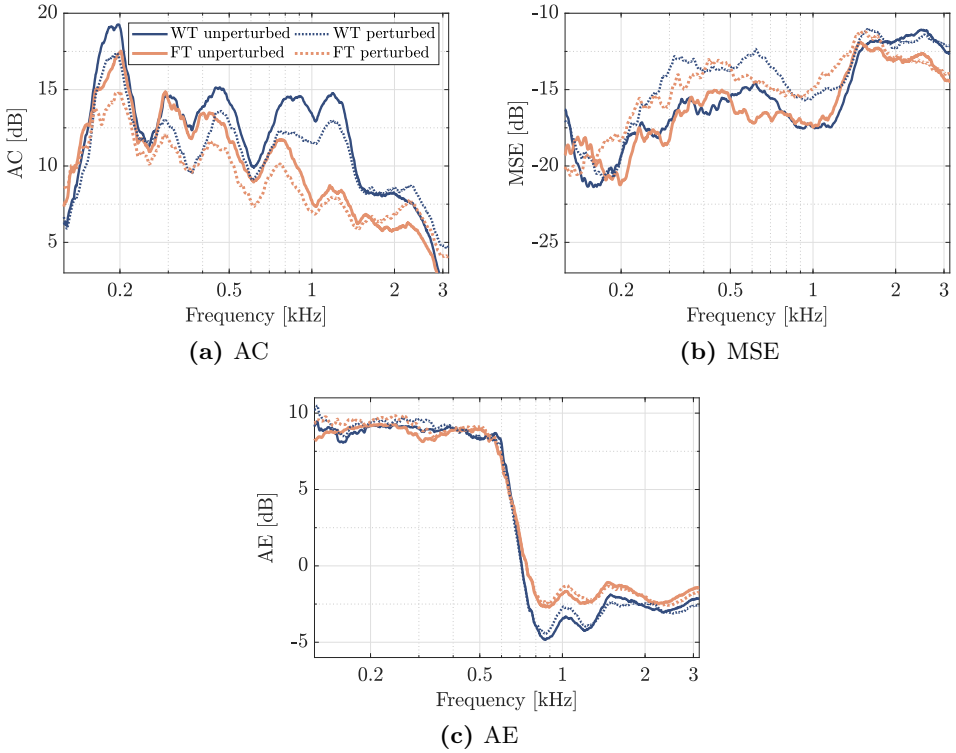

(a) AC **(b)** MSE **(c)** AE

Figure 5.13: Performance for WT and FT as a function of frequency when the perturbations produced by to persons located within the zones are considered in terms of: acoustic contrast in (a), MSE in the bright zone in (b), and array effort in (c). An effort constraint $\mathrm{AE}_{\mathrm{max}} = 10$ dB is considered. The performance of the filters evaluated without perturbations is also shown for comparison purposes.

5.4 Performance evaluation in a listening room

In this section, the proposed target selection is evaluated in the listening room at the Audio and Communications Signal Processing Group of the Institute of Telecommunications and Multimedia Applications (iTEAM), which presents lower reverberation time than the office-like room considered in Section 5.3.

5.4.1 Setup and methodology

Setup

The experimental evaluations have been carried out in the listening room at iTEAM, which presents a reverberation time T_{60} of 180 ms and a size of $9.07 \times 4.45 \times 2.65$ m. The walls of the listening room are acoustically treated with absorber panels. The setup is formed by one bright and one dark zone, as shown in Fig. 5.14a. In each zone, two different grids of microphones are used for spatial sampling, such that the RIRs measured at the control and validation grids are used to compute the filters and to evaluate their performance, respectively. A linear array of 8 two-way loudspeakers with an inter-element distance of 0.18 m is used (see Fig. 5.14b). Each loudspeaker in the array is formed by a woofer Beyma 5" MP60/N 8 OH [139] and a tweeter Beyma T-2030 8 OH [140]. The RIRs were measured using the swept-sine technique [69] with a sampling frequency of 44100 Hz, and then downsampled to 6300 Hz, obtaining impulse responses of length

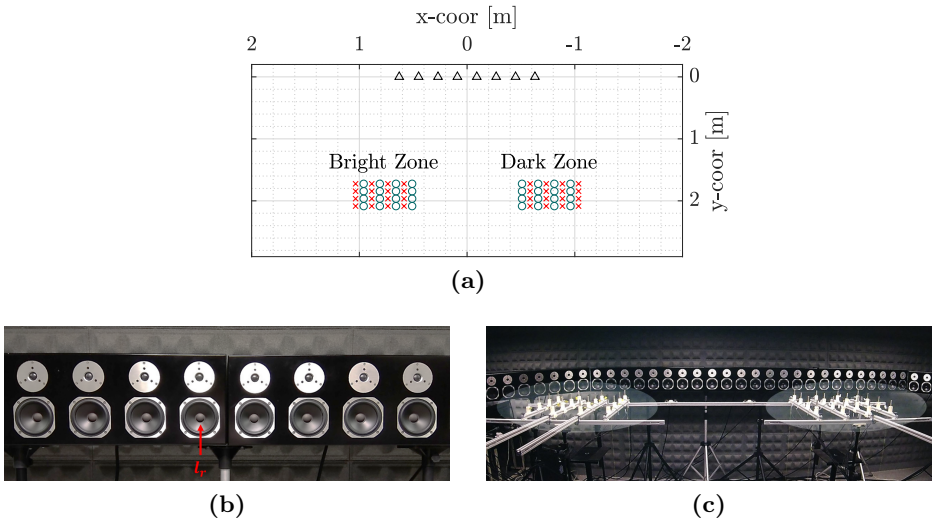

Figure 5.14: Setup used for the evaluations in (a), where ○ and × denote control and validation points, respectively, and ▲ denotes a loudspeaker. The walls are in $x = \pm 4.53$ m, $y = \{-0.46, 3.99\}$ m, and $z = \{0, 2.65\}$ m, and the loudspeakers and microphones are at a height of 1.51 m. The array of 8 loudspeakers is shown in (b). The two grids of 4×4 microphones used for measuring the RIRs in the control/validation points are shown in (c).

$I_\mathrm{h} = 1170$. Two grids of 4×4 Brüel & Kjær microphones Type 4958 [74], previously calibrated with a Brüel & Kjær sound calibrator Type 4231 [75], were used to measure the RIRs at the control/validation points (as shown in Fig. 5.14c). The distance between the elements of the grid is 0.15 m.

Methodology

The methodology presented in Section 5.3.1 is used here to compute and to evaluate the filters. We show in Fig. 5.15a and 5.15b examples of target impulse and frequency responses, respectively, in the bright zone with $I_\mathrm{w} = 51$ and $I_\mathrm{w} = \infty$.

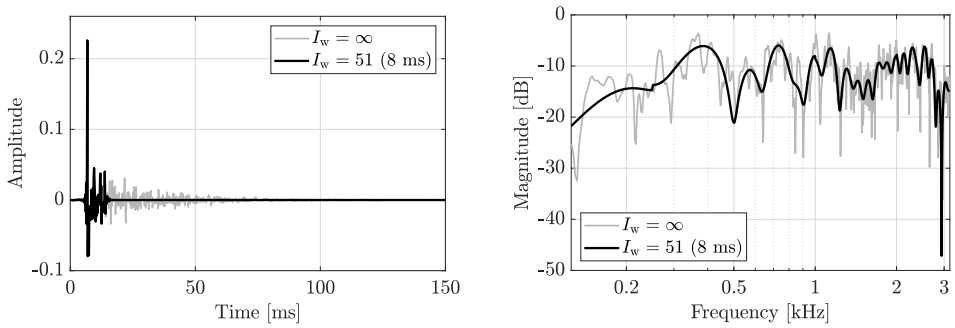

Figure 5.15: Target impulse response and target frequency response in (a) and (b), respectively, in the 0-th control point of the bright zone for two window lengths. The modelling delay is not considered in (a).

5.4.2 Kurtosis of RIRs

Before evaluating the performance of the proposed approach, we study the Kurtosis of the RIRs measured in the listening room. We show in Fig. 5.16 the average Kurtosis of the RIRs, which is computed with (5.10) considering a segment length $I_\mathrm{s} = 126$, i.e., 20 ms, as suggested in [137]. The Kurtosis presents high values for times smaller than 10 ms, while it drops below 3 after 10 ms. Again, this fact indicates that the RIRs start to behave randomly following a Gaussian PDF after 10 ms, so the reverberant components for this scenario can be assumed approximately diffuse after this time.

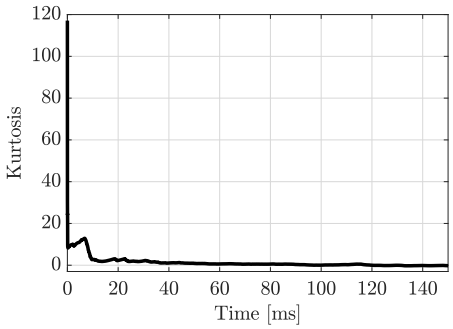

Figure 5.16: Average Kurtosis of the RIRs in the listening room.

5.4.3 Evaluation of windowed targets

Next, we study the performance of the proposed target in the listening room. Fig. 5.17 shows the performance as a function of I_{w} and frequency in terms of: acoustic contrast (in Fig. 5.17a-b), MSE in the bright zone (in Fig. 5.17c-d), and array effort (in Fig. 5.17e-f). In Fig. 5.17, the metrics in the left-column are computed with $\mathrm{AE}_{\mathrm{max}} = 10$ dB, whereas $\mathrm{AE}_{\mathrm{max}} = 0$ dB is used for the right-column. Again, the performance is similar for both constraints at frequencies above 800 Hz, as is the effect of the window length for frequencies below 800 Hz in both cases. Similarly to Section 5.3.3, we can see in Fig. 5.17c-d that very short windows (of 1 ms or less) lead to a much higher MSE than longer windows, while the acoustic contrast is similar. Then, selecting a window that is too short can significantly degrade the performance. Also, we can see that very long windows lead to better acoustic contrast and MSE for frequencies below 700 Hz than shorter ones. For frequencies above 700 Hz, the acoustic contrast is better for short windows (of about 4 to 10 ms) than for longer ones. However, we can also see in Fig. 5.17c-d that, in general, the MSE is also higher for short windows. In this case, the higher acoustic contrast when using short windows comes at the cost of higher MSE in the bright zone. Then, it is not clear so far whether windowing the target offers performance improvements in this scenario. Furthermore, there is a close relation between the results for frequencies above 700 Hz in Fig. 5.17 and the Kurtosis in Fig. 5.16, which illustrates the use of the Kurtosis in estimating the window length, although only at higher frequencies, in this case, with a short reverberation time.

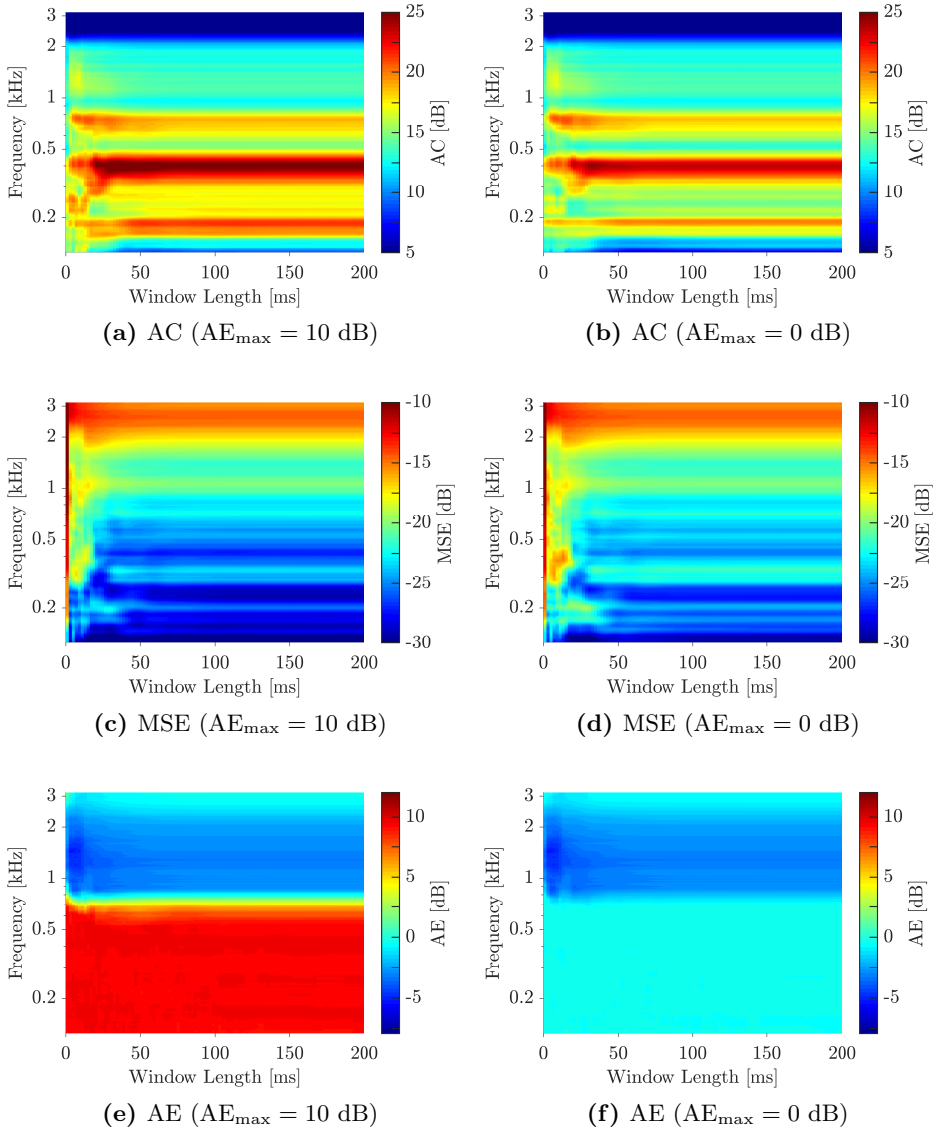

(a) AC (AE_{max} = 10 dB) **(b)** AC (AE_{max} = 0 dB)

(c) MSE (AE_{max} = 10 dB) **(d)** MSE (AE_{max} = 0 dB)

(e) AE (AE_{max} = 10 dB) **(f)** AE (AE_{max} = 0 dB)

Figure 5.17: Performance of the proposed target selection in (5.3) as a function of the window length and frequency in terms of: acoustic contrast in (a, b), MSE in the bright zone in (c, d), and array effort in (e, f). For the left-column figures AE_{max}=10 dB is selected, and AE_{max}=0 dB for the right-column figures.

To further study if windowing the target offers performance improvements in this scenario, we compare next the following configurations:

- Windowed Target (WT): $I_{\mathrm{w}} = 51$ (8 ms) and $\bar{\mu}_f = 0.5$.
- Full Target (FT): $I_{\mathrm{w}} = \infty$ and $\bar{\mu}_f = 0.5$.
- Full Target with Frequency Dependent $\bar{\mu}_f$ (FT-FD): $I_{\mathrm{w}} = \infty$ and $\bar{\mu}_f$ selected as shown in Fig. 5.18 to achieve the same MSE as WT.

The performance of these configurations is shown in Fig. 5.19 in terms of: acoustic contrast (in Fig. 5.19a), MSE in the bright zone (in Fig. 5.19b), and array effort (in Fig. 5.19c). We only present results for $\mathrm{AE}_{\mathrm{max}}$=10 dB to avoid redundancy. First, we can see that FT has a significantly lower MSE than WT, and consequently, than FT-FD, for all frequencies. FT-FD presents higher acoustic contrast than WT and approximately equal MSE for frequencies 150-1000 Hz, which indicates that windowing the target can not improve the acoustic contrast for those frequencies. However, for the same MSE level, WT offers about 2 dB better acoustic contrast than FT-FD in 125-150 Hz and above 1 kHz. Then, windowing the target in this scenario offers performance improvements in certain frequencies, however, these are more limited than those obtained for the office-like room in Section 5.3.3. From these results and the results in Section 5.3.3, we can conclude that the optimal window length is frequency and scenario dependent, and also, that the higher the reverberation in the room, the greater the improvement obtained by windowing the target response in the bright zone.

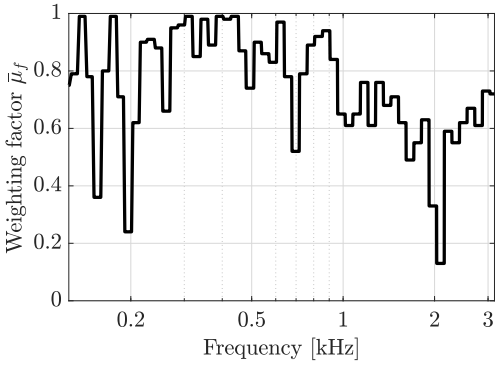

Figure 5.18: Weighting factor $\bar{\mu}_f$ selected for FT-FD.

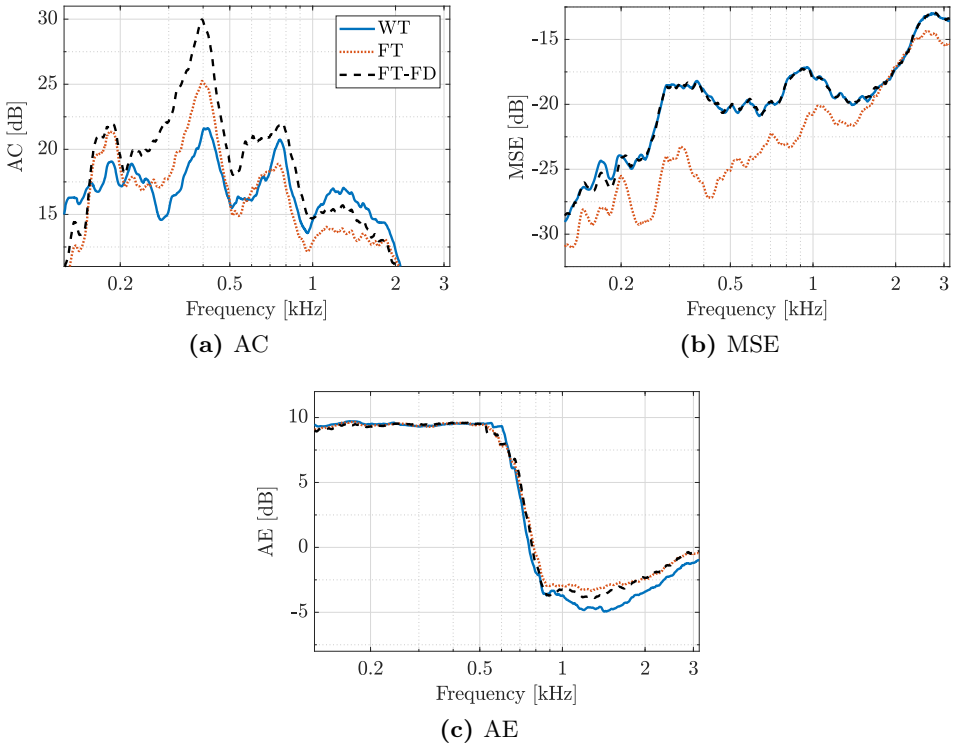

(a) AC **(b)** MSE

(c) AE

Figure 5.19: Performance for three different configurations as a function of frequency in terms of: acoustic contrast in (a), MSE in the bright zone in (b), and array effort in (c). An effort constraint $\mathrm{AE}_{\mathrm{max}} = 10$ dB is considered.

5.5 Summary

In this chapter we proposed a novel approach to select the target response in the bright zone for the weighted Pressure Matching (wPM) algorithm. In previous works, the target for the bright zone has generally been selected to be the Room Impulse Response (RIR) from one loudspeaker to all the control points in the bright zone. The aim is thus to synthesize the direct propagation component and all the reverberant components in the bright zone, while minimizing the energy of all components in the dark zone. The late reverberant components, however, are diffuse above the Schroeder frequency. We showed theoretically that there is no set of filters

that can lead to large differences between the energy of the diffuse reverberant components in the bright and dark zones, so trying to synthesize the diffuse reverberation components in the bright zone while minimizing their energy in the dark zone is not a good strategy. Alternatively, we proposed windowing the RIRs from one loudspeaker to all the control points in the bright zone, and use these responses as targets for the bright zone. This approach allows us to select which reverberant components we want to synthesize and which ones we want to suppress in the bright zone by choosing the window length. Then, the proposed approach, with a proper window length selection, can be used to obtain a target for wPM that aims to suppress the diffuse components both in the bright and dark zones. We presented experimental evaluation results in two rooms with different levels of reverberation to show the effect of windowing the target response. For the evaluations, because of its simplicity for the comparison of the different targets, we used wPM-F. Nevertheless, our findings can be generalized to the other formulations of wPM. The results revealed that windowing the target response can lead to higher acoustic contrast than the case without windowing, with similar Mean Squared Error (MSE) in the bright zone. Specifically, improvements of up to 6 dB in the acoustic contrast are observed for a room with $T_{60} = 500$ ms when a window length of 12 ms is used in the target impulse responses. Also, the results indicate that the window length that offers best performance is, in general, both frequency and scenario dependent. The Kurtosis of the RIRs, which is related to their level of diffuseness, is shown to give a good indication of the set of window lengths that offer performance improvements. Also, we observed that greater improvements with respect to the case without windowing are obtained for mid-high frequencies. Finally, we showed that the improvements obtained by windowing the target are greater for scenarios with high reverberation levels.

Chapter 6

Conclusions and future work

This chapter summarizes the results of this thesis. First, we review the main conclusions and contributions of this work. Next, based on the knowledge gained from this research, recommendations for future research are presented. Finally, the publications related to the outcome of this work are listed.

6.1 Main conclusions and contributions

This thesis focuses on the optimization algorithms required to compute the filters for Personal Sound Zones (PSZ) systems in real acoustic environments, which aim to deliver independent sounds to a number of listeners sharing an acoustic space through the use of loudspeakers. Next, we review the main conclusions and contributions.

In Chapter 2 we discussed the fundamental theory related to PSZ systems, giving special attention to the use of loudspeaker array processing to focus sound at low and mid frequencies. We reviewed the state-of-the-art algorithms for PSZ systems and determined that weighted Pressure Matching (wPM), either with time or frequency domain formulations, is the most suitable algorithm for these systems, since it allows to balance the interference level between zones and the audio quality of the signal rendered to the users. Previous works compared the performance of the time and frequency domain formulations of wPM, i.e., wPM-T and wPM-F, respectively, in reverberant environments. However, these works did not consider in the comparison aspects such as the filter length, the modelling delay or

the regularization level. Then, we presented original experimental results to compare the performance of wPM-T and wPM-F in a reverberant environment, taking into account the effect of the filter length, the modelling delay, and the regularization level. The results indicated that both algorithms present almost equal performance when long filters and appropriate modelling delays are considered. However, wPM-T clearly outperforms wPM-F at low frequencies when either short filters or too short modelling delays are used. Also, the effect of the regularization seems relevant, since increasing the regularization level leads to smaller differences between both algorithms, but at the cost of worsening the performance of both algorithms. Hence, we concluded that wPM-T offers superior performance to wPM-F for systems in which short modelling delays or short filters are desired.

Both formulations of wPM, i.e., wPM-T and wPM-F, involve a Least Squares (LS) problem to compute the optimal filters. A key difference is that the LS problem for wPM-T includes a larger number of unknown parameters than that for wPM-F. Then, although wPM-T may outperform wPM-F in some cases, it requires higher computational complexity, which is an important drawback for systems with limited processing capabilities. Thus, in Chapter 3 we discussed and evaluated different solvers to efficiently compute the filters for wPM-T. On the one hand, we studied a classic solver based on the Cholesky factorization, which does not assume any specific structure for the matrices of the LS problem. On the other hand, we considered the FAEST solver and the superfast solver [79], which take advantage of the block-toeplitz structure of the matrices of the LS problem to efficiently solve it. The accuracy of the solvers, their influence on the performance of a PSZ system, and their computational demands were experimentally evaluated in a reverberant environment. The results indicated that the Cholesky solver presents the highest accuracy among the studied solvers, but it requires very high computational complexity. Also, we showed that the FAEST and the superfast solvers are not suitable when extremely low regularization factors are considered, since FAEST diverges and the superfast solver requires very large approximation orders. However, extremely low regularization factors are not used in practice for PSZ systems, mainly to assure robustness against perturbations in the environment. For moderately high regularization factors, which are typically used in practical PSZ systems, FAEST and the superfast solver offer good accuracy and very similar performance to that obtained with the Cholesky

solver. Moreover, the evaluations revealed that FAEST requires significantly lower computational complexity than the Cholesky solver, but even larger computational savings are obtained with the superfast solver. Consequently, we concluded that the superfast solver proposed in [79] seems a good candidate to compute the filters for wPM-T in practical PSZ systems, since it can obtain good accuracy and presents affordable computational demands. In any case, we also showed that the computational complexity for wPM-T with any of the considered solvers is higher than for wPM-F, so wPM-F is preferred when low computational complexity is required to compute the filters.

The results in Chapters 2 and 3 revealed that wPM-F presents low computational complexity but exhibits bad performance for short system delays, whereas wPM-T presents good performance for short system delays but requires high computational complexity. Consequently, PSZ systems would benefit from an alternative approach that offers good performance for short system delays and low computational complexity. In this regard, we proposed in Chapter 4 using subband filtering for PSZ systems by means of GDFT filter banks. We presented a novel subband formulation for the PSZ problem that makes use of the subband decomposition [102] of the Room Impulse Responses (RIR). The subband decomposition algorithm presented in [102] is further optimized in this work to reduce its computational complexity. The main advantage of the proposed subband formulation for PSZ is that the filters for each subband can be independently optimized, which provides versatility to select different system configurations in each subband. To compute the subband filters, we proposed the weighted Pressure Matching with Subband-Domain Formulation (wPM-S) algorithm, which formulates an independent time-domain optimization for each subband using the wPM criterion. The proposed algorithm was experimentally evaluated in a reverberant environment. First, we studied the influence of the configuration of the filter bank on wPM-S and determined that good performance is achieved when the Reconstruction Error (RE) and the Alias-To-Signal Ratio (ASR) of the filter bank are below -35 dB. Next, we showed that wPM-S outperforms the algorithm proposed in [47], which also makes use of subband filtering. Also, we confirmed that wPM-S and wPM-T offer almost equal performance, although wPM-S presents an additional delay due to the effect of the filter bank. Furthermore, we determined that wPM-S presents better performance than wPM-F when short modelling delays are considered, even when the additional delay produced

by the filter bank is taken into account for wPM-F. Moreover, we evaluated the versatility of wPM-S to use different configurations in each subband. In particular, we showed that the filter length, the number of loudspeakers, and the approximation order for the superfast solver [79] can be reduced in certain subbands with negligible performance loss. Also, the computational complexity of wPM-S was compared with that of wPM-T and wPM-F. We determined that the computational savings offered by wPM-S are minor when the same configuration is used in all subbands. However, very important savings are obtained when the versatility of wPM-S is exploited to use suitable configurations in each subband. In that case, wPM-S requires substantially lower computational efforts than wPM-T to compute the filters. Still, wPM-S presents higher computational complexity than wPM-F. From these results, we concluded that wPM-S is a good alternative to wPM-T and wPM-F for PSZ systems, since it presents better performance than wPM-F for short system delays and lower computational complexity than wPM-T.

An important aspect that influences the performance of wPM is the target response selected for the bright zone, since different targets lead to different levels of interference between zones. In Chapter 5 we proposed a novel approach to select the target response in the bright zone for wPM. In previous works, the target for the bright zone was generally selected to be the RIR from one loudspeaker to all the control points in the bright zone. The aim is thus to synthesize the direct propagation component and all the reverberant components in the bright zone, while minimizing the energy of all components in the dark zone. The late reverberant components, however, are diffuse above the Schroeder frequency. We showed theoretically that there is no set of filters that can lead to large differences between the energy of the diffuse reverberant components in the bright and dark zones, so trying to synthesize the diffuse reverberation components in the bright zone while minimizing their energy in the dark zone is not a good strategy. Alternatively, we proposed windowing the RIRs from one loudspeaker to all the control points in the bright zone, and use these responses as targets for the bright zone. This approach allows us to select which reverberant components we want to synthesize and which ones we want to suppress in the bright zone by choosing the window length. Then, the proposed approach, with a proper window length selection, can be used to obtain a target for wPM that aims to suppress the diffuse components both in the bright and dark zones. We presented experimental evaluation results

in two rooms with different levels of reverberation to show the effect of windowing the target response. From these results, we concluded that the proposed approach can lead to higher acoustic isolation between the zones than the case without windowing, with similar reproduction errors in the bright zone. Furthermore, the results indicated that the window length that offers best performance is, in general, both frequency and scenario dependent. We showed that the Kurtosis of the RIRs, which is related to their level of diffuseness, gives a good indication of the set of window lengths that are potentially offering performance improvements. Also, we observed that greater improvements with respect to the case without windowing are obtained for mid-high frequencies, and that these improvements are larger for scenarios with high reverberation levels.

Finally, we presented in Appendix A an in-depth analysis of the computational complexity of the different algorithms studied in this work, and in Appendix B we detailed the method used to design the prototype filter for the GDFT filter bank employed with wPM-S.

6.2 Future work

Further to the research described in this thesis, we discuss below several lines of research that remain open.

In this thesis we studied the performance of different algorithms for PSZ systems operating in reverberant environments. An important aspect is that we assumed that full knowledge of the RIRs in the control points is available to compute the optimal filters, however, this is not always possible. For example, the number of positions in which the RIRs should be measured can be very large for PSZ systems involving a lot of users. Then, a very time-consuming measurement stage is required to obtain all the required RIRs. To avoid the measurement stage, the free-field propagation model has been used in the literature to estimate the RIRs, however, this model is not accurate enough for low and mid frequencies. In this regard, it would be very interesting to study alternative methods to estimate the RIRs in any desired position within a shared acoustic environment.

We proposed the wPM-S algorithm that allows to use different configurations for the system in each subband. In particular, we studied the use of different filter lengths, number of loudspeakers, and solvers in each sub-

band. However, the versatility of wPM-S could be further investigated. For instance, it would be interesting to study the use of different regularization and weighting factors in each subband. On the one hand, the regularization factor is related to the robustness of the system to perturbations, so it could be beneficial to select a subband-specific regularization factor that guarantees high robustness in all the operation bandwidth. On the other hand, the weighting factor influences the balance between the interference in the dark zone and the reproduction error in the bright zone, so selecting suitable weighting factors in each subband may be beneficial for the system. The weighting factor in each subband could be selected based on a perceptual criterion that would take into account the annoyance of the interferences in the dark zone and the perceived quality of the audio delivered to the bright zone. Moreover, we determined in this thesis that windowing the target response for the bright zone can improve the isolation between zones, but the optimal window length is frequency dependent. Then, investigating the use of different window lengths in each subband for wPM-S seems an interesting topic that could lead to further improvements in the performance of PSZ systems.

Finally, there are many interesting research questions that remain open regarding dynamic PSZ systems, in which the filters of the system must be re-calculated frequently because either the position of the users or the number of users is time-varying. For instance, it would be interesting to investigate how often the filters must be re-calculated, according to factors as the speed at which the users move within the shared space. It would be also interesting to study if the filters for a present time instant can be updated efficiently from the filters for past time instants.

6.3 List of publications

The following contributions were published during the course of this work:

Conference proceedings

- V. Molés-Cases, G. Piñero, A. Gonzalez, and M. de Diego, "Providing Spatial Control in Personal Sound Zones Using Graph Signal Processing," in *Proceedings of the 27th European Signal Processing Conference (EUSIPCO)*, A Coruña (Spain), 2019.

Journal publications

- V. Molés-Cases, G. Piñero, M. de Diego, and A. Gonzalez, "Personal Sound Zones by Subband Filtering and Time Domain Optimization," *IEEE/ACM Transactions on Audio, Speech, and Language Processing*, vol. 28, pp. 2684-2696, 2020.
- V. Molés-Cases, S. J. Elliott, J. Cheer, G. Piñero, and A. Gonzalez, "Weighted pressure matching with windowed targets for personal sound zones," *The Journal of the Acoustical Society of America*, vol. 151, pp. 334-345, 2022.
- V. Molés-Cases, G. Piñero, and A. Gonzalez, "On the Performance of Personal Sound Zones Systems with Subband Filtering," Submitted to *IEEE/ACM Transactions on Audio, Speech, and Language Processing*, 2022.

Appendix A

Computational complexity analysis

In this appendix we study the computational complexity of the algorithms studied throughout this work. In particular, we focus on the number of Floating Point Operations (FLOPs) required by the different algorithms. Other computational aspects, as memory allocation and memory displacements, are not considered next.

The algorithms have been implemented using C language, and the FLOPs counts are based on this specific implementation. The Basic Linear Algebra Subprograms (BLAS) [141] included in Intel MKL v.2017.0.31 [142] and the Linear Algebra Package (LAPACK) v.3.7.0 [143] are used for all algebra-related operations. For DFT computations, the Fastest Fourier Transform in the West (FFTW) v.3.3.5 [144] is used. We provide the code for the different algorithms discussed in this appendix in [145].

We consider that one FLOP is one of the following operations in real arithmetic: addition, subtraction, multiplication, and division. Also, we consider that 2 FLOPs are required for complex addition or subtraction, and 6 FLOPs for complex multiplication or division. Furthermore, we assume that a N-point DFT with complex-valued input and output requires $5N \log_2 N$ FLOPs, while half the number of FLOPs are required when either the input or the output are real-valued [146]. The number of FLOPs required by the routines of BLAS/LAPACK can be found in [147]. Nonetheless, we consider that other procedures that only involve memory displacements, e.g., truncation or decimation of signals, do not require any FLOPs.

All the algorithms studied next require at some point to solve a system of linear equations of the form $\mathbf{AX} = \mathbf{B}$, where $\mathbf{A}$ is a $N_\mathrm{a}\times N_\mathrm{a}$ positive-definite matrix, $\mathbf{B}$ is a $N_\mathrm{a}\times N_\mathrm{b}$ matrix, and $\mathbf{X}$ is a $N_\mathrm{a}\times N_\mathrm{b}$ matrix. Such a system is said to have N_b right-hand sides. We use notation $\mathbf{A}\backslash\mathbf{B} \rightarrow \mathbf{X}$ to denote the operations required to solve the system. In this appendix, we employ the Cholesky factorization to solve this kind of system. For real-valued matrices $\mathbf{A}$, $\mathbf{B}$, and $\mathbf{X}$, LAPACK routine `dpotrf` is used to compute the Cholesky factorization of $\mathbf{A}$, i.e., $\mathbf{A} = \mathbf{L}\mathbf{L}^T$, and `dpotrs` to solve the triangular systems $\mathbf{LY} = \mathbf{B}$ and $\mathbf{L}^T\mathbf{X} = \mathbf{Y}$. Otherwise, for complex-valued matrices, routine `zpotrf` is used to compute the Cholesky factorization of $\mathbf{A}$, i.e., $\mathbf{A} = \mathbf{L}\mathbf{L}^H$, and `zpotrs` to solve $\mathbf{LY} = \mathbf{B}$ and $\mathbf{L}^H\mathbf{X} = \mathbf{Y}$.

In this appendix, we consider a PSZ system with L loudspeakers, M control points, and RIRs h_{ml} of length I_h.

A.1 Computational complexity of wPM-T

Next, we detail the number of operations required to compute the I_g-length optimal filters for wPM-T using the three solvers studied in Chapter 3.

A.1.1 Cholesky solver

First, we focus on the Cholesky solver studied in Section 3.3. So far, we assumed that the matrix $\mathbf{R}$ and the vector $\mathbf{c}$ required to obtain the optimal solution are explicitly computed as $\mathbf{R} = \mathbf{H}^T\mathbf{H} + \beta\,\mathbf{I}_{LI_\mathrm{g}}$ and $\mathbf{c} = \mathbf{H}^T\mathbf{d}$, respectively. However, alternative expressions can be derived that require lower computational efforts. Then, we first derive these expressions, and later, we study the computational complexity of the Cholesky solver.

Computation of R

Let us define the $L\times L$ correlation matrix at frequency f as

$$\bar{\mathbf{R}}_f = \bar{\mathbf{H}}_f^H\bar{\mathbf{H}}_f + \beta\,\mathbf{I}_L, \tag{A.1}$$

where $\bar{\mathbf{H}}_f$ is a $M\times L$ matrix defined in (2.15), and $\bar{\mathbf{R}}_f$ is an hermitian matrix with $L\,(L{+}1)/2$ unique elements. Also, let us define the $LI_\mathrm{d}\times LI_\mathrm{d}$ block-diagonal matrix containing $\bar{\mathbf{R}}_f$ for all control frequencies as

$$\bar{\mathbf{R}} = \mathrm{diag}\left\{\bar{\mathbf{R}}_{f_0} \quad \ldots \quad \bar{\mathbf{R}}_{f_{I_\mathrm{d}-1}}\right\}, \tag{A.2}$$

which can be alternatively expressed as

$$\bar{\mathbf{R}} = \bar{\mathbf{H}}^H \bar{\mathbf{H}} + \beta \mathbf{I}_{LI_\mathrm{d}}, \tag{A.3}$$

where $\bar{\mathbf{H}}$ is a block-diagonal matrix defined in (3.19) containing $\bar{\mathbf{H}}_{f_k}$ for all control frequencies. Now, let us define the $LI_\mathrm{d} \times LI_\mathrm{d}$ extended time-domain correlation matrix $\mathbf{R}_\mathrm{e}$ as

$$\mathbf{R}_\mathrm{e} = \mathbf{F}_L^H \bar{\mathbf{R}} \mathbf{F}_L, \tag{A.4}$$

where $\mathbf{F}_L$ is defined in (3.16) as the matrix of a I_d-point DFT with blocks of size L. Since $\mathbf{R}_\mathrm{e}$ is hermitian, it can be alternatively expressed as

$$\mathbf{R}_\mathrm{e} = \begin{bmatrix} \mathbf{R}_0 & \dots & \mathbf{R}_{I_\mathrm{d}-1}^H \\ \vdots & \mathit{toeplitz} & \\ \mathbf{R}_{I_\mathrm{d}-1} & & \end{bmatrix}, \tag{A.5}$$

in which

$$\mathbf{R}_n = \sum_{k=0}^{I_\mathrm{d}-1} \Phi_{I_\mathrm{d}}^{(k,n)*} \, \bar{\mathbf{R}}_{f_k}, \tag{A.6}$$

where $\Phi_{I_\mathrm{d}}^{(k,n)}$ is the coefficient for the n-th time index and the k-th frequency bin of a I_d-point DFT. Hence, the required $\mathbf{R}_n$ to form $\mathbf{R}_\mathrm{e}$ can be computed with $L\,(L{+}1)/2$ IDFTs of size I_d, because $\bar{\mathbf{R}}_{f_k}$ is hermitian. Also, we showed in Section 3.5 that $\mathbf{H}$ can be expressed as

$$\mathbf{H} = \mathbf{F}_M^H \, \bar{\mathbf{H}} \, \mathbf{F}_L \mathbf{T}^T, \tag{A.7}$$

where $\mathbf{T}$ is a truncation matrix defined in (3.17). Then, using (A.7), we can write $\mathbf{R}$ as

$$\mathbf{R} = \mathbf{T}\mathbf{F}_L^H \left(\bar{\mathbf{H}}^H \bar{\mathbf{H}} + \beta \mathbf{I}_{LI_\mathrm{g}} \right) \mathbf{F}_L \mathbf{T}^T, \tag{A.8}$$

where we took into account that $\mathbf{T}\mathbf{T}^T = \mathbf{I}_{LI_\mathrm{g}}$ and that $\mathbf{F}_L$ is a unitary matrix. From (A.1)-(A.4) and (A.8), $\mathbf{R}$ can be expressed as

$$\mathbf{R} = \mathbf{T}\mathbf{R}_\mathrm{e}\mathbf{T}^T, \tag{A.9}$$

which is equivalent to set $\mathbf{R}$ as the $LI_\mathrm{g} \times LI_\mathrm{g}$ upper-left block of $\mathbf{R}_\mathrm{e}$, i.e.,

$$\mathbf{R} = [\mathbf{R}_\mathrm{e}]_{(0:LI_\mathrm{g}-1, 0:LI_\mathrm{g}-1)}. \tag{A.10}$$

Then, $\mathbf{R}$ is a truncated version of $\mathbf{R}_\mathrm{e}$. Since $\mathbf{R}_\mathrm{e}$ can be computed using the FFT algorithm and does not require to explicitly form $\mathbf{H}$, (A.10) is preferred to $\mathbf{R} = \mathbf{H}^T\mathbf{H} + \beta \mathbf{I}_{LI_\mathrm{g}}$.

Computation of c

Let us define the $L\times 1$ cross-correlation vector at control frequency f as

$$\bar{\mathbf{c}}_f = \bar{\mathbf{H}}_f \bar{\mathbf{d}}_f, \tag{A.11}$$

where $\bar{\mathbf{H}}_f$ is a $M\times L$ matrix defined in (2.15), and $\bar{\mathbf{d}}_f$ is a $M\times 1$ vector defined in (2.22). Moreover, let us define a $LI_\mathrm{d}\times 1$ vector containing $\bar{\mathbf{c}}_f$ for all control frequencies as

$$\bar{\mathbf{c}} = \begin{bmatrix} \bar{\mathbf{c}}_{f_0}^T & \dots & \bar{\mathbf{c}}_{f_{I_\mathrm{d}-1}}^T \end{bmatrix}^T, \tag{A.12}$$

which can be also expressed as

$$\bar{\mathbf{c}} = \bar{\mathbf{H}}\mathbf{F}_M \mathbf{d}. \tag{A.13}$$

Also, let us define the $LI_\mathrm{d}\times 1$ extended time-domain correlation vector as

$$\mathbf{c}_\mathrm{e} = \mathbf{F}_L^H \bar{\mathbf{c}} = \begin{bmatrix} \mathbf{c}_0^T & \dots & \mathbf{c}_{I_\mathrm{d}-1}^T \end{bmatrix}^T, \tag{A.14}$$

in which

$$\mathbf{c}_n = \sum_{k=0}^{I_\mathrm{d}-1} \Phi_{I_\mathrm{d}}^{(k,n)*} \bar{\mathbf{c}}_{f_k}, \tag{A.15}$$

where $\Phi_{I_\mathrm{d}}^{(k,n)}$ is the coefficient for the n-th time index and the k-th frequency bin of a I_d-point DFT. Hence, the required $\mathbf{c}_n$ to form $\mathbf{c}_\mathrm{e}$ can be computed using L IDFTs of size I_d. Now, from (A.7), we can express $\mathbf{c}$ as

$$\mathbf{c} = \mathbf{T}\mathbf{F}_L^H \bar{\mathbf{H}}\mathbf{F}_M \mathbf{d}. \tag{A.16}$$

From (A.13)-(A.14) and (A.16), $\mathbf{c}$ can be alternatively expressed as

$$\mathbf{c} = \mathbf{T}\mathbf{c}_\mathrm{e}, \tag{A.17}$$

which is equivalent to set $\mathbf{c}$ as the LI_g first elements of $\mathbf{c}_\mathrm{e}$, i.e.,

$$\mathbf{c} = [\mathbf{c}_\mathrm{e}]_{(0:LI_\mathrm{g}-1)}. \tag{A.18}$$

Then, $\mathbf{c}$ is a truncated version of $\mathbf{c}_\mathrm{e}$. Since $\mathbf{c}_\mathrm{e}$ can be computed using the FFT algorithm and does not require to explicitly form $\mathbf{H}$, (A.18) is preferred to $\mathbf{c} = \mathbf{H}^T\mathbf{d}$.

	Operation	Routine	Calls	FLOPs/call
Comp. $\mathbf{R}$	DFT of $h_{ml} \rightarrow \bar{\mathbf{H}}_f$	FFTW/`dft_r2c`	ML	$\frac{5}{2}N\log_2 N$
	$\bar{\mathbf{H}}_f^H \bar{\mathbf{H}}_f + \beta \mathbf{I}_L \rightarrow \bar{\mathbf{R}}_f$	BLAS/`zherk`	$\frac{1}{2}N$	$4ML(L+1)$
	IDFT of $\bar{\mathbf{R}}_f \rightarrow \mathbf{R}_\mathrm{e}$	FFTW/`dft_c2r`	$\frac{L(L+1)}{2}$	$\frac{5}{2}N\log_2 N$
	$[\mathbf{R}_\mathrm{e}]_{(0:LI_\mathrm{g}-1,0:LI_\mathrm{g}-1)} \rightarrow \mathbf{R}$	-	-	-
Comp. $\mathbf{c}$	DFT of $d_m \rightarrow \bar{\mathbf{d}}_f$	FFTW/`dft_r2c`	M	$\frac{5}{2}N\log_2 N$
	$\bar{\mathbf{H}}_f^H \bar{\mathbf{d}}_f \rightarrow \bar{\mathbf{c}}_f$	BLAS/`zgemv`	$\frac{1}{2}N$	$8ML$
	IDFT of $\bar{\mathbf{c}}_f \rightarrow \mathbf{c}_\mathrm{e}$	FFTW/`dft_c2r`	L	$\frac{5}{2}N\log_2 N$
	$[\mathbf{c}_\mathrm{e}]_{0:LI_\mathrm{g}-1} \rightarrow \mathbf{c}$	-	-	-
Solve with Chol. fact. $\mathbf{R} \setminus \mathbf{c} \rightarrow \mathbf{g}_\mathrm{opt}$		LAPACK/`dpotrf`	1	$\frac{1}{3}(LI_\mathrm{g})^3 + \frac{1}{2}(LI_\mathrm{g})^2 + \frac{1}{6}(LI_\mathrm{g})$
		LAPACK/`dpotrs`	1	$2\,(LI_\mathrm{g})^2$

Table A.1: Operations required by the Cholesky solver to compute the filters for wPM-T, considering a system with L loudspeakers, M control points, filters of length I_g, and targets of length $I_\mathrm{d} = I_\mathrm{g}+I_\mathrm{h}-1$. The size for the DFTs/IDFTs is $N = I_\mathrm{d}$.

Computational complexity

In Table A.1, we present the steps required to compute the optimal filters for wPM-T using a Cholesky solver, which are based on Algorithm 3.1 and on the previous derivations. For each step, we show the associated routine, the number of calls to the routine, and the number of FLOPs required to execute each routine. The DFTs/IDFTs in Table A.1 are of size $N = I_\mathrm{d}$, because $I_\mathrm{d} = I_\mathrm{g}+I_\mathrm{h}-1$ control frequencies are required to compute $\mathbf{R}$ and $\mathbf{c}$ using (A.10) and (A.18), respectively. Also, let us note that h_{ml} and d_m are real-valued, and then, their DFTs have hermitian symmetry. Hence, all the computations in Table A.1 for individual frequencies are computed only for the $N/2$ control frequencies in the positive spectrum[1]. Let us point

[1] For a N-point DFT, the number of frequency bins in the positive spectrum is $\lfloor \frac{N}{2} \rfloor + 1$. We assume that $\frac{N}{2} \approx \lfloor \frac{N}{2} \rfloor + 1$ to simplify the computational cost expressions.

out that the names of the routines of FFTW are shortened in Table A.1 for the sake of simplicity, e.g., `fftw_execute_dft_r2c` is presented as `dft_r2c`. This naming criteria is used from now on. From Table A.1, the number of FLOPs for the Cholesky solver is:

$$N_{\text{flop}} = \left[\frac{L^3}{3}\right] I_{\text{g}}^3 + \left[\frac{5L^2}{2}\right] I_{\text{g}}^2 + \left[\frac{5}{2}\left(ML{+}M{+}\frac{1}{2}L^2{+}\frac{3}{2}L\right)\right] I_{\text{d}} \log_2 I_{\text{d}} + \left[2ML\,(L{+}3)\right] I_{\text{d}} + \left[\frac{L}{6}\right] I_{\text{g}}. \tag{A.19}$$

In the previous expression, we gathered the different terms according to their computational order. It is clear that the Cholesky factorization of matrix $\mathbf{R}$ becomes the dominant operation as I_{g} approaches infinity.

A.1.2 FAEST

Now, we investigate the computational complexity of the FAEST solver studied in Section 3.4. In Table A.2, we show the steps required to compute the optimal filters for wPM-T using the FAEST solver, which are based on Algorithm 3.2. The optimal solution is obtained by time-updating the optimal filters for $I_{\text{d}}{=}I_{\text{g}}{+}I_{\text{h}}{-}1$ iterations. In each iteration, the auxiliary variables for FAEST are updated, and then, an estimate $\widehat{\mathbf{g}}_n$ is obtained. Let us note that in each iteration we must solve the systems $\mathbf{\Gamma}_n^{-1}\mathbf{E}_n^{\text{b}} = \mathbf{R}_n^{\text{b}}$ and $\mathbf{\Gamma}_n^{-1}\mathbf{e}_n = \mathbf{r}_n$, which require the factorization of the same matrix. Then, the Cholesky factorization of $\mathbf{\Gamma}_n^{-1}$ is performed only once per iteration to solve both systems. From Table A.2, the total number of FLOPs for the FAEST solver is:

$$N_{\text{flop}} = \left[10ML^2{+}4ML\right] I_{\text{g}} I_{\text{d}} + \left[\frac{1}{3}\left(M^3{+}L^3\right){+}8\left(M^2L{+}ML^2\right){+}\frac{1}{2}\left(5M^2{+}L^2\right){+}\frac{1}{6}\left(M{+}L\right)\right] I_{\text{d}}, \tag{A.20}$$

Again, we gathered the different terms according to their computational order. The operations involving matrices $\mathbf{G}_n$ and $\overleftarrow{\mathbf{H}}_n$ become dominant as I_{g} approaches infinity, because their size is related to I_{g}.

	Operation	Routine	Calls	FLOPs/call
Iterate for $n = 0, \ldots, I_\mathrm{d}-1$	$\mathbf{H}_n - \overleftarrow{\mathbf{H}}_{n-1} \boldsymbol{\Psi}^\mathrm{f}_{n-1} \rightarrow \mathbf{E}^\mathrm{f}_n$	BLAS/`dgemm`	I_d	$2ML^2I_\mathrm{g}$
	$\boldsymbol{\Gamma}_{n-1} \mathbf{E}^\mathrm{f}_n \rightarrow \mathbf{R}^\mathrm{f}_n$	BLAS/`dsymm`	I_d	$2M^2L$
	Solve with Chol. fact. $\boldsymbol{\Omega}^\mathrm{f}_{n-1} \setminus \left(\mathbf{E}^\mathrm{f}_n\right)^T \rightarrow \boldsymbol{\Phi}_1$	LAPACK/`dpotrf`	I_d	$\frac{1}{3}L^3 + \frac{1}{2}L^2 + \frac{1}{6}L$
		LAPACK/`dpotrs`	I_d	$2ML^2$
	$\mathbf{G}_{n-1} - \boldsymbol{\Psi}^\mathrm{f}_{n-1} \boldsymbol{\Phi}_1 \rightarrow \boldsymbol{\Phi}_2$	BLAS/`dgemm`	I_d	$2ML^2I_\mathrm{g}$
	$\left[\boldsymbol{\Phi}_1; [\boldsymbol{\Phi}_2]_{(0:L(I_\mathrm{g}-1)-1)}\right] \rightarrow \boldsymbol{\Theta}_1$	-	-	-
	$[\boldsymbol{\Phi}_2]_{(L(I_\mathrm{g}-1):LI_\mathrm{g}-1)} \rightarrow \boldsymbol{\Theta}_2$	-	-	-
	$\boldsymbol{\Theta}_1 + \boldsymbol{\Psi}^\mathrm{b}_{n-1} \boldsymbol{\Theta}_2 \rightarrow \mathbf{G}_n$	BLAS/`dgemm`	I_d	$2ML^2I_\mathrm{g}$
	$\boldsymbol{\Gamma}^{-1}_{n-1} + \mathbf{E}^\mathrm{f}_n \boldsymbol{\Phi}_1 \rightarrow \left(\boldsymbol{\Gamma}^\mathrm{e}_n\right)^{-1}$	BLAS/`dgemm`	I_d	$2M^2L$
	$\left(\boldsymbol{\Gamma}^\mathrm{e}_n\right)^{-1} - \mathbf{E}^\mathrm{b}_n \boldsymbol{\Theta}_2 \rightarrow \boldsymbol{\Gamma}^{-1}_n$	BLAS/`dgemm`	I_d	$2M^2L$
	$\beta \boldsymbol{\Theta}_2^T \boldsymbol{\Omega}^\mathrm{b}_{n-1} \rightarrow \mathbf{E}^\mathrm{b}_n$	BLAS/`dsymm`	I_d	$2ML^2$
	Solve with Chol. fact. $\boldsymbol{\Gamma}^{-1}_n \setminus \mathbf{E}^\mathrm{b}_n \rightarrow \mathbf{R}^\mathrm{b}_n$	LAPACK/`dpotrf`	I_d	$\frac{1}{3}M^3 + \frac{1}{2}M^2 + \frac{1}{6}M$
		LAPACK/`dpotrs`	I_d	$2M^2L$
	$\boldsymbol{\Omega}^\mathrm{f}_{n-1} + \left(\mathbf{E}^\mathrm{f}_n\right)^T \mathbf{R}^\mathrm{f}_n \rightarrow \boldsymbol{\Omega}^\mathrm{f}_n$	BLAS/`dgemm`	I_d	$2ML^2$
	$\boldsymbol{\Omega}^\mathrm{b}_{n-1} + \left(\mathbf{E}^\mathrm{b}_n\right)^T \mathbf{R}^\mathrm{b}_n \rightarrow \boldsymbol{\Omega}^\mathrm{b}_n$	BLAS/`dgemm`	I_d	$2ML^2$
	$\boldsymbol{\Psi}^\mathrm{f}_{n-1} + \mathbf{G}_{n-1} \mathbf{R}^\mathrm{f}_n \rightarrow \boldsymbol{\Psi}^\mathrm{f}_n$	BLAS/`dgemm`	I_d	$2ML^2I_\mathrm{g}$
	$\boldsymbol{\Psi}^\mathrm{b}_{n-1} + \mathbf{G}_n \mathbf{R}^\mathrm{b}_n \rightarrow \boldsymbol{\Psi}^\mathrm{b}_n$	BLAS/`dgemm`	I_d	$2ML^2I_\mathrm{g}$
	$\mathbf{d}_n - \overleftarrow{\mathbf{H}}_n \widehat{\mathbf{g}}_{n-1} \rightarrow \mathbf{e}_n$	BLAS/`dgemv`	I_d	$2MLI_\mathrm{g}$
	Solve with Chol. fact. $\boldsymbol{\Gamma}^{-1}_n \setminus \mathbf{e}_n \rightarrow \mathbf{r}_n$	LAPACK/`dpotrs`	I_d	$2M^2$
	$\widehat{\mathbf{g}}_{n-1} + \mathbf{G}_n \mathbf{r}_n \rightarrow \widehat{\mathbf{g}}_n$	BLAS/`dgemv`	I_d	$2MLI_\mathrm{g}$
$\widehat{\mathbf{g}}_{I_\mathrm{d}-1} \rightarrow \mathbf{g}_\mathrm{opt}$		-	-	-

Table A.2: Operations required by the FAEST solver to compute the filters for wPM-T, considering a system with L loudspeakers, M control points, filters of length I_g, and targets of length $I_\mathrm{d} = I_\mathrm{g} + I_\mathrm{h} - 1$.

	Operation	Routine	Calls	FLOPs/call
Comp. $\mathbf{g}_{\text{fd}}$	DFT of $h_{ml} \rightarrow \bar{\mathbf{H}}_f$	FFTW/`dft_r2c`	ML	$\frac{5}{2}N\log_2 N$
	DFT of $d_m \rightarrow \bar{\mathbf{d}}_f$	FFTW/`dft_r2c`	M	$\frac{5}{2}N\log_2 N$
	$\bar{\mathbf{H}}_f^H\bar{\mathbf{H}}_f+\beta\mathbf{I}_L \rightarrow \bar{\mathbf{R}}_f$	BLAS/`zherk`	$\frac{1}{2}N$	$4ML(L+1)$
	Solve with Chol. fact. $\bar{\mathbf{R}}_f \setminus \bar{\mathbf{H}}_f^H \rightarrow \bar{\mathbf{H}}_f^\dagger$	LAPACK/`zpotrf`	$\frac{1}{2}N$	$\frac{4}{3}L^3+3L^2+\frac{5}{3}L$
		LAPACK/`zpotrs`	$\frac{1}{2}N$	$8ML^2$
	$\bar{\mathbf{H}}_f^\dagger\bar{\mathbf{d}}_f \rightarrow \bar{\mathbf{q}}_{\text{opt},f}$	BLAS/`zgemv`	$\frac{1}{2}N$	$8ML$
	Form $\bar{\mathbf{q}}_{\text{opt}}$ using $\bar{\mathbf{q}}_{\text{opt},f}$	-	-	-
	$\mathbf{TF}_L^H\bar{\mathbf{q}}_{\text{opt}} \rightarrow \mathbf{g}_{\text{fd}}$	FFTW/`dft_c2r`	L	$\frac{5}{2}N\log_2 N$
Comp. correction term	$\bar{\mathbf{H}}_f^\dagger\bar{\mathbf{H}}_f \rightarrow \bar{\mathbf{\Lambda}}_f$	BLAS/`zgemm`	$\frac{1}{2}N$	$8ML^2$
	Form $\bar{\mathbf{\Lambda}}$ using $\bar{\mathbf{\Lambda}}_f$	-	-	-
	$\mathbf{B}\bar{\mathbf{q}}_{\text{opt}} \rightarrow \bar{\mathbf{r}}_0$	FFTW/`dft_c2r`	L	$\frac{5}{2}N\log_2 N$
		FFTW/`dft_r2c`	L	$\frac{5}{2}N\log_2 N$
	$\bar{\mathbf{\Lambda}}\bar{\mathbf{r}}_{p-1} \rightarrow \bar{\mathbf{r}}'_p$, for $p>0$	BLAS/`zgemv`	$\frac{1}{2}PN$	$8L^2$
	$\mathbf{B}\bar{\mathbf{r}}'_p \rightarrow \bar{\mathbf{r}}_p$, for $p>0$	FFTW/`dft_c2r`	PL	$\frac{5}{2}N\log_2 N$
		FFTW/`dft_r2c`	PL	$\frac{5}{2}N\log_2 N$
	$\sum_{p=0}^{P}\bar{\mathbf{r}}_p \rightarrow \bar{\mathbf{r}}$	C/`+`	$\frac{1}{2}PLN$	2
	$\bar{\mathbf{\Lambda}}\bar{\mathbf{r}} \rightarrow \bar{\mathbf{r}}$	BLAS/`zgemv`	$\frac{1}{2}N$	$8L^2$
	$\mathbf{TF}_L^H\bar{\mathbf{r}} \rightarrow \mathbf{r}$	FFTW/`dft_c2r`	L	$\frac{5}{2}N\log_2 N$
$\mathbf{g}_{\text{fd}}+\mathbf{r} \rightarrow \mathbf{g}_{\text{ap},P}$		C/`+`	LI_{g}	1

Table A.3: Operations required by the superfast solver [79] to compute the P-th order approximation of the filters for wPM-T, considering a system with L loudspeakers, M control points, filters of length I_{g}, and targets of length $I_{\text{d}} = I_{\text{g}}+I_{\text{h}}-1$. The size of the DFTs/IDFTs is $N = I_{\text{d}}$.

A.1.3 Superfast solver

Last, we discuss the superfast solver [79] studied in Section 3.5. In Table A.3, we show the steps required to compute the P-th order approximation of the filters for wPM-T using the superfast solver, which are based

on Algorithm 3.3. All the DFTs/IDFTs in Table A.3 are of size $N = I_\mathrm{d}$, because $I_\mathrm{d} = I_\mathrm{g}+I_\mathrm{h}-1$ control frequencies are considered for the superfast solver. Since h_{ml} and d_m are real-valued, all the computations for individual frequencies must be computed only for the $N/2$ control frequencies in the positive spectrum. Furthermore, we showed in Section 3.5 that $\bar{\mathbf{\Lambda}}$ is a block-diagonal matrix of size $LI_\mathrm{d}\times LI_\mathrm{d}$ that is formed by I_d blocks of size $L\times L$. Due to the hermitian symmetry, the product of $\bar{\mathbf{\Lambda}}$ and a vector of size $LI_\mathrm{d}\times 1$ can be alternatively performed as $I_\mathrm{d}/2$ independent products of matrices of size $L\times L$ and vectors of size $L\times 1$. Also, let us note that pre-multiplication by $\mathbf{F}_L^H$ is equivalent to perform L IDFTs of size I_d, so it can be computed by calling L times to routine `dft_c2r`. Moreover, pre-multiplication by $\mathbf{T}$ is equivalent to truncate L impulse responses of length I_d to length I_g, which is an arbitrary operation that does not involve any FLOPs. Nonetheless, we studied in Section 3.5 that pre-multiplication by $\mathbf{B}$ is equivalent to transform L frequency responses to the time-domain by using I_d-point IDFTs, set to zero their first I_g samples, and transform back to the frequency-domain by using I_d-point DFTs. Then, pre-multiplication by $\mathbf{B}$ can be computed by calling L times to routines `dft_c2r` and `dft_r2c`. From Table A.3, the total number of FLOPs for the superfast solver is:

$$N_\mathrm{flop} = \left[5L\right] PI_\mathrm{d}\log_2 I_\mathrm{d} + \left[4L^2+L\right] PI_\mathrm{d} + \left[\frac{5}{2}ML+\frac{5}{2}M+10L\right] I_\mathrm{d}\log_2 I_\mathrm{d} + \left[\frac{2}{3}L^3+\frac{11}{2}L^2+\frac{5}{6}L+2ML(5L+3)\right] I_\mathrm{d} + \left[L\right] I_\mathrm{g}, \tag{A.21}$$

From the previous expression, it is clear that the I_d-point DFTs and IDFTs required to compute the P correction terms become the dominant operations as I_g and P approach infinity.

A.2 Computational complexity of wPM-F

In this section, we study the computational complexity of wPM-F. In Table A.4, we show the required steps to compute the filters of length I_g for wPM-F, which are based on the method described in Section 2.2.3 using cost function (2.23). We consider that the number of control frequencies for which the optimal responses are computed is $I_\mathrm{d} = I_\mathrm{g}+I_\mathrm{h}-1$, so the DFTs/IDFTs in Table A.4 are of size $N = I_\mathrm{d}$. It is worth noting that other sizes could be used. Since h_{ml} and d_m are real-valued, all the computations

Operation	Routine	Calls	FLOPs/call
DFT of $h_{ml} \rightarrow \bar{\mathbf{H}}_f$	FFTW/`dft_r2c`	ML	$\frac{5}{2}N\log_2 N$
DFT of $d_m \rightarrow \bar{\mathbf{d}}_f$	FFTW/`dft_r2c`	M	$\frac{5}{2}N\log_2 N$
$\bar{\mathbf{H}}_f^H \bar{\mathbf{H}}_f + \beta \mathbf{I}_L \rightarrow \bar{\mathbf{R}}_f$	BLAS/`zherk`	$\frac{1}{2}N$	$4ML(L+1)$
$\bar{\mathbf{H}}_f^H \bar{\mathbf{d}}_f \rightarrow \bar{\mathbf{c}}_f$	BLAS/`zgemv`	$\frac{1}{2}N$	$8ML$
Solve with Chol. fact. $\bar{\mathbf{R}}_f \setminus \bar{\mathbf{c}}_f \rightarrow \bar{\mathbf{q}}_{\mathrm{opt},f}$	LAPACK/`zpotrf`	$\frac{1}{2}N$	$\frac{4}{3}L^3 + 3L^2 + \frac{5}{3}L$
	LAPACK/`zpotrs`	$\frac{1}{2}N$	$8L^2$
Form $\bar{\mathbf{q}}_{\mathrm{opt}}$ using $\bar{\mathbf{q}}_{\mathrm{opt},f}$	-	-	-
$\mathbf{TF}_L^H \bar{\mathbf{q}}_{\mathrm{opt}} \rightarrow \mathbf{g}_{\mathrm{fd}}$	FFTW/`dft_c2r`	L	$\frac{5}{2}N\log_2 N$

Table A.4: Operations required to compute the filters for wPM-F, considering a system with L loudspeakers, M control points, filters of length I_{g}, and targets of length $I_{\mathrm{d}} = I_{\mathrm{g}} + I_{\mathrm{h}} - 1$. The size for the DFTs/IDFTs is $N = I_{\mathrm{d}}$.

for individual frequencies must be computed only for the $N/2$ control frequencies in the positive spectrum. From Table A.4, we can conclude that the total number of FLOPs is:

$$N_{\mathrm{flop}} = \left[\frac{5}{2}\left(ML+M+L\right)\right] I_{\mathrm{d}} \log_2 I_{\mathrm{d}} + \left[\frac{2}{3}L^3 + 2ML^2 + 6ML + \frac{11}{2}L^2 + \frac{5}{6}L\right] I_{\mathrm{d}}. \tag{A.22}$$

Then, the I_{d}-point DFTs and IDFTs become the dominant operations in Table A.4 as I_{g} approaches infinity.

A.3 Computational complexity of wPM-S

In this section, we study the computational complexity of wPM-S. We consider a GDFT filter bank with K subbands, resampling factor R, and prototype filter p of length I_{p}. Since the subband decomposition of the RIRs and the target impulse responses is required to compute the subband filters for wPM-S, we first study the computational complexity of the subband

decomposition, and later, we discuss the complexity required to compute the subband filters.

A.3.1 Subband decomposition

First, we discuss the computational complexity of the subband decomposition of a generic signal a of length I_{a}. We assume that $\widetilde{a}_k$ is the $I_{\widetilde{\mathrm{a}},k}$-length signal at the output of the k-th subband of the analysis filter bank when is fed with a, where

$$I_{\widetilde{\mathrm{a}},k} = \lceil (I_{\mathrm{a}}+I_{\mathrm{p}}-1)/R \rceil , \tag{A.23}$$

and that a_k is the $I_{\mathrm{a},k}$-length subband component of a in the k-th subband, where

$$I_{\mathrm{a},k} = I_{\widetilde{\mathrm{a}},k} - \lceil I_{\mathrm{p}}/R \rceil +1. \tag{A.24}$$

Next, we study the original method proposed in [102], and later, the method proposed in Section 4.2.3.

Original

Reilly et al. [102] proposed to compute the subband component of a in the k-th subband as

$$\mathbf{a}_{\mathrm{opt},k} = \left(\widetilde{\mathbf{\Delta}}_k^H \widetilde{\mathbf{\Delta}}_k \right)^{-1} \widetilde{\mathbf{\Delta}}_k^H \widetilde{\mathbf{a}}_k, \tag{A.25}$$

where $\widetilde{\mathbf{a}}_k$ is a vector defined in (4.43) that contains the samples of $\widetilde{a}_k$, and $\widetilde{\mathbf{\Delta}}_k$ is a matrix defined in (4.44) that contains shifted versions of $\widetilde{\delta}_k = (u_k)_{\downarrow R}$. The previous expression can be alternatively written as

$$\mathbf{a}_{\mathrm{opt},k} = \widetilde{\mathbf{R}}_k^{-1} \widetilde{\mathbf{c}}_k, \tag{A.26}$$

where $\widetilde{\mathbf{R}}_k = \widetilde{\mathbf{\Delta}}_k^H \widetilde{\mathbf{\Delta}}_k$ and $\widetilde{\mathbf{c}}_k = \widetilde{\mathbf{\Delta}}_k^H \widetilde{\mathbf{a}}_k$. Since $\widetilde{\mathbf{\Delta}}$ is a toeplitz matrix, it is easy to see that (A.26) has the same form as (3.3). Then, the solvers described for wPM-T can be easily extended to compute (A.26), taking into account that it involves complex-valued matrices. In particular, we consider next the Cholesky solver discussed in Section A.1.1, i.e., $\widetilde{\mathbf{R}}_k$ and $\widetilde{\mathbf{c}}_k$ are computed using DFTs and the system is solved using the Cholesky factorization.

Operation		Routine	Calls	FLOPs/call
Comp. $\widetilde{\mathbf{R}}_k$	$u_k \to (u_k)_{\downarrow R} \to \widetilde{\delta}_k$	-	-	-
	DFT of $\widetilde{\delta}_k \to \widetilde{\Delta}_k(f)$	FFTW/`dft`	$\frac{1}{2}K$	$5N\log_2 N$
	$\widetilde{\Delta}_k^*(f)\widetilde{\Delta}_k(f) \to \widetilde{R}_k(f)$	C/`*`	$\frac{1}{2}KN$	6
	IDFT of $\widetilde{R}_k(f) \to \widetilde{\mathbf{R}}_{\mathrm{e},k}$	FFTW/`dft`	$\frac{1}{2}K$	$5N\log_2 N$
	$\big[\widetilde{\mathbf{R}}_{\mathrm{e},k}\big]_{(0:I_{\mathrm{a},k}-1,0:I_{\mathrm{a},k}-1)} \downarrow \widetilde{\mathbf{R}}_k$	-	-	-
Comp. $\widetilde{\mathbf{c}}_k$	$a \to \widetilde{a}_k$	`polyphase` [148]	Q	$(I_\mathrm{a}/R)\big[2I_\mathrm{p}+ 2K+ 5K\log_2 K\big]$
	DFT of $\widetilde{a}_k \to \widetilde{A}_k(f)$	FFTW/`dft`	$\frac{1}{2}KQ$	$5N\log_2 N$
	$\widetilde{\Delta}_k^*(f)\widetilde{A}_k(f) \to \widetilde{C}_k(f)$	C/`*`	$\frac{1}{2}KNQ$	6
	IDFT of $\widetilde{C}_k(f) \to \widetilde{\mathbf{c}}_{\mathrm{e},k}$	FFTW/`dft`	$\frac{1}{2}KQ$	$5N\log_2 N$
	$\big[\widetilde{\mathbf{c}}_{\mathrm{e},k}\big]_{0:I_{\mathrm{a},k}-1} \to \widetilde{\mathbf{c}}_k$	-	-	-
Solve with Chol. fact. $\widetilde{\mathbf{R}}_k \setminus \widetilde{\mathbf{c}}_k \to \mathbf{a}_{\mathrm{opt},k}$		LAPACK/`zpotrf`	$\frac{1}{2}K$	$\frac{4}{3}I_{\mathrm{a},k}^3+ 3I_{\mathrm{a},k}^2+\frac{5}{3}I_{\mathrm{a},k}$
		LAPACK/`zpotrs`	$\frac{1}{2}KQ$	$8I_{\mathrm{a},k}^2$

Table A.5: Operations required by the approach proposed in [148] to compute the subband components in all subbands for Q signals a of length I_a, considering a GDFT filter bank with K subbands, resampling factor R, and prototype filter of length I_p. The size for the DFTs/IDFTs is $N = I_{\widetilde{\mathrm{a}},k}$.

For wPM-S, we are interested in the subband decomposition of multiple signals of equal length. Then, rather than studying the subband decomposition of a single signal, we consider the subband decomposition of Q signals, since many computations are common to all of them. We show in Table A.5 the steps required to compute the optimal subband components of a set of Q signals a of equal length I_a using the approach previously described. In Table A.5, the analysis signals $\widetilde{a}_k$ are computed with the polyphase implementation proposed by [148], which involves DFTs of size K. The other DFTs/IDFTs in Table A.5 are of size $N = I_{\widetilde{\mathrm{a}},k}$. Let us note

that the optimal subband components are only computed for the $K/2$ subbands in the positive spectrum due to the hermitian symmetry. Moreover, $\widetilde{\mathbf{R}}_k$ in (A.26) is common for all Q signals. Then, for each subband, $\widetilde{\mathbf{R}}_k$ and its Cholesky factorization only need to be computed once for all Q signals. Also, it is worth noting that we consider that the decimation operation required to compute $\widetilde{\delta}_k$ does not require any FLOPs. From Table A.5, the number of FLOPs required to compute the optimal subband components for the Q signals and K subbands is:

$$N_{\text{flop}} = \left[\frac{2}{3}K\right] I_{\text{a},k}^3 + \left[K\left(\frac{3}{2}+4Q\right)\right] I_{\text{a},k}^2 + \left[5K\left(Q+1\right)\right] I_{\widetilde{\text{a}},k}\log_2 I_{\widetilde{\text{a}},k} + \left[\frac{5}{6}K\right] I_{\text{a},k} + \left[\frac{Q}{R}\left(2I_{\text{p}}+2K+5K\log_2 K\right)\right] I_{\text{a}} + \left[3K\left(Q+1\right)\right] I_{\widetilde{\text{a}},k}. \tag{A.27}$$

Proposed approach for subband decomposition

In Section 4.2.3, we proposed to compute the optimal subband component of a in the k-th subband as

$$\mathbf{a}_{\text{opt},k} = \mathbf{E}_k^H \left(\mathbf{P}^T\mathbf{P}\right)^{-1} \mathbf{P}^T \mathbf{T}_k^H \widetilde{\mathbf{a}}_k, \tag{A.28}$$

where $\mathbf{P}$ is a matrix defined in (4.50) that contains shifted versions of the downsampled prototype filter $p_{\downarrow R}$, and $\mathbf{T}_k$ and $\mathbf{E}_k$ are diagonal matrices defined in (4.48) and (4.49), respectively, that contain exponential terms. Now, let us define

$$\mathbf{a}_{\text{opt},k}^{\phi} = \mathbf{E}_k \mathbf{a}_{\text{opt},k}, \tag{A.29}$$

$$\widetilde{\mathbf{a}}_k^{\phi} = \mathbf{T}_k^H \widetilde{\mathbf{a}}_k, \tag{A.30}$$

which are phase-shifted versions of $\mathbf{a}_{\text{opt},k}$ and $\widetilde{\mathbf{a}}_k$, respectively. Then, instead of directly computing $\mathbf{a}_{\text{opt},k}$, we can compute $\mathbf{a}_{\text{opt},k}^{\phi}$ as

$$\mathbf{a}_{\text{opt},k}^{\phi} = \left(\mathbf{P}^T\mathbf{P}\right)^{-1} \mathbf{P}^T \widetilde{\mathbf{a}}_k^{\phi}, \tag{A.31}$$

and then, we can compute the optimal solution as $\mathbf{a}_{\text{opt},k} = \mathbf{E}_k^H \mathbf{a}_{\text{opt},k,\phi}$. Now, we can express (A.31) as

$$\mathbf{a}_{\text{opt},k}^{\phi} = \mathbf{R}_{\text{p}}^{-1} \widetilde{\mathbf{c}}_k^{\phi}, \tag{A.32}$$

Operation		Routine	Calls	FLOPs/call
Comp. $\mathbf{R}_\mathrm{p}$	$p \to p_{\downarrow R}$	-	-	-
	DFT of $p_{\downarrow R} \to P_{\downarrow R}(f)$	FFTW/`dft_r2c`	1	$\frac{5}{2}N\log_2 N$
	$P^*_{\downarrow R}(f)P_{\downarrow R}(f) \to R_\mathrm{p}(f)$	C/*	$\frac{1}{2}N$	6
	IDFT of $R_\mathrm{p}(f) \to \mathbf{R}_\mathrm{e,p}$	FFTW/`dft_c2r`	1	$\frac{5}{2}N\log_2 N$
	$\left[\mathbf{R}_\mathrm{e,p}\right]_{(0:I_{\mathrm{a},k}-1,0:I_{\mathrm{a},k}-1)} \downarrow \mathbf{R}_\mathrm{p}$	-	-	-
Comp. $\widetilde{\mathbf{c}}_k^\phi$	$a \to \widetilde{a}_k$	`polyphase` [148]	Q	$(I_\mathrm{a}/R)\left[2I_\mathrm{p}+ 2K+ 5K\log_2 K\right]$
	Phase shift $\widetilde{a}_k \to \widetilde{a}_k^\phi$	C/*	$\frac{1}{2}KNQ$	6
	DFT of $\widetilde{a}_k^\phi \to \widetilde{A}_k^\phi(f)$	FFTW/`dft`	$\frac{1}{2}KQ$	$5N\log_2 N$
	$P^*_{\downarrow R}(f)\widetilde{A}_k^\phi(f) \to \widetilde{C}_k^\phi(f)$	C/*	$\frac{1}{2}KNQ$	6
	IDFT of $\widetilde{C}_k^\phi(f) \to \widetilde{\mathbf{c}}_{\mathrm{e},k}^\phi$	FFTW/`dft`	$\frac{1}{2}KQ$	$5N\log_2 N$
	$\left[\widetilde{\mathbf{c}}_{\mathrm{e},k}^\phi\right]_{0:I_{\mathrm{a},k}-1} \to \widetilde{\mathbf{c}}_k^\phi$	-	-	-
Chol. fact. $\mathbf{R}_\mathrm{p} \to \mathbf{L}_\mathrm{p}$		LAPACK/`dpotrf`	1	$\frac{1}{3}I_{\mathrm{a},k}^3+ \frac{1}{2}I_{\mathrm{a},k}^2+\frac{1}{6}I_{\mathrm{a},k}$
Solve with Chol. fact. $\mathbf{R}_\mathrm{p} \setminus \Re\left\{\widetilde{\mathbf{c}}_k^\phi\right\} \to \Re\left\{\widetilde{\mathbf{a}}_{\mathrm{opt},k}^\phi\right\}$		LAPACK/`dpotrs`	$\frac{1}{2}KQ$	$2I_{\mathrm{a},k}^2$
Solve with Chol. fact. $\mathbf{R}_\mathrm{p} \setminus \Im\left\{\widetilde{\mathbf{c}}_k^\phi\right\} \to \Im\left\{\widetilde{\mathbf{a}}_{\mathrm{opt},k}^\phi\right\}$		LAPACK/`dpotrs`	$\frac{1}{2}KQ$	$2I_{\mathrm{a},k}^2$
$\mathbf{E}_k^H\widetilde{\mathbf{a}}_{\mathrm{opt},k}^\phi \to \widetilde{\mathbf{a}}_{\mathrm{opt},k}$		C/*	$\frac{1}{2}KQI_{\mathrm{a},k}$	6

Table A.6: Operations required by the approach proposed in Section 4.2.3 to compute the subband components in all subbands for Q signals a of length I_a, considering a GDFT filter bank with K subbands, resampling factor R, and prototype filter of length I_p. The size for the DFTs/IDFTs is $N = I_{\widetilde{\mathrm{a}},k}$.

in which $\mathbf{R}_\mathrm{p} = \mathbf{P}^T\mathbf{P}$, and $\widetilde{\mathbf{c}}_k^{\,\phi} = \mathbf{P}^T\widetilde{\mathbf{a}}_k^{\,\phi}$. Since $\mathbf{R}_\mathrm{p}$ is a real matrix, the real and imaginary components of $\mathbf{a}_{\mathrm{opt},k}^{\,\phi}$ can be independently computed by solving two real-valued systems of linear equations that involve matrix $\mathbf{R}_\mathrm{p}$ (which is common for all subbands). Moreover, the systems for the real and imaginary components have the same form as (3.3). Hence, we consider that the Cholesky solver discussed in Section A.1.1 is used to solve the systems, i.e., $\mathbf{R}_\mathrm{p}$ and $\widetilde{\mathbf{c}}_k$ are computed using DFTs and the systems related to the real and imaginary components are solved using the Cholesky factorization.

We show in Table A.6 the steps required to compute the optimal subband components of a set of Q signals a of equal length I_a using the approach previously described. Some aspects, as the computation of $\widetilde{a}_k$, are common for Tables A.5 and A.6, so they are not discussed again here. Let us note that $\mathbf{R}_\mathrm{p}$ in (A.26) is common for all subbands and all signals. Then, $\mathbf{R}_\mathrm{p}$ and its Cholesky factorization only need to be computed once for the K subbands and Q signals, while $K/2$ factorizations are required for the approach proposed in [102]. This is the main strength of the proposed method. From Table A.6, the number of FLOPs required to compute the optimal subband components for the Q signals and K subbands is:

$$\begin{aligned} N_\mathrm{flop} = &\left[\frac{1}{3}\right] I_{\mathrm{a},k}^3 + \left[2QK+\frac{1}{2}\right] I_{\mathrm{a},k}^2 + \left[5\,(QK+1)\right] I_{\widetilde{\mathrm{a}},k}\log_2 I_{\widetilde{\mathrm{a}},k} + \\ &\left[3QK+\frac{1}{6}\right] I_{\mathrm{a},k} + \left[\frac{Q}{R}\,(2I_\mathrm{p}+2K+5K\log_2 K)\right] I_\mathrm{a} + \left[6QK+3\right] I_{\widetilde{\mathrm{a}},k}. \end{aligned} \tag{A.33}$$

From (A.27) and (A.33), we can see that the proposed approach requires approximately $2K$ times less FLOPs than the original approach [102].

A.3.2 Computation of subband filters

Now, we focus on the computational complexity required to compute the subband filters of length $I_{\mathrm{g},k}$ for wPM-S, assuming that the subband components $h_{ml,k}$ and $d_{m,k}$ are already known. We showed in Section 4.3.4, that the optimal subband filters in the k-th subband for wPM-S can be computed as

$$\dot{\mathbf{g}}_{\mathrm{opt},k} = \left(\dot{\mathbf{H}}_k^H\dot{\mathbf{H}}_k + \dot{\beta}_k\mathbf{I}_{LI_{\mathrm{g},k}}\right)^{-1}\dot{\mathbf{H}}_k^H\dot{\mathbf{d}}_k, \tag{A.34}$$

or alternatively as

$$\dot{\mathbf{g}}_{\mathrm{opt},k}=\dot{\mathbf{R}}_k^{-1}\dot{\mathbf{c}}_k, \tag{A.35}$$

where $\dot{\mathbf{R}}_k = \dot{\mathbf{H}}_k^H\dot{\mathbf{H}}_k+\dot{\beta}_k\mathbf{I}_{LI_{\mathrm{g},k}}$, and $\dot{\mathbf{c}}_k = \dot{\mathbf{H}}_k^H\dot{\mathbf{d}}_k$. In the previous expressions, we did not consider the weighting matrix $\dot{\mathbf{W}}_k$. Again, we can see that (A.35) has the same form as (3.3). Then, the solvers described for wPM-T can be easily extended to compute (A.35), taking into account that it involves complex-valued matrices.

	Operation	Routine	Calls	FLOPs/call
Comp. $\dot{\mathbf{R}}_k$	DFT of $h_{ml,k} \rightarrow \bar{\mathbf{H}}_{f,k}$	FFTW/`dft`	ML	$5N\log_2 N$
	$\bar{\mathbf{H}}_{f,k}^H\bar{\mathbf{H}}_{f,k}+\beta_k\mathbf{I}_L \rightarrow \bar{\mathbf{R}}_{f,k}$	BLAS/`zherk`	N	$4ML(L+1)$
	IDFT of $\bar{\mathbf{R}}_{f,k} \rightarrow \dot{\mathbf{R}}_{\mathrm{e},k}$	FFTW/`dft`	$\frac{L(L+1)}{2}$	$5N\log_2 N$
	$\left[\dot{\mathbf{R}}_{\mathrm{e},k}\right]_{(0:LI_{\mathrm{g},k}-1,0:LI_{\mathrm{g},k}-1)} \downarrow \dot{\mathbf{R}}_k$	-	-	-
Comp. $\dot{\mathbf{c}}_k$	DFT of $d_{m,k} \rightarrow \bar{\mathbf{d}}_{f,k}$	FFTW/`dft`	M	$5N\log_2 N$
	$\bar{\mathbf{H}}_{f,k}^H\bar{\mathbf{d}}_{f,k} \rightarrow \bar{\mathbf{c}}_{f,k}$	BLAS/`zgemv`	N	$8ML$
	IDFT of $\bar{\mathbf{c}}_{f,k} \rightarrow \dot{\mathbf{c}}_{\mathrm{e},k}$	FFTW/`dft`	L	$5N\log_2 N$
	$[\dot{\mathbf{c}}_{e,k}]_{0:LI_{\mathrm{g},k}-1} \rightarrow \dot{\mathbf{c}}_k$	-	-	-
Solve with Chol. fact. $\dot{\mathbf{R}}_k \setminus \dot{\mathbf{c}}_k \rightarrow \dot{\mathbf{g}}_{\mathrm{opt},k}$		LAPACK/`zpotrf`	1	$\frac{4}{3}(LI_{\mathrm{g},k})^3+3(LI_{\mathrm{g},k})^2+\frac{5}{3}(LI_{\mathrm{g},k})$
		LAPACK/`zpotrs`	1	$8\,(LI_{\mathrm{g},k})^2$

Table A.7: Operations required by the Cholesky solver to compute the subband filters in the k-th subband for wPM-S, considering a system with L loudspeakers, M control points, subband filters of length $I_{\mathrm{g},k}$, and targets of length $I_{\mathrm{d},k} = I_{\mathrm{g},k}+I_{\mathrm{h},k}-1$. The size for the DFTs/IDFTs is $N = I_{\mathrm{d},k}$. We assume that $h_{ml,k}$ and $d_{m,k}$ are known.

Cholesky solver

We consider next the Cholesky solver discussed in Section A.1.1, i.e., $\dot{\mathbf{R}}_k$ and $\dot{\mathbf{c}}_k$ are computed using DFTs and the system is solved using the Cholesky factorization. In Table A.7, we present the steps required to compute the optimal subband filters for the k-th subband using the approach previously described. The DFTs/IDFTs in Table A.7 required to compute $\dot{\mathbf{R}}_k$ and $\dot{\mathbf{c}}_k$ are of size $N = I_{\mathrm{d},k} = I_{\mathrm{g},k}+I_{\mathrm{h},k}-1$. The subband filters are only computed for $K/2$ subbands due to the hermitian symmetry of the GDFT filter bank. Then, from Table A.7, the number of FLOPs needed to compute all the subband filters is:

$$N_{\mathrm{flop}}=\sum_{k=0}^{K/2-1}\left(\left[\frac{4}{3}L^3\right]I_{\mathrm{g},k}^3+\left[11L^2\right]I_{\mathrm{g},k}^2+\left[5\left(ML+M+\frac{1}{2}L^2+\frac{3}{2}L\right)\right]I_{\mathrm{d},k}\log_2 I_{\mathrm{d},k}+\left[4ML\,(L+3)\right]I_{\mathrm{d},k}+\left[\frac{5}{3}L\right]I_{\mathrm{g},k}\right). \tag{A.36}$$

Superfast solver

We consider now the superfast solver [79] discussed in Section 3.5 to compute the subband filters for wPM-S. The expressions presented in Section 3.5 for the superfast solver can be directly used for computing the subband filters by adding subbindex k to all the elements of the expressions, and also by taking into consideration that the time domain signals in this case are complex-valued. In Table A.8, we present the steps required to compute the P_k-th order approximation of the subband filters for the k-th subband using the superfast solver. The DFTs/IDFTs in Table A.8 are of size $N = I_{\mathrm{d},k} = I_{\mathrm{g},k}+I_{\mathrm{h},k}-1$. The subband filters are only computed for $K/2$ subbands due to the hermitian symmetry of the GDFT filter bank. Then, from Table A.8, the number of FLOPs needed to compute all the subband filters is:

$$N_{\mathrm{flop}}=\sum_{k=0}^{K/2-1}\left(\left[10L\right]P_k I_{\mathrm{d},k}\log_2 I_{\mathrm{d},k}+\left[5ML+5M+20L\right]I_{\mathrm{d},k}\log_2 I_{\mathrm{d},k}+\left[8L^2+2L\right]P_k I_{\mathrm{d},k}+\left[\frac{4}{3}L^3+11L^2+\frac{5}{3}L+4ML(5L+3)\right]I_{\mathrm{d},k}+\left[2L\right]I_{\mathrm{g},k}\right). \tag{A.37}$$

	Operation	Routine	Calls	FLOPs/call
Comp. $\dot{\mathbf{g}}_{\mathrm{fd},k}$	DFT of $h_{ml,k} \rightarrow \bar{\mathbf{H}}_{f,k}$	FFTW/`dft`	ML	$5N\log_2 N$
	DFT of $d_{m,k} \rightarrow \bar{\mathbf{d}}_{f,k}$	FFTW/`dft`	M	$5N\log_2 N$
	$\bar{\mathbf{H}}_{f,k}^H \bar{\mathbf{H}}_{f,k} + \beta_k \mathbf{I}_L \rightarrow \bar{\mathbf{R}}_{f,k}$	BLAS/`zherk`	N	$4ML(L+1)$
	Solve with Chol. fact. $\bar{\mathbf{R}}_{f,k} \setminus \bar{\mathbf{H}}_{f,k}^H \rightarrow \bar{\mathbf{H}}_{f,k}^\dagger$	LAPACK/`zpotrf`	N	$\frac{4}{3}L^3 + 3L^2 + \frac{5}{3}L$
		LAPACK/`zpotrs`	N	$8ML^2$
	$\bar{\mathbf{H}}_{f,k}^\dagger \bar{\mathbf{d}}_{f,k} \rightarrow \bar{\mathbf{q}}_{\mathrm{opt},f,k}$	BLAS/`zgemv`	N	$8ML$
	Form $\bar{\mathbf{q}}_{\mathrm{opt},k}$ using $\bar{\mathbf{q}}_{\mathrm{opt},f,k}$	-	-	-
	$\mathbf{T}_k \mathbf{F}_{L,k}^H \bar{\mathbf{q}}_{\mathrm{opt},k} \rightarrow \dot{\mathbf{g}}_{\mathrm{fd},k}$	FFTW/`dft`	L	$5N\log_2 N$
Comp. correction term	$\bar{\mathbf{H}}_{f,k}^\dagger \bar{\mathbf{H}}_{f,k} \rightarrow \bar{\mathbf{\Lambda}}_{f,k}$	BLAS/`zgemm`	N	$8ML^2$
	Form $\bar{\mathbf{\Lambda}}_k$ using $\bar{\mathbf{\Lambda}}_{f,k}$	-	-	-
	$\mathbf{B}_k \bar{\mathbf{q}}_{\mathrm{opt},k} \rightarrow \bar{\mathbf{r}}_{0,k}$	FFTW/`dft`	L	$5N\log_2 N$
		FFTW/`dft`	L	$5N\log_2 N$
	$\bar{\mathbf{\Lambda}}_k \bar{\mathbf{r}}_{p-1,k} \rightarrow \bar{\mathbf{r}}'_{p,k}$, for $p > 0$	BLAS/`zgemv`	$P_k N$	$8L^2$
	$\mathbf{B}_k \bar{\mathbf{r}}'_{p,k} \rightarrow \bar{\mathbf{r}}_{p,k}$, for $p > 0$	FFTW/`dft`	$P_k L$	$5N\log_2 N$
		FFTW/`dft`	$P_k L$	$5N\log_2 N$
	$\sum_{p=0}^{P} \bar{\mathbf{r}}_{p,k} \rightarrow \bar{\mathbf{r}}_k$	C/`+`	$P_k LN$	2
	$\bar{\mathbf{\Lambda}}_k \bar{\mathbf{r}}_k \rightarrow \bar{\mathbf{r}}_k$	BLAS/`zgemv`	N	$8L^2$
	$\mathbf{T}_k \mathbf{F}_{L,k}^H \bar{\mathbf{r}}_k \rightarrow \dot{\mathbf{r}}_k$	FFTW/`dft`	L	$5N\log_2 N$
$\dot{\mathbf{g}}_{\mathrm{fd},k} + \dot{\mathbf{r}}_k \rightarrow \dot{\mathbf{g}}_{\mathrm{ap},P_k,k}$		C/`+`	$LI_{\mathrm{g},k}$	2

Table A.8: Operations required by the superfast solver [79] to compute the P_k-th order approximation of the subband filters in the k-th subband for wPM-S, considering a system with L loudspeakers, M control points, subband filters of length $I_{\mathrm{g},k}$, and targets of length $I_{\mathrm{d},k} = I_{\mathrm{g},k} + I_{\mathrm{h},k} - 1$. The size for the DFTs/IDFTs is $N = I_{\mathrm{d},k}$. We assume that $h_{ml,k}$ and $d_{m,k}$ are known.

A.3.3 Total computational complexity

The total computational complexity of wPM-S is the combination of the computational complexities required to compute the subband decomposition of h_{ml} and d_m, and to compute the optimal subband filters. The number of FLOPs required to compute the subband components of h_{ml} are obtained by setting $Q{=}ML$, $I_{\mathrm{a}}{=}I_{\mathrm{h}}$, $I_{\tilde{\mathrm{a}},k}{=}I_{\tilde{\mathrm{h}},k}$, and $I_{\mathrm{a},k}{=}I_{\mathrm{h},k}$ in (A.33), where $I_{\tilde{\mathrm{h}},k}{=}\lceil (I_{\mathrm{h}}{+}I_{\mathrm{p}}{-}1)\,/R \rceil$ and $I_{\mathrm{h},k}{=}I_{\tilde{\mathrm{h}},k}{-}\lceil I_{\mathrm{p}}/R \rceil{+}1$. Similarly, the number of FLOPs required to compute the subband components of d_m are obtained by setting $Q{=}M$, $I_{\mathrm{a}}{=}I_{\mathrm{d}}$, $I_{\tilde{\mathrm{a}},k}{=}I_{\tilde{\mathrm{d}},k}$, and $I_{\mathrm{a},k}{=}I_{\mathrm{d},k}$ in (A.33), where $I_{\tilde{\mathrm{d}},k}{=}\lceil (I_{\mathrm{d}}{+}I_{\mathrm{p}}{-}1)\,/R \rceil$ and $I_{\mathrm{d},k}{=}I_{\tilde{\mathrm{d}},k}{-}\lceil I_{\mathrm{p}}/R \rceil{+}1$. Finally, the number of FLOPs required to compute the subband filters is obtained with (A.36) for the Cholesky solver and with (A.37) for the superfast solver.

Appendix B

Prototype filter design for GDFT filter banks

In this appendix we describe the method used in this work for designing the prototype filters for GDFT filter banks. We studied in Section 4.2 that a broadband system can be accurately approximated using a GDFT filter bank if conditions (4.34) and (4.35) are fulfilled, which are directly related to the Reconstruction Error (RE) and the Alias-To-Signal Ratio (ASR) of the filter bank, respectively. Then, we propose designing the prototype filter by minimizing the ASR and the RE of the filter bank. We consider a GDFT filter bank with even number of subbands K, resampling factor R, and a symmetric prototype filter p, i.e., with linear phase, of odd length I_{p}. First, we derive the formulation that is later used to define the optimization proposed to compute the prototype filters. Afterwards, we show the impulse and frequency responses of prototype filters obtained with the proposed method for different filter bank configurations.

B.1 Formulation

Next, we derive suitable expressions for the ASR and the RE, such that we can define a cost function for designing the prototype filter p. Let us start by defining a $I_{\mathrm{p}}\times 1$ vector of the coefficients of the prototype filter as

$$\mathbf{p}_{\mathrm{full}} = \begin{bmatrix} p(0) & \dots & p(I_{\mathrm{p}}-1) \end{bmatrix}^T. \tag{B.1}$$

Since we assume that p is symmetric and that I_{p} is odd, $\mathbf{p}_{\mathrm{full}}$ only contains $Q_{\mathrm{p}} = (I_{\mathrm{p}}+1)/2$ unique elements. Then, it can be expressed as

$$\mathbf{p}_{\mathrm{full}} = \mathbf{\Pi}\mathbf{p}, \tag{B.2}$$

where $\mathbf{p}$ is a $Q_\mathrm{p}\times 1$ vector containing the unique elements of $\mathbf{p}_\mathrm{full}$, i.e.,

$$\mathbf{p} = \begin{bmatrix} p(0) & \dots & p(Q_\mathrm{p}-1) \end{bmatrix}^T, \tag{B.3}$$

and $\mathbf{\Pi}$ is a $I_\mathrm{p}\times Q_\mathrm{p}$ matrix given by

$$\mathbf{\Pi} = \begin{bmatrix} & \mathbf{I}_{Q_\mathrm{p}} & \\ \begin{bmatrix} \mathbf{J}_{Q_\mathrm{p}-1} & \mathbf{0}_{(Q_\mathrm{p}-1)\times 1} \end{bmatrix} & & \end{bmatrix}, \tag{B.4}$$

in which $\mathbf{J}_{Q_\mathrm{p}-1}$ is the reversed identity matrix of size $Q_\mathrm{p}-1\times Q_\mathrm{p}-1$. Next, we use $\mathbf{p}$ instead of $\mathbf{p}_\mathrm{full}$ to implicitly incorporate the symmetry of the prototype filter in the formulation.

B.1.1 Alias-To-Signal Ratio (ASR)

First, we derive an expression for the ASR as a function of $\mathbf{p}$. In Section 4.2, we defined the ASR as

$$\mathrm{ASR} = \frac{\frac{1}{R-1}\sum_{k=0}^{K-1}\sum_{i=1}^{R-1}\int_0^{2\pi}\left|U_k^*(e^{j\omega})U_k(e^{j\omega}\Phi_R^i)\right|^2 d\omega}{\sum_{k=0}^{K-1}\int_0^{2\pi}\left|U_k(e^{j\omega})\right|^2 d\omega}. \tag{B.5}$$

Taking into account that the frequency response of the analysis filter in the k-th subband for a GDFT filter bank with K even is defined as

$$U_k(e^{j\omega}) = P\left(e^{j\left(\omega-\frac{2\pi}{K}\left(k+\frac{1}{2}\right)\right)}\right),$$

we can write (B.5) as

$$\mathrm{ASR} = \frac{\frac{1}{R-1}\sum_{i=1}^{R-1}\int_0^{2\pi}\left|P^*(e^{j\omega})P(e^{j\omega}\Phi_R^i)\right|^2 d\omega}{\int_0^{2\pi}\left|P(e^{j\omega})\right|^2 d\omega}. \tag{B.6}$$

Now, considering that $\mathcal{F}^{-1}\left\{P^*(e^{j\omega})P(e^{j\omega\Phi_R^i})\right\} = p(-n)*\left(p(n)e^{j\frac{2\pi ni}{R}}\right)$ and using Parseval's identity [130], we can finally express the ASR as a function

of the impulse response of the prototype filter as

$$\mathrm{ASR} = \frac{\frac{1}{R-1}\sum_{i=1}^{R-1}\sum_{n\in\mathbb{Z}} \left|p(-n) * a_i(n)\right|^2}{\sum_{n\in\mathbb{Z}} \left|p(n)\right|^2}, \tag{B.7}$$

where $a_i(n) = p(n)e^{j\frac{2\pi ni}{R}}$ is the impulse response of the i-th aliasing component. Now, let us define

$$\mathbf{\Theta}_i = \mathrm{diag}\left\{\left[e^{j\frac{2\pi 0 i}{R}} \quad \dots \quad e^{j\frac{2\pi (I_\mathrm{p}-1) i}{R}}\right]\right\}, \tag{B.8}$$

which is a $I_\mathrm{p}\times I_\mathrm{p}$ matrix containing the exponential terms required for computing a_i. Hence, we can define

$$\mathbf{a}_i = \mathbf{\Theta}_i \mathbf{\Pi} \mathbf{p}, \tag{B.9}$$

which is a $I_\mathrm{p}\times 1$ vector of the samples of a_i. The convolution $p(-n) * a_i(n)$ can be computed using DFTs of size $N = 2I_\mathrm{p}-1$, since $p(n)$ and $a_i(n)$ are finite responses of length I_p. Then, let us define $\mathbf{F}$ as the $2I_\mathrm{p}\text{–}1\times 2I_\mathrm{p}\text{–}1$ matrix for a DFT of size $N = 2I_\mathrm{p}\text{–}1$. Also, let us define

$$\mathbf{F}_\mathrm{p} = \left[\mathbf{F}\right]_{(:,0:I_\mathrm{p}-1)}, \tag{B.10}$$

which is a $2I_\mathrm{p}\text{–}1\times I_\mathrm{p}$ matrix used to compute the DFT of size $2I_\mathrm{p}\text{–}1$ of a response of length I_p. Then, we can define

$$\bar{\mathbf{a}}_i = \mathbf{F}_\mathrm{p}\mathbf{a}_i = \mathbf{F}_\mathrm{p}\mathbf{\Theta}_i\mathbf{\Pi}\mathbf{p}, \tag{B.11}$$

which is a $2I_\mathrm{p}\text{–}1\times 1$ vector containing the DFT of the i-th aliasing component a_i. Similarly, let us define

$$\bar{\mathbf{P}} = \mathrm{Diag}\left\{\mathbf{F}_\mathrm{p}\mathbf{\Pi}\mathbf{p}\right\}, \tag{B.12}$$

which is a $2I_\mathrm{p}\text{–}1\times 2I_\mathrm{p}\text{–}1$ diagonal matrix containing the DFT of the prototype filter p. Thus, let us define

$$\mathbf{y}_i = \mathbf{F}^H\bar{\mathbf{P}}^*\bar{\mathbf{a}}_i, \tag{B.13}$$

which is a $2I_\mathrm{p}\text{–}1\times 1$ vector containing the samples of $p(-n) * a_i(n)$. Using (B.11) and (B.12), we can alternatively express (B.13) as

$$\mathbf{y}_i = \mathbf{A}_i\mathbf{p},$$

where $\mathbf{A}_i$ is a $2I_{\mathrm{p}}{-}1{\times}Q_{\mathrm{p}}$ matrix given by

$$\mathbf{A}_i = \mathbf{F}^H \bar{\mathbf{P}}^* \mathbf{F}_{\mathrm{p}} \mathbf{\Theta}_i \mathbf{\Pi}.$$

Moreover, we can define a $(R{-}1)(2I_{\mathrm{p}}{-}1){\times}Q_{\mathrm{p}}$ matrix $\mathbf{Z}$ as

$$\mathbf{Z} = \frac{1}{\sqrt{(R{-}1)\left\|\mathbf{\Pi p}\right\|^2}} \begin{bmatrix} \mathbf{A}_1 \\ \vdots \\ \mathbf{A}_{R-1} \end{bmatrix}.$$

where the term $\left\|\mathbf{\Pi p}\right\|^2$ is the energy of the prototype filter. Finally, the ASR can be expressed as

$$\mathrm{ASR} = \left\|\mathbf{Z p}\right\|^2, \tag{B.14}$$

which is not a quadratic function, since $\mathbf{Z}$ is also dependent on $\mathbf{p}$.

B.1.2 Reconstruction Error (RE)

Now, we derive an expression for the RE as a function of $\mathbf{p}$. We studied in Section 4.2 that the RE is given by

$$\mathrm{RE} = \frac{1}{2\pi} \int_0^{2\pi} \left| T(e^{j\omega}) - e^{-j\omega(I_{\mathrm{p}}-1)} \right|^2 d\omega, \tag{B.15}$$

where we assumed that the scaling and the delay produced by the filter bank are $\rho_{\mathrm{f}} = 1$ and $\tau_{\mathrm{f}} = I_{\mathrm{p}}{-}1$, respectively. In (B.15), $T(e^{j\omega})$ represents the distortion transfer function of the filter bank, which was derived in Section 4.1.2 and can be expressed as

$$T(e^{j\omega}) = \frac{1}{R} \sum_{k=0}^{K-1} U_k(e^{j\omega}) V_k(e^{j\omega}). \tag{B.16}$$

For a GDFT filter bank, the frequency response of the synthesis filters is given by

$$V_k(e^{j\omega}) = U_k^*(e^{j\omega}) e^{-j\omega(I_{\mathrm{p}}-1)}, \tag{B.17}$$

so we can write (B.16) as

$$T(e^{j\omega}) = \frac{e^{-j\omega(I_{\mathrm{p}}-1)}}{R} \sum_{k=0}^{K-1} U_k(e^{j\omega}) U_k^*(e^{j\omega}). \tag{B.18}$$

Then, using (B.18), we can re-write (B.15) as

$$\mathrm{RE} = \frac{1}{2\pi}\int_0^{2\pi}\left|\left(\frac{1}{R}\sum_{k=0}^{K-1}U_k(e^{j\omega})U_k^*(e^{j\omega})\right)-1\right|^2 d\omega, \tag{B.19}$$

which, considering that $\mathcal{F}^{-1}\left\{U_k(e^{j\omega})U_k^*(e^{j\omega})\right\} = u_k(n) * u_k^*(-n)$ and using Parseval's identity [130], can be alternatively expressed as

$$\mathrm{RE} = \sum_{n\in\mathbb{Z}}\left|\left(\frac{1}{R}\sum_{k=0}^{K-1}u_k(n) * u_k^*(-n)\right)-\delta(n)\right|^2. \tag{B.20}$$

Since $u_k(n) = p(n)e^{j\frac{2\pi}{K}(k+\frac{1}{2})n}$, we can write

$$\sum_{k=0}^{K-1}u_k(n) * u_k^*(-n) = e^{j\frac{\pi n}{K}}\sigma_n r_\mathrm{p}(n), \tag{B.21}$$

where $r_\mathrm{p}(n) = p(n) * p(-n)$ is the auto-correlation of $p(n)$, and σ_n is a scalar term defined as

$$\sigma_n = \sum_{k=0}^{K-1}e^{-j\frac{2\pi kn}{K}} = \begin{cases} K & \text{if } n \bmod K = 0 \\ 0 & \text{otherwise} \end{cases}. \tag{B.22}$$

Consequently, $\sum_{k=0}^{K-1}u_k(n) * u_k^*(-n)$ is different from 0 only in those time instants that are multiple of K, since for other time instants the components for the different subbands cancel each other out. Using (B.20)-(B.22), we can express the RE as

$$\mathrm{RE} = \sum_{n\in\mathbb{Z}}\left|\frac{K}{R}r_\mathrm{p}(nK)-\delta(nK)\right|^2, \tag{B.23}$$

in which the term $e^{j\frac{\pi n}{K}}$ has been omitted because it has no influence in the expression. From (B.23), we can conclude that perfect reconstruction is achieved when $r_\mathrm{p}(0) = R/K$ and $r_\mathrm{p}(qK) = 0$ for $q \in \mathbb{Z}\backslash 0$. Now, let us define a $2I_\mathrm{p}{-}1{\times}1$ vector containing the non-zero samples of $r_\mathrm{p}(n)$ as

$$\mathbf{r} = \begin{bmatrix} r_\mathrm{p}(0) & \dots & r_\mathrm{p}(I_p{-}1) & r_\mathrm{p}(-I_p{+}1) & \dots & r_\mathrm{p}(-1) \end{bmatrix}^T. \tag{B.24}$$

Since the values of $r_{\mathrm{p}}(n)$ can be computed using DFTs of size $2I_{\mathrm{p}}$–1, the previous vector can be alternatively defined as

$$\mathbf{r} = \mathbf{F}^H \bar{\mathbf{P}}^* \mathbf{F}_{\mathrm{p}} \mathbf{\Pi} \mathbf{p}, \tag{B.25}$$

where it is important to notice that in the definition of $\mathbf{r}$ in (B.24) we considered the circularity of the DFT. Since p is a filter of length I_{p}, $r_{\mathrm{p}}(nK)$ might be different from 0 only for $n = -I_{\mathrm{p}\downarrow}{+}1, \ldots, I_{\mathrm{p}\downarrow}{-}1$, with $I_{\mathrm{p}\downarrow} = \lceil I_{\mathrm{p}}/K \rceil$. Then, let us define a $2I_{\mathrm{p}\downarrow}$–1×1 vector of the samples of $r_{\mathrm{p}}(nK)$ as

$$\mathbf{r}_\downarrow = \begin{bmatrix} r_{\mathrm{p}}(0) & r_{\mathrm{p}}(K) & \ldots & r_{\mathrm{p}}((I_{\mathrm{p}\downarrow}{-}1)\,K) & r_{\mathrm{p}}((-I_{\mathrm{p}\downarrow}{+}1)\,K) & \ldots & r_{\mathrm{p}}(-K) \end{bmatrix}^T, \tag{B.26}$$

which can be alternatively defined as

$$\mathbf{r}_\downarrow = \mathbf{C}\mathbf{r} = \mathbf{C}\mathbf{F}^H \bar{\mathbf{P}}^* \mathbf{F}_{\mathrm{p}} \mathbf{\Pi} \mathbf{p}, \tag{B.27}$$

where $\mathbf{C}$ is a $2I_{\mathrm{p}\downarrow}$–1×$2I_{\mathrm{p}}$–1 matrix whose element in the i-th row and q-th column is defined as

$$[\mathbf{C}]_{(i,q)} = \begin{cases} 1 & \text{if } i = q \text{ and } (i \bmod K = 0 \text{ or } i{-}2I_{\mathrm{p}}{+}1 \bmod K = 0) \\ 0 & \text{otherwise} \end{cases}. \tag{B.28}$$

Now, we can express $\mathbf{r}_\downarrow$ as

$$\mathbf{r}_\downarrow = \mathbf{T}\mathbf{p}, \tag{B.29}$$

where $\mathbf{T}$ is a $2I_{\mathrm{p}\downarrow}$–1×$Q_{\mathrm{p}}$ matrix given by

$$\mathbf{T} = \mathbf{C}\mathbf{F}^H \bar{\mathbf{P}}^* \mathbf{F}_{\mathrm{p}} \mathbf{\Pi}. \tag{B.30}$$

Also, let us define a $2I_{\mathrm{p}\downarrow}$–1×1 vector $\mathbf{d}_\delta$ as

$$\mathbf{d}_\delta = \begin{bmatrix} 1 & \mathbf{0}_{1\times 2I_{\mathrm{p}\downarrow}-2} \end{bmatrix}^T. \tag{B.31}$$

Then, the RE can be expressed as

$$\mathrm{RE} = \left\| \mathbf{T}\mathbf{p} - \mathbf{d}_\delta \right\|^2, \tag{B.32}$$

which is not a quadratic function, since $\mathbf{T}$ is also dependent on $\mathbf{p}$.

B.2 Optimization

Next, we describe the optimization used for computing the prototype filter. In particular, we propose to compute the prototype filter by minimizing the weighted sum of the RE and the ASR, i.e.,

$$\mathbf{p}_{\text{opt}} = \arg\min_{\mathbf{p}} \Big(\text{RE}(\mathbf{p}) + \gamma \text{ASR}(\mathbf{p}) \Big), \tag{B.33}$$

where γ is a weighing term that balances the effort used to minimize each component. Using the formulation presented in Section B.1, we can write (B.33) as

$$\mathbf{p}_{\text{opt}} = \arg\min_{\mathbf{p}} \left(\left\| \begin{bmatrix} \mathbf{T}(\mathbf{p}) \\ \sqrt{\gamma}\, \mathbf{Z}(\mathbf{p}) \end{bmatrix} \mathbf{p} - \begin{bmatrix} \mathbf{d}_\delta \\ \mathbf{0} \end{bmatrix} \right\|^2 \right), \tag{B.34}$$

where notation $\mathbf{T}(\mathbf{p})$ and $\mathbf{Z}(\mathbf{p})$ is used instead of $\mathbf{T}$ and $\mathbf{Z}$, respectively, to indicate the dependency of these matrices on the filters $\mathbf{p}$. It is important to highlight that (B.34) is not a quadratic optimization problem, so non-linear optimization methods must be used to find the optimal solution. In particular, we propose using the Iterative Least Squares (ILS) method [100, 149], i.e., the solution to (B.34) is found iteratively by approximating the cost function by a quadratic function. Then, with ILS for each iteration i we aim to find

$$\check{\mathbf{p}}_i = \arg\min_{\mathbf{p}} \left(\left\| \begin{bmatrix} \mathbf{T}(\check{\mathbf{p}}_{i-1}) \\ \sqrt{\gamma}\, \mathbf{Z}(\check{\mathbf{p}}_{i-1}) \end{bmatrix} \mathbf{p} - \begin{bmatrix} \mathbf{d}_\delta \\ \mathbf{0} \end{bmatrix} \right\|^2 \right), \tag{B.35}$$

where the filter for iteration $i-1$, i.e., $\check{\mathbf{p}}_{i-1}$, is used to approximate the original non-quadratic function by a quadratic function. The solution for each iteration can be obtained as

$$\check{\mathbf{p}}_i = \left(\mathbf{T}^H(\check{\mathbf{p}}_{i-1}) \mathbf{T}(\check{\mathbf{p}}_{i-1}) + \gamma \mathbf{Z}^H(\check{\mathbf{p}}_{i-1}) \mathbf{Z}(\check{\mathbf{p}}_{i-1}) \right)^{-1} \mathbf{T}^H(\check{\mathbf{p}}_{i-1}) \mathbf{d}_\delta. \tag{B.36}$$

Moreover, to add robustness to the convergence of the ILS algorithm we consider the following averaging for instants i–1 and i [149]

$$\check{\mathbf{p}}_i = (1-\vartheta)\, \check{\mathbf{p}}_i + \vartheta\, \check{\mathbf{p}}_{i-1}, \tag{B.37}$$

where $0 \leq \vartheta \leq 1$ is a forgetting factor. Also, we consider that the prototype filter is computed using N_{iter} iterations, but the algorithm stops if

Algorithm B.1: ILS method to compute the prototype filter.

Select I_{p}, N_{iter}, γ, ϑ, and ϵ_{th};
Initialize $\check{\mathbf{p}}_{-1}$ as a square-root raised cosine FIR filter of length I_{p};
for $i = 0, ..., N_{\mathrm{iter}}$ **do**
  $\check{\mathbf{p}}_i = \left(\mathbf{T}^H(\check{\mathbf{p}}_{i-1})\mathbf{T}(\check{\mathbf{p}}_{i-1}) + \gamma \mathbf{Z}^H(\check{\mathbf{p}}_{i-1})\mathbf{Z}(\check{\mathbf{p}}_{i-1})\right)^{-1} \mathbf{T}^H(\check{\mathbf{p}}_{i-1})\mathbf{d}_\delta$;
  $\check{\mathbf{p}}_i = (1-\vartheta)\,\check{\mathbf{p}}_i + \vartheta, \check{\mathbf{p}}_{i-1}$;
  if $(\|\check{\mathbf{p}}_i - \check{\mathbf{p}}_{i-1}\| \,/\, \|\check{\mathbf{p}}_{i-1}\|) < \epsilon_{\mathrm{th}}$ **then**
    break;
  end
end

the normalized variation $\|\check{\mathbf{p}}_i - \check{\mathbf{p}}_{i-1}\| \,/\, \|\check{\mathbf{p}}_{i-1}\|$ is lower than a threshold ϵ_{th}. The proposed algorithm for computing the prototype filter is summarized in Algorithm B.1. Specifically, in this work we use in all cases $N_{\mathrm{iter}} = 20$, $\vartheta = 0.5$, and $\epsilon_{\mathrm{th}} = 1{\cdot}10^{-3}$, and a search is carried to select γ such that similar values are obtained for the RE and the ASR. Also, we consider that the initial prototype filter $\check{\mathbf{p}}_{-1}$ is selected as a square-root raised cosine FIR filter of energy R/K, which we obtain using MATLAB's function `rcosdesign` with a roll-off factor R/K.

B.3 Design examples

Next, we show some examples of prototype filters obtained with the method described in Section B.2. The impulse and frequency responses of the designed filters for a length $I_{\mathrm{p}} = 55$ are shown in Fig. B.1, in which we consider the following combinations of number of subbands and resampling factors: 1) $K = 8$ and $R = 6$; 2) $K = 8$ and $R = 8$; 3) $K = 16$ and $R = 10$; 4) $K = 16$ and $R = 16$. Also, for these same combinations, the impulse and frequency responses of the designed filters for a length $I_{\mathrm{p}} = 95$ are shown in Fig. B.2. In these results, we can see how the proposed method can effectively provide prototype filters that minimize the ASR and the RE. In particular, the longer the filter length, the lower the ASR and the RE.

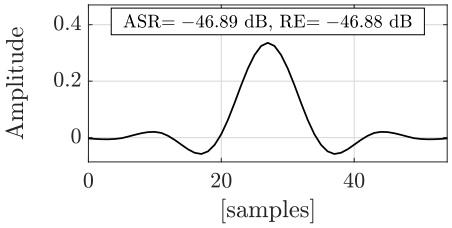

(a) Impulse Response ($K = 8$, $R = 6$)

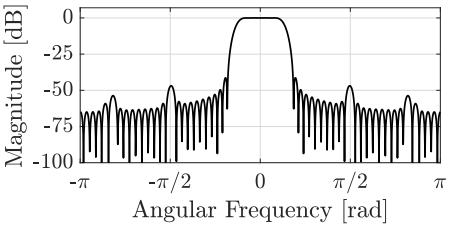

(b) Freq. Response ($K = 8$, $R = 6$)

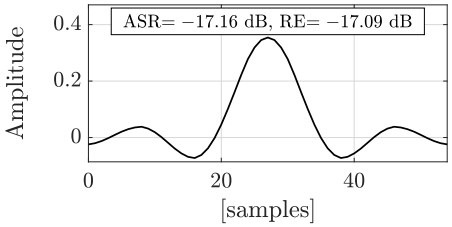

(c) Impulse Response ($K = 8$, $R = 8$)

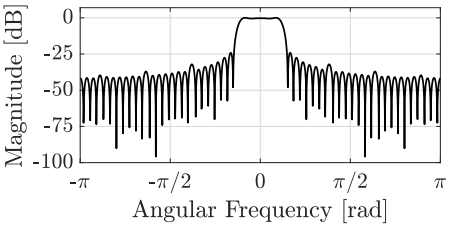

(d) Freq. Response ($K = 8$, $R = 8$)

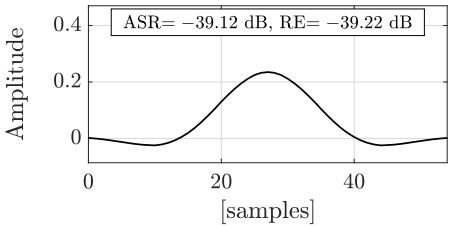

(e) Impulse Response ($K = 16$, $R = 10$)

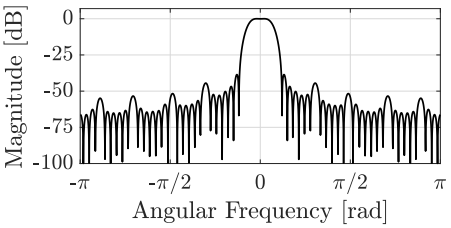

(f) Freq. Response ($K = 16$, $R = 10$)

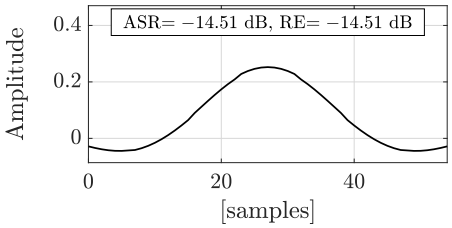

(g) Impulse Response ($K = 16$, $R = 16$)

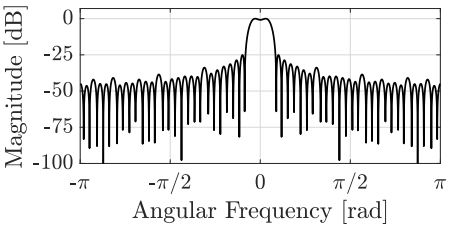

(h) Freq. Response ($K = 16$, $R = 16$)

Figure B.1: Examples of the prototype filter designed with the proposed method. The impulse and frequency responses of the prototype filter are shown in (a,c,e,g) and (b,d,f,h), respectively, for 4 combinations of K and R. A filter length $I_{\mathrm{p}} = 55$ is considered. The ASR and the RE for each case is displayed in the graphs.

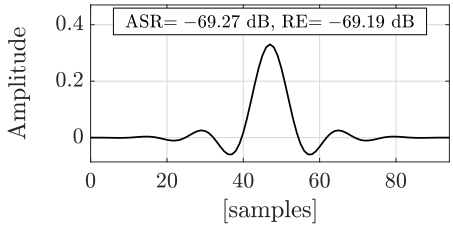

(a) Impulse Response ($K = 8$, $R = 6$)

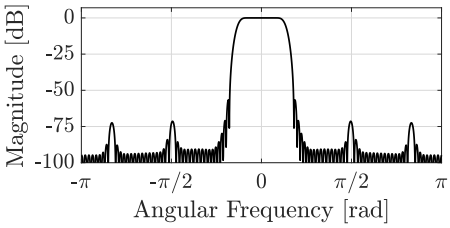

(b) Freq. Response ($K = 8$, $R = 6$)

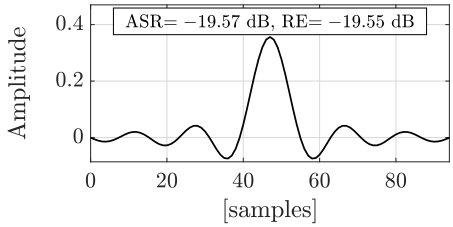

(c) Impulse Response ($K = 8$, $R = 8$)

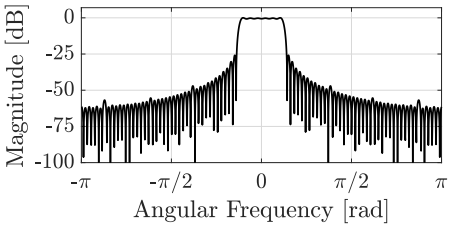

(d) Freq. Response ($K = 8$, $R = 8$)

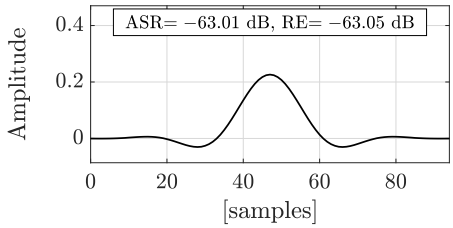

(e) Impulse Response ($K = 16$, $R = 10$)

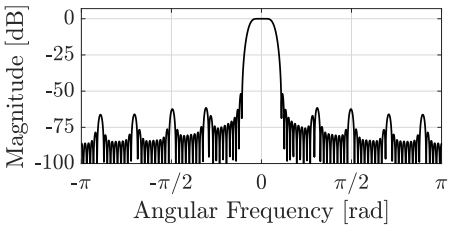

(f) Freq. Response ($K = 16$, $R = 10$)

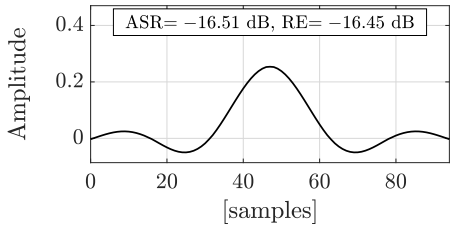

(g) Impulse Response ($K = 16$, $R = 16$)

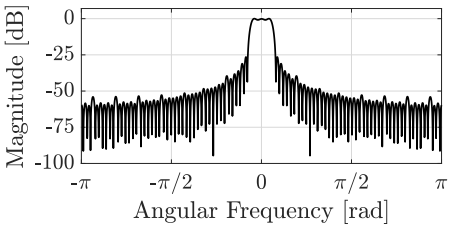

(h) Freq. Response ($K = 16$, $R = 16$)

Figure B.2: Examples of the prototype filter designed with the proposed method. The impulse and frequency responses of the prototype filter are shown in (a,c,e,g) and (b,d,f,h), respectively, for 4 combinations of K and R. A filter length $I_{\mathrm{p}} = 95$ is considered. The ASR and the RE for each case is displayed in the graphs.

Bibliography

[1] W. F. Druyvesteyn and J. Garas, "Personal sound," *Journal of the Audio Engineering Society*, vol. 45, no. 9, pp. 685–701, 1997.

[2] T. M. Nelson and T. H. Nilsson, "Comparing headphone and speaker effects on simulated driving," *Accident Analysis and Prevention*, vol. 22, no. 6, pp. 523–529, 1990.

[3] B. B. Bauer, "Improving Headphone Listening Comfort," *The Journal of the Acoustical Society of America*, vol. 37, no. 6, pp. 1210–1210, 1965.

[4] A. Zelechowska, V. E. Gonzalez-Sanchez, B. Laeng, and A. R. Jensenius, "Headphones or Speakers? An Exploratory Study of Their Effects on Spontaneous Body Movement to Rhythmic Music," *Frontiers in Psychology*, vol. 11, no. April, pp. 1–19, 2020.

[5] T. Betlehem, W. Zhang, M. A. Poletti, and T. Abhayapala, "Personal Sound Zones: Delivering interface-free audio to multiple listeners," *IEEE Signal Processing Magazine*, vol. 32, no. 2, pp. 81–91, 2015.

[6] "Personal Sound Zones," Fraunhofer Institute for Digital Media Technology IDMT, Technical Report, 2015.

[7] M. F. Simón Gálvez, D. Menzies, and F. M. Fazi, "Dynamic Audio Reproduction with Linear Loudspeaker Arrays," *Journal of the Audio Engineering Society*, vol. 67, no. 4, pp. 190–200, 2019.

[8] P. Coleman, "Loudspeaker Array Processing for Personal Sound Zone Reproduction," Ph.D. thesis, University of Surrey, 2014.

[9] J. W. Choi and Y. H. Kim, "Generation of an acoustically bright zone with an illuminated region using multiple sources," *The Journal of the Acoustical Society of America*, vol. 111, no. 4, pp. 1695–1700, 2002.

[10] M. F. Simón Gálvez, "Design of an Array-Based Aid for the Hearing Impaired," Ph.D. thesis, University of Southampton, 2014.

[11] J. Cheer, S. J. Elliott, and M. F. Simón Gálvez, "Design and Implementation of a Car Cabin Personal Audio System," *Journal of the Audio Engineering Society*, vol. 61, no. 6, pp. 412–424, 2013.

[12] L. L. Beranek, *Acoustics*. New York: Acoustical Society of America, 1993.

[13] F. Fahy, *Foundations of Engineering Acoustics*. London: Academic Press, 2000.

[14] J. Kuutti, J. Leiwo, and R. Sepponen, "Local Control of Audio Environment: A Review of Methods and Applications," *Technologies*, vol. 2, no. 1, pp. 31–53, 2014.

[15] "Meyer Sound SB-1 Resources," 1997. [Online] Available: https://meyersound.com/download/sb-1-resources/. Accessed: 2022-04-07

[16] N. R. French and J. C. Steinberg, "Factors Governing the Intelligibility of Speech Sounds," *The Journal of the Acoustical Society of America*, vol. 19, no. 1, pp. 90–119, 1947.

[17] M. Yoneyama, J. Fujimoto, Y. Kawamo, and S. Sasabe, "The audio spotlight: An application of nonlinear interaction of sound waves to a new type of loudspeaker design," *The Journal of the Acoustical Society of America*, vol. 73, no. 5, pp. 1532–1536, 1983.

[18] P. J. Westervelt, "Parametric Acoustic Array," *The Journal of the Acoustical Society of America*, vol. 35, pp. 535–537, 1963.

[19] R. San Martín, P. Tello, A. Valencia, and A. Marzo, "Experimental Evaluation of Distortion in Amplitude Modulation Techniques for Parametric Loudspeakers," *Applied Sciences*, vol. 10, no. 6, pp. 1–11, 2020.

[20] N. Tanaka and M. Tanaka, "Active noise control using a steerable parametric array loudspeaker," *The Journal of the Acoustical Society of America*, vol. 127, pp. 3526–3537, 2010.

[21] "Focusonics Directional Speaker Model A." [Online] Available: https://www.focusonics.com/product/focusonics-model-a/. Accessed: 2022-04-07

[22] "Holosonics Audio Spotlight 16iX." [Online] Available: https://www.holosonics.com/audio-spotlight-16ix. Accessed: 2022-04-07

[23] J. Droppo, I. J. Tashev, and M. L. Seltzer, "Personal Audio Space: The Headphones Experience sans Headphones," 2007. [Online] Available: https://www.microsoft.com/en-us/research/blog/personal-audio-space-headphones-experience-sans-headphones/. Accessed: 2022-04-07

[24] "Tech entrepreneurs unveil 3D audio gaming sound bar at CES," 2019. [Online] Available: https://www.southampton.ac.uk/engineering/news/2019/01/audio-gaming-sound-bar.page. Accessed: 2022-04-07

[25] D. H. Johnson and D. E. Dudgeon, *Array Signal Processing: Concepts and Techniques*. New York: Prentice Hall, 1993.

[26] W. Roh, J. Y. Seol, J. H. Park, B. Lee, J. Lee, Y. Kim, J. Cho, K. Cheun, and F. Aryanfar, "Millimeter-Wave Beamforming as an Enabling Technology for 5G Cellular Communications: Theoretical Feasibility and Prototype Results," *IEEE Communications Magazine*, vol. 52, no. 2, pp. 106–113, 2014.

[27] M. L. Seltzer, B. Raj, and R. M. Stern, "Likelihood-Maximizing Beamforming for Robust Hands-Free Speech Recognition," *IEEE Transactions on Speech and Audio Processing*, vol. 12, no. 5, pp. 489–498, 2004.

[28] I. Wolff and L. Malter, "Directional radiation of sound," *The Journal of the Acoustical Society of America*, vol. 2, no. 2, pp. 201–241, 1930.

[29] A. J. Berkhoul, D. de Vries, and P. Vogel, "Acoustic control by wave field synthesis," *The Journal of the Acoustical Society of America*, vol. 93, no. 5, pp. 2764–2778, 1993.

[30] S. Cecchi, A. Carini, and S. Spors, "Room Response Equalization - A Review," *Applied Sciences*, vol. 8, no. 1, pp. 1–47, 2018.

[31] Y. J. Wu and T. D. Abhayapala, "Spatial Multizone Soundfield Reproduction: Theory and Design," *IEEE Transactions on Audio, Speech, and Language Processing*, vol. 19, no. 6, pp. 1711–1720, 2011.

[32] W. Zhang, T. D. Abhayapala, T. Betlehem, and F. M. Fazi, "Analysis and control of multi-zone sound field reproduction using modal-domain approach," *The Journal of the Acoustical Society of America*, vol. 140, no. 3, pp. 2134–2144, 2016.

[33] J. Zhang, W. Zhang, T. D. Abhayapala, and L. Zhang, "2.5D multi-zone reproduction using weighted mode matching: Performance analysis and experimental validation," *The Journal of the Acoustical Society of America*, vol. 147, pp. 1404–1417, 2020.

[34] M. F. Simón Gálvez, S. J. Elliott, and J. Cheer, "A superdirective array of phase shift sources," *The Journal of the Acoustical Society of America*, vol. 132, no. 2, pp. 746–756, 2012.

[35] F. Olivieri, F. M. Fazi, M. Shin, and P. A. Nelson, "Pressure-Matching Beamforming Method for Loudspeaker Arrays with Frequency Dependent Selection of Control Points," in *Proceedings of the 138th Audio Engineering Society Convention*, 2015.

[36] D. Wallace and J. Cheer, "Design and evaluation of personal audio systems based on speech privacy constraints," *The Journal of the Acoustical Society of America*, vol. 147, no. 4, pp. 2271–2282, 2020.

[37] M. Ebri, N. Strozzi, F. M. Fazi, A. Farina, and L. Cattani, "Individual Listening Zone with Frequency-Dependent Trim of Measured Impulse Responses," in *Proceedings of the 149th Audio Engineering Society Convention*, 2020.

[38] M. Shin, S. Q. Lee, F. M. Fazi, P. A. Nelson, D. Kim, S. Wang, K. Ho Park, and J. Seo, "Maximization of acoustic energy difference between two spaces," *The Journal of the Acoustical Society of America*, vol. 128, pp. 121–131, 2010.

[39] M. F. Simón Gálvez, S. J. Elliott, and J. Cheer, "Time Domain Optimization of Filters Used in a Loudspeaker Array for Personal Audio," *IEEE/ACM Transactions on Audio, Speech, and Language Processing*, vol. 23, no. 11, pp. 1869–1878, 2015.

[40] C. House, S. Dennison, D. G. Morgan, N. Rushton, G. V. White, J. Cheer, and S. J. Elliott, "Personal Spatial Audio in Cars: Development of a loudspeaker array for multi-listener transaural reproduction in a vehicle," in *Proceedings of the Institute of Acoustics*, 2017.

[41] F. Olivieri, F. M. Fazi, S. Fontana, D. Menzies, and P. A. Nelson, "Generation of Private Sound With a Circular Loudspeaker Array and the Weighted Pressure Matching Method," *IEEE/ACM Transactions on Audio, Speech, and Language Processing*, vol. 25, no. 8, pp. 1579–1591, 2017.

[42] L. E. Kinsler, A. R. Frey, A. B. Coppens, and J. V. Sanders, *Fundamentals of Acoustics*. New York: John Wiley & Sons, 2000.

[43] R. Rabenstein and S. Spors, "Spatial Aliasing Artifacts Produced by Linear and Circular Loudspeaker Arrays used for Wave Field Synthesis," in *Proceedings of the 120th Audio Engineering Society Convention*, 2006.

[44] B. Van Veen and K. Buckley, "Beamforming: A Versatile Approach to Spatial Filtering," *IEEE ASSP Magazine*, vol. 5, no. 2, pp. 4–24, 1988.

[45] M. F. Simón Gálvez, S. J. Elliott, and J. Cheer, "The effect of reverberation on personal audio devices," *The Journal of the Acoustical Society of America*, vol. 135, pp. 2654–2663, 2014.

[46] S. Widmark, "Causal MSE-Optimal Filters for Personal Audio Subject to Constrained Contrast," *IEEE/ACM Transactions on Audio Speech, and Language Processing*, vol. 27, no. 5, pp. 972–987, 2019.

[47] H. So and J. W. Choi, "Subband Optimization and Filtering Technique for Practical Personal Audio Systems," in *Proceedings of the IEEE International Conference on Acoustics, Speech, and Signal Processing*, 2019.

[48] Y. Cai, M. Wu, and J. Yang, "Design of a time-domain acoustic contrast control for broadband input signals in personal audio systems," in *Proceedings of the IEEE International Conference on Acoustics, Speech, and Signal Processing*, 2013.

[49] D. H. M. Schellekens, M. B. Møller, and M. Olsen, "Time domain acoustic contrast control implementation of sound zones for low-frequency input signals," in *Proceedings of the IEEE International Conference on Acoustics, Speech, and Signal Processing*, 2016.

[50] J. H. Chang and F. Jacobsen, "Sound field control with a circular double-layer array of loudspeakers," *The Journal of the Acoustical Society of America*, vol. 131, pp. 4518–4525, 2012.

[51] M. B. Møller and M. Olsen, "Sound Zones: On Performance Prediction of Contrast Control Methods," in *Proceedings of the Audio Engineering Society International Conference on Sound Field Control*, 2016.

[52] M. Schneider and E. A. P. Habets, "Iterative DFT-Domain Inverse Filter Optimization Using a Weighted Least-Squares Criterion," *IEEE/ACM Transactions on Audio, Speech, and Language Processing*, vol. 27, no. 12, pp. 1957–1969, 2019.

[53] M. B. Møller and J. Ostergaard, "A Moving Horizon Framework for Sound Zones," *IEEE/ACM Transactions on Audio, Speech, and Language Processing*, vol. 28, pp. 256–265, 2020.

[54] S. J. Elliott and J. Cheer, "Regularisation and Robustness of Personal Audio Systems," Institute of Sound and Vibration Research, Technical Report, 2011.

[55] Y. Cai, M. Wu, L. Liu, and J. Yang, "Time-domain acoustic contrast control design with response differential constraint in personal audio systems," *The Journal of the Acoustical Society of America*, vol. 135, pp. 252–257, 2014.

[56] J. Cheer, S. J. Elliott, Y. Kim, and J. W. Choi, "Practical Implementation of Personal Audio in a Mobile Device," *Journal of the Audio Engineering Society*, vol. 61, no. 5, pp. 290–300, 2013.

[57] J. Cheer and S. J. Elliott, "Design and implementation of a personal audio system in a car cabin," in *Proceedings of the Meetings on Acoustics*, 2013.

[58] P. A. Nelson, F. Orduña-Bustamante, and H. Hamada, "Inverse Filter Design and Equalization Zones in Multichannel Sound Reproduction," *IEEE Transactions on Speech and Audio Processing*, vol. 3, pp. 185–192, 1995.

[59] S. T. Neely and J. B. Allen, "Invertibility of a room impulse response," *The Journal of the Acoustical Society of America*, vol. 66, no. 1, pp. 165–169, 1979.

[60] L. Vindrola, M. Melon, J. C. Chamard, B. Gazengel, and G. Plantier, "Personal Sound Zones: A Comparison between Frequency and Time Domain Formulations in a Transportation Context," in *Proceedings of the 147th Audio Engineering Society Convention*, 2019.

[61] S. J. Elliott, J. Cheer, J. W. Choi, and Y. Kim, "Robustness and Regularization of Personal Audio Systems," *IEEE Transactions on Audio, Speech, and Language Processing*, vol. 20, no. 7, pp. 2123–2133, 2012.

[62] M. A. Poletti, "An Investigation of 2D Multizone Surround Sound Systems," in *Proceedings of the 125th Audio Engineering Society Convention*, 2008.

[63] P. Coleman, P. J. Jackson, M. Olik, and J. A. Pedersen, "Personal audio with a planar bright zone," *The Journal of the Acoustical Society of America*, vol. 136, pp. 1725–1735, 2014.

[64] T. Lee, J. K. Nielsen, J. R. Jensen, and M. G. Christensen, "A Unified Approach to Generating Sound Zones Using Variable Span Linear Filters," in *Proceedings of the IEEE International Conference on Acoustics, Speech, and Signal Processing*, 2018.

[65] M. B. Møller, M. Olsen, and F. Jacobsen, "A Hybrid Method Combining Synthesis of a Sound Field and Control of Acoustic Contrast," in *Proceedings of the 132nd Audio Engineering Society Convention*, 2012.

[66] M. Olik, J. Francombe, P. Coleman, P. J. Jackson, M. Olsen, M. B. Møller, R. Mason, and S. Bech, "A Comparative Performance Study of Sound Zoning Methods in a Reflective Environment," in *Proceedings of the 52nd Audio Engineering Society International Conference*, 2013.

[67] M. Hu and J. Lu, "Theoretical explanation of uneven frequency response of time-domain acoustic contrast control method," *The Journal of the Acoustical Society of America*, vol. 149, no. 6, pp. 4292–4297, 2021.

[68] D. Wallace, "Practical audio system design for private speech reproduction," Ph.D. thesis, University of Southampton, 2020.

[69] A. Farina, "Simultaneous Measurement of Impulse Response and Distortion with a Swept-Sine Technique," in *Proceedings of the 108th Audio Engineering Society Convention*, 2000.

[70] M. F. Simón Gálvez and F. M. Fazi, "Listener Adaptive Filtering Strategies for Personal Audio Reproduction over Loudspeaker Arrays," in *Proceedings of the Audio Engineering Society International Conference on Sound Field Control*, no. 2, 2016, pp. 327–335.

[71] D. Wallace and J. Cheer, "The Design of Personal Audio Systems for Speech Transmission Using Analytical and Measured Responses," in *Proceedings of the IEEE International Conference on Acoustics, Speech, and Signal Processing*, 2019.

[72] A. H. Sayed, *Fundamentals of Adaptive Filtering*. New Jersey: John Wiley & Sons, 2003.

[73] "JBL 305P MkII Professional Loudspeakers." [Online] Available: https://jblpro.com/en-US/products/305p-mkii. Accessed: 2022-04-07

[74] "Brüel & Kjær Precision Microphone Type 4958." [Online] Available: https://www.bksv.com/en/transducers/acoustic/microphones/special-microphones/4958. Accessed: 2022-04-07

[75] "Brüel & Kjær Sound Calibrator Type 4231." [Online] Available: https://www.bksv.com/en/transducers/acoustic/calibrators/sound-calibrator-4231. Accessed: 2022-04-07

[76] P. D. Hatziantoniou and J. N. Mourjopoulos, "Generalized Fractional-Octave Smoothing of Audio and Acoustic Responses," *Journal of the Audio Engineering Society*, vol. 48, no. 4, pp. 259–280, 2000.

[77] G. H. Golub and C. F. Van Loan, *Matrix Computations*. Baltimore: The Johns Hopkins University Press, 1996.

[78] G. Carayannis, D. G. Manolakis, and N. Kalouptsidis, "A Fast Sequential Algorithm for Least-Squares Filtering and Prediction," *IEEE Transactions on Acoustics, Speech, and Signal Processing*, vol. 31, no. 6, pp. 1394–1402, 1983.

[79] M. A. Poletti and P. D. Teal, "A Superfast Toeplitz Matrix Inversion Method for Single- and Multi-Channel Inverse Filters and its Application to Room Equalization," *IEEE/ACM Transactions on Audio, Speech, and Language Processing*, vol. 29, pp. 3144–3157, 2021.

[80] A. González and J. J. López, "Fast Transversal Filters for Deconvolution in Multichannel Sound Reproduction," *IEEE Transactions on Speech and Audio Processing*, vol. 9, no. 4, pp. 429–440, 2001.

[81] O. Kochukhov, V. Makaganiuk, and N. Piskunov, "Least-squares deconvolution of the stellar intensity and polarization spectra," *Astronomy and Astrophysics*, vol. 524, no. 1, pp. 1–14, 2010.

[82] S. Jose, N. Mohan, V. Sowmya, and K. P. Soman, "Least Square Based Image Deblurring," *International Conference on Advances in Computing, Communications and Informatics*, 2017.

[83] S. Haykin, *Adaptive Filter Theory.* New Jersey: Prentice Hall, 1995.

[84] Björck, Ake, *Numerical methods for LS Problem.* Philadelphia: Society for Industrial and Applied Mathematics, 1996.

[85] A. Uncini, *Fundamentals of Adaptive Signal Processing.* New York: Springer, 2015.

[86] A. H. Sayed and T. Kailath, "A State-Space Approach to Adaptive RLS Filtering," *IEEE Signal Processing Magazine*, vol. 11, no. 3, pp. 18–60, 1994.

[87] J. M. Cioffi and T. Kailath, "Fast, Recursive-Least-Squares Transversal Filters for Adaptive Filtering," *IEEE Transactions on Acoustics, Speech, and Signal Processing*, vol. 32, no. 2, pp. 304–337, 1984.

[88] N. Kalouptsidis, G. Carayannis, and D. G. Manolakis, "A Fast Covariance Type Algorithm for Sequential Least-Squares Filtering and Prediction," *IEEE Transactions on Automatic Control*, vol. 29, no. 8, pp. 752–755, 1984.

[89] K. Gallivan, S. Thirumalai, and P. Van Dooren, "A block toeplitz look-ahead schur algorithm," in *SVD and Signal Processing III.* Amsterdam: Elsevier Science, 1995.

[90] T. Laudadio, N. Mastronardi, and P. Van Dooren, "The Generalized Schur Algorithm and Some Applications," *Axioms*, vol. 7, no. 4, pp. 1–18, 2018.

[91] H. Park and L. Eldén, "Schur-Type Methods for Solving Least Squares Problems with Toeplitz Structure," *SIAM Journal on Scientific Computing*, vol. 22, no. 2, pp. 406–430, 2000.

[92] G. S. Ammar and W. B. Gragg, "The generalized Schur algorithm for the superfast solution of Toeplitz systems," in *Rational Approximation and its Applications in Mathematics and Physics*. Berlin: Springer, 1987.

[93] Y. S. Boutalis, S. D. Kollias, and G. Carayannis, "A Fast Multichannel Approach to Adaptive Image Estimation," *IEEE Transactions on Acoustics, Speech, and Signal Processing*, vol. 37, no. 7, pp. 1090–1098, 1989.

[94] G. W. Stewart, *Matrix Algorithms: Volume 1: Basic Decompositions*. Philadelphia: Society for Industrial and Applied Mathematics, 1998.

[95] "754-2008 - IEEE Standard for Floating-Point Arithmetic," IEEE Computer Society, Technical Report, 2008.

[96] "MEX File Functions - MATLAB & Simulink." [Online] Available: https://www.mathworks.com/help/matlab/call-mex-file-functions.html. Accessed: 2022-04-07

[97] H. Hacihabibouglu and Z. Cvetkovic, "Multichannel Dereverberation Theorems and Robustness Issues," *IEEE Transactions on Audio, Speech, and Language Processing*, vol. 20, no. 2, pp. 676–689, 2012.

[98] S. M. Kuo, B. H. Lee, and W. Tian, *Real-Time Digital Signal Processing: Implementations and Applications*. New York: Wiley, 2013.

[99] P. P. Vaidyanathanm, *Multirate Systems And Filter Banks*. New Jersey: Prentice Hall, 1993.

[100] S. Weiss, "On adaptive filtering in oversampled subbands," Ph.D. thesis, University of Strathclyde, 1998.

[101] N. D. Gaubitch and P. A. Naylor, "Equalization of Multichannel Acoustic Systems in Oversampled Subbands," *IEEE Transactions on Audio, Speech, and Language Processing*, vol. 17, no. 6, pp. 1061–1070, 2009.

[102] J. P. Reilly, M. Wilbur, M. Seibert, and N. Ahmadvand, "The Complex Subband Decomposition and its Application to the Decimation of Large Adaptive Filtering Problems," *IEEE Transactions on Signal Processing*, vol. 50, no. 11, pp. 2730–2743, 2002.

[103] R. E. Crochiere and L. R. Rabiner, *Multirate Digital Signal Processing.* New Jersey: Prentice Hall, 1985.

[104] B. Suter, *Multirate and Wavelet Signal Processing.* London: Academic Press, 1997.

[105] M. Bosi, "Filter Banks in Perceptual Audio Coding," in *Proceedings of the 17th Audio Engineering Society International Conference*, 1999.

[106] T. Painter and A. Spanias, "Perceptual Coding of Digital Audio," *Proceedings of the IEEE*, vol. 88, no. 4, pp. 451–512, 2000.

[107] V. Strela, P. N. Heller, G. Strang, P. Topiwala, and C. Heil, "The Application of Multiwavelet Filterbanks to Image Processing," *IEEE Transactions on Image Processing*, vol. 8, no. 4, pp. 548–563, 1999.

[108] S. I. Park, M. J. Smith, and R. M. Mersereau, "Improved Structures of Maximally Decimated Directional Filter Banks for Spatial Image Analysis," *IEEE Transactions on Image Processing*, vol. 13, no. 11, pp. 1424–1431, 2004.

[109] M. Cimpoi, S. Maji, and A. Vedaldi, "Deep Filter Banks for Texture Recognition and Segmentation," in *Proceedings of the IEEE Computer Society Conference on Computer Vision and Pattern Recognition*, 2015.

[110] V. Andrearczyk and P. F. Whelan, "Using filter banks in Convolutional Neural Networks for texture classification," *Pattern Recognition Letters*, vol. 84, pp. 63–69, 2016.

[111] M. Bellanger, "FS-FBMC: An alternative scheme for filter bank based multicarrier transmission," in *Proceedings of the 5th International Symposium on Communications Control and Signal Processing*, 2012.

[112] R. Nissel, S. Schwarz, and M. Rupp, "Filter Bank Multicarrier Modulation Schemes for Future Mobile Communications," *IEEE Journal on Selected Areas in Communications*, vol. 35, no. 8, pp. 1768–1782, 2017.

[113] S. Cecchi, A. Terenzi, V. Bruschi, A. Carini, and S. Orcioni, "A subband implementation of a multichannel and multiple position adaptive room response equalizer," *Applied Acoustics*, vol. 173, pp. 1–12, 2021.

[114] W. Kellermann, "Analysis and Design of Multirate Systems for Cancellation of Acoustical Echoes." in *Proceedings of the IEEE International Conference on Acoustics, Speech, and Signal Processing*, 1988.

[115] A. Gilloire and M. Vetterli, "Adaptive Filtering in Subbands with Critical Sampling: Analysis, Experiments, and Application to Acoustic Echo Cancellation," *IEEE Transactions on Signal Processing*, vol. 40, no. 8, pp. 1862–1875, 1992.

[116] S. J. Park, J. H. Yun, Y. C. Park, and D. H. Youn, "A Delayless Subband Active Noise Control System for Wideband Noise Control," *IEEE Transactions on Speech and Audio Processing*, vol. 9, no. 8, pp. 892–899, 2001.

[117] J. Cheer and S. Daley, "An Investigation of Delayless Subband Adaptive Filtering for Multi-Input Multi-Output Active Noise Control Applications," *IEEE/ACM Transactions on Audio, Speech, and Language Processing*, vol. 25, no. 2, pp. 359–373, 2017.

[118] P. P. Vaidyanathan, "Multirate Digital Filters, Filter Banks, Polyphase Networks, and Applications: A Tutorial," *Proceedings of the IEEE*, vol. 78, no. 1, pp. 56–93, 1990.

[119] Norbert Fliege, *Multirate Digital Signal Processing: Multirate Systems, Filter Banks, Wavelets.* New York: John Wiley & Sons, 1994.

[120] G. J. Dolecek, *Advances in multirate systems.* New York: Springer, 2018.

[121] L. Milić, *Multirate Filtering for Digital Signal Processing: MATLAB Applications*. London: Information Science Reference, 2008.

[122] K. A. Lee, W. S. Gan, and S. M. Kuo, *Subband Adaptive Filtering: Theory and Implementation*. New York: John Wiley & Sons, 2010.

[123] P. P. Vaidyanathan, "Quadrature Mirror Filter Banks, M-Band Extensions and Perfect-Reconstruction Techniques," *IEEE ASSP Magazine*, vol. 4, no. 3, pp. 4–20, 1987.

[124] T. Q. Nguyen, "Near-Perfect-Reconstruction Pseudo-QMF Banks," *IEEE Transactions on Signal Processing*, vol. 42, no. 1, pp. 65–76, 1994.

[125] S. Weiss, L. Lampe, and R. W. Stewart, "Efficient subband adaptive filtering with oversampled GDFT filter banks," in *Proocedings of the IEE Colloquium Adaptive Signal Processing for Mobile Communication Systems*, 1997.

[126] K. Nayebi, T. P. Barnwell, and M. J. Smith, "Nonuniform Filter Banks: A Reconstruction and Design Theory," *IEEE Transactions on Signal Processing*, vol. 41, no. 3, pp. 1114–1127, 1993.

[127] P. Q. Hoang and P. P. Vaidyanathan, "Non-Uniform Multirate Filter Banks: Theory and Design," in *Proceedings of the IEEE International Symposium on Circuits and Systems*, 1989.

[128] M. Harteneck, S. Weiss, and R. W. Stewart, "Design of Near Perfect Reconstruction Oversampled Filter Banks for Subband Adaptive Filters," *IEEE Transactions on Circuits and Systems II: Analog and Digital Signal Processing*, vol. 46, no. 8, pp. 1081–1085, 1999.

[129] H. Kuttruff, *Room Acoustics*. London: Spon Press, 2009.

[130] J. G. Proakis and D. G. Manolakis, *Digital Signal Processing*. New Jersey: Prentice Hall, 2006.

[131] L. Vindrola, M. Melon, J. C. Chamard, and B. Gazengel, "Pressure Matching With Forced Filters for Personal Sound Zones Application," *Journal of the Audio Engineering Society*, vol. 68, no. 11, pp. 832–842, 2020.

[132] F. Jacobsen, M. Olsen, M. B. Møller, and F. Agerkvist, "A comparison of two strategies for generating sound zones in a room," in *Proceedings of the 18th International Congress on Sound and Vibration*, 2011, pp. 10–14.

[133] P. Coleman, P. J. Jackson, M. Olik, M. B. Møller, M. Olsen, and J. A. Pedersen, "Acoustic contrast, planarity and robustness of sound zone methods using a circular loudspeaker array," *The Journal of the Acoustical Society of America*, vol. 135, pp. 1929–1940, 2014.

[134] P. A. Naylor, *Speech Dereverberation*. London: Springer, 2010.

[135] Q. Zhu, P. Coleman, M. Wu, and J. Yang, "Robust Acoustic Contrast Control with Reduced In-situ Measurement by Acoustic Modeling," *Journal of the Audio Engineering Society*, vol. 65, no. 6, pp. 460–473, 2017.

[136] D. G. Beech, M. G. Kendall, and A. Stuart, *The Advanced Theory of Statistics, Volume 1: Distribution Theory*. London: Charles Griffin & Company, 1959.

[137] C. H. Jeong, "Kurtosis of room impulse responses as a diffuseness measure for reverberation chambers," *The Journal of the Acoustical Society of America*, vol. 139, no. 5, pp. 2833–2841, 2016.

[138] P. Bloomfield, *Fourier Analysis of Time Series: An Introduction*. New York: Wiley, 1976.

[139] "Beyma Loudspeaker AL-5""MP60/N 8 OH." [Online] Available: https://www.beyma.com/en/products/c/low-mid-frequency/205MP6N8/altavoz-5mp60-n-8-oh/. Accessed: 2022-04-07

[140] "Beyma Loudspeaker T-2030 8 OH." [Online] Available: https://www.beyma.com/productos/c/dome-tweeter/2TW20308/twt-t-2030-8-oh/. Accessed: 2022-04-07

[141] "BLAS (Basic Linear Algebra Subprograms)." [Online] Available: http://www.netlib.org/blas/. Accessed: 2022-04-07

[142] "Intel® oneAPI Math Kernel Library (MKL)." [Online] Available: https://www.intel.com/content/www/us/en/develop/documentation/get-started-with-mkl-for-dpcpp/top.html. Accessed: 2022-04-07

[143] "LAPACK (Linear Algebra PACKage)." [Online] Available: http://www.netlib.org/lapack/. Accessed: 2022-04-07

[144] "FFTW (Fastest Fourier Transform in the West)." [Online] Available: https://www.fftw.org/. Accessed: 2022-04-07

[145] V. Molés-Cases, "PSZ toolbox." [Online] Available: https://github.com/VicentMolesCases/PSZtoolbox. Accessed: 2022-05-24

[146] M. Frigo and S. G. Johnson, "FFTW manual," Technical Report, 2020.

[147] E. Anderson, J. Dongarra, and S. Ostrouchov, "LAPACK Working Note 41 Installation Guide for LAPACK," Technical Report, 1994.

[148] S. Weiss, M. Harteneck, and R. W. Stewart, "On Implementation and Design of Filter Banks for Subband Adaptive Systems," in *Proceedings of the IEEE Workshop on Signal Processing Systems*, 1998.

[149] M. Rossi, J. Y. Zhang, and W. Steenaart, "Iterative Least Squares Design of Perfect Reconstruction QMF Banks," in *Proocedings of the Canadian Conference on Electrical and Computer Engineering*, 1996.